Siderophile element systematics and Hf-Os isotope signatures of carbonatites: Insights into the origin of Earth's most unusual magmas

KATHARINA MARGRET SCHWEITZER

Siderophile element systematics and Hf-Os isotope signatures of carbonatites: Insights into the origin of Earth's most unusual magmas

Thesis submitted for the degree of Ph.D.

Department of Earth Sciences

Durham University, United Kingdom

in collaboration with

Steinmann Institut für Geologie, Paläontologie und Mineralogie

Rheinische Friedrich-Wilhelms-Universität Bonn, Germany

December 2018

Katharina Margret Schweitzer

Student ID 000631204

„Believe you can and you're halfway there."

–Theodore Roosevelt

Statement given upon oath

I hereby confirm, that the PhD thesis in hand with the title:

"Siderophile element systematics and Hf-Os isotope signatures of carbonatites: Insights into the origin of Earth's most unusual magmas"

was written independently and without illegitimate outside help. I have not used references and methods other than described and I have highlighted all corresponding quotes. This work has not been handed in to any other jury in this or a similar form.

Karlsruhe, 13.05.2019 K Schweitzer

Place, date Katharina M. Schweitzer

Abstract

Carbonatites are considered to be one of the most unusual magmas on Earth, but their source and genesis remain poorly understood and the subject of much debate. Chemical exchange with the mantle and/or crust, and re-equilibration during post-magmatic processes can lead to open system behaviour of carbonatites on a whole-rock scale, thereby hampering identification and characterisation of the carbonatitic source. To date, only a small number of studies have addressed carbonatite genesis using Lu-Hf or Re-Os isotope systems. In this thesis I present the first combined Lu-Hf, Sm-Nd, Rb-Sr and Re-Os isotope data together with highly siderophile element abundances to address carbonatite genesis, identify the source of carbonatites and to understand secular changes of the mantle they are sourced by throughout time.

Samples from ten different global localities were studied at the whole-rock, carbonate, non-carbonate, and mineral scale, varying in age from present day to ca. 3 Ga and covering four different carbonatite compositional types. Existing methods to successfully analyse the different isotope systems were assessed and improved in order to deal with the unusually Ca-rich matrix of carbonatites. These methods were then applied to three separate studies: 1) a global lithophile element isotope study, 2) a global whole-rock Re-Os isotope and HSE abundances study and 3) a combined lithophile and Re-Os isotope case study of the Fen complex in Norway. In all three projects, carbonatites are shown to record open system behaviour, resulting in implausible age corrected εHf values (<initial of Earth) for most carbonate fractions and many whole-rock samples, Lu-Hf isotopic disequilibrium between carbonate and non-carbonate fractions that yield isochron ages that do not match the published ages, as well as equally inapplicable $^{187}Os/^{188}Os$ ratios at time of eruption (<0 to 259).

The combined geochemical and petrographic data presented in this thesis demonstrate that: 1) carbonatites have experienced a complex petrological history influenced by post-magmatic processes; 2) results obtained on the whole-rock, carbonate and non-carbonate scale must be considered with great caution; 3) young carbonatites (*e.g.* Oldoinyo Lengai and Fogo) are less influenced by post-emplacement radiogenic ingrowth and can thus retain source information; and 4) the non-carbonate fractions of carbonatites are less affected by post-emplacement processes and for Hf and Nd isotopes record a close to chondritic uniform mantle source over time. Further understanding on the origin and petrogenetic evolution of carbonatites requires isotope investigation at the scale of individual minerals (*e.g.* calcite, dolomite, apatite, magnetite, phlogopite, BMS) together with a detailed geochemical and petrographic characterisation.

Acknowledgements

It is no secret that working with carbonatites in the lab is difficult. There were ups and downs and I am happy to now be able to present these results, but I would not have come as far without the help of a lot of different people:

First of all, I would like to thank my supervisory team Geoff Nowell, Kevin Burton and Ambre Luguet for giving me the opportunity to work on this project, for expanding my knowledge and for helping me improve trouble shooting skills.

Thank you also to: Frances Wall, the Natural History Museum in London, Lotte Larsen, Hilary Downes, Kate Moore, Sam Broom-Fendley and Thomas Meisel for providing or helping me in getting my samples. Special thanks also go to Sven Dahlgren for organising the field trip to the Fen carbonatite complex. Edward Inglis is thanked for help regarding the stable Fe analyses (appendix) and Giacomo Pozzi and Geoff Nowell are thanked for visiting my first ever carbonatite outcrop with me in Assynt. Additionally, Malcom Spence and Sven Oliver Franz are kindly thanked for performing major element analyses on the XRF for me. Thank you also to Kirsten Drüppel and Elisabeth Eiche from KIT for allowing me to use the microscope at AGW KIT, Karlsruhe.

I would also like to thank a lot of staff from Durham University for being of assistance regarding this project or organisational matters: Chris Ottley, Ian Chaplin, Sophie Edwards, Chris Dale, Dave Selby, Karen Atkinson, Paula Elliott, Jeroen van Hunen, Jo Banner, Laura Haswell and James Dyson.

Thank you also to my review team, Ed Llewellin and Dave Selby, who prepared me well for my viva and always had thought-provoking questions.

Sally Gibson and Julie Prytulak: Thank you for taking the time to read through this piece of work and for judging it.

Antonia and Dominikus, where shall I beGIN? Thank you for supporting me throughout my time in Durham, for a lot of lovely memories, for helping me out in the field, and always giving honest feedback, both regarding my work and in personal matters! It would have not been the same without you!

Special thanks also go to the rest of the Durham gang, where I especially want to mention my lab buddies Fienke, Kate H., Kate G., Alex M., Mathieu and Jo P. but also several people

that made my time in Durham memorable: Jo H., Antonio, Nico, Christian, Mateja, Erin, Alex L. and many many more.

Mario Valdivia-Manchego, thank you for a lot of inspiration regarding teaching and outreach and for making geology so interesting for me in the first place.

I would also like to thank two of my closest friends: Rana and Thea, thank you for being there for me in difficult times, for skyping with me week after week and for making me feel better when it was much needed.

Caspar, thank you for coming to the UK with me in 2015 and for supporting my decision to leave Germany and study abroad. I am happy that we found each other and am looking forward to a bright future, wherever it may take us!

Last but not least, I would like to thank my family, for always being there for me, for supporting me in every possible way, for following every step I take and for never letting me down. Thank you for every opportunity you gave me, for a lovely childhood and for catching me when I fall!

Kathi

Table of contents

List of abbreviations

Element groups

HFSE	High field strength elements
HSE	Highly siderophile elements
LILE	Large ion lithophile elements
PGE	Platinum group elements
IPGE	Ir-group PGEs
PPGE	Pt-group PGEs
REE	Rare earth elements
LREE	Light rare earth elements
HREE	Heavy rare earth elements

Mineral fractions

BMS	Base metal sulphides
PGM	Platinum group mineral
C	Carbonate fraction
NC	Non-carbonate fraction
WR/B	Whole-rock/bulk
CC	Calcite
Mt/M	Magnetite
H	Hematite
Cpx	Clinopyroxene
Po	Pyrrhotite
Py	Pyrite
Sph	Sphalerite
Cp	Chalcopyrite
Pn	Pentlandite

Terrestrial reservoirs/melts

BSE	Bulk silicate Earth
CHUR	Chondritic uniform reservoir
DMM	Depleted MORB mantle
EM1	Enriched mantle 1
EM2	Enriched mantle 2
HIMU	High μ
MORB	Mid-ocean ridge basalt
OIB	Ocean island basalt
PUM	Primitive upper mantle

Instruments and methods

ESI	Elemental Scientific Incorporation
PFA	Perfluoroether
PTX	Pressure-temperature-composition
2SD	2× standard deviation
2SE	2× standard error
bdl	Below detection limit
cps	Counts per second
TPB	Total procedural blanks
HPA-S	High pressure Asher
CT	Carius tube
ICP-MS	Inductively coupled plasma mass spectrometry (HR = high resolution, MC = multi-collector, Q = quadrupole)
N-TIMS	Negative thermal ionisation mass spectrometry
MQ	Milli-Q, ultrapure water (18.2 MΩ*cm at 25°C)

Concentrations

ppm	parts per million (µg/g)
ppb	parts per billion (ng/g)
ppt	parts per trillion (pg/g)

Others

fO_2	Oxygen fugacity
fS_2	Sulphur fugacity
FMQ	Fayalite-magnetite-quartz buffer
SCSS	Sulphur contents at sulphide saturation
WP	Waypoint

Formulas used

Calculations for initial values	$D_t = D - N(e^{\lambda t}-1)$
Calculations for epsilon values	$\varepsilon = ((D_{sample}/D_{chondrite}) -1) \times 10{,}000$
Calculations for delta values	$\delta = ((D_{sample}/D_{standard}) -1) \times 1{,}000$
Calculation for T_{MA} model age	$T_{MA} = 1/\lambda \times \ln ((D_{chondrite} - D_{sample})/(N_{chondrite} - N_{sample}) + 1)$
Fayalite-Magnetite-Quartz buffer	$\log fO_2 = -24{,}441.9/T + 8.29$ (1 kbar, 600°C-1140°C, Myers and Eugster, 1983)

*with D = daughter isotope ratio, N = parent isotope ratio, λ = decay constant and t = age in years (a)

List of figures

Chapter 1 - Introduction

Chapter 2 - Petrography

Chapter 3 - Methods

Chapter 4 - Major and trace elements

Chapter 5 - Lithophile element isotope study

Chapter 6 - Highly siderophile elements and Re-Os isotope study

Chapter 7 - Case study - The Fen complex

Chapter 8 - Summary and overall conclusion

Chapter 10 - Appendix

List of tables

Chapter 1 - Introduction

Chapter 2 - Petrography

Chapter 3 - Methods

Chapter 4 - Major and trace elements

Chapter 5 - Lithophile element isotope studies

Chapter 6 - Highly siderophile elements and Re-Os isotope study

Chapter 7 - Case study - The Fen complex

Chapter 10 - Appendix

Chapter 1 : Introduction

1.1. What are carbonatites?

Carbonatites are magmatic, carbonate-rich (>50 wt%, Streckeisen, 1979, 1978) silica-poor (<20 wt%, Maitre et al., 2002) rocks, which are often (80% of all carbonatites, Woolley and Kjarsgaard, 2008) associated with alkaline igneous complexes. They are characterized by high Light Rare Earth Element (LREE) and other trace element (Ba, Sr, Nb, Th, U) concentrations (*i.e.* LREE up to 10,000× the concentration of chondrite, Nelson et al., 1988). They also have a low melting temperature (*e.g.* Oldoinyo Lengai lava <600°C, Dawson et al., 1990; Jones et al., 2013) and a low viscosity (0.008 to 0.155 Pas; Dobson et al., 1996; Wolff, 1994). As a consequence of their high mobility they have the potential to act as effective metasomatic agents, and are thought to percolate through mantle peridotites at a rate as high as several millimetres per hour by dissolution-precipitation processes (Hammouda and Laporte, 2000).

Carbonatites are commonly classified into five compositional types: 1) Calcite-carbonatite/calciocarbonatite, in which the main carbonate phase is calcite; 2) Dolomite carbonatite/magnesiocarbonatite, dominated by dolomite; 3) Natrocarbonatite, which has carbonate phases enriched in Na, K and Ca (Le Bas, 1981); 4) Ankerite carbonatite/Ferrocarbonatite, in which the main carbonate phase is Fe-rich; and 5) Silicocarbonatite, in which the SiO_2 content exceeds 20 wt% (Maitre et al., 2002). Only carbonatites with >80 wt.% CaO in relation to their MgO and FeO+Fe_2O_3+MnO-content are classified as calciocarbonatite, while anything <80 wt.% CaO but >50 wt.% of either MgO or FeO+Fe_2O_3+MnO is considered magnesiocarbonatite or ferrocarbonatite, respectively (Figure 1.1). Calciocarbonatites can be subdivided into *søvite* when they are fine grained and *alvikite* when they are coarse grained. Alternative names for magnesiocarbonatites are *rauhaugite* or *beforsite* (Maitre et al., 2002). Natrocarbonatites only occur at Oldoinyo Lengai in Tanzania. Hence, they are excluded from the classification diagram (Figure 1.1). At Oldoinyo Lengai the cationic abundances follow Na>Ca>K>Mg>Fe, whereas in all other carbonatites it is usually Ca>Mg>Fe>Na+K (Le Bas, 1981).

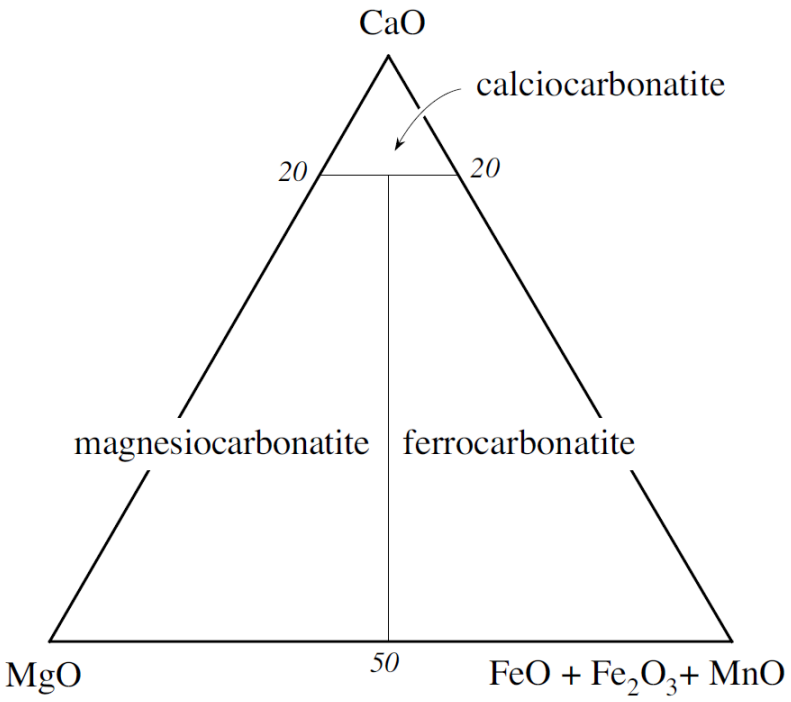

Figure 1.1 **Discrimination diagram for carbonatites with SiO_2 <20% using wt.% of major oxides (Woolley and Kempe, 1989).**

Roughly 90% of the known carbonatites are formed either in plutonic or hypabyssal environments and only about 10% are extrusive (Woolley and Church, 2005). These latter 10% comprise 49 known occurrences, of which half are associated with tephra cones, tuff rings, maars and diatremes (*e.g.* Cupaello, Italy; Melkfontain, South Africa; Woolley and Church, 2005), while the other half are associated with large volcanoes (*e.g.* Kaiserstuhl, Germany; Oldoinyo Lengai, Tanzania; Woolley and Church, 2005), which are generally strato-volcanoes. Small volcanic edifices (*e.g.* tephra cones, tuff rings, maars and diatremes) are formed by high energy eruptions, which are thought to be more likely to preserve the geochemical signature of the source and generally occur in association with only small volumes of silicate melt (Woolley and Church, 2005). This combined with the unique compositions of carbonatites, leads to the suggestion that carbonatites are genetically related to lamproites and kimberlites (*e.g.* Tappe et al., 2008). In comparison, carbonatites found in association with strato-volcanoes are linked with larger volumes of silicate melt and follow a more complex genesis, such as melt separation by immiscibility or fractional crystallisation within the mantle or crust (Woolley and Church, 2005).

Differentiation of carbonatite magmas

Carbonatite emplacement sequences have been described by several authors in the past (Dixon and Collins, 1977; Gaspar and Wyllie, 1983; Le Bas, 1981) and appear to be similar for several localities (*e.g.* Jacupiranga, Brazil; Ruri, Kenya). Le Bas (1981) describes the first sequence (C1) as the earliest carbonatite emplacement, usually made up of søvite. Sequence C1 is followed by an alvikite and magnesiocarbonatite sequence (C2), which can be found as swarms of dykes and cone-sheets. Sequence C3 consists mainly of ferrocarbonatite dykes and veins which crosscut sequences C1 and C2 and is followed by a late-stage residual calciocarbonatite sequence (C4) in the form of thin veins. Gaspar and Wyllie, (1983) also describe a later C5 sequence in Jacupiranga that is mainly made up of rauhaugite. This observed intrusion sequence follows the crystal fractionation sequence of carbonatites which was determined by Rosenberg (1967) and Wyllie (1965) whilst studying the $CaCO_3$-$MgCO_3$-$FeCO_3$ system. Differentiation further becomes evident when using the most abundant trace elements, Sr, Ba, REE and Mn: Sr decreases with differentiation of the carbonatite melts, while Ba, Mn and the REE increase by an order of magnitude (Le Bas, 1981). When taking into account oxygen isotopes, sequence C1 søvite as well as natrocarbonatite show $\delta^{18}O$ values less than +10, while later sequences possess $\delta^{18}O$ values of +30 (Suwa et al., 1975).

Petrography

Carbonatites are among the most unusual rocks in terms of their mineralogy. Carbonatite forming minerals are calcite, dolomite, ankerite, siderite, apatite and Na- and K-carbonates (*e.g.* nyerereite and gregoryite). Less common minerals associated with carbonatites include for example, bastnäsite, pyrochlore, calzirtite, arfvedsonite, barite, strontianite, parisite, xenotime or vermiculite. Further common mineral phases in carbonatites include phlogopite, monazite, magnetite, fluorite, base metal sulphides, aegirine, aegirine-augite, baddeleyite, ilmenite, perovskite, zirconolite, zircon, orthoclase, olivine, thorite and uraninite (Chakhmouradian, 2006; Le Bas, 1981; Woolley and Kjarsgaard, 2008). Mineral formulas are given in the appendix (Table 10.1).

Economic interest

There are 102 economically viable mines and resources recorded, of which 31 are still actively mined (Woolley and Kjarsgaard, 2008). Carbonatites were and are mined for copper (*e.g.* Phalaborwa, South Africa), iron (*e.g.* Fen, Norway; Bugge, 1978; Notholt et al., 1990), phosphate (*e.g.* Phalaborwa, South Africa and Kovdor, Russia; Petrov, 2004), lime (*e.g.* Koru, Kenya; van Straaten, 2002), pyrochlore/niobium (*e.g.* Oka, Canada; Richardson and Birkett,

1996; Rowe, 1958), tantalum (*e.g.* Verity, Canada; Commerce Resources Corporation, 2007), fluorite (*e.g.* Amba Dongar, India; Mariano, 1989; Notholt et al., 1990), vermiculite (*e.g.* Sevvatur, India; Notholt et al., 1990), rare earth elements (*e.g.* Bayan Obo, China; Notholt et al., 1990), titanium (*e.g*. Tapira, Brazil; Biondi, 2005; Mariano, 1989), uranium-thorium (*e.g.* Sandkopsdrif, South Africa; Verwoerd, 1986), vanadium (*e.g.* Potash Sulphur Springs, USA; Woolley, 1987), olivine (*e.g.* Lesnaya Varaka, Russia; Petrov, 2004) and gold (*e.g.* Lac Shortt, Canada; *Canadian mines handbook.*). A growing demand for REE (5% growth per year until 2020; Dutta et al., 2016) in, for example, the industrial sector makes the REEs one of the most important natural resources that carbonatites are mined for. Minerals bearing precious REE include bastnäsite and monazite, but also apatite and xenotime. These minerals are commonly associated with igneous complexes comprised of alkaline rocks and carbonatites (Long et al., 2010) with carbonatites currently being the largest REE deposits (Van Gosen et al., 2014).

Fenitisation

The process of fenitisation was named after the alteration of country rock gneiss by alkaline fluids released during emplacement of the Fen alkaline complex (Brøgger, 1921). Rocks experiencing this type of metasomatic overprinting are called fenites and a comprehensive review of fenites is given by Elliott et al. (2018). However, fenitisation was observed much earlier at the contact of nepheline syenite and gneiss country rock in Alnö in Sweden by Högbom (1893). Here, Högbom describes the fenite as a 150-300 m wide border zone between the nepheline syenite and gneiss comprised mainly of an orthoclase-albite and occasionally microcline-albite perthite. At the type locality of fenite in the Norwegian Fen complex, Brøgger (1921) defines fenites as rocks created by the reaction between the ijolite-melteigite series (pyroxene-nepheline rocks) with the country rock gneiss. They are described as leucocratic rocks with 70 to >90% alkali feldspar (micro- and cryptoperthite) and 30 to <10% accessory minerals (*e.g.* aegirine, hornblende, arfvedsonite, titanite, apatite, calcite, pyrite, biotite, magnetite, quartz, limonite, fuorite, hematite; *e.g.* Brøgger, 1921; Högbom, 1893; Le Bas, 1981). Fenites are further characterised by a general increase in alkalis (Na_2O+K_2O) (Bardina and Popov, 1994). However, they are not only related to the emplacement of alkaline rocks such as ijolite but can also be found associated with carbonatite emplacement. Fenites can form zones of ≥100 m width surrounding, for example, søvite but are also known adjacent to alvikite dikes and cone-sheets (Le Bas, 1981). Fluids released during cooling of carbonatitic or alkaline magmas are a major constituent of the intruding melt. Thus, characterisation of fenites is essential to understand the original

composition of carbonatite melts (Elliott et al., 2018). The loss of alkalis from carbonatites or other alkaline rocks (*e.g.* ijolite) due to the fenitisation processes (Woolley, 1969) has led to the conclusion that chemical analyses of whole rock carbonatites do not represent the chemistry of the source from which carbonatites are derived, but rather reflects the result of extensive re-crystallisation processes (Barker, 1989). For example, not only loss of volatile components changes the composition of the original carbonatite melt, but secondary alteration can further result in the growth of secondary REE-enriched minerals as well as dolomitisation (Woolley and Church, 2005).

Carbonatite metasomatism

As mentioned previously, carbonatites are thought to be efficient metasomatic agents in Earth's mantle, as has been observed in a number of studies (*e.g.* Gorring and Kay, 2000; Green and Wallace, 1988; Hauri et al., 1993; Pokhilenko et al., 2015). Examples for evidence of carbonatite metasomatism in peridotites include for instance the presence of accessory carbonate, monazite and apatite, high Na_2O/Al_2O_3 and CaO/Al_2O_3 ratios, extreme large ion lithophile element (LILE) and LREE enrichment, low Ti/Eu ratios, high Zr/Hf and La/Yb ratios, high field strength element (HFSE) depletion, Th and U enrichment or redistribution/mobilisation of platinum group elements (PGEs; Akizawa et al., 2017; Gorring and Kay, 2000; Rudnick et al., 1993; Yaxley et al., 1998, 1991). Modelling of carbonatites as potential metasomatic agent in Earth's mantle is increasingly common, thus for a better understanding of carbonatite metasomatism, a global database of carbonatites is essential.

1.2. Origin and Genesis

Strontium, Nd, and Pb isotope ratios of carbonatites are similar to those of nephelinites and alkali basalts associated with carbonatites and differ clearly from sedimentary carbonates (Bell et al., 1973; Lancelot and Allègre, 1974; Pineau and Allègre, 1972; Richard et al., 1974), which is taken to suggest a mantle origin for carbonatites (Le Bas, 1981). A study of Mg, C, Sr, Nd and O isotopes in carbonatites found light $\delta^{26}Mg$ and slightly heavy $\delta^{13}C$ as well as mantle-like signatures for Nd-Sr-O isotopes in magnesiocarbonatites, which when combined suggest a deep mantle origin with involvement of recycled sedimentary carbonates (Cheng et al., 2017). An influence from subducted oceanic crust in carbonatitic melt evolution has also been suggested by Walter et al. (2008). In contrast, Mata et al. (2010) suggest a mantle origin for carbon in carbonatites. However, all three studies (Cheng et al., 2017; Mata et al., 2010; Walter et al., 2008) suggest that a mantle plume is involved in producing the carbonatite melt and aiding transport from the deep mantle or transition zone. The involvement of a mantle plume in the genesis of carbonatites has also been suggested by

several other authors (*e.g.* Bell, 2001; Bell et al., 2004; Holm et al., 2006). Further evidence for a mantle origin for carbonatites was presented by Woolley and Church (2005) who noted the presence of mantle xenoliths and xenocrysts within carbonatite bodies. They suggest that this was caused by energetic emplacement ensuring preservation of denser sample material within the carbonatites and is thought to indicate that some carbonatites have not formed by crystal fractionation or immiscibility processes. However, mantle xenoliths are not a common feature of carbonatites and only 16 out of the 49 extrusive carbonatites contain mantle xenoliths or megacrysts (Woolley and Church, 2005).

Fluid inclusions in apatite have been used to estimate the composition of the original carbonatite melt, which led to the suggestion of an alkali- and sulphate-rich carbonatite magma (Aspden, 1981, 1980, 1977; Le Bas, 1981; Rankin, 1977). Le Bas (1981) suggests that, while this original carbonatite magma cools and crystallises, it loses the majority of its alkalis by reacting with the surrounding crust (fenitisation) leaving behind a Ca-rich carbonatite body derived from something close to natrocarbonatite.

Each carbonatite locality appears to have experienced a different petrological history and although it is clear that carbonatites are derived from the mantle, their source and genesis remain highly debated (*e.g.* Le Bas, 1989; Lentz, 1999; Nelson et al., 1988; Nielsen and Veksler, 2002; Pirajno, 2015; Veksler and Lentz, 2006; Watkinson and Wyllie, 1971). This has led to several theories on how these melts have formed, including:

1) *Carbonatites are direct products of low-degree partial melting of a carbonated mantle source.* This hypothesis is based on the high abundance of LREE, which is thought to be caused by < 1% melting of a CO_2- and volatile-rich source influenced by subducted oceanic lithosphere (Nelson et al., 1988). Sweeney (1994) and Wallace and Green (1988) proposed that carbonatites might originate from carbonate liquids derived from partial melting of a carbonated lithospheric mantle (*i.e.* carbonated by decarbonation of subducted slabs or transport of carbonates into great depths, Huang et al., 1975; Schrauder and Navon, 1993) or a source such as a carbonated eclogite (Pirajno, 2015). Based on experimental data by Gudfinnsson and Presnall (2005) and Veksler and Lentz (2006) it is suggested that carbonate melts may be generated at depths greater than 70 km, which in theory makes this scenario possible.

2) *Carbonatites are formed by immiscibility from a carbonated silicate melt.*
The studies of Hamilton et al. (1979), Freestone and Hamilton (1980), Le Bas (1981) and Amundsen, (1987) were amongst the first to suggest that carbonatites are derived

from an originally homogeneous carbonated silicate melt by immiscible liquid separation. Two decades later, Veksler and Lentz (2006) carried out experiments in which they detected silicate-carbonate immiscibility from peralkaline nephelinitic magmas under the microscope. This experiment showed that immiscible separation from a carbonated silicate melt is a possible scenario for carbonatite formation and would also support the association with other alkaline igneous complexes.

3) *Carbonatites are a result of crystal fractionation from a carbonated alkali-rich silicate melt.*

On the other hand, Watkinson and Wyllie (1971), Gittins (1989) and Gittins and Jago (1998) have suggested that carbonatites form by fractional crystallisation of a mantle-derived alkali-rich silicate melt at crustal pressures. Phase equilibrium suggests that minerals such as nepheline or melilite crystallise first, leaving behind a CO_2-rich residual fluid (Watkinson and Wyllie, 1971). This is followed by further removal of the remaining alkalis by fenitisation processes and finally crystallisation of carbonate minerals (Pirajno, 2015; Watkinson and Wyllie, 1971).

4) *Carbonatites can be products of contact metasomatism between intrusions and carbonate wall rock.*

Lentz (1999) has described the possibility of carbonatite formation by flux melting of carbonates. He suggests that decarbonation reactions caused by hydrothermal activity found in skarn-forming environments, releases CO_2. Together with additional fluxes (*e.g.* H_2O, HF, HCl) derived from magma intrusion, flux melting can be triggered. However, Lentz (1999) makes the point that this is not an alternative model for mantle derived carbonatites, but a means of distinguishing between mantle and crustal derived carbonatites when trying to interpret their source.

Based on these different genesis models, Bell and Rukhlov (2004) compiled a list of criteria to evaluate the origin of carbonatites:

Table 1.1 Criteria to evaluate the origin of carbonatites (Bell and Rukhlov, 2004). Text in italic is modified from the original text.

Crystal fractionation	
1.	Composition transitional from early calcitic to late dolomitie-ankeritic or sideritic
2.	Associated with silicate rocks
3.	Silicate rocks transitional between parental melt and carbonatite
4.	Zoned phenocryst phases of appropriate compositions in silicate rocks
5.	Cumulate rocks such as clinopyroxenites, olivinites, calcite carbonatites
6.	Silicate rocks and carbonatites should have the same *initial* radiogenic isotopic signatures, assuming closed chemical behaviour*
Direct partial melting	
1.	Composition mainly dolomitic
2.	Few, if any, related silicate rocks
3.	Rocks should have high Ni and Cr abundances, accompanied by high Mg#, *unless the source is strongly influenced by i.e. a recycled component*
4.	Silica contents should not be <~4 wt.%
Liquid immiscibility	
1.	Globules of carbonate-rich material with silicate matrix, and vice versa
2.	No silicate rocks of intermediate composition
3.	Phases in both silicate and carbonate-rich material of similar composition
4.	Distribution coefficients for element abundances between silicate and carbonate rocks should be similar to those determined experimentally, although these are pressure-temperature-composition (PTX) dependent. Strong preference for Zr, Ta and other HFSE (except Nb) in the silicate liquids
5.	Silicate rocks and carbonatites should have the same *initial* radiogenic isotopic signatures, assuming closed chemical behaviour*

*Supporting, but not essential, evidence.

1.3. Scientific interest and objectives

As outlined before, the source and genesis of carbonatites remain highly debated. Re-equilibration in the mantle or crust can lead to open system behaviour for both the whole-rock and mineral phases. In addition to that, post-magmatic alteration can result in re-crystallisation and chemical re-equilibration of mineral phases. This makes identifying the source of carbonatites highly challenging. Additionally, the effect of carbonatite metasomatism appears to be more frequently documented and is poorly understood. Hence it is important to identify the origin of those melts and to understand the petrogenetic evolution of carbonatites as well as the evolution of their mantle source by using new approaches. The Lu-Hf, Re-Os and HSE abundances in carbonatites have been little studied and the global database for those elements is not representative (Bizimis et al., 2003; Bizzarro et al., 2002; Cheng et al., 2003; Escrig et al., 2005; Widom et al., 1999). Thus, the aim of this study is to:

- Establish a new method or improve already existing methods to increase yields and reliably analyse Hf isotopes in a carbonatite matrix
- Identify the source of carbonatites
- Better understand carbonatite petrogenesis
- Determine the potential compositional changes of Earth's mantle throughout time by looking at carbonatites of different ages
- Collect data to extend the global database for Lu-Hf and Re-Os isotopes as well as HSE abundances of carbonatites

This is approached by:

- Measuring Lu-Hf, Sm-Nd and Rb-Sr isotopes on whole-rock, carbonate and non-carbonate fractions of global carbonatites
- Analysing whole-rock Re-Os isotope signatures combined with HSE abundances of global carbonatites
- Conducting a case study on the Fen carbonatite complex using Lu-Hf, Sm-Nd, Rb-Sr and Re-Os isotopes together with HSE abundances

1.3.1. Radiogenic isotope systems

As mentioned in section 1.3, Lu-Hf and Re-Os isotope systematics together with highly siderophile element abundances in carbonatites have only been addressed by a limited number of studies. Hafnium is a lithophile element (*e.g.* McDonough, 2003), while the highly siderophile elements (HSE) are mostly found in base metal sulphides (BMS) in mantle samples (*e.g.* Mitchell and Keays, 1981; Luguet and Reisberg, 2016). In carbonatites both silicate and BMS can be found alongside the dominant carbonate minerals (*c.f.* chapter 1.1). Different geochemical behaviours as well as different host minerals for Lu-Hf and Re-Os isotopes could affect these systems in various different ways during partial melting, chemical exchange within the mantle, crustal contamination or post-magmatic processes. Therefore, the combined study of lithophile (Lu-Hf, Sm-Nd and Rb-Sr) and Re-Os isotope systems potentially provides new insights into the origin and genesis of carbonatite melts. A simplified illustration of the behaviour of the radiogenic isotope systems and highly siderophile element abundances in mantle-derived melts can be found in Figure 1.2.

Lithophile elements

Lutetium, Hf, Sm, Nd, Rb and Sr are all lithophile elements (Goldschmidt, 1937). Lutetium fractionates from Hf, and Sm from Nd during partial melting of the mantle (*c.f.* step 1, Figure 1.2). This is due to both Nd and Hf being more incompatible than Sm and Lu during melting, and results in lower Sm/Nd and Lu/Hf ratios in the melt compared to the residual mantle (*e.g.* Vervoort, 2015) though this fractionation is stronger for Lu-Hf than for Sm-Nd isotopes (Stosch, 2004). ^{176}Lu decays to ^{176}Hf by β- decay, which occurs with a half-life of 36.4 Ga (*e.g.* Kossert et al., 2013) and ^{147}Sm decays to ^{143}Nd by α decay with a half-life of 106 Ga (DePaolo and Wasserburg, 1976a). This leads to radiogenic ingrowth and an increase of the ^{176}Hf/^{177}Hf and ^{143}Nd/^{144}Nd ratio in the mantle residue over time (*c.f.* Figure 1.2). Similar behaviour of Nd and Hf in mantle processes results in the correlation of both isotope systems defined by a linear relationship called the “mantle array” (*e.g.* Vervoort et al., 1999). For Rb-Sr isotopes the opposite behaviour is observed: Rubidium behaves more incompatibly than Sr, leading to higher Rb/Sr ratios in the melt compared to the residual mantle. ^{87}Rb decays to ^{87}Sr by β-decay with a half-life of 48.8 Ga (Jäger, 1979; Steiger and Jäger, 1977). Over time this results in stronger radiogenic ingrowth and increase of ^{87}Sr/^{86}Sr in the melt compared to the mantle (*c.f.* step 1, Figure 1.2).

The crust has formed by melting from Earth’s mantle (*e.g.* Carlson, 1994; Condie, 1989). Thus, the crust has high Rb/Sr, but low Lu/Hf and Sm/Nd ratios compared to the residual mantle (Figure 1.2). Over time, radiogenic ingrowth will result in changes in the isotopic composition

of the mantle; hence partial melting in the mantle produces melts with time-integrated isotopic signatures. Furthermore, subduction can lead to recycling of crustal material and consequently to changes in the local isotopic signature of the mantle (Figure 1.2). This makes those three isotope systems powerful tools to trace crust-mantle processes such as recycling or contamination.

Highly siderophile elements and Re-Os isotopes

Rhenium behaves incompatibly, and Pt and Pd moderately incompatible during partial melting, whereas Os, Ir and Ru are compatible (*e.g.* Barnes et al., 1985; Day, 2013 and references therein). This results in fractionation of the highly siderophile elements (HSE) between partial melt and mantle residue and leads to high Re/Os ratios in the melt. ^{187}Re decays to ^{187}Os by emitting a β- particle with a half-life of ~42 Ga (Smoliar et al., 1996). Over time this leads to more substantial radiogenic ^{187}Os/^{188}Os ingrowth in the partial melt (*c.f.* step 1, Figure 1.2), compared to the residual mantle, which will also have radiogenic ingrowth, but is generally left with an unradiogenic ^{187}Os/^{188}Os signature. Due to the chalcophile behaviour of HSEs in Earth's silicate mantle (Mitchell and Keays, 1981), HSEs can be found in base metal sulphides, though Re can also be hosted by silicate phases (*e.g.* Burton et al., 1999). Base metal sulphides can be of residual or metasomatic origin and a sample can contain different generations of BMS. Different generations of BMS could have formed by, for example, partial melting itself, interaction with the mantle and crust during ascent (*c.f.* step 2 and 3, Figure 1.2) and/or post-magmatic alteration (*c.f.* step 4, Figure 1.2), each potentially recording a different Re-Os isotope or HSE signature.

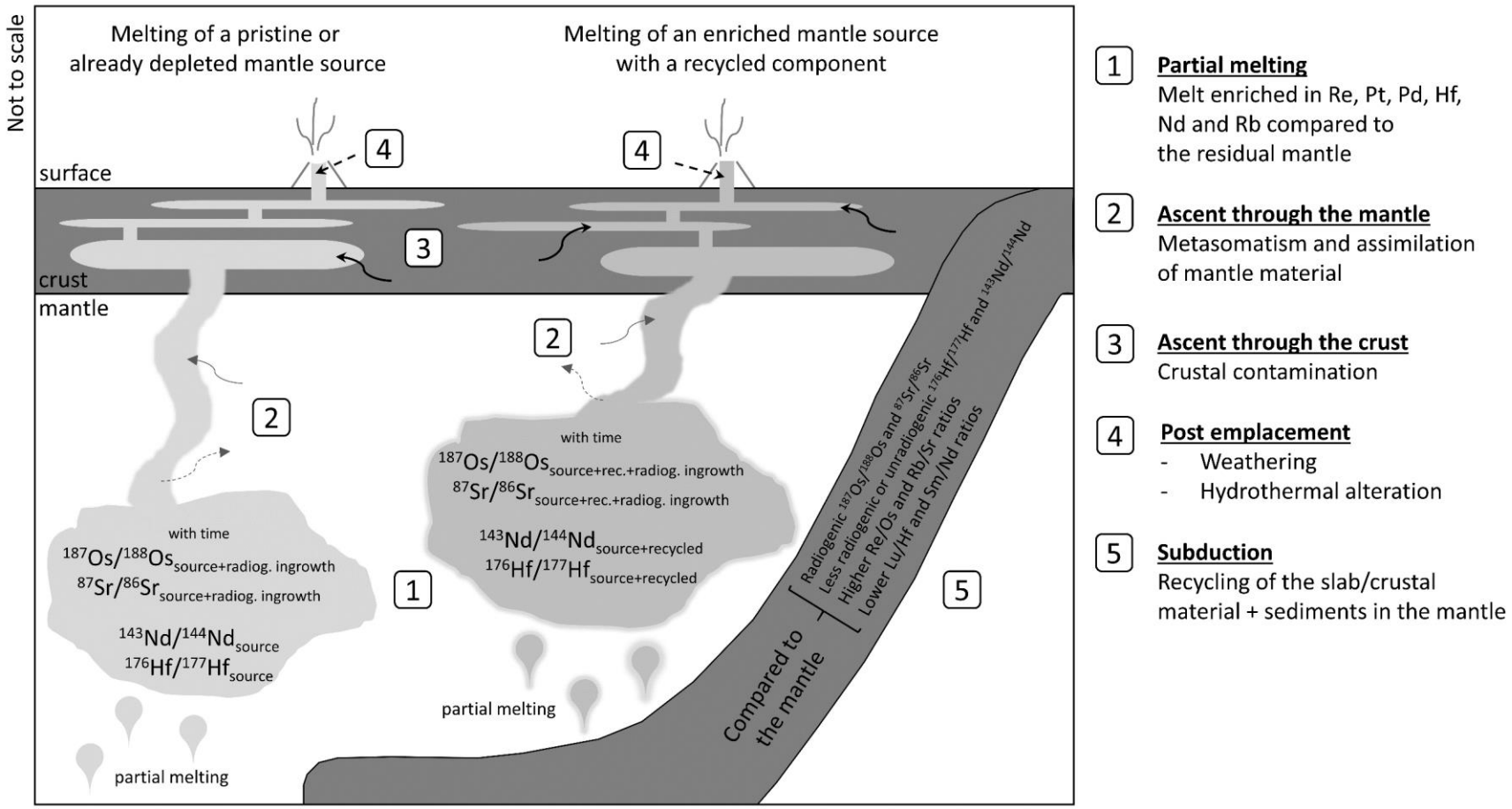

Figure 1.2 **Simplified illustration of the behaviour of the radiogenic isotope systems in mantle-derived melts. Ascent through mantle and crust can result in either chemical exchange with the mantle or crustal contamination, which can influence the isotope systems to different extents; for example, if mantle BMS are assimilated, HSEs could be re-enriched, thus possibly changing the $^{187}Os/^{188}Os$ signature of the melt. Weathering or hydrothermal alteration can further lead to elemental fractionation and can have an influence on the isotopic signatures. Each process and the according influence on the isotope system strongly depend on factors such as time, degree of partial melting, S-solubility, P-T-X conditions or the composition of overprinting fluids.**

1.4. Occurrences

There are currently 527 carbonatite occurrences described (Figure 1.3; Woolley and Kjarsgaard, 2008), of which 35% are found on the African continent adjacent to cratons or associated with the East African rift. The majority of carbonatites are located in intracontinental settings (*i.e.* continental intraplate volcanism), often associated to rifting, mantle plumes and/or close to orogenic belts (*e.g.* Jones et al., 2013; Marty et al., 1998; Widom et al., 1999). In contrast, only three carbonatite complexes are found in oceanic intraplate settings associated to mantle plumes, namely Cape Verde, the Canary Islands and Kerguelen (Woolley and Church, 2005). Carbonatites range in age from present day to 3007 Ma (Bizzarro et al., 2002).

1.4.1. Sample localities from this study

Oldoinyo Lengai, Tanzania

The Oldoinyo Lengai volcano is located in the East African Rift (Gregory Rift), south of Lake Natron in Tanzania and is currently the only active carbonatite volcano. Early volcanic activity at Oldoinyo Lengai started with nephelinitic and phonolitic eruptions which were then followed by natrocarbonatite lava and ash eruptions (Dawson, 1989). Volumetrically, Oldoinyo Lengai has produced more silicate magmas (*e.g.* Klaudius and Keller, 2006) but due to its unique natrocarbonatite lavas and strongly alkaline composition, it has become one of the most interesting carbonatites to study as an endmember of such melts. In this study we have analysed two samples from Oldoinyo Lengai.

Fogo, Cape Verde

Fogo island is one of ten islands in the Cape Verde archipelago located in the Atlantic off the coast of Senegal and Mauritania. Carbonatites found on Fogo island belong to the rare group of oceanic intraplate carbonatites. The only other oceanic carbonatites can be found in Fuerteventura, Kerguelen and other Cape Verde islands (Woolley and Kjarsgaard, 2008). The carbonatitic and alkaline magmas forming the islands of Cape Verde are thought to be related to a mantle plume of which Fogo is believed to be located above the central part of the plume (Courtney and White, 1986; White, 1989). The carbonatite eruption is dated to 3.2-5.1 Ma (K-Ar on biotite, *e.g.* Lancelot and Allègre, 1974; Madeira et al., 2005) and is thought to be part of the older basement of Fogo and Brava island (Assunção et al., 1966; Madeira et al., 2005). Carbonatites found on Fogo are all described as søvite (Hoernle et al., 2002). Two samples from Fogo were investigated in this study.

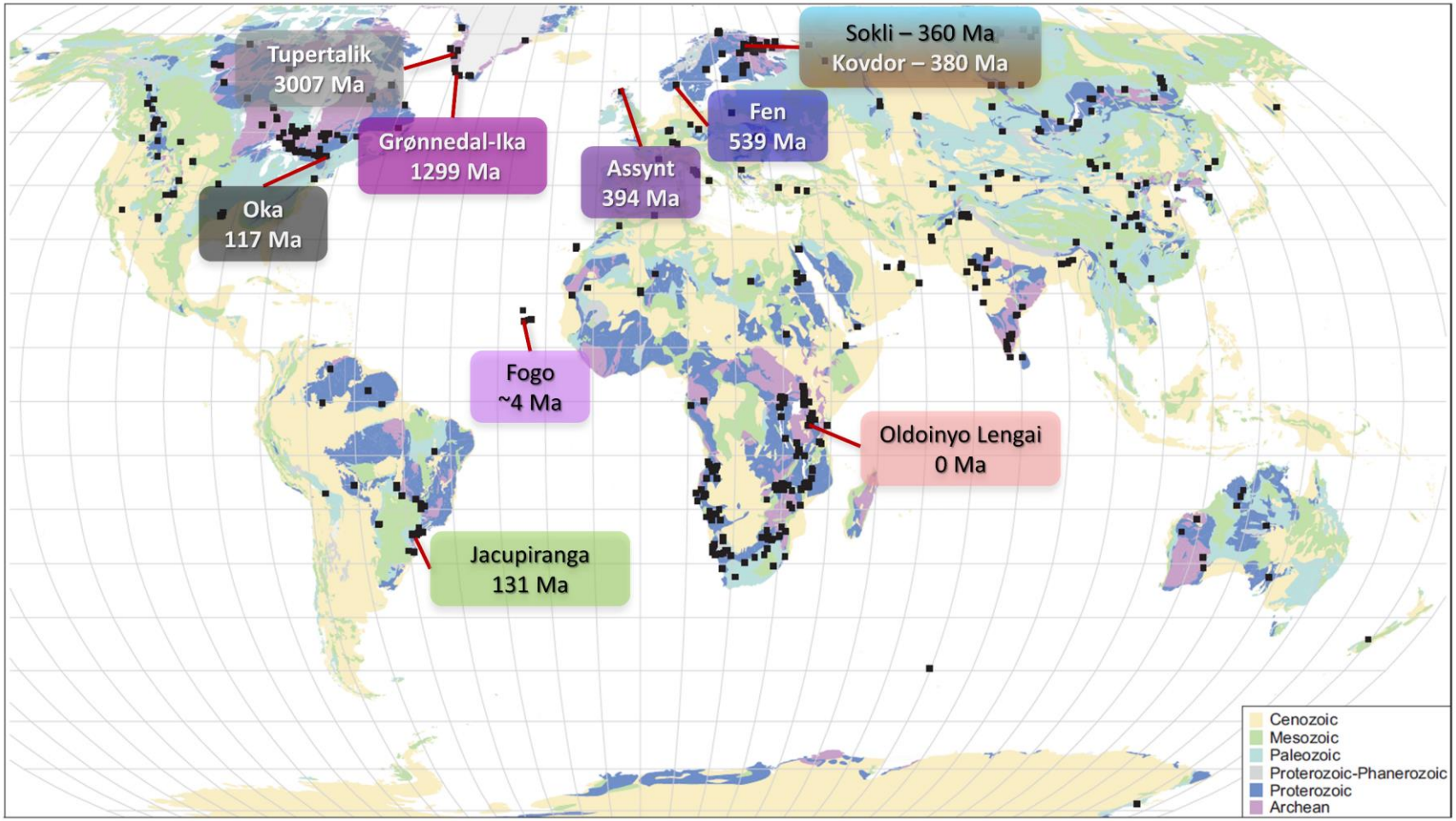

Figure 1.3 **World map showing all carbonatite localities (black squares, Woolley and Kjarsgaard, 2008). Sample localities from this study are marked by the red lines. Colours highlighting the names and ages of each locality were chosen based on colour codes used for plotting trace element and isotope data (*c.f.* Table 4.2).**

Jacupiranga, Brazil

The Jacupiranga carbonatite 230 km southwest of São Paulo, Brazil covers an area of 1000 × 250 m within a 65 km^2 large oval-shaped intrusion that further includes peridotite, pyroxenite, jacupirangite, ijolite, nepheline syenite and fenite (Woolley, 1987, p. 193). It has intruded granodiorite and mica schists of the basement and is particularly interesting because the carbonatite contains an intact sequence of five intrusions (C_1-C_5; *c.f.* chapter 1.1 and Gaspar and Wyllie, 1983; Le Bas, 1981). Thus, calciocarbonatite, magnesiocarbonatite and ferrocarbonatite can be found in Jacupiranga. In this study we have investigated samples from the C1, C2, C4 and C5 sequence (four samples in total). Herz (1977) suggests that the Jacupiranga province has formed in association with a hot spot related to a triple junction that resulted from the opening of the South Atlantic Ocean. Jacupiranga was dated to ~131 Ma using K-Ar dating (Amaral, 1978).

Sokli, Finland

Sokli is located in the municipality of Savukoski on the Kola Peninsula in Lapland, Finland close to the Finnish-Russian border. The Sokli carbonatite is one of the largest intrusive carbonatite bodies known and has more than 20 km^2 of exposure. The carbonatite intruded the granite gneiss basement and is surrounded by a fenitised aureole (Paarma, 1970). Its 360 Ma age was determined by U-Pb and Th-Pb on pyrochlore as well as Rb-Sr and K-Ar on phlogopite (Kononova and Shanin, 1971; Vartiainen and Woolley, 1974). The main carbonatite facies found is søvite (calciocarbonatite) and rarely rauhaugite (magnesiocarbonatite) (Paarma, 1970). In comparison to other carbonatite bodies, Sokli is not associated with any silicate alkaline complex (Heinrich, 1966, p.16). The occurrence of the Sokli complex together with other magmatic complexes in the region (Kola, Finland, Sweden and Norway) is thought to be associated with the Kandalaksha deep fracture zone, which is thought to be linked to the Rhine graben and the intercontinental rift belt (Kukharenko, 1967; Paarma and Talvitie, 1976; Vartiainen and Paarma, 1979). Four samples from Sokli were analysed in this study.

Kovdor, Russia

The Kovdor massif is located in Oblast Murmansk on the Kola Peninsula in Russia close to the Finnish border and is a 40.5 km^2 large ultrabasic-alkaline complex in which carbonatite occurs at the contact of ijolite and pyroxenite intrusions along an extension of the Kandalaksha Graben (Amelin and Zaitsev, 2002; Lee et al., 2006a). Carbonatite intrusions on the Kola Peninsula are thought to have been emplaced in old suture zones or reactivated graben structures. The Kovdor carbonatite has intruded the basement gneisses of the Belomorian

group (Lee et al., 2006a), which is thought to be the same basement intruded by the Sokli carbonatite in Finland (Paarma and Talvitie, 1976). Th-Pb and U-Pb dating by Amelin and Zaitsev (2002) revealed an age of 380 to 376 Ma for the Kovdor carbonatite. It occurs at depths of up to 1.5 km^2 and possibly beyond, as it forms conduits and veins of mainly calciocarbonatite and magnesiocarbonatite (Amelin and Zaitsev, 2002). It is thought that at least two mantle sources are responsible for the generation of carbonatites on the Kola Peninsula, which were closed systems for at least 3 Ga: One end-member enriched, the other one depleted (Bell and Rukhlov, 2004). This, however, is not consistent with Lu-Hf or Sm-Nd isotope systematics, which suggest a depleted mantle reservoir older than 3 Ga (Rukhlov and Bell, 2003). Veksler et al. (1998) and Bell and Rukhlov (2004) suggest that the Kovdor carbonatite was formed by fractional crystallisation. This is based on several lines of evidence: 1) Melt inclusions in cumulus olivine, clinopyroxene, melilite and perovskite found in carbonatites and associated silicate rocks 2) oxygen and carbon isotopes, 3) its association with silicate rocks, 4) a continuous composition from silicate to carbonatite, 5) phenocrysts of calcite found in associated silicate rocks/dykes, 6) findings of cumulates and 7) finding of late-stage ankerite-dolomite carbonatites. Eight samples from Kovdor were investigated in this study.

Assynt, United Kingdom

A small outcrop of carbonatite can be found in the southwest corner of the outer contact of the Loch Borralan alkaline intrusion. It is located on the shore of Loch Urigill along the western edge of the Moine Thrust Zone in the Assynt region of the NW Highlands of Scotland (Young et al., 1994). The Loch Borralan intrusion was dated at 430±4 Ma by Breemen et al. (1979) using U-Pb on Zircons, while Deans et al. (1971) determined an age of 394±15 Ma for the carbonatite by dating the surrounding fenite. The carbonatite found near the Loch Borralan alkaline complex is emplaced in Durness Group dolomite and is mainly søvite *(*calciocarbonatite). However, minor occurrences of foliated silicocarbonatite have also been observed (Young et al., 1994). One carbonatite sample from Assynt was analysed in the global study.

Fen, Norway

The Fen complex consists of alkaline rocks and carbonatites, with the latter making up almost 60% of the surface of the complex (Andersen, 1987). It is located in Telemark, SE Norway approximately 120 km southwest of Oslo close to the late Palaeozoic Oslo Rift. The whole alkaline complex has intruded into Precambrian Telemark gneisses (Lie and Østergaard, 2011) and carbonatite emplacement is thought to have occurred 539±14 Ma ago,

determined by whole-rock Pb-Pb dating (Andersen and Taylor, 1988). Calciocarbonatite (*søvite*) is the dominant type of carbonatite in Fen, but magnesiocarbonatite (rauhaugite) and ferrocarbonatite (rødbergite) can also be found (Lie and Østergaard, 2011). For the global study, three carbonatite samples were analysed, while an additional seven samples were investigated in the Fen case study. *A more detailed description of Fen can be found in chapter 0.*

Grønnedal-Ika, Greenland

Grønnedal-Ika is an alkaline complex dominated by foyaitic nepheline syenites as well as carbonatites which have intruded the surrounding gneisses and metasediments. It is located in the Gardar Province, South Greenland near the abandoned mining town Ivittuut (Emeleus, 1964). The complex has an age of ~1299 Ma determined using Rb-Sr chronology by Blaxland et al. (1978). Three major carbonatite outcrops (up to 0.7 km^2) can be found in the Grønnedal-Ika complex and a few smaller outcrops are associated with faulting (Bedford, 1989; Emeleus, 1964). The carbonatites from the Grønnedal-Ika complex are mainly calcite-rich. However, variations in the abundance of calcite, magnetite and siderite have been observed (Halama, 2005). Four samples were analysed from Grønnedal-Ika.

Tupertalik, Greenland

The Tupertalik intrusion is a small carbonatite intrusion (500 x 200 m) close to the Qaqarssuk complex in southern West Greenland (Larsen and Pedersen, 1982). It was emplaced as a circa 10 m thick sheet and in form of veins into the countryrock gneiss (Larsen and Pedersen, 1982). The Tupertalik carbonatite was initially determined to have an age of 2650 Ma by Larsen et al. (1983) using K-Ar dating, but later revised to 3007±2 Ma using Ub-Pb dating on baddeleyite (Bizzarro et al., 2002) and is as such the oldest carbonatite documented thus far, on Earth. Carbonatites from Tupertalik are either calciocarbonatites or contain calcite and dolomite moving towards magnesiocarbonatitic compositions (Larsen and Pedersen, 1982). Three samples from Tupertalik were studied here.

The table on the next pages lists all samples described and analysed in this study:

Table 1.2 **List of samples from this study incl. age (Amaral, 1978; Amelin and Zaitsev, 2002; Andersen and Taylor, 1988; Blaxland et al., 1978; Deans et al., 1971; Larsen et al., 1983; Madeira et al., 2005; Shafiqullah et al., 1970; Vartiainen and Woolley, 1974), sample type and origin of the samples. LUH = Leibniz Universität Hannover, Institute for Mineralogy; NHM = Natural history museum; BBK: Birkbeck, University of London; CSM = Camborne school of mines, University of Exeter; USGS = United States geological survey; GEUS = Geological survey of Denmark and Greenland; DU = Durham University.**

Sample No	Locality	Age (Ma)	Sample Type	Provided by
OL-1	Oldoinyo Lengai, Tanzania	0	Natrocarbonatite	*Stephan Schuth, LUH*
BM.2004,P12(132)			Natrocarbonatite	*NHM London*
LI 23/02/08	Fogo, Cape Verde	4	Carbonatite	*Hilary Downes, BBK*
BM.2004.P9(9)			Carbonatite	*NHM London*
J1-C1	Jacupiranga, Brazil	131	Calciocarbonatite	*Kate Moore, CSM*
91/66 - C2			Magnesiocarbonatite with apatite and magnetite	*Mike LeBas/NHM London*
91/62 - C4			Apatite-magnetite-pyrrhotite-carbonatite	*Mike LeBas/NHM London*
91/60 - C5			Magnesiocarbonatite	*Mike LeBas/NHM London*
COQ-1*	Oka, Canada	117	Carbonatite	*USGS*
BM.1998,P18(44)	Sokli, Finland	360	Søvite	*NHM London*
BM.1998,P18(119)			Calciocarbonatite	*NHM London*
BM.1998,P18(183)			Carbonatite	*NHM London*
BM.1998,P18(229)			Søvite	*NHM London*
BM.2000,P11(14)	Kovdor, Russia	376	Carbonatite	*NHM London*
BM.2000,P11(16)			Carbonatite	*NHM London*
BM.2000,P11(22)			Carbonatite with apatite and mafics	*NHM London*
BM.2000,P11(23)			Carbonatite	*NHM London*
BM.2000,P11(29)			Magnesiocarbonatite	*NHM London*
BM.2000,P11(42)			Magnesiocarbonatite	*NHM London*
BM.2000,P14(24)			Carbonatite	*NHM London*
BM.2000,P14(25)			Carbonatite	*NHM London*
ASS-1	Assynt, UK	394	Calciocarbonatite	*Schweitzer/Nowell/Pozzi DU*
4808	Fen, Norway	539	Carbonatite (søvite) with uranium-bearing pyrochlore (Elsworthite)	*Durham University*
10160			Søvite with fenite	*Durham University*
16462			Carbonatite	*Durham University*
TS 498 E			Ankerite carbonatite	*Schweitzer/Dahlgren/Hofmann*
TS 51.5 E			Magnesiocarbonatite	*Schweitzer/Dahlgren/Hofmann*

Table 1.2 (continued)

Sample No	Locality	Age (Ma)	Sample Type	Provided by
MTGS	Fen, Norway	539	Ijolite	*Schweitzer/Dahlgren/Hofmann*
THY			Phlogopite bearing carbonatite	*Schweitzer/Dahlgren/Hofmann*
CQW-1			Phlogopite søvite	*Schweitzer/Dahlgren/Hofmann*
CQW-2			Amphibole søvite	*Schweitzer/Dahlgren/Hofmann*
TS 531 W			BMS vein	*Schweitzer/Dahlgren/Hofmann*
19777	Grønnedal-Ika, Greenland	1299	Carbonatite	*Durham University*
19780			Carbonatite from 1m sheet gneiss	*Durham University*
19781			Ferrocarbonatite	*Durham University*
25810			Carbonatite	*Durham University*
GGU 252833	Tupertalik, Greenland	3007	Calciocarbonatite	*Lotte Larsen, former GEUS*
GGU 252874			Magnesiocarbonatite	*Lotte Larsen, former GEUS*
GGU 253528			Magnesiocarbonatite	*Lotte Larsen, former GEUS*

*Certified USGS rock standard

Chapter 2 : Petrography

Petrographic study was carried out using polarisation microscopy, electron microprobe analysis, and reflected-light microscopy on 20-30 µm and 200 µm thick thin-sections as well as polished rock and sulphide fragments.

2.1. Oldoinyo Lengai, Tanzania

Due to the strong alteration of natrocarbonatites when in contact with water and when exposed to air, Oldoinyo Lengai samples were not made into thin sections but instead were embedded as rock fragments in resin and were then polished under water-free conditions. The petrography is based on reflected-light microscopy of samples from a similar lava flow, because the samples used for isotope analysis were only available in powder form. Optical distinction between minerals was difficult using reflected light microscopy. Nyerereite and gregoryite are the most common phases in samples from Oldoinyo Lengai (*e.g.* McKie and Frankis, 1976; Zaitsev and Keller, 2006). The major mineral phase of the polished fragments examined here was identified as nyerereite.

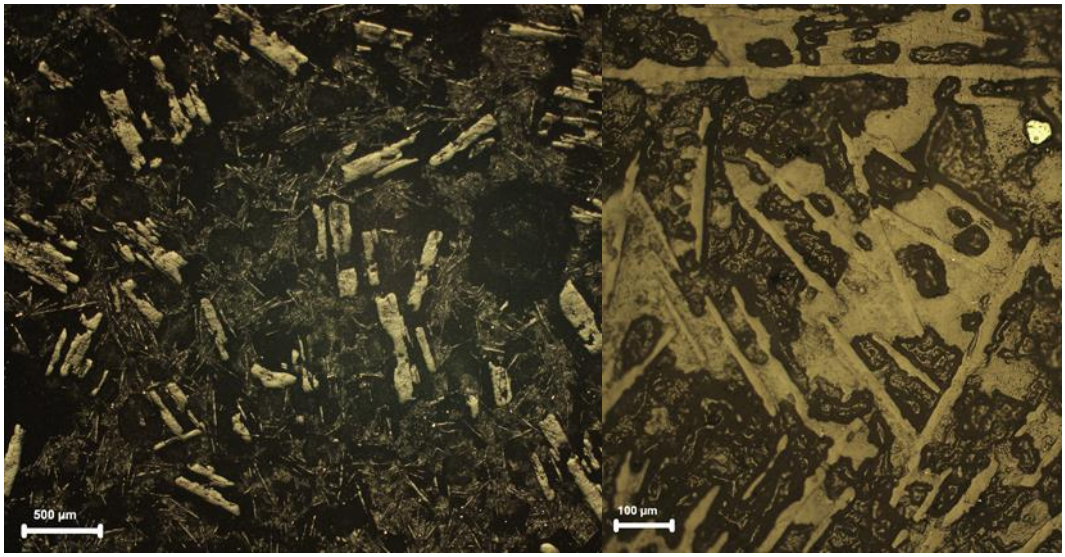

Figure 2.1 Reflected light images from Oldoinyo Lengai samples BM.2004,P12(103) (left) and BM.2004,P12(131) (right).

Nyerereite is present in the form of tabular up to 600 µm large phenocyrsts, as well as small needles in the groundmass (*c.f.* Figure 2.1, BM.2004,P12(103)). The more rounded similar sized (up to 600 µm) minerals could be gregoryite grains. Compared to BM.2004,P12(103), sample BM.2004,P12(131) does not show a porphyritic texture, but appears more phaneritic (*c.f.* Figure 2.1, BM.2004,P12(131)). Again, tabular nyerereite can be identified, while the

other mineral phases are difficult to identify. Both samples possess abundant sulphides of up to 600 µm. Other phases known to occur in samples from Oldoinyo Lengai include fluorite, sylvite, nepheline, aegirine, diopside, alumoåkermanite as well as the alteration products pirssonite and thermonartite (*e.g.* Wiedenmann et al., 2009; Zaitsev and Keller, 2006).

2.2. Fogo, Cape Verde

LI 23/02/08

The thin section shows patches of brown alteration in between mineral grains, but this does not affect the whole sample. Subhedral carbonate is the dominant mineral phase (80-90%) and is mainly equigranular (<1 mm) with the occasional carbonate grain more variable in size (<1mm to ca. 2 mm) (see Figure 2.3 D). Further major phases are up to 5 mm in diameter, and include brown phlogopite and green pyroxenes (possibly aegirine), as well as smaller (<1 mm) opaque phases (possibly magnetite and/or hematite) and apatite. The pyroxene is strongly altered and fractured and is partly intergrown with strongly fractured phlogopite. Some micas show masked interference while others do not, indicating variability in the mica chemistry.

BM.2004.P9(9)

Alteration is also visible in this sample, though stronger than in LI 23/02/08. The alteration creates a grey "cloudy" matrix that looks similar to sericitisation in feldspars. Subhedral carbonate (0.4 to 4 mm) is found in altered matrix together with apatite, up to 5 mm in diameter, and large green pleochroic pyroxene crystals, up to 2mm in diameter. Alteration in form of a grey coating is also visible on the sub- to euhedral apatite. Additionally, there are fractures throughout the thin section, which show brown alteration. As minor phases, this thin section contains opaque phases (likely magnetite), which tend to grow in fractures and around the grain boundaries of other mineral grains.

2.3. Jacupiranga, Brazil

J1-C1

This sample contains large sulphides, up to 7 mm in diameter, surrounded by carbonates, up to 4 mm long. Carbonate is the dominant phase (around 90% of the rock), while acicular apatite makes up around 5%. The carbonate is anhedral, variable in size and has fringed grain boundaries, while the euhedral apatite tends to grow in assemblages to sizes of up to 3 mm. The other 5% comprises colourless micas (up to 1.4 mm long) and base metal sulphide, while other opaque phases were not observed in the thin section.

91/66 – C2

This thin section is dominated by dolomite and calcite (>90%) with an average grain size of around 0.6 mm. Apatite makes up around 5% of the sample, while the remaining 5% comprises base metal sulphides, magnetite and minor amounts of mica. The base metal sulphides grow in elongated assemblages and are oriented the same way. The same orientation can be observed for up to 400 µm assemblages of apatite, while smaller opaque phases (200 µm) are randomly distributed in the thin section. The carbonates are mostly subhedral, but some are also anhedral.

91/62 – C4

This sample is very heterogeneous. There is a unit of very large (ca. 7 mm) euhedral magnetite crystals surrounded by carbonate (0.4 to 3 mm) and another unit dominated by apatite (0.3 to 1 mm, *c.f.* Figure 2.2 A). Base metal sulphides and carbonates can be found as inclusions in magnetite. The carbonate in this sample is anhedral, shows a grey alteration, has partly porous textures and shows fringed grain boundaries in some grains, while others have sharp boundaries. Apatite is subhedral to euhedral and the micas present show chloritisation and appear to be quite altered. While apatite dominates the sample with around 40%, carbonate makes up around 30%, magnetite 25% and olivine, mica and base metal sulphides a combined 5%. Although apatite dominates the thin section, this does not necessarily imply that the whole-rock shows similar abundances. Due to areas of different mineralogy, it might be that an apatite-rich fraction of the rock was sampled that is not necessarily representative. In this case whole-rock chemical results need to be treated with caution due to the strong heterogeneity of this sample.

91/60 – C5

The major phases in this sample are carbonate (85%, dolomite and calcite), apatite (10%), chloritized mica (4%) and opaque phases such as magnetite (1%). The carbonate is variable in size (0.2 to 1.8 mm) and mostly anhedral. In some areas of the thin section, carbonate grain boundaries show brown alteration. Apatite is euhedral to subhedral and carbonate growing close to apatite tends to be smaller in size than in other areas of the thin section.

2.4. Kola Peninsula

2.4.1. Sokli, Finland

BM.1998,P18(44)

In this sample, large anhedral carbonate grains (2-3 mm) are present in a fine grained (0.2 mm) carbonate matrix. Euhedral and rounded apatite crystals (0.4 mm) can be found evenly distributed throughout the sample. Beside apatite and carbonate, phlogopite is another major phase. Phlogopite is similar in size to apatite, reddish-brown in colour when fresh and shows pleochroism. Altered phlogopite is colourless to green due to transformation to chlorite. Base metal sulphides can only be found locally, following an orientation that is not resolved for the other mineral phases.

BM.1998,P18(119)

More than 90% of this thin section is made up of equigranular (0.2 mm), subhedral carbonate (dolomite and/or calcite). Small (50 µm) euhedral diamond shaped dolomite crystals grow locally in thin bands. Base metal sulphides are present as a 4 mm wide vein and make up almost all of the remaining 10% of this thin section. However, BMS are not evenly distributed, hence, the estimates given do not necessarily apply to the whole-rock. Other minor to accessory phases are euhedral opaque phases (possibly magnetite).

BM.1998,P18(229)

Major phases in this sample consist of carbonate, apatite, phlogopite and magnetite. Pyrochlore is also present as minor phase. Carbonate dominates this sample with ca. 90% (apatite: 5%, magnetite, phlogopite & pyrochlore: 5%) and grows as large patchy, mostly anhedral crystals with grain sizes varying between 0.6 to 1.4 mm. Apatite crystals tend to grow as elongated assemblages along carbonate grain boundaries oriented in one direction. Magnetite grows as large euhedral to sometimes subhedral grains, while the euhedral to subhedral pyrochlore is smaller (*c.f.* Figure 2.2 B).

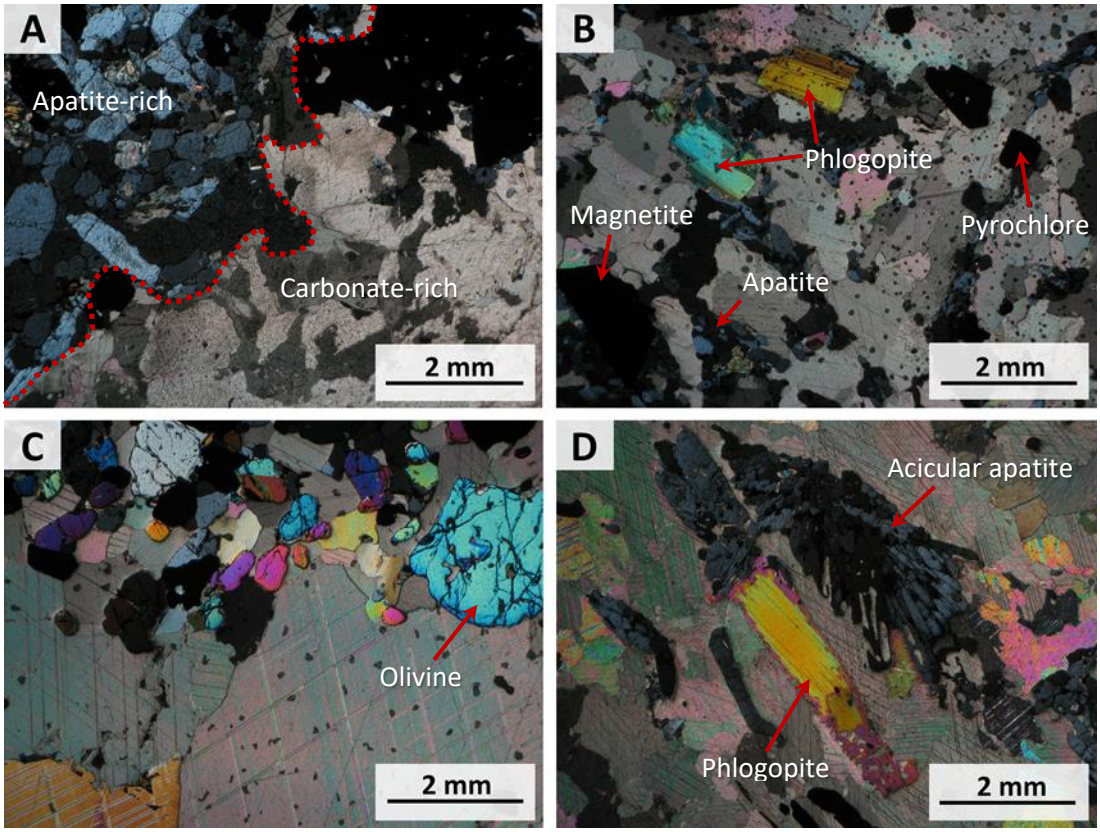

Figure 2.2 **Photos of thin sections from different localities in cross-polarised light (XPL); A: 91/62 – C4 from Jacupiranga, Brazil: B: BM.1998,P18(229) from Sokli, Finland; C: BM.2000,P11(22) from Kovdor, Russia; and D: CQW-1 from Fen, Norway.**

2.4.2. Kovdor, Russia

BM.2000,P11(22)

Similar to sample *91/62 – C4,* this sample is heterogeneous. It has bands of different mineralogy, with the top and lower part being fine grained and enriched in apatite, magnetite, olivine and smaller amounts of carbonate; while the central part is dominated by larger (up to 6 mm) carbonates (*c.f.* Figure 2.2 C). In the top and lower region, carbonate grows as anhedral grains between euhedral apatite, magnetite and olivine. In the central part, carbonate is anhedral with slightly fringed edges. Apatite is also present in this part of the sample but is less abundant than in the top and lower part. The contact between the different areas of the sample is smooth pointing towards flow structures.

BM.2000,P14(24)

The thin section is dominated by anhedral 0.4 to 1 mm large carbonate (80%) with no clear orientation. Distinction between calcite and dolomite is difficult, but it would appear both are present in this sample. Apatite can only be found as accessory phase. Two straight lines crosscutting each other at an angle of ca. 30° are defined by oriented and elongated phlogopite as well as base metal sulphide grains (together 20%). The phlogopite (1 mm) grows as euhedral to subhedral grains and contains inclusions (possibly carbonate), while the base metal sulphides (2-3 mm) look like melt "blobs" and are thus anhedral. The straight lines are also defined by a grey alteration coating that affects the carbonate but not the phlogopite and base metal sulphide.

BM.2000,P14(25)

In comparison to sample *BM.2000,P14(24)*, this sample is more altered. Again, like sample *BM.2000,P11(22)* and *91/62 – C4*, this sample has areas with slightly different mineral modes. The top of the thin section consists of a large (5 mm x 1 cm) assemblage of magnetite that is adjacent to an assemblage of phlogopite and one of apatite. The gaps are filled by anhedral carbonate. In contrast, the bottom half is dominated by anhedral intergrown carbonate (0.4 to 1.6 mm) and assemblages of apatite. In this lower part only one phlogopite crystal was found. The carbonate in this part of the thin section is variable in size and again a distinction between calcite and dolomite is difficult. However, it looks like dolomite is the predominant phase. Apatite is acicular and in the form of clusters rather than elongated and some of the euhedral phlogopite grains show zonation.

2.5. Fen, Norway

4808

This sample is dominated by calcite (60%) and apatite (up to 30%), while the remaining 10% are made up by torn-apart chlorite (5%), and subhedral to anhedral pyrochlore (5%). While carbonate (0.1-0.8 mm) in this thin section is anhedral, apatite is subhedral. Base metal sulphides of up to and >1 mm are present as accessory phases. Apatite shows microscale inclusions which cannot be clearly identified.

10160

This sample is banded and can be divided into two parts: the lower part appears to be extremely altered with brownish fragments that are surrounded by sub- to anhedral carbonate and minor amounts of pyrochlore. The brownish fragments consist of phlogopite,

carbonate and an undefined fine-grained matrix similar to sericite. In contrast, the upper part is made up of anhedral equigranular carbonate (ca. 0.6 mm), elongated assemblages of apatite, magnetite and phlogopite and does not have any of the alteration features visible in the lower part.

16462

Sample 16462 consists of 80-90% anhedral irregularly intergrown calcite and dolomite (*c.f.* Figure 2.3 C and *c.f.* appendix Table 10.12), while the remaining 10-20% consist of phlogopite (*c.f.* appendix Table 10.14), apatite (*c.f.* appendix Table 10.13), subhedral to anhedral opaque phases (possibly magnetite) and large >2 mm long base metal sulphide grains. The dominant base metal sulphide is pyrrhotite, but pyrite with sphalerite inclusions can also be found (*c.f.* appendix Table 10.11). This sample further contains accessory REE-phases enriched in La and Ce (*c.f.* appendix Table 10.15) and has a grain size of 0.2 to 0.8 mm.

CQW-1

This sample contains 80% carbonate, 10% magnetite, 5% phlogopite and 5% apatite. Pyrite (*c.f.* appendix Table 10.11) can be found as minor phase. Carbonate crystals are on average ca. 1-2 mm large, anhedral and show interlocked growth with no sharp grain boundaries. Magnetite (up to 5 mm) grows subhedral and elongated, with single grains showing orientation. The partly acicular growing apatite (*c.f.* Figure 2.2 D) tends to grow in elongated assemblages, which also follow the orientation of the magnetite. Magnetite further shows apatite inclusions, which contain micro inclusions (possibly fluid inclusions). Phlogopite grows sub- to anhedral and is partly torn apart or has started to transform into chlorite along the edges.

CQW-2

Compared to *CQW-1*, this sample additionally contains fibrous and very altered amphibole (5%). Carbonate (70%), apatite (15%) and opaques (magnetite and sulphides, 10%) make up the remaining 95%, while phlogopite is only a minor to accessory phase in this sample. Around 10% of the carbonate has brighter interference colours in cross-polarised light either originating from dolomite or another carbonate phase. In general, the carbonate is anhedral and grains have grown interlocked, with a grainsize between 0.4 and 1.6 mm. Magnetite is with 4 mm much larger and is also mostly euhedral, though broken apart. Smaller magnetite crystals grow around the larger magnetite as well as associated sulphides. Apatite is also

often associated with the magnetite and grows in form of large assemblages in between the carbonate grains.

TS 498 E

With an average grain size around 0.2 mm, this sample is much finer grained than *e.g. CQW-1* and *CQW-2*. It is very homogeneous and consists of around 95% mostly equigranular anhedral carbonate. The remaining 5% is made up of base metal sulphide "blobs". Furthermore, smaller bands and cumulates of slightly larger (up to 0.8 mm) carbonates can be found in the thin section. Those larger carbonates tend to be slightly more altered than the smaller ones. Additionally, there are fractures running through the sample. Brownish alteration is present in several local areas of the sample, which could be either very disintegrated altered minerals or just local alteration of the sample.

TS 51.5 E

Like *TS 498 E*, this sample is finer grained (0.2 mm) and not as variable in terms of mineralogy as some of the other carbonatites in this study. It consists mainly of equigranular carbonate (70%) and elongated smaller apatite (30%). Although similar in grain size, *TS 51.5 E* has subhedral alongside anhedral carbonate grains. The grain boundaries tend to be slightly sharper than in *TS 498 E*. Larger fractures crosscut the sample.

THY

Carbonate makes up 80% of this sample, followed by ca. 15% apatite and 5% consisting of magnetite, base metal sulphide, mica and pyrochlore. The grain size is between 0.4 and 1.3 mm. The carbonate grains tend to grow in assemblages of similar size, but due to anhedral growth there are no clear boundaries between larger or smaller grained areas that might suggest cumulate textures. Apatite grows in larger assemblages and is mostly either elongated or acicular. One pyrochlore grain was found divided by an elongated apatite grain. Mica in this sample is colourless and euhedral to subhedral with slightly altered edges. Sub- to euhedral base metal sulphides can be found associated to magnetite.

MTGS

This sample is not a carbonatite but an associated silicate rock, called ijolite. It consists of pyroxene, nepheline and mica, while carbonate and apatite are only minor phases. Base metal sulphides and magnetite can be found as accessory phases. Mica grows as large patches around 8 mm in diameter in between pyroxene and has partly transformed to chlorite. It is generally subhedral, but can also be anhedral, filling in gaps with other phases.

The green 0.3 mm euhedral and elongated pyroxene crystals grow without particular orientation, while the large (2 mm) nepheline grows as anhedral patches in the "background".

TS 531 W

There is no thin section of this sample, instead a mount was made with a larger piece (ca. 2 cm diameter) embedded in resin. This sample comes from a sulphide vein crosscutting the Fen carbonatite complex. It comprises pyrite (see appendix Table 10.11) and minor amounts of magnetite.

2.6. Greenland

2.6.1. Grønnedal-Ika

19777

Anhedral calcite makes up >90% of this fine-grained (0.25 to 0.45 mm) equigranular sample. The sample is slightly altered and further contains black and reddish opaque phases. A brownish strongly altered mineral grows interstitially between carbonate grains and shows interference colours similar to carbonate. Identification of this altered phase is difficult. Other mineral phases were not identified.

19780

This sample is quite altered and contains large (up to 2.8 mm) patchy calcite (*c.f.* appendix Table 10.12) that is overgrown by fibrous pale green/brown to blue, up to 2 mm long, arfvedsonite crystals (see Figure 2.3 B; *c.f.* appendix Table 10.14). Further mineral phases are apatite (*c.f.* appendix Table 10.13) and base metal sulphides dominantly consisting of pyrite (*c.f.* appendix Table 10.11). The sample appears to be banded, with bands consisting either of blue amphibole and pale green amphibole while other bands contain only pale green amphibole and more calcite. There are also unidentified phases that contain minor amounts of U and Ca or Ce (*c.f.* appendix Table 10.15).

19781

The two main phases in sample 19781 are calcite (75%, *c.f.* appendix Table 10.12) and Fe-oxides (25%, likely magnetite *c.f.* appendix Table 10.16) of which the latter is oriented such that the sample appears banded. The 0.2 to 0.8 mm long carbonate crystals are subhedral and show triple-junctions along the grain boundaries (*c.f.* Figure 2.3 A). However, brown alteration is also visible along some carbonate grain boundaries. Apatite (*c.f.* appendix Table

10.13) can also be found as a minor phase throughout the sample, while base metal sulphides are only present as strongly altered accessory phases (fresh BMS <10µm). Base metal sulphides occur together with magnetite and tend to alter into a more Fe-oxide-rich phase. Only six analyses of two altered grains could be measured, one being pyrite and the other pyrrhotite (*c.f.* appendix Table 10.11). Additionally, this sample contains unidentifiable phases containing Ca, La, Ce, P and/or U (*c.f.* appendix Table 10.15)

<u>25810</u>

Compared to other samples from Grønnedal-Ika, this sample shows larger abundances of dolomite. Although dominated by calcite, dolomite can be found as bands in between the patchier 0.4 to 3 mm large calcite crystals. Additionally, the cleavage in the calcite is slightly deformed. Minor phases in this sample are pyrochlore (3 mm) and magnetite.

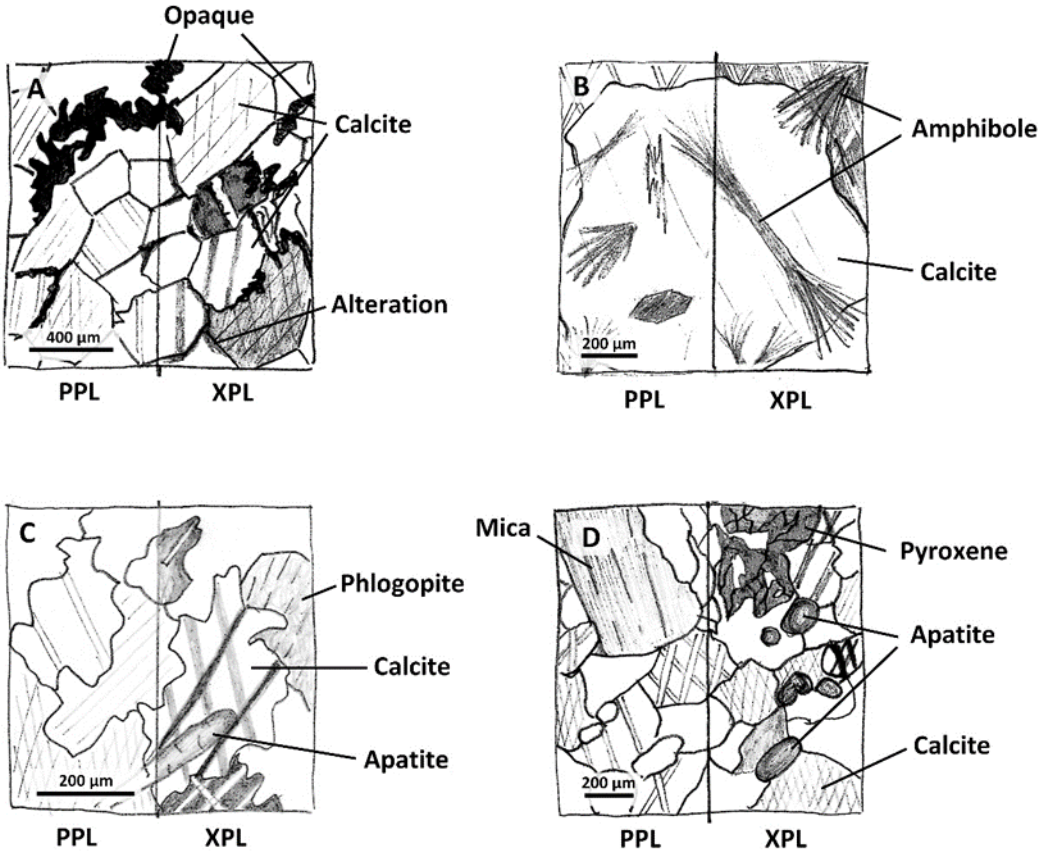

Figure 2.3 **Sketches from polarisation microscopy of 4 thin sections (A: 19781 Grønnedal-Ika, B: 19780 Grønnedal-Ika, C: 16462 Fen, D: LI 23/02/08 Fogo. The main mineral phase in all thin sections is calcite, but the textures vary strongly from euhedral/subhedral growth (A) to irregularly intergrown crystals (C).**

2.6.2. Tupertalik

The microscopy for the following thin sections was carried out by Lotte Melchior Larsen (Geological Survey of Denmark and Greenland, ml@geus.dk), who kindly provided sample powder for chemical analyses of these samples. She could not send the thin sections and thus sent us her bullet points of the petrography, which are reported here.

GGU 252833

This sample has a foliated texture, somewhat cataclastic and the grain size falls between 0.1 and 1 mm. Major phases are carbonate, olivine, phlogopite and magnetite, while a colourless silicate (possibly diopside) is present as a minor phase. Zircon can be found as an accessory mineral phase. Minerals are unevenly distributed and can thus cause variation in the chemical signature of the whole-rock.

GGU 252874

Compared to 252833, this sample is coarser grained (0.5 to 2 mm) but also shows slight foliation. Carbonate is the dominant phase, accompanied by olivine, magnetite and green spinel (hercynite). A red semi translucent oxide is present as minor phase, while accessory phases are zircon and sulphide.

Table 2.1 Table showing the modal abundances of the major mineral phases identified using a polarisation microscope. Numbers are given in %. BMS = Base metal sulphides. Magnesiocarbonatites (MC), Natrocarbonatites (NC) and Ferrocarbonatites (FC) are highlighted in the sample ID. Microprobe data can be found in in the appendix Table 10.12, Table 10.13, Table 10.14, Table 10.15 and Table 10.16.

Sample ID	Carbonate	Apatite	Mica	Magnetite	Pyroxene	Amphibole	Others		Microprobe data	Comments
NC: Oldoinyo Lengai	90	-	-	-	2	-	8	BMS, nepheline		
LI 23/02/08	90	3	3	1	3	-	-			Pyroxene and phlogopite intergrown, brown alteration between mineral grains
BM.2004.P9(9)	70	10	-	1	19	-	-			Magnetite grows in fractures, alteration visible
J1-C1	90	5	3	-	-	-	2	BMS		
MC: 91/66 – C2	90	5	1	2	-	-	2	BMS		
91/62 – C4	30	40	2	25	-	-	3	BMS, Olivine		Micas transformation to chlorite, inhomogeneous sample
MC: 91/60 – C5	85	10	4	1	-	-	-			Carbonate: calcite and dolomite, mica transformation to chlorite
BM.1998,P18(44)	85	10	3	1	-	-	1	BMS		Mica transformation to chlorite, BMS oriented
BM.1998,P18(119)	90	-	-	1	-	-	9	BMS		Calcite and dolomite present, BMS vein
BM.1998,P18(229)	90	5	2	2	-	-	1	Pyrochlore		Apatite oriented
BM.2000,P11(22)	70	25	-	4	-	-	1	Olivine		Flow bands (apatite-calcite) thus inhomogeneous
BM.2000,P14(24)	80	1	15	3	-	-	1	BMS		Phlogopite oriented with inclusions, carbonate altered
BM.2000,P14(25)	75	5	10	10	-	-	-			Alteration visible, inhomogeneous, zoning in phlogopite
4808	60	30	5	-	-	-	5	Pyrochlore, BMS		Mica mainly chlorite, apatite shows microscale inclusions
10160	68	10	10	-	-	-	12	Fine grained material, pyrochlore, BMS		Strongly altered, thin section banded
16462	86	5	5	2	-	-	2	BMS	BMS = pyrrhotite, pyrite with sphalerite inclusions; REE-bearing phases	
CQW-1	80	5	5	9	-	-	1	BMS	BMS = pyrite	Phlogopite transformation into chlorite, magnetite and apatite oriented, apatite inclusions in magnetite
CQW-2	70	14	1	8	-	5	2	BMS		Amphibole fibrous and altered
FC: TS 498 E	95	-	-	-	-	-	5	BMS		Brown alteration visible, fractures visible
MC: TS 51.5 E	70	30	-	-	-	-	-			Fractures crosscutting the sample
THY	80	15	2	2	-	-	1	BMS, Pyrochlore		BMS associated to magnetite
19777	95	-	-	-	-	-	5	Undefined opaques		Alteration visible
19780	50	5	-	-	-	44	1	BMS	Amphibole = arfvedsonite; apatite; BMS = pyrite; phases containing U, Ca or Ce present,	Sample banded, alteration visible
19781	70	2	-	27	-	-	1	BMS	Carbonate = calcite; BMS = pyrite and pyrrhotite; phases containing La, Ce, P and U	Sample is banded, brown alteration at carbonate grain boundaries
25810	92	5	-	1	-	-	2	Pyrochlore		
GGU 252833	70	10	5	5	-	-	10	Olivine, diopside, zircon		
MC: GGU 252874	85	5	-	5	-	-	5	Olivine, hercynite, zircon, BMS		

Chapter 3 : Methods

Carbonatites are very difficult rocks to work with in the laboratory as they pose a lot of analytical challenges. This methods chapter addresses those challenges and contains all approaches that were tested to acquire the data presented in Chapters 4, 5, 6 and 7.

3.1. Analytical challenges

Carbonatites are enriched in Ca, Mg and/or Na. These cations are mainly present in carbonate phases (*e.g.* calcite and dolomite). Silicate, oxide and base metal sulphide phases are only present in minor amounts (*c.f.* Chapter 2 and Table 2.1). Hafnium tends to reside in silicate phases (*e.g.* Bizimis et al., 2003), thus to recover Hf and break the SiO_4-bonds of phases such as amphibole, micas and pyroxenes, the use of hydrofluoric acid (HF) is necessary. Calcium together with HF forms fluorites ($CaCO_3 + 2HF \rightarrow CaF_2 + CO_2 + H_2O$). This reaction is instant and can be observed as soon as HF is added to the sample. Due to the strong Ca-enrichment and the high molarity (29M) of HF, the amount of fluorite precipitate can be significant. The fluorite precipitate is difficult to dissolve and to reach full dissolution, a larger acid volume (up to 20 ml) combined with higher temperatures (>120°C) and regular ultrasonication is required. Unfortunately, Hafnium tends to coprecipitate into fluorite (*c.f.* Tanaka et al., 2003). Additionally, due to the high amount of Ca, columns are easily saturated, leading to fluorite or other Ca-rich phase precipitation even after two separate column procedures (*c.f.* chapter 3.6.9). Thus, if samples do not reach full dissolution prior to each stage of the column chemistry, a significant amount of Hf can be lost into the fluorite precipitate decreasing Hf-yields significantly before and throughout column chemistry.

Due to the strong reactivity of carbonate with concentrated acids such as HCl and HNO_3 accompanied by release of CO_2, decarbonisation of samples needs to be implemented prior to the high pressure/temperature digestions required for highly siderophile element chemistry (*c.f.* chapter 3.7.1 and 3.7.2). Without a decarbonisation step, there is a risk of vessel failure (Carius tubes) or leakage (high pressure asher vessels) due to internal CO_2 gas pressure. Decarbonisation can only be carried out using HCl as OsO_4 is highly volatile and can form in combination with oxidising acids such as HNO_3. Thus, to prevent strong reaction of residual material with the later added HNO_3 (*c.f.* Chapter 3.7.4) and risking loss of Os, the amount of HCl and subsequently the amount of HNO_3 needs to be increased.

Concentrations in highly siderophile elements are usually low (ppt-level). Total procedural blanks are quite variable (*c.f.* appendix Table 10.4 and Table 10.5) and thus the detection

limit for some elements (*e.g.* Ir and Pd) is also high. Therefore, blank contribution can be high (>50%) and a lot of samples analysed fall below detection limit, which makes a reliable interpretation of the data impossible.

Carbonatites cause further a problem when being dried down in that a thick carapace forms over the still liquid sample, thus preventing it from drying down properly. If a change in acid is required (*e.g.* prior to column chemistry), carbonatite samples need to be agitated regularly to break this skin and promote sample dry down. This problem appears to be particularly profound when drying down HCl and aqua regia.

3.2. Sample preparation

Alteration crust and heterogeneous parts (*e.g.* cumulates) of the sample were removed and samples were dried overnight. The samples were crushed with a hammer, followed by powdering in an agate planetary mill for 2-5 min. per sample.

For mineral picking, samples were crushed and then sieved using 1 mm and 500 µm meshed sieves in a sieve tower. The mineral fraction <1 mm and >500 µm was used for mineral picking. Only grains without visible inclusions and adjacent minerals were picked for analysis.

Polished thin sections of 25-30 and 200 µm were prepared in the thin section preparation laboratory at the Department of Earth Sciences, Durham University. Samples from Oldoinyo Lengai were embedded in resin and polished water-free to avoid alteration of the polished surface.

3.3. Electron microprobe

Single carbonates, base metal sulphides, silicates and minor phases (*e.g.* apatite) in 25-30 and 200 µm thick polished thin sections were analysed for their major and trace element contents using a *JEOL JXA 8900* electron microprobe at Steinmann-Institute, University of Bonn, Germany. Measurements were carried out in wavelength dispersive mode (WDS), employing 15 kV acceleration voltage and 15 nA beam current. Base metal sulphide calibration was performed using Co-, Ni- and Cu-metal, while for silicates VG2 basaltic glass was used by measuring the peak and background positions for 10 and 5 s, respectively. For verification of reproducibility and measurement accuracy, natural and synthetic minerals and glasses were chosen and analysed. Element distribution maps were created to further characterise minerals and resolve zonation within single mineral grains.

3.4. Major element procedure

Spectroflux ($Li_2B_4O_7$) and dried sample were weighed (ratio 10:1), mixed and melted to produce fused beads for XRF analysis at Steinmann-Institut, Universität Bonn, Germany. Samples 10160, 19777 and 25810 (*c.f.* Table 1.2) crystallised; thus, the ratio of flux to sample needed to be increased to 20:1. Samples were analysed on fused beads by wavelength dispersive X-ray fluorescence (WDXRF) using 65 certified standards for calibration on a *PANalytical AXIOS (3kW) X-ray spectrometer.* However, because of analytical problems at Steinmann-Institut, samples were sent to the Chemical, Imaging and Mineralogical Facility of the University of Exeter to be analysed by XRF in form of pressed powder pellets. Exeter analysed the samples by semi-quantitative standardless XRF on a *Bruker S4 Pioneer X-ray spectrometer.*

3.5. Trace element procedure

3.5.1. General whole-rock method

The conventional dissolution method for trace element analysis follows the procedure of Ottley et al., (2003): A total amount of 100 mg of sample powder was fluxed with 1 ml Analar 16M HNO_3 and 4 ml Analar 29M HF in a 22 ml *Savillex* Teflon beaker and was then left on a hotplate capped at ~130-150°C for 24 h. After 24 h the beaker was opened and left on the hotplate to evaporate for several hours at 130-150°C. Then 1 ml of Analar 16M HNO_3 was added to the dried sample and evaporated. This step is repeated once more. Afterwards, the sample was fluxed with 2.5 ml of Analar 16M HNO_3 and 10-15 ml of MQ and was left on the hotplate, capped, at 130°C for at least 2 h. A volume of 1 ml of 1 ppm Re-Rh spike was added to the sample and the solution was transferred to a 50 ml pre-cleaned polypropylene centrifuge tube for Q-ICP-MS measurement using a *Thermo Scientific XSERIES 2 ICP-MS* at the Department of Earth Sciences, Durham University.

3.5.2. Method for measuring aliquots of different carbonatite fractions

Due to difficulties in digesting carbonatite fractions in the general whole-rock method described above, samples were subsequently digested as described later in section 3.6.8 and 3.6.8.1. Following digestion 5% aliquots of the whole-rock (WR), carbonate (C) and non-carbonate (NC) fractions were diluted up to 10 ml (total dissolved solids ≈ WR: 0.08 mg/ml; C: 0.09 mg/ml; NC: 0.01 mg/ml) to reach full dissolution, and measured on a *Thermo Scientific XSERIES 2 ICP-MS*.

Table 3.1 **Detection limits in ppb for XSeries analyses using a *CETAC Aridus™ I* desolvator. Detection limits were calculated by multiplying the standard deviation of each, wash solution (n=10), blank solution (n=3) and total procedural blanks (n=3) with 3.**

	Wash	Blank solution	TPB
La	0.115	0.069	0.056
Ce	0.206	0.107	0.118
Pr	0.022	0.010	0.014
Nd	0.10	0.036	0.071
Sm	0.017	0.003	0.014
Eu	0.004	0.0003	0.003
Gd	0.013	0.004	0.010
Tb	0.001	0.0003	0.001
Dy	0.007	0.001	0.005
Ho	0.001	0.001	0.0004
Er	0.001	0.001	0.0001
Yb	-	0.001	-
Lu	0.0004	0.0002	-
Hf	0.017	0.004	0.011
Rb	0.0345	0.0233	0.0236
Sr	0.330	0.268	0.400
U	0.0008	0.0006	0.0006

Determining Lu/Hf ratios for the various carbonatite fractions can be problematic because of very high REE abundances. Several REE cause isobaric interferences on Lu and Hf when present as oxides. The following table shows the most common interferences and their theoretical probabilities of formation for ^{175}Lu, ^{177}Hf and ^{178}Hf:

Table 3.2 Isobaric interferences on ^{175}Lu, ^{177}Hf and ^{178}Hf and their probabilities based on isotopic abundances.

Isotope	Potential isobaric interferences	Probability (%)
^{175}Lu	^{159}Tb+^{16}O	99.8
	^{158}Gd+^{17}O	0.01
	^{143}Nd+^{16}O$_2$	12.1
	^{135}Ba+^{40}Ar	6.57
	^{163}Dy+^{12}C	24.6
	^{162}Dy+^{13}C	0.27
	^{161}Dy+^{14}N	18.8
^{177}Hf	^{161}Dy+^{16}O	18.9
	^{160}Gd+^{17}O	0.01
	^{160}Dy+^{17}O	0.001
	^{145}Nd+^{16}O$_2$	8.26
	^{137}Ba+^{40}Ar	11.2
	^{165}Ho+^{12}C	98.9
	^{163}Dy+^{14}N	24.8
^{178}Hf	^{162}Dy+^{16}O	25.4
	^{146}Nd+^{16}O$_2$	17.2
	^{138}Ba+^{40}Ar	71.4
	^{138}La+^{40}Ar	0.09
	^{138}Ce+^{40}Ar	0.25

1 ppm solutions of Ba, La, Ce, Dy, Tb and Nd were analysed on a *Thermo Scientific XSERIES 2 ICP-MS*. For each solution the counts per second (cps) on the corresponding Lu or Hf isotope were used to calculate the percentage of oxide formation on the appropriate Lu and Hf mass and thus calculate the contribution of the isobaric interference on each isotope. Following these measurements, three solutions with known Lu/Hf ratios and doped with the elements that form molecular interferences were measured. The solutions were doped according to the abundance of elements in natural carbonatite samples. For this a solution representing a non-carbonate fraction (Lu/Hf: 0.001) and two representing carbonate fractions (Lu/Hf: 10 and 50) were chosen. The oxide formation factors derived from the 1 ppm single element solutions were then used to calculate the amount of counts on ^{175}Lu, ^{177}Hf and ^{178}Hf caused by the interferences. It is clear, that samples with low Lu/Hf ratios (in this example 0.001, representative of a non-carbonate fraction) are not strongly affected by the isobaric interferences (*c.f.* Figure 3.1). However, as the Lu/Hf ratio increases – and hence the amount

of REE increases – the effect of isobaric interferences becomes more evident (*c.f.* Figure 3.2 and Figure 3.3). This is especially the case for ^{177}Hf, which has a major interference caused by ^{161}Dy^{16}O. Although the probability of ^{61}Dy^{16}O is fairly low (18.9%, *c.f.* Table 3.2), the Dy/Hf ratio in the sample is such that it has a large influence on the number of counts on ^{177}Hf (≈45-60% caused by ^{161}Dy^{16}O for Lu/Hf of 10 to 50, representative of a carbonate fraction, Figure 3.2 and Figure 3.3).

One way to decrease oxide isobaric interferences (*e.g.* ^{161}Dy^{16}O), is to desolvate the sample using a *CETAC Aridus^{TM} Desolvating Nebulizer System*. The desolvator dries the sample prior to introduction to the plasma, reducing the available O from the acid solvent and hence the oxide formation rates. To test and confirm reduction in oxides, the same 1 ppm Ba, La, Ce, Dy, Tb and Nd solutions measured by wet plasma were re-measured with a high uptake glass nebuliser (1 ml/min) and with an *Elemental Scientific Incorporation* (ESI) PFA low uptake nebuliser (50 µl/min) coupled to the *Cetac Aridus^{TM}*. From Figure 3.2 and Figure 3.3 it is clear, that the desolvator reduces oxides by a factor of up to 15 (*e.g.* Figure 3.2, ^{177}Hf: DyO reduces from ~60% to ~4%) and is thus the method of choice for analysing elemental concentrations, and more importantly Lu/Hf ratios in high REE samples.

For mass 178 in test solution 3 with Lu/Hf of 50, it is also clear that the amount of BaAr is reduced by use of the low uptake PFA-50 nebuliser together with the *Aridus* (*c.f.* Figure 3.3, glass neb and ESI PFA neb). However, it is unclear whether the BaAr is truly BaAr or whether there is another interference sitting on the mass of ^{138}Ba, which was used to calculate the interference when using the high uptake nebuliser on the *Aridus*.

Test solution 1

Lu/Hf: 0.001

Lu	*Hf*	*Ba*	*La*	*Ce*	*Dy*	*Tb*	*Nd*
2 ppb	2 ppm	2 ppm	200 ppb	200 ppb	20 ppb	2 ppb	200 ppb

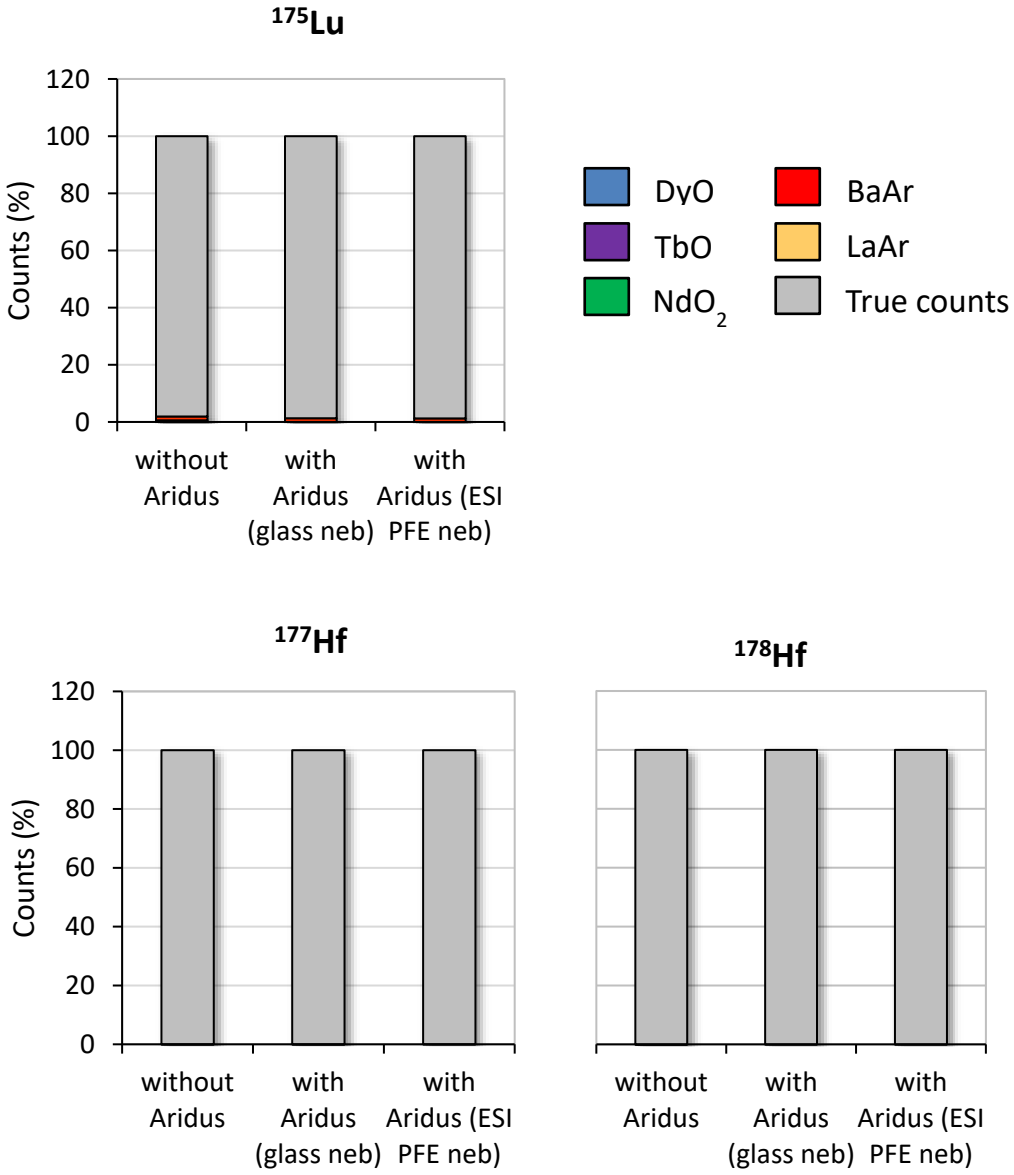

Figure 3.1 Comparison of % of counts caused by isobaric interferences on ^{175}Lu, ^{177}Hf and ^{178}Hf for a test solution representing a non-carbonate fraction of a carbonatite (Lu/Hf: 0.001) for wet plasma (without *Aridus*) and using a desolvator (*Cetac Aridus*^{TM}) with two different nebulisers (glass neb: high uptake of 1 ml/min, *ESI* PFA: low uptake of 50 µl/min). Different colours represent the species responsible for the % of counts; grey: calculated true counts of the isotope of interest. Non-carbonate fractions show low Lu/Hf ratios, which are low in REE. Thus, isobaric interference effects are minor.

Test solution 2

Lu/Hf: 10

Lu	*Hf*	*Ba*	*La*	*Ce*	*Dy*	*Tb*	*Nd*
20 ppb	2 ppb	20 ppm	20 ppm	20 ppm	2 ppm	0.2 ppm	20 ppm

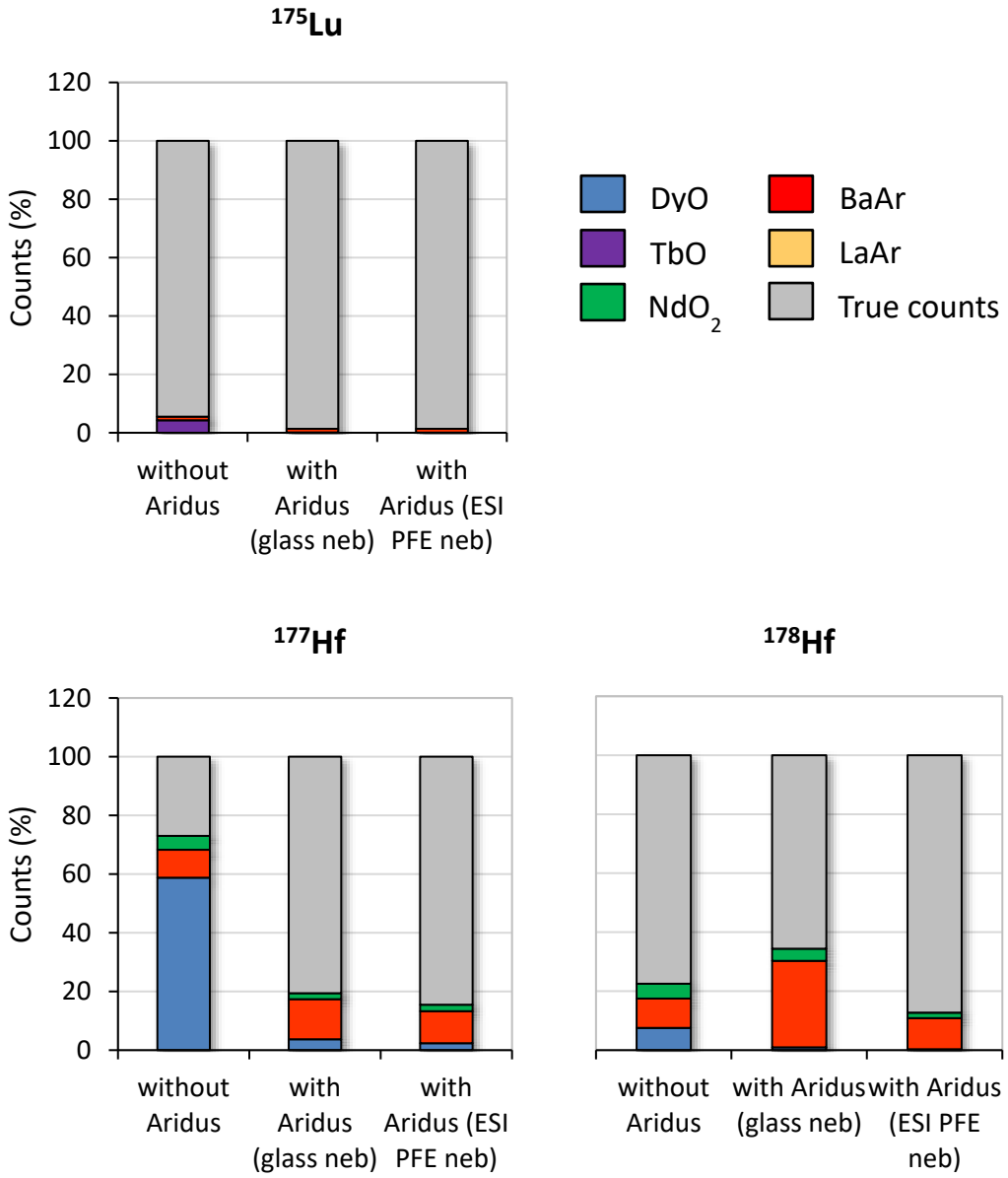

Figure 3.2 **Comparison of % of counts caused by isobaric interferences on ^{175}Lu, ^{177}Hf and ^{178}Hf for a test solution representing a carbonate fraction of a carbonatite (Lu/Hf: 10) for wet plasma and using a desolvator (*Cetac Aridus*^{TM}) with two different nebulisers (glass neb: high uptake of 1 ml/min, *ESI* PFA: low uptake of 50 µl/min). Different colours represent the species responsible for the % of counts; grey: calculated true counts of the isotope of interest. Carbonate fractions show higher Lu/Hf ratios with higher concentrations in REE. Thus, isobaric interference effects on Hf isotopes are strong (>50% of mass 177 is caused by DyO).**

Test solution 3

Lu/Hf: 50

Lu	*Hf*	*Ba*	*La*	*Ce*	*Dy*	*Tb*	*Nd*
200 ppb	4 ppb	20 ppm	20 ppm	20 ppm	2 ppm	200 ppb	20 ppm

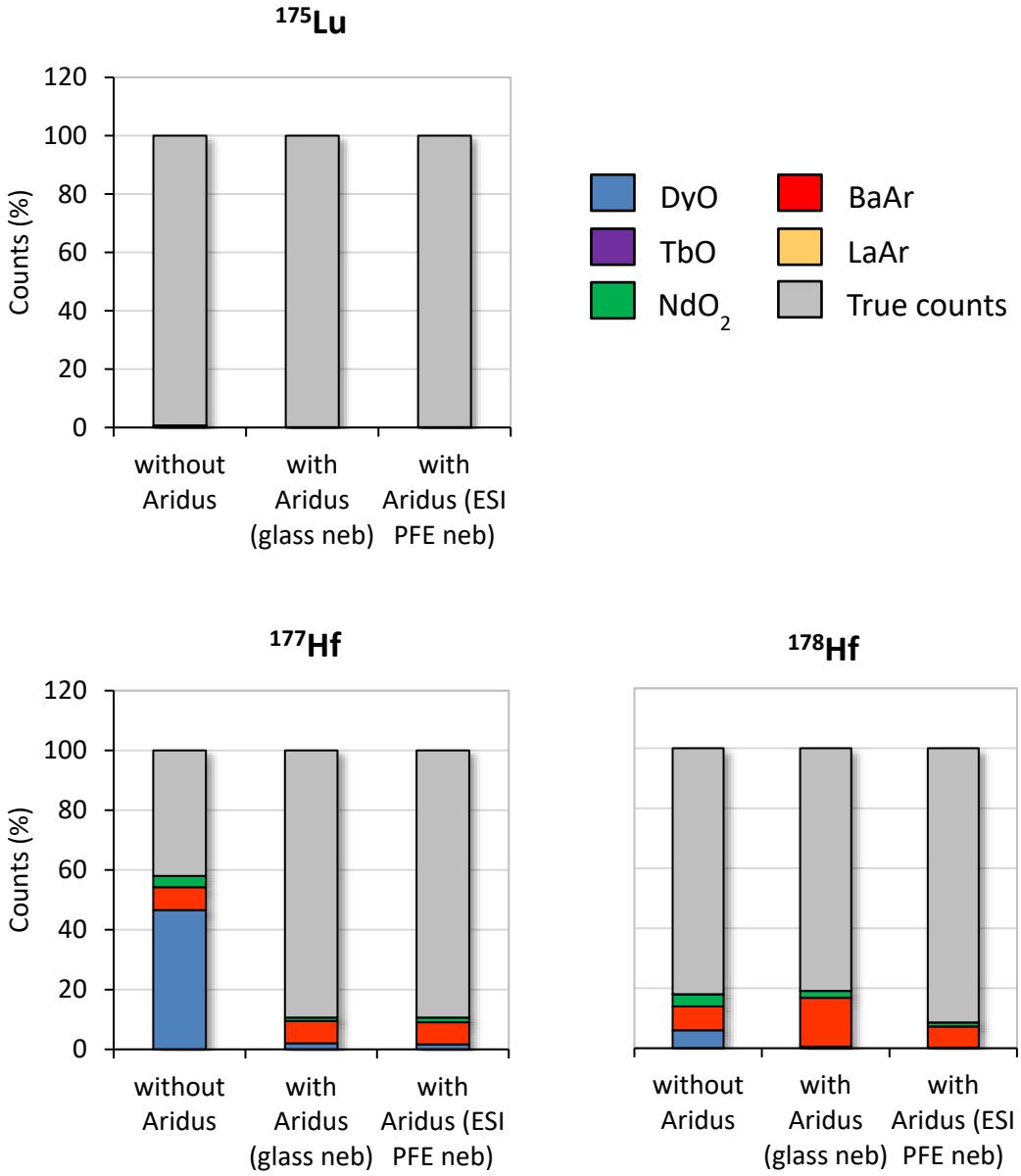

Figure 3.3 **Comparison of % of counts caused by isobaric interferences on ^{175}Lu, ^{177}Hf and ^{178}Hf for a test solution representing a carbonate fraction of a carbonatite (Lu/Hf: 50) for wet plasma and using a desolvator (*Cetac Aridus*^{TM}) with two different nebulisers (glass neb: high uptake of 1 ml/min, *ESI* PFA: low uptake of 50 µl/min). Different colours represent the species responsible for the % of counts; grey: calculated true counts of the isotope of interest. Carbonate fractions show higher Lu/Hf ratios with higher concentrations in REE and subsequently are more prone to isobaric interferences (Isobaric interferences on ^{177}Hf caused by DyO make up >40% of the signal).**

3.5.3. X-Series (Q-ICP-MS)

Trace element concentrations were analysed using a *Thermo-Finnigan X-Series 2* Q-ICP-MS. To ensure reproducibility and accuracy as well as for calibration purposes, replicate analyses of six international reference materials (W2, BHVO-1, BE-N, BIR-1, SRM 688, AGV-1) were carried out. Certified USGS reference material COQ-1 was analysed in each sample batch to monitor dilution corrections and digestion methods. Measurements were either carried out with a cyclonic spray chamber (incl. impact bead) to cover a range of trace elements or by using a *CETAC Aridus*^{TM} desolvator to analyse the REE as well as the mother-daughter elements for isotope calculations (Lu-Hf, Rb-Sr and Sm-Nd). The desolvator was used to boost sensitivity and reduce oxides. Nitrogen is added for further signal enhancement (<1 ml/min). Improvements in the oxide formation rates caused by the desolvator are further described in chapter 3.5.2.

3.6. Lithophile elements isotope geochemistry

Due to difficulties with dissolving carbonate-rich samples with unusual major and trace element abundances (*e.g.* high REE concentrations), standard dissolution methods were problematic. Consequently, other methods were evaluated to adjust and improve standard dissolution methods. In total, seven methods were tested and are described below.

All Hafnium analyses and tests have been carried out on a *Thermo Scientific Finnigan Neptune MC-ICP-MS* using a *Cetac Aridus II*^{TM} desolvator in the Arthur Holmes Isotope Laboratories at Durham University. The chemistry protocol described below is also used for Sr and Nd isotopes, which can then be analysed on the same aliquot as Hf. Thus, Sr and Nd do not have a separate methods description.

3.6.1. Method 1 – testing the standard dissolution procedure

The normal sample dissolution method uses a 3:1 ratio of 29M HF to 16M HNO_3 but in the case of the carbonatites and total procedural blanks (TPBs) the ratio was reduced to 1:1. 200 mg of sample powder was dissolved in 2 ml conc. HNO_3 and 2 ml conc. HF. The rock standard BHVO-1 was dissolved in 1 ml HNO_3 and 3 ml HF. Samples were left on the hotplate at 100°C for 24 h and were then dried down. This was followed by two rounds of re-dissolution of the dried sample in 2 ml conc. HNO_3 and subsequent dry down to get rid of any fluorine present in the sample. Afterwards, samples were re-dissolved in 4 ml conc. HCl and left on the hotplate at 150°C overnight to then be dried down the following day. The dried sample was

re-dissolved in 3M HNO_3, transferred to centrifuge tubes, centrifuged and was then ready for column chemistry.

Observations

A large amount of fluorite precipitated immediately when HF was added to the samples and created a gel when dried down. Following chemistry, signal intensities measured by MC-ICP-MS on ^{179}Hf were very low (0.004 to 0.56 V), with reference sample 16462 showing the lowest signal intensities (0.004 V, ~0.03% yield, *c.f.* Table 3.3).

3.6.2. Method 2 – decarbonating samples prior to standard procedure

a) 200 mg; b) 100 mg of sample powder was decarbonated with 2 ml of 6M HCl and then left on the hotplate overnight at 100°C. Afterwards samples were transferred into a centrifuge tube and centrifuged. The carbonate fraction, now dissolved in 6M HCl, was pipetted into a second centrifuge tube.

a) The sample residue in the first centrifuge tube was transferred back into the beaker and was re-dissolved using the method in 3.6.1 but using 0.5 ml conc. HNO_3 and 1.5 ml conc. HF (1:3 ratio). Samples were then dried down, followed by two rounds of re-dissolution of the dried sample in 2 ml conc. HNO_3 and subsequent dry down to get rid of any fluorine present in the sample. The HCl fraction in centrifuge tube 2, from the decarbonisation step, was now added back to the dried down sample and was then left on the hotplate to dry down. Afterwards, the sample was re-dissolved in 4 ml of conc. HCl and left on the hotplate at 150°C overnight to then be dried down the following day. The dried sample was re-dissolved in 3M HNO_3, transferred to centrifuge tubes, centrifuged and was then ready for column chemistry.

b) The residue (non-carbonate) in the first centrifuge tube was washed with MQ, centrifuged and the MQ transferred to separate centrifuge tubes. The remaining residue was dried down and then re-dissolved in 1 ml conc. HNO_3 and 3 ml 29M HF and left on a hotplate set at 90°C overnight. The beakers were then uncapped and left to dry to a translucent gel on a hotplate set at 90°C. Once dry, 3 ml conc. HNO_3 was added to the residue and left to re-dissolve with the beaker capped on a hotplate set at 90°C followed by evaporation to dryness at 90°C. The HNO_3 dry down was repeated several times. All samples were then re-dissolved in 1 ml 3M HNO_3 ready for column chemistry. The carbonate fraction in 6M HCl was dried down and then re-dissolved in 1 ml 3M HNO_3, ready to be passed through the columns separately from the residual non-carbonate fraction.

Observations

a) By decarbonating the samples first, the HF-HNO_3 dissolution resulted in a smaller amount of fluorite precipitating from the solution. This increased signal intensities measured by MC-ICP-MS on ^{179}Hf for some samples from 0.05 V to 2.19 V and 0.56V to 9.05 V. For the other samples no drastic change could be observed and the reference sample 16462, with 0.001 V (~0.01% yield, *c.f.* Table 3.3), had even lower intensities than for method 1.

b) First tests of 1% aliquots of the 3M HNO_3 prior to Sr-spec column chemistry resulted in yields as high as 58% for the residual non-carbonate fraction and 3.8% for the carbonate fraction. Mass balance calculations reveal that ca. 2-3% of the bulk sample Hf is resides in the carbonate fraction, while the remaining 97-98% resides in the non-carbonate fraction. Thus, the yields were calculated assuming 97% of the bulk Hf is residing in the non-carbonate fraction and 3% in the carbonate fraction (*c.f.* chapter 3.6.7 and 4.2). Following the column chemistry, the samples were analysed: The non-carbonate fraction generated signals up to 8.3 V on ^{179}Hf (~ 67% yield) and unradiogenic $^{176}Hf/^{177}Hf$ ratios, whereas the carbonate fraction yielded much lower signal intensities than the non-carbonate fraction (0.04 V on ^{179}Hf, ~ 20% yield) but radiogenic $^{176}Hf/^{177}Hf$. It appears that there is still significant suppression in the carbonate fraction leading to low yields. However, signal intensities did increase significantly compared to method 1 and 2a (from 0.001-0.004 V to 0.025-0.038 V when adjusting for variations in sensitivity, *c.f.* Table 3.3).

3.6.3. Method 3 – addition of Al-solution, excess of HNO_3 over HF and use of boric acid

a) 200 mg; b) 100 mg of sample material was weighed and doped with 3 ml of *10,000 ppm ROMIL PrimAg® Mono-Component Al-Solution*. By adding Al to the samples the coprecipitation of Hf in the fluorites is thought to be suppressed (Tanaka et al., 2003).

a) After adding the Al-solution to the sample, 1 ml of HNO_3 was added and left to react with the sample for at least 30 minutes with the lid on loosely. This was followed by addition of 3 ml of conc. HF. The samples were capped and left on the hotplate set at 100°C overnight and were uncapped and dried down to a translucent gel the following day. Once dry, 2 ml of conc. HNO_3 was added to the sample and left to re-dissolve overnight on the hotplate set at 100°C. Samples were then dried down followed by addition of another 2 ml of HNO_3 and immediate dry down. Once dry, 5 ml of 3% H_3BO_3 in 2.5M HCl was added to each sample to break down any leftover fluorites (Yang et al., 2011) and left on the hotplate set at 80°C overnight. This was followed by dry down and two additions of 1 ml 6M HCl with subsequent dry downs. Afterwards, the samples were re-dissolved in 1 ml conc. HNO_3 and dried down before finally being re-dissolved in 1 ml 3M HNO_3 ready for purification by column chemistry.

b) The Al-solution added to the sample was dried down. Afterwards, 3 ml conc. HNO_3 and 1 ml 29M HF were added to the sample and left to react on the hotplate capped at <100°C overnight. The HNO_3/HF ratio was changed from 1:3 to 3:1 as carbonatites only have minor amounts of silicate. Additionally, by adding less HF, the amount of fluorite was thought to be reduced. The beakers were then uncapped and left to dry to a translucent gel. Once dry, 3 ml conc. HNO_3 was added to the sample and then left to dry down on a hotplate set at 90°C. The HNO_3 dry down step was repeated. Afterwards, samples were re-dissolved in 5 ml 3% H_3BO_3 (in 2.5M HCl) and were left on the hotplate set at 80°C overnight. The next day, the beakers were uncapped and left to dry <100°C. Once dry, another 2 ml of H_3BO_3 (in 2.5M HCl) was added and dried down. This was repeated twice after and was followed by multiple additions of 3 ml conc. HNO_3 and subsequent dry downs on a hotplate set at 90°C. To prepare the samples for column chemistry, 1 ml of 3M HNO_3 was added to each sample.

Observations

a) Signal intensities after column chemistry for sample 16462 after only one H_3BO_3 dry down was 1.14 V (^{179}Hf), which leads to a yield of approximately 10% (*c.f.* Table 3.3).

b) Unlike method 3a, the yields for more boric acid dry downs resulted in 18% after column chemistry. Signal intensities did not exceed 1.82 V on ^{179}Hf (1.14 V after adjusting the day's sensitivity to 500 V/ppm, *c.f.* Table 3.3).

3.6.4. Method 4 – ammonium fluoride digestion

The following procedure was adapted from Hu et al. (2013): 100 mg of sample powder was weighed in a *Savillex* beaker followed by addition of 600 mg of NH_4F (ammonium fluoride) to each sample. This was done to again reduce fluorite formation. To wet the mixture, a few drops of MQ were added. The beakers were capped and placed on a hotplate set at 230°C for 2 h. Once the beakers cooled down, 3 ml conc. HNO_3 was added and the mixture was then evaporated to near dryness on a hotplate set at 160°C. This was repeated. Then additional rounds of HNO_3 dry down were carried out with the hotplate set at 90°C. Finally, the sample was re-dissolved in 1 ml 3M HNO_3 ready for column chemistry.

Observations

Prior to Sr-spec columns, the samples were completely dissolved in a clear solution. However, after drying down the Hf-Nd fraction, there was a lot of residue left. Following the Sr-spec columns, the amount of residue for the samples treated with ammonium fluoride was larger than for the other methods. This was also observed following cation and anion column chemistry. For other methods, no residue was left after the final anion column chemistry. Furthermore, this method only gave dissolution yields of max. 2.8%. After column chemistry the measurement resulted in signal intensities of <0.04 V on ^{179}Hf which is equivalent to a yield of 0.3%. Thus, this method was abandoned.

3.6.5. Method 5 – addition of Al-solution and excess of HNO_3 over HF during dissolution

Based on former experiments with addition of Al-solution (Method 3, Tanaka et al., 2003), 100 mg of sample powder were doped with 3 ml *10,000 ppm ROMIL PrimAg® Mono-Component Al-Solution*. The mixture was dried down prior to further treatment. Once the sample was dry, 3 ml of conc. HNO_3 and 1 ml of 29M HF were added to the sample. The beakers were capped and placed on a hotplate set at 100°C overnight. The dissolved samples were then left to dry on a hotplate set at 90°C. Once dry, 2 ml of conc. HNO_3 was added to each beaker, left to re-dissolve and then dried down at 90°C. This was repeated several times until the amount of fluorite had decreased notably. Once dry, samples were re-dissolved in 1 ml 3M HNO_3 to be purified using column chemistry.

Observations

Signal intensities on ^{179}Hf varied from 0.52 to 0.92 V (0.33-0.58 V when adjusting for variations in MC-ICP-MS sensitivity) for this method after purification by column chemistry. The yields were as high as 12.6% for a 1% aliquot tested prior to column chemistry, but only 8% after column chemistry (*c.f.* Table 3.3).

3.6.6. Method 6 – change of major element composition for Al-Mg-Fe

Tanaka et al. (2003) suggest that by changing the matrix of Ca-rich samples to a major element composition similar to known standards, it is possible to suppress Hf coprecipitation into fluorites. In former experiments (Method 3 and Method 5) the major element composition was changed by adding Al to the samples prior to the ongoing chemistry. Now, 3 ml *10,000 ppm ROMIL PrimAg® Mono-Component Al-Solution*, 1.5 ml *10,000 ppm ROMIL PrimAg® Mono-Component Mg-Solution* and 0.8 ml *10,000 ppm ROMIL PrimAg® Mono-Component Fe-Solution* was added to 100 mg of carbonatite powder to create a matrix similar to BHVO-1. The mixture was dried down and then re-dissolved in 3 ml of conc. HNO_3 and 1 ml of 29M HF on a hotplate set at 100°C. After the samples had cooled, the beakers were uncapped, and the samples evaporated to near dryness on a hotplate set at 90°C. Once dry, 2 ml of conc. HNO_3 was added to each sample, left to re-dissolve and then dried down. This was repeated until the amount of fluorite had decreased evidently. Then, the samples were re-dissolved in 1 ml 3M HNO_3 ready to go onto the first column.

Observations

Signal intensities on ^{179}Hf varied from 0.89 to 2.36 V (0.53-1.48 V adjusted for instrument sensitivity variations) for this method and gave yields of up to 5.3% for a 1% aliquot tested prior to column chemistry. After column chemistry the yield increased to 20%, which is likely caused by less sample matrix suppression after column chemistry compared to the 1% aliquot testing (*c.f.* Table 3.3).

3.6.7. Summary of methods 1 to 6

Method 4 showed very low yields (0.3%; *c.f.* Table 3.3) and was thus neglected for further experiments. The same applied for method 1 and 2a (yields 0.03% and 0.01%, respectively). The low signal intensities and thus yields were likely caused by the loss of Hf by extensive crystallisation of fluorites prior to purification by column chemistry. Although signal intensities varied for method 5 and 6, the $^{176}Hf/^{177}Hf$ ratio was relatively reproducible among the two different approaches. For both methods yields were still relatively low (8% and 20%, respectively) but had improved massively (>800%) compared to method 1 and 2a. Method

3a showed a similar yield (10%) but the isotope ratio did not match that of method 3b (yield 18%), 5 or 6. For method 3a sample 16462 was not replicated, thus it is not clear whether the method itself or the analysis is responsible for the different ratio. Method 2b showed unradiogenic $^{176}Hf/^{177}Hf$ and yields of 67% for the non-carbonate fraction and highly radiogenic $^{176}Hf/^{177}Hf$ and yields of 20% for the carbonate fraction. The radiogenic nature of the carbonate fraction is probably due to high Lu/Hf ratios in this fraction, as most of the Hf from this sample is sitting in the non-carbonate fraction and not the carbonate, which is further reflected by the signal intensities (*c.f.* Table 3.3). This was also observed by Bizimis et al. (2003).

It appears that method 2b) is the most appropriate dissolution method to use for carbonatites as it is associated with the lowest degree of fluorite formation that may lead to Hf loss. To compare both non-carbonate and carbonate fraction to whole-rock analyses, the latter is performed using the approach of method 5. Method 5 was chosen over method 6 and 3b, because less *ROMIL PrimAg® Mono-Component Solution* and in general less acids and thus less blank is added to the sample. Additionally, method 5 was chosen, because it is simpler to perform.

Table 3.3 **Summary of different method approaches on the example of sample 16462 from Fen, Norway. Yields were calculated assuming no interferences on Hf isotopes when analysed using the *XSeries* and were calculated using the whole-rock Hf composition for methods 1-6 and calculated using trace element analysis for each fraction for method 7. DNR = did not run.**

Example of sample 16462 from Fen								
Method	**Method description**	**Sample amount (g)**	**Replicates**	**Hf yields**	**Signal intensities ^{179}Hf (V)**	**Sensitivity (V/ppm)**	**^{176}Hf/^{177}Hf**	**1SE**
1	**Standard procedure**	0.2	-	0.03%	0.004	500	DNR	
2	**Decarbonating samples**							
	a) Join fractions back together	0.2	-	0.01%	0.001	500	DNR	
	b) Treat fractions separately	0.1						
	Non-carbonate		3	67%	7.1 - 8.3	800	0.282570	0.000002
	Carbonate fraction		3	20%	0.04 - 0.06	800	0.3004655	0.000055
3	**Addition of Al and H_3BO_3**	0.1						
	a) 1 x boric acid dry down		-	10%	1.14	500	0.282325	0.000006
	b) 4x boric acid dry down		3	18%	1.4 - 1.82	800	0.283106	0.000005
4	**Ammonium fluoride**	0.1	3	0.3%	0.04	800	DNR	
5	**Al addition and excess HNO_3**	0.1	3	8%	0.52 - 0.92	800	0.283058	0.000006
6	**Change of major element composition**	0.1	3	20%	0.89 - 2.36	800	0.283025	0.000004
7	**Final procedure**	0.2						
	Non-carbonate fraction		2	59%	4.3-4.7	450	0.282577	0.000002
	Carbonate fraction		2	8%	0.008-0.016	450	0.305828	0.000212
	Whole-rock		2	99%	5.8	455	0.282340	0.000011

3.6.8. Final procedure/method 7 - testing of isotopic equilibrium between carbonate and non-carbonate-fraction

Testing the isotopic equilibrium between the carbonate and non-carbonate fractions of carbonatites was addressed by Bizimis et al. (2003). For this purpose, they separated carbonate from non-carbonate fraction, similar to the approach used in this study. In this final procedure, method 2b) was used for testing carbonate and non-carbonate fraction, and method 5 for testing the whole-rock composition, with the latter being slightly changed regarding the timing of Al-addition to the sample. A simplified illustration of the final procedure is shown in Figure 3.4. In this final method 7, samples were prepared and then aliquoted before going onto the first set of columns. Aliquoting was carried out once the sample was completely dissolved. The aliquots (5%) of each sample (whole-rock, carbonate and non-carbonate fraction) were then taken and diluted to be tested for trace element concentrations (*c.f.* chapter 3.5.2).

In first experiments of the final method 7, 10 samples were treated, of which sample 16462 was duplicated (whole-rock, method 5) to test two different dissolution and dilution approaches prior to aliquoting for measurements on the *Thermo Scientific XSERIES 2 ICP-MS* (wet plasma). This was done to make sure that the sample is completely dissolved before being aliquoted. One approach involved dissolution in diluted HNO_3 and the other in conc. HCl. The sample dissolved in conc. HCl still contained relatively large amounts of precipitate, although being dissolved in 5 ml conc. HCl, while the duplicate was almost dissolved in 1 ml conc. HNO_3 and completely dissolved following addition of 4 ml of MQ.

If samples contained large, difficult-to-dissolve, oxide phases after HNO_3-HF digestion, they were dissolved with either 2 ml (non-carbonate fraction) or 5 ml (whole-rock) conc. HCl and left on the hotplate at 150°C. The vapour pressure created by HCl and the increased temperature usually dissolved those phases within 24 h. Samples that were treated to dissolve oxides were then dried down.

After digestion all samples and fractions were re-dissolved to be diluted for aliquoting, first in 1 ml conc. HNO_3, to which 4 ml of MQ were added at a later stage. Samples were ultra-sonicated when residue was still present and were then aliquoted (5%). Addition of Al to whole-rock samples was carried out when the sample was completely dissolved, but after aliquoting. The mixture was dried down as to then be taken up in 1 ml 3M HNO_3 ready to go on the Sr-spec columns. Carbonate and non-carbonate fractions were directly dried down

after aliquoting and were re-dissolved in 1 ml 3M HNO_3. All three different fractions (carbonate, non-carbonate and whole-rock) were then passed through the Sr-spec, cation columns and anion columns.

Often there was still a substantial amount of precipitate forming after the cation columns. When drying down, this baked onto the bottom of the beaker and was then difficult to re-dissolve in the 0.52 N H_2SO_4 + 5% H_2O_2 used to load the samples onto the final anion columns. If this happened, the residual material was re-dissolved in conc. HCl, then dried down and taken back up in 1M HCl to be passed through the cation column a second time to remove more Ca.

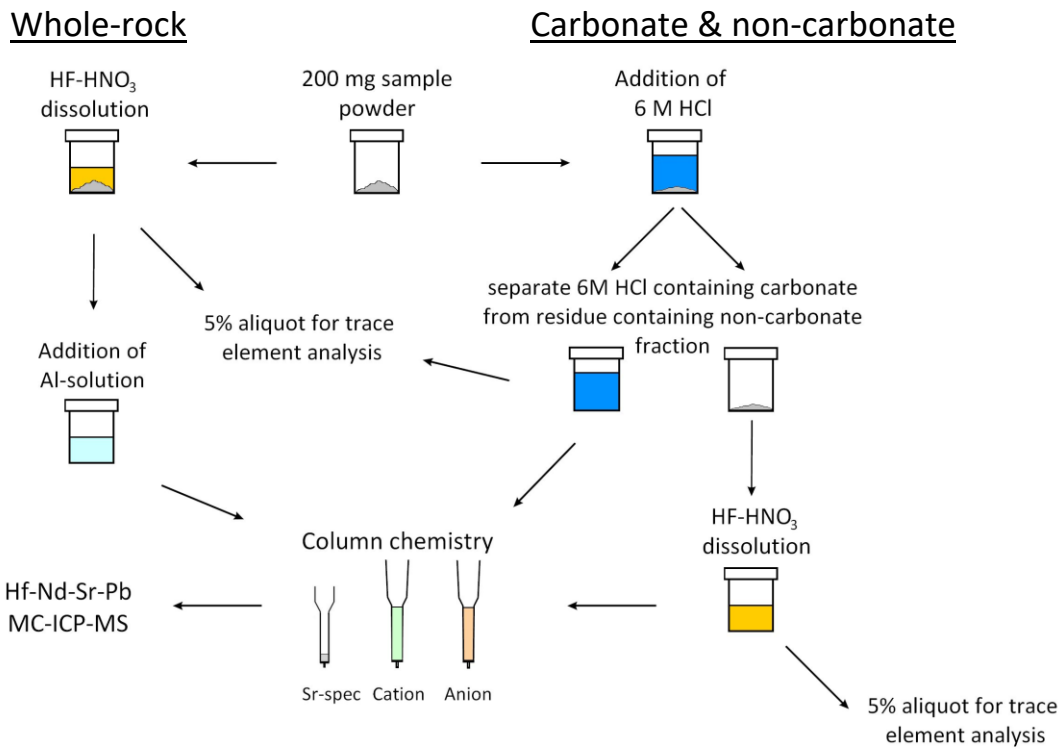

Figure 3.4 Simplified sketch of the final Hf-Nd-Sr procedure. The left side of the image shows the procedure for whole-rock samples, while the right part shows the separation of carbonate from non-carbonate fraction. The amount of 200 mg was weighed twice, once for whole-rock and once for the carbonate/non-carbonate separation.

3.6.8.1. Adjustments to the final method 7

Following the previous experiment, a new batch of 18 samples was processed. This included samples from Jacupiranga, Sokli, Fen, Grønnedal-Ika, Kovdor and USGS reference material COQ-1 from Oka. This new batch of samples was processed with the aim to re-produce data from previous experiments and to increase Hf yields by further reducing the amount of Ca and REE. This was approached by adjusting the method as follows:

Prior to the first Sr-spec column step, carbonate and whole-rock fractions were dissolved in 4 ml of 3M HNO_3 to maximize the amount of sample material in solution. The whole-rock and carbonate fractions in 4 ml 3M HNO_3 each, were then split into 4 × 1 ml aliquots and passed through separate Sr-spec columns (*c.f.* Figure 3.5). This resulted in four columns per sample and was done to remove more Ca and potentially REE prior to the second stage cationic columns. All fractions collected from the four columns were re-combined, dried down and then re-dissolved in 2 ml 1M HCl. The whole-rock and carbonate fractions in 2 ml 1M HCl each were then split into 2 × 1 ml aliquots and were passed through separate cation columns (*c.f.* Figure 3.5) to further remove Ca and REE. The collected fractions were again re-combined, dried down and taken up in 1 ml of 0.52 N H_2SO_4 + 5% H_2O_2 ready to be passed through the final anionic columns. Because the non-carbonate fraction does not or only contains minor amounts of Ca, the yield issue is not as susceptible to suppression by fluorites or interferences by REE, thus the non-carbonate fraction was processed through columns as illustrated in Figure 3.4. Samples were then analysed using an additional *CETAC Aridus™* desolvator on the *XSeries* (Chapter 3.5.2).

An additional batch of samples processed following the above approach was prepared. This batch included the samples collected from the Fen carbonatite complex, as well as samples from Fogo, Tupertalik and a replicate from the non-carbonate fraction of one of the samples from Jacupiranga (J2-C2).

Table 3.4 **Summary of signal intensity variations for whole-rock (n=46), carbonate (n=45) and non-carbonate fractions (n=46) of all batches.**

Fraction		^{179}Hf Signal intensity (V)
Whole-rock	MIN	0.05
	MAX	17.47
	Average	6.25
Carbonate	MIN	0.004
	MAX	0.82
	Average	0.11
Non-carbonate	MIN	0.02
	MAX	16.5
	Average	5.52

Observations

On the basis of sample 16462 it appears that method 7 drastically improved Hf yields for whole-rock samples (99%, *c.f.* Table 3.3), while there was no clear improvement to be observed for the carbonate and non-carbonate fractions. However, if we look at the range of signal intensities for whole-rock (0.05 to 17.47 V), carbonate (0.004 to 0.82 V) and non-carbonate fractions (0.02 to 16.5 V; *c.f.* Table 3.4) of all batches combined it is clear that, in general, the different samples tend to show high variability. However, the average Hf beam intensities of 6.25 V, 0.11 V and 5.52V for whole-rock samples, carbonate and non-carbonate fractions, respectively, are acceptable for carbonatite Hf isotope analyses.

Sample 16462 was used as a reference material for yield testing, but because of high variability in Hf-concentrations as well as different responses to the chemistry of carbonatites, some samples provide us with better yields and thus better signal intensities than others. With carbonatites being so highly variable in composition, I suggest that this final approach (section 3.6.8) is the best possible approach without using isotope dilution. Though, isotope dilution might only improve the accuracy of concentration measurements but not necessarily of isotope ratio analyses, which is why it was not used for this project.

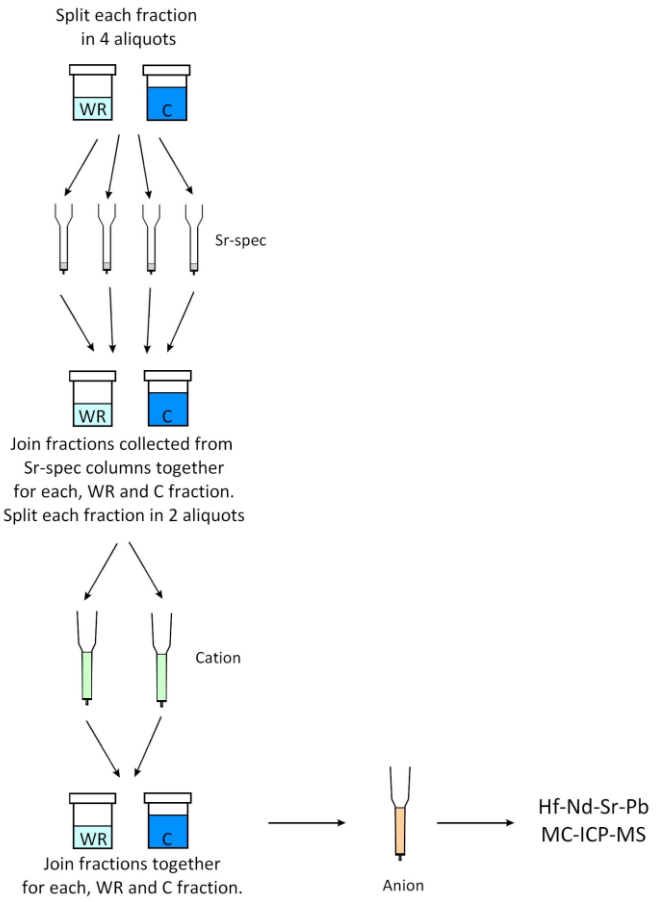

Figure 3.5 Simplified sketch of the changes applied to the column chemistry for the whole-rock (WR) and carbonate (C) fractions.

3.6.9. Mineral fraction chemistry

Calcite (2.0603 g), phlogopite (0.6432 g), magnetite (2.2054), apatite (0.019 g) and chlorite (0.0388 g) from sample CQW-1 (Fen, Norway) were picked for mineral analyses. For analyses of apatite and chlorite, the whole fraction was used, for calcite 1 g of sample was weighed twice, for phlogopite 0.2 g of sample was weighed three times and for magnetite 0.1 g was weighed three times. Calcite was dissolved using 1 ml conc. HCl and 4 ml 6M HCl and left on a hotplate to react overnight at 100°C. Needles of apatite or other trace phase growing inside the calcite crystals - that were not dissolved in HCl - were separated from the solution by centrifuging the sample. The solution was then dried down and re-dissolved in 10 ml 3% HNO_3. Phlogopite was first dissolved in 1 ml conc. HNO_3 and 3 ml conc. HF and left on a hotplate overnight at 100°C. The samples were uncapped and evaporated to dryness and refluxed and dried down in 1 ml conc. HNO_3 twice to remove leftover fluorine. The phlogopite was still intact, though colourless, and was thus re-dissolved in 4 ml conc. HCl and left on a

hotplate at 120°C overnight. The phlogopite was then dried down, refluxed in 0.5 ml conc. HNO_3 to be transferred into a nitric matrix, dried down again and then re-dissolved in 5 ml 3% HNO_3. Magnetite was dissolved in 2 ml conc. HCl and left on a hotplate set at 120°C overnight. The fraction was then evaporated to dryness and once dry, re-dissolved in 0.5 ml conc. HNO_3 to transfer into a nitric form to be dried down again. Once dry, the magnetite fraction was re-dissolved in 5 ml 3% HNO_3. Apatite was separated from calcite by leaching it in, first 0.25M HCl, then 1M HCl (apatite weight before leaching: 0.0857g). The residue was washed with MQ, dried and then dissolved in 2 ml conc. HCl. However, the HCl did not affect the apatite and was thus dried down. The apatite fraction was then dissolved in 0.5 ml conc. HNO_3 and 1 ml conc. HF and left on a hotplate at 100°C overnight. The solution was dried down and once dry, refluxed with conc. HNO_3 twice and dried down to drive off fluorine. Once dry, the apatite was again re-dissolved in conc. HCl to bring the residual material into solution. Afterwards, the apatite fraction was dried down, refluxed in conc. HNO_3, dried again to then be re-dissolved in 5 ml 3% HNO_3. Chlorite was dissolved in 1 ml conc. HNO_3 and 3 ml conc. HF and left to react on a hotplate set at 100°C overnight. The sample was uncapped and evaporated to dryness the next day and refluxed and dried down with conc. HNO_3 twice to evaporate remaining fluorine. Once dry, the sample was re-dissolved in conc. HCl, dried down, then refluxed in conc. HNO_3, dried down and finally re-dissolved in 5 ml 3% HNO_3.

Once all mineral fractions were fully dissolved in 3% HNO_3, 5% of each fraction was aliquoted for trace element analysis. The remaining sample in solution was dried down and then re-dissolved in 1 ml 3M HNO_3, except for the calcite fraction which was re-dissolved in 4 ml 3M HNO_3 ready for column chemistry. The calcite fraction was divided into 4 x 1 ml fractions and run through four Sr-spec columns and later through two cation and two anion columns.

3.6.10. Column chemistry

Three sets of columns were used for purification of the samples prior to analysis with a MC-ICP-MS: 1) Sr-spec columns (*Sr-spec* resin), 2) cationic columns (*Bio-Rad AG50 W-X8* resin) and 3) anionic columns (*Bio-Rad AG1-X8* resin). Sr-spec columns were used to separate elements such as Ca and Ba, as well as alkali and alkaline earth metals from Sr. During this separation three fractions were collected: 1) Nd-Hf, 2) Sr and 3) Pb. Afterwards, cation resin columns were used for separation of Nd from Hf. Furthermore, this resin allows effective separation of Lu and other REE from Hf (Dowall et al., 2003). Anion resin columns were used for the final purification of Hf, removing any Ti left in the sample matrix. The recipes for the

respective column chemistry can be found in the appendix (Table 10.8, Table 10.9 and Table 10.10).

Throughout the column chemistry, Sr, Nd and Pb were also collected and not discarded.

3.6.11. Neptune and Neptune Plus (MC-ICP-MS)

The isotope ratios $^{87}Sr/^{86}Sr$, $^{176}Hf/^{177}Hf$ and $^{143}Nd/^{144}Nd$ were analysed using a *Thermo Scientific Neptune* Multi Collector (MC) ICP-MS. Standard material was analysed four times at the start, once every five samples and twice at the end of a run to ensure instrument performance. The data given in the appendix (Table 10.32, Table 10.33, Table 10.34, Table 10.38, Table 10.39, Table 10.40) was analysed over several analytical sessions, of which the details (standard normalisation, precision and accuracy) are given as abbreviations below the tables.

Table 3.5 Cup configurations for analysing $^{176}Hf/^{177}Hf$, $^{143}Nd/^{144}Nd$ and $^{87}Sr/^{86}Sr$. Masses used for isobaric element interference corrections following the approach of Nowell et al. (2008) are underlined.

Element	L4	L3	L2	L1	C	H1	H2	H3	H4
Hf	$^{172}\underline{Yb}$	$^{173}\underline{Yb}$	^{175}Lu	^{176}Hf	^{177}Hf	^{178}Hf	^{179}Hf	^{180}Hf	
Nd	^{142}Nd	^{143}Nd	^{144}Nd	^{145}Nd	^{146}Nd	$^{147}\underline{Sm}$	^{148}Nd	$^{149}\underline{Sm}$	^{150}Nd
Sr	$^{82}\underline{Kr}$	$^{83}\underline{Kr}$	^{84}Sr	$^{85}\underline{Rb}$	^{86}Sr	^{87}Sr			

Strontium and Nd were analysed in solution mode, using a *PFA 50* nebuliser in a cinnabar spray chamber, a standard sampler cone and an H skimmer cone. Sensitivities were usually around 45-68 V/ppm. Neodymium was analysed from the bulk REE fraction collected of the columns. To verify corrections for isobaric element interferences, *JNd$_i$*. was analysed alongside a Sm-doped *JNd$_i$* standard (Sm/Nd: 0.2). The average of the combined standards is given as abbreviations below Table 10.33 and Table 10.39 in the appendix. For $^{87}Sr/^{86}Sr$, standard *NBS987* was used.

Hafnium was analysed using a *CETAC Aridus II^{TM}* desolvator to boost sensitivity to 400-600 V/ppm. This was accompanied by an additional nitrogen flow of 3-4 ml/min. The nebuliser used was a *Cetac C-flow 50* with an average uptake rate of 70-90 µl/min. A standard sampler cone was combined with a X skimmer cone and *JMC475* was used as standard for $^{176}Hf/^{177}Hf$.

3.6.12. The influence of wet vs. dry plasma on $^{176}Lu/^{177}Hf$ ratios and the implication for age corrected $^{176}Hf/^{177}Hf$ ratios

As described and shown in chapter 3.5.2, the influence of isobaric interferences on ^{177}Hf can have a substantial impact on the $^{176}Lu/^{177}Hf$ ratio calculated from trace element analysis. The reduction of oxide formation rates by introducing the sample through a desolvator has reduced those interferences significantly. For geologically young samples minor variations/inaccuracies in the $^{176}Lu/^{177}Hf$ ratio do not have as large an impact as they have for old samples when it comes to age correcting $^{176}Hf/^{177}Hf$ ratios and εHf values.

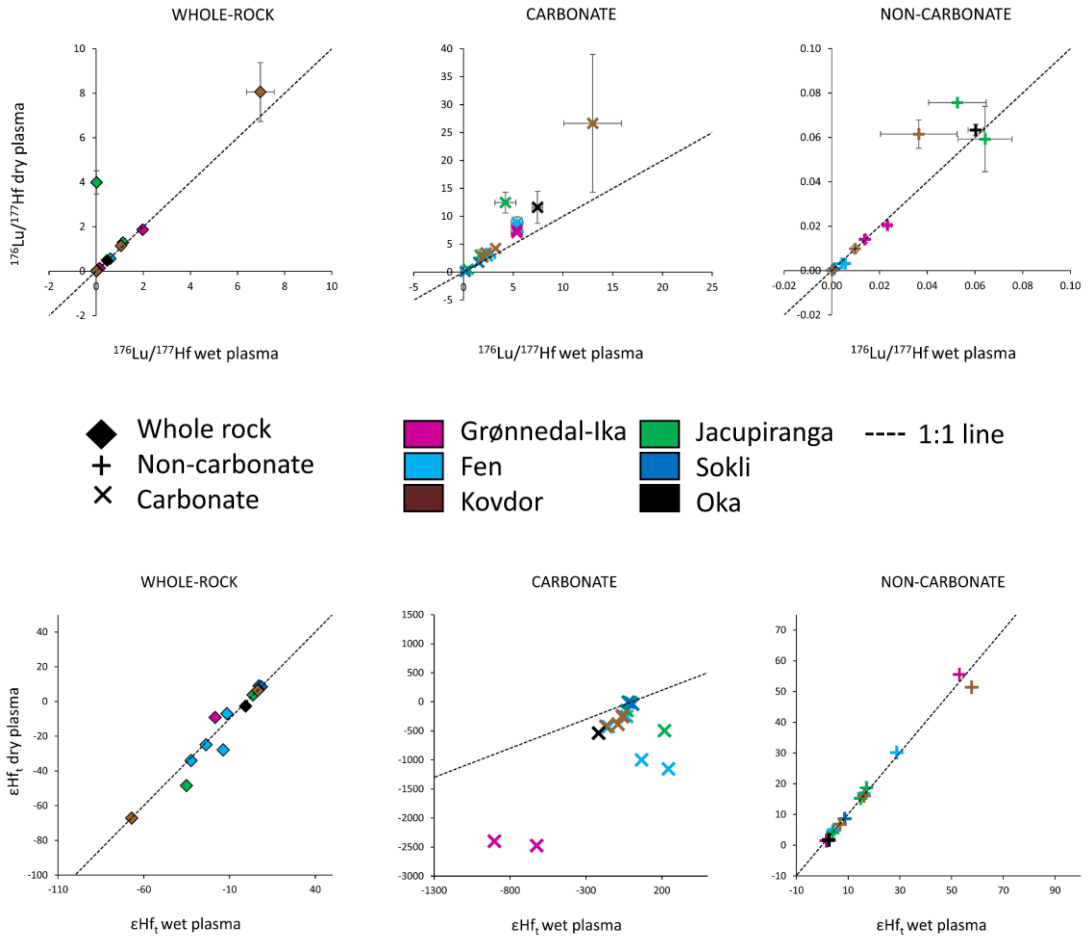

Figure 3.6 **Differences between *Aridus* and solution mode plotted as $^{176}Lu/^{177}Hf_{dry\ plasma}$ vs. $^{176}Lu/^{177}Hf_{wet\ plasma}$ (top) and $\varepsilon Hf(t)_{dry\ plasma}$ vs. $\varepsilon Hf(t)_{wet\ plasma}$ (bottom) for whole-rock, carbonate and non-carbonate fractions.**

When comparing the calculated $^{176}Lu/^{177}Hf$ ratios from *Aridus* (dry plasma) and wet plasma trace element analyses in Figure 3.6, all fractions should fall onto a 1:1 line if there were no

analytical differences between the two methods. However, there is one whole-rock data point from Jacupiranga which yields a much lower $^{176}Lu/^{177}Hf$ for wet plasma versus dry plasma analysis. This can also be observed for several carbonate fractions. As shown in section 3.5.2, the measured signal intensity for ^{177}Hf (for high Lu/Hf samples) in wet plasma mode can be overestimated due to various molecular isobaric interferences on mass 177, which in turn leads to an underestimation of the $^{176}Lu/^{177}Hf$ ratio if interference corrections are not applied or are inaccurate. This could explain the offset from the 1:1 line. In contrast, for the non-carbonate fraction there is no appreciable difference between wet and dry plasma methods considering the uncertainty on the ratios. This shows that the impact of REE oxides interferences on Hf for the non-carbonate fraction is only minor and can easily be corrected for. The impact of REE oxide interferences on ^{177}Hf becomes more problematic when considering the age corrected Hf isotope data plotted as $\varepsilon Hf(t)_{dry\ plasma}$ vs. $\varepsilon Hf(t)_{wet\ plasma}$ (bottom Figure 3.6). For the non-carbonate fraction all the samples plot on or very close to the 1:1 line, whereas for the carbonate fractions, hardly any samples plot on the 1:1 correlation. The carbonate fraction is generally characterised by high $^{176}Lu/^{177}Hf$ ratios (up to ~13; Figure 3.6) compared to the non-carbonate fraction. If the $^{176}Lu/^{177}Hf$ for the carbonate fraction is inaccurate due to unaccounted-for isobaric interferences on ^{177}Hf in wet plasma mode, the age corrected $^{176}Hf/^{177}Hf$ ratios and hence εHf_t values will also be inaccurate. The greater the age correction the greater the impact on the initial $^{176}Hf/^{177}Hf$ (*c.f.* carbonate fraction from Grønnedal-Ika in Figure 3.6 bottom). For the Grønnedal-Ika samples, $\varepsilon Hf(t)_{dry\ plasma}$ are much lower than for $\varepsilon Hf(t)_{wet\ plasma}$. With less isobaric interferences, the *Aridus* data should be more accurate which suggests that these unrealistically low values are due to geological processes rather than analytical artefacts.

For the whole-rock $\varepsilon Hf(t)_{dry\ plasma}$ vs. $\varepsilon Hf(t)_{wet\ plasma}$, there is also an offset from the 1:1-line observable, however not as distinct as for the carbonate fraction.

This suggests that data generated by using wet plasma needs to be treated with great caution and that samples analysed by dry plasma are more representative.

3.6.13. Lu-Hf data quality

Figure 3.7 shows the signal intensity of ^{179}Hf against the measured $^{176}Hf/^{177}Hf$ ratios. The majority of the data plots between 0.283 and 0.285 for $^{176}Hf/^{177}Hf$, independent of the variable signal intensities (0.003 to >17 V). Non-carbonate fractions plot between 0.281 and 0.284 with ^{179}Hf signal intensities of between 0.006 and 16.5V (average 5V). The whole-rock fractions and carbonate fractions are more radiogenic and variable in their $^{176}Hf/^{177}Hf$ ratios (0.275 to 0.380 and 0.282 to 0.830, respectively) with the average ^{179}Hf intensity for whole-rock at 4.5V and for carbonate fraction at 0.11V.

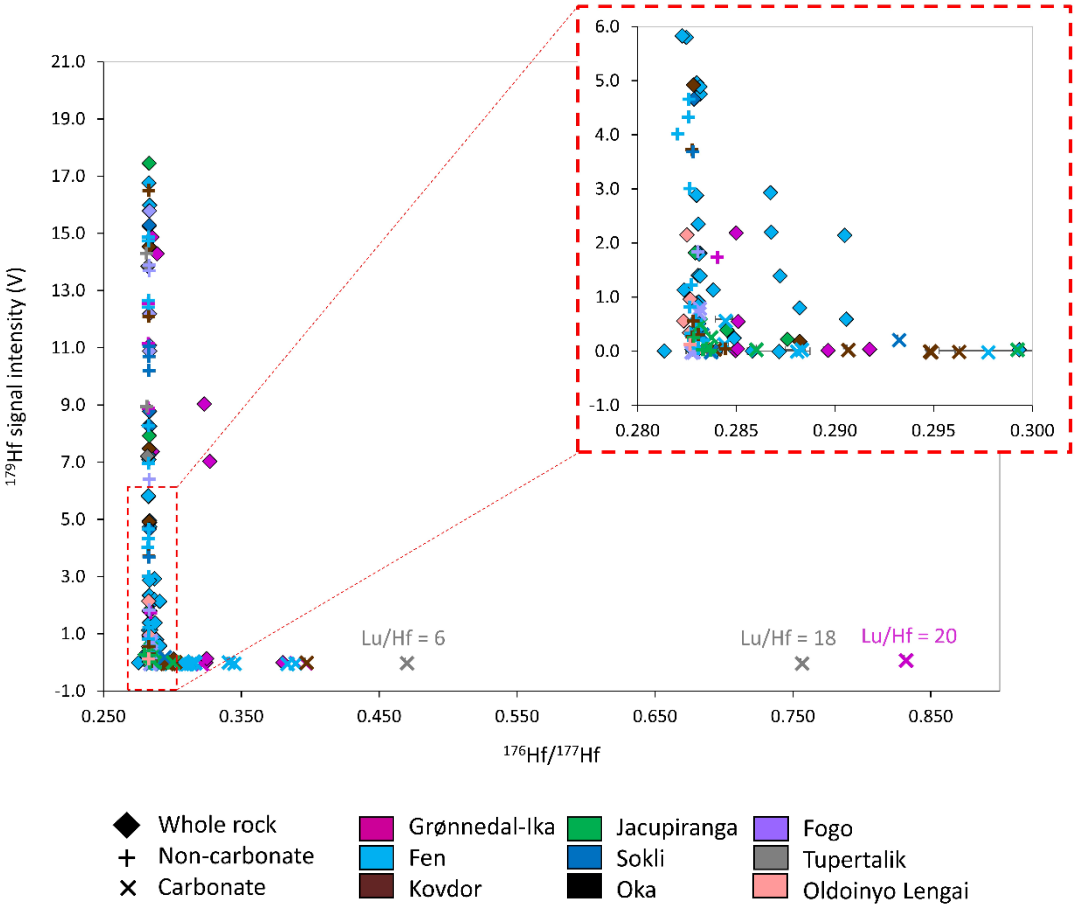

Figure 3.7 **Signal intensity of ^{179}Hf (V) plotted versus the measured $^{176}Hf/^{177}Hf$ ratio for whole-rock, carbonate and non-carbonate fractions of carbonatite samples from different localities. Samples with particularly high Lu/Hf ratios were indicated as they are expected to be more radiogenic. A lot of samples plot close to zero, but no signal intensity is negative. Content of red square represents a magnification. Error bars are smaller than the symbol.**

There is no obvious correlation between ^{179}Hf intensity and measured $^{176}Hf/^{177}Hf$ ratio for the different carbonatite fractions. Although all samples with high $^{176}Hf/^{177}Hf$ ratios have low signal intensities, they are also the oldest samples (1299 and 3007 Ma) with the highest Lu/Hf

ratios so a high $^{176}Hf/^{177}Hf$ ratio is to be expected through radiogenic ingrowth of ^{176}Hf (*c.f.* Figure 3.7). Samples with very high $^{176}Hf/^{177}Hf$ ratios will also have a greater proportion of radiogenic ^{176}Hf and a corresponding higher beam size for ^{176}Hf not reflected by the ^{179}Hf beam size. The higher proportion of ^{176}Hf in radiogenic samples helps mitigate against the effects of isobaric interferences on ^{176}Hf. Thus, despite the large range in measured $^{176}Hf/^{177}Hf$ ratio and the large variation in Hf signal size during analysis there is no clear reason to discount analyses carried out at low ^{179}Hf intensities.

Corrections for isobaric interferences on $^{176}Hf/^{177}Hf$ ratios are applied using the measured signal intensities of ^{175}Lu and ^{173}Yb (*c.f.* Chapter 3.6.11). To exclude interferences as the cause of high $^{176}Hf/^{177}Hf$ ratios for low beam sizes (^{179}Hf), the $^{173}Yb/^{179}Hf$ ratio of signal intensities from carbonatites analysed in this study were plotted versus the measured $^{176}Hf/^{177}Hf$ (Figure 3.8). In a previous independent study (personal communication G.M. Nowell) carried out with exactly the same analytical and interference correction protocol, the Hf standard JMC475 was analysed as a pure solution (100 ppb), doped with 1 ppb Yb+Lu and doped with 5 ppb Yb+Lu. This was used to validate the accuracy of the correction method applied for Yb and Lu to REE/Hf ratios greater than encountered during typical analyses of samples processed though columns. The results of pure and doped JMC475 are plotted on the same $^{173}Yb/^{179}Hf$ vs. $^{176}Hf/^{177}Hf_m$ as uncorrected values ($^{176}Hf/^{177}Hf_m$: black solid line, Figure 3.8) and as $^{176}Hf/^{177}Hf_{corr}$ corrected for isobaric interferences (^{176}Yb, ^{176}Lu; grey solid line, Figure 3.8). Uncorrected $^{176}Hf/^{177}Hf_m$ for pure and doped JMC475 plot up to values of 0.422 for a $^{173}Yb/^{179}Hf$ ratio as high as 0.14. After correction for isobaric interferences, the average of pure *and* doped JMC475 yields a $^{176}Hf/^{177}Hf$ ratio of 0.282152±0.000009 (2SD, n=12), which agrees with the accepted value ($^{176}Hf/^{177}Hf$: 0.28216, Nowell et al., 1998a). Hence, the interference corrections applied to the measured ^{176}Hf intensity, based on ^{173}Yb and ^{175}Lu appear to be sufficient for $^{173}Yb/^{179}Hf$ of up to 0.14, which is well above the range of carbonatites from this study. A lot of whole-rock, carbonate and non-carbonate fractions from this study have lower $^{173}Yb/^{179}Hf$ yet highly radiogenic $^{176}Hf/^{177}Hf_m$ (up to 0.83; *c.f.* Figure 3.8). As was shown in Figure 3.7, the most radiogenic samples ($^{176}Hf/^{177}Hf_m$: 0.469, 0.755 and 0.83) also have the highest Lu/Hf ratios (6, 18 and 20, respectively). As applied isobaric interference corrections appear to be sufficient, the radiogenic nature of samples plotting to the right of the black solid line, representing uncorrected JMC475 $^{176}Hf/^{177}Hf$ ratios (Figure 3.8), must be due to radiogenic ingrowth and is not caused by interferences from Yb or Lu.

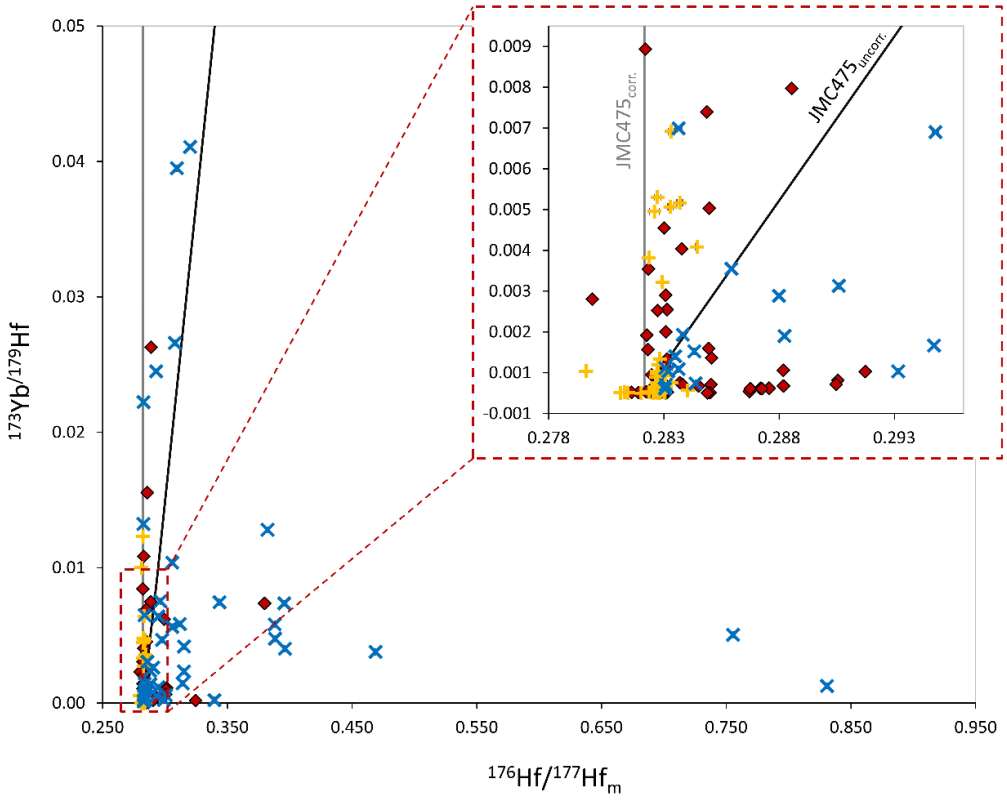

Figure 3.8 **$^{173}Yb/^{179}Hf$ ratio of signal intensities versus measured $^{176}Hf/^{177}Hf$ ratios for whole-rock (red diamonds), carbonate (blue ×) and non-carbonate fractions (yellow +) of carbonatites from this study. Black solid line represents uncorrected $^{176}Hf/^{177}Hf_m$ measurements of pure, doped with 1 ppb Yb+Lu and doped with 5 ppb Yb+Lu JMC475 (100 ppb). Grey solid line represents the $^{176}Hf/^{177}Hf_m$ of the same three 100 ppb JMC475 standard solutions corrected for isobaric interferences (^{176}Yb and ^{176}Lu).**

Chapter 3.5.2 and 3.1 described the difficulties in determining the $^{176}Lu/^{177}Hf$ ratios from trace element analyses. Not only do the low concentrations of Hf present a challenge, but also the high abundance in interfering REE-oxides. Differences between Lu/Hf measurements in wet plasma solution mode and dry plasma mode, using a desolvating nebuliser, have demonstrated that minor changes in the sample introduction technique can change the results dramatically (*c.f.* Chapter 3.6.11). It could be argued that isotope dilution would deliver more accurate $^{176}Lu/^{177}Hf$ ratios for carbonatites. However, this will only be effective if sample-spike equilibrium can be achieved and does not overcome the problem of secondary processes overprinting the Lu/Hf ratio (Chapter 5.2.1, 5.2.2 and 5.2.3). The measured $^{176}Hf/^{177}Hf$ ratios, which for many samples/fractions are already mantle-like or just below the mantle array, would need $^{176}Lu/^{177}Hf$ ratios that are very low or even negative (*c.f.* Table 3.6) to age-correct and yield mantle-like compositions. This then raises the question, as to whether isotope dilution would show a different outcome than that provided by the techniques used here.

Table 3.6 **Table showing the measured $^{176}Lu/^{177}Hf$ and the $^{176}Lu/^{177}Hf$ values needed to correct the measured $^{176}Hf/^{177}Hf$ values from Table 10.32 to values that fall onto the mantle array for their given $^{143}Nd/^{144}Nd$ values. B= bulk, C = carbonate, NC = non-carbonate.**

Sample name	Fraction	$^{176}Lu/^{177}Hf$ needed for mantle value	$^{176}Lu/^{177}Hf$ measured
LI 23/02/08 (n=2)	**B**	0.00001	0.11547
	C	<0	2.70060
	NC	<0	0.00409
BM.2004.P9(9) (n=2)	**B**	<0	0.01563
	C	<0	0.29694
	NC	<0	0.00572
J1-C1	**B**	0.01266	3.98956
	C	0.04410	12.46263
	NC	0.00104	0.05925
91/66 - C2	**B**	<0	0.01681
	C	0.00201	0.51605
	NC	<0	0.00031
91/60 - C5	**B**	0.00434	1.29275
	C	0.00821	3.04911
	NC	0.00113	0.07568
BM.1998,P18(119)	**B**	0.00008	0.03653
	C	0.02736	1.74027
	NC	<0	0.00103
BM.1998,P18(229)	**B**	<0	0.00670
	C	0.00042	0.11423
	NC	<0	0.00011
BM.2000,P11(22) (n=3)	**B**	<0	0.00854
	C	0.03310	2.94890
	NC	<0	0.00007
BM.2000,P14(24)	**B**	0.04760	8.05808
	C	0.30535	26.64265
	NC	0.00395	0.04369
BM.2000,P14(25)	**B**	0.01407	1.14374
	C	0.04793	4.22361
	NC	0.00027	0.01003
4808	**B**	0.01419	0.56280
	C	0.16346	8.86541
	NC	0.00107	0.00300
10160	**B**	0.01022	0.47873
	C	0.15270	8.07137
	NC	0.00007	0.00393
16462 (n=2)	**B**	<0	0.07019
	C	0.06166	3.11981
	NC	<0	0.00095
19780 (n=2)	**B**	0.00562	0.13142
	C	0.28947	7.27844
	NC	<0	0.01457
19781	**B**	0.11078	1.86607
	C	1.45392	20.64746
	NC	0.00319	0.01963
GGU 252833	**B**	<0	0.02366
	C	1.21425	18.45027
	NC	<0	0.00179
GGU 252874	**B**	<0	0.01745
	C	0.47772	6.75349
	NC	<0	0.00248

3.7. Highly siderophile elements geochemistry

The highly siderophile element (HSE) abundances as well as $^{187}Os/^{188}Os$ isotopes were determined by isotope dilution. However, there is no spike for carbonatites and thus a mixed spike designed for basalt samples was used (*c.f.* appendix Table 10.2).

3.7.1. Carius tube digestion

A total amount of 1 to 2 g of sample powder was added to a long Carius tube and fluxed with 2.5 ml of cold SpA conc. HCl. The mixture was left to react for 1 hour to remove CO_2 from the system prior to the actual digestion. After adding the appropriate amount of mixed HSE basalt spike, the spike transfer beaker was rinsed with an additional 0.5 ml SpA conc. HCl, which was also added to the Carius tube. The Carius tube containing the sample-HCl mixture was then placed in a container with dry ice. After the sample was frozen, 6 ml of sparged SpA conc. HNO_3 was added. The tube was then sealed, left to defrost and placed in metal jackets in the oven at 220°C for 48 h. The Carius tubes were removed from the oven and left to cool before opening.

Most mineral phases were dissolved by the Carius tube digestion, although some minor phases were not completely dissolved. Those latter phases might require higher pressures for complete dissolution. Thus, sample digestion was repeated using the HP Asher digestion.

3.7.2. HP Asher digestion

An aliquot of 2 g of sample powder was weighed and dissolved in 2 ml of SpA conc. HCl. The mixture was left to react for approx. 1 hour to assure maximum release of CO_2 from the sample. Then the appropriate amount of basalt spike was added with the remaining 0.5 ml SpA conc. HCl followed by addition of 5 ml of sparged SpA conc. HNO_3. However, due to a still very strong reaction of sample material with HNO_3, the amount of acid was increased to 3 ml SpA conc. HCl and 6 ml sparged SpA conc. HNO_3. The quartz vessels were sealed and then placed in the Asher for 13 h at 230°C and 100 bar to digest.

3.7.3. Comparison of Carius tube and HP Asher digestions

For comparison, 10 samples were digested with both Carius tubes and the HP Asher. Although it appeared that some phases were not properly dissolved during Carius tube

digestion, it did not apparently have a major impact on the measured Re and Os concentrations or, in most cases the $^{187}Os/^{188}Os$ isotope signature (*c.f.* appendix Table 10.3).

Only one sample (91/60 – C5) shows reproducibility for all elements for both methods. Carbonatites are generally low in HSEs and thus even slight sample heterogeneity will affect the concentration; hence, lack of reproducibility between the methods could also be caused by sample heterogeneity with sample 91/60 – C5 being more homogeneous. Neither digestion method has systematically elevated concentrations, which would have been an indication of better recovery and thus, it is difficult to say which method delivers the better recovery results. Some samples digested in Carius tubes yielded higher Os signal intensities on N-TIMS (*e.g.* sample 4808 $^{187}Os^{16}O_3$Carius: 102,000 cps, $^{187}Os^{16}O_3$Asher: 640 cps). However, this does not necessarily mean that the digestion method was better, as yields can also be decreased, or Osmium lost during the extraction chemistry and/or micro-distillation. Although variable (*c.f.* Chapter 3.7.8), blanks from Carius tube digestions were on average much lower than for high pressure asher digestions (*c.f.* appendix Table 10.4 and Table 10.5) if taking into account all highly siderophile elements. Because of the lower blanks, Carius tube digestions were used for further chemistry.

3.7.4. HSE chemical procedure

The chemical procedure was carried out following the approaches of several authors (*e.g.* Cohen and Waters, 1996; Pearson and Woodland, 2000; Ishikawa et al., 2014;.Chu et al., 2015). After digesting the samples, aqua regia together with the remaining sample residue was transferred to a centrifuge tube. For Os-extraction 3 ml of Chloroform ($CHCl_3$) was added to the same centrifuge tube, which was then sealed and mixed using a vortex shaker. The samples were left to settle until the aqua regia, and the chloroform were completely separated. The 3 ml of Chloroform, now containing the Os, was then extracted and transferred into a 15 ml Savillex beaker containing 1 ml of conc. HBr. The chloroform-procedure was repeated twice, using 2 ml chloroform for each step to extract all the Os from the aqua regia. Another 3 ml of HBr was added to the Savillex beaker already comprising 7 ml chloroform and 1 ml of HBr. Subsequently, the chloroform-HBr mixture was placed on a rocking plate. After 12-24 h the beaker was removed from the rocking plate and left to settle. Because chloroform is denser than HBr, it has settled to the bottom of the beaker. Additionally, all the Os should have partitioned into the HBr. Hence, the chloroform was extracted and discarded. The beaker containing the HBr was then dried down at 80°C.

A conical vial was prepared by adding 10 µl of HBr to the tip of the vial. The dried down Os fraction was re-dissolved in 10 µl of 12M H_2SO_4 and was then, together with 10 µl of CrO_3-solution, transferred to the lid of the conical vial for micro-distillation.

The aqua regia and sample residue leftover after Os-extraction was dried down and then fluxed with 1 ml of conc. HNO_3 and 4 ml of conc. HF. The beaker was capped and left on the hotplate at 120°C overnight before being dried down. To evaporate leftover fluorine, 1-2 ml of conc. HNO_3 was added and dried down. This step is repeated twice, followed by re-dissolution in 2 ml conc. HCl and dry down. Depending on the amount of fluorite that has formed, this last step was repeated several times. Finally, the sample was re-dissolved in 10 ml of 1M HCl and centrifuged before being loaded on the anion and then the LN-spec columns.

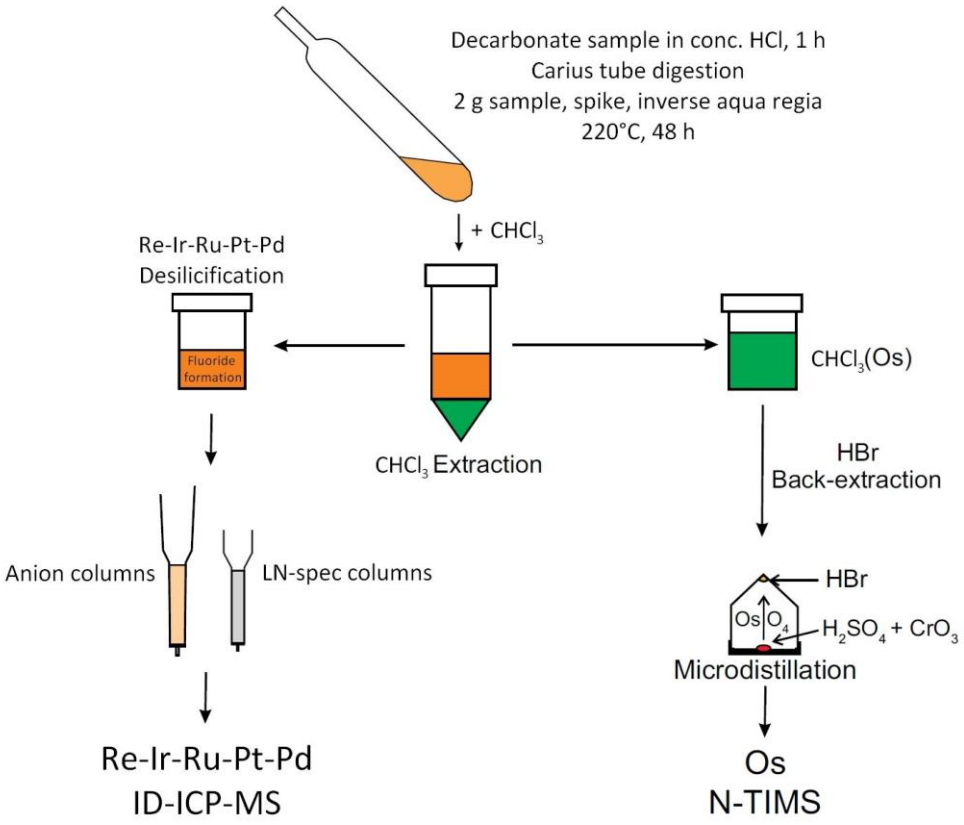

Figure 3.9 **Simplified sketch of the different steps of the HSE procedure for Carius tubes, image modified from CHU et al. (2014) and used in a similar form in Schweitzer (2015).**

3.7.5. Column calibration for the HSE procedure

Sample 16462 was used for calibrating HSE columns. 1 g of 16462 was dissolved in inverse aqua regia (2.5 ml conc. HCl + 5 ml conc. HNO_3). The beaker containing the sample solution was then placed on a hotplate at 120°C. However, it needed to be removed from the hotplate after only 5 minutes, because the sample started to degas strongly, building up the pressure inside the beaker. Therefore, the beaker containing the sample-acid mix was slightly unscrewed and left in a fume cupboard to cold-react until the solution turned from dark brown/green to light yellow in colour. The beaker was then placed on the hotplate at 150°C to dry down. After the sample had dried down completely, 2 ml conc. HNO_3 and 3 ml conc. HF were added, and the beaker was placed on a hotplate at 120°C overnight to re-equilibrate with the residue. The sample was then dried down and 2 ml of conc. HNO_3 was added and dried down straight away. This step was repeated to evaporate any fluorine left in the sample. Finally, the sample was re-dissolved in 2 ml of concentrated HCl for 1 hour at 120°C and left to dry down again. To prepare the sample for column chemistry, it was re-dissolved in 10 ml of 0.5 M HCl. Since the concentration of HSEs in 16462 is unknown but likely to be extremely low, HSEs from five *ROMIL PrimAg® 1000 ppm mono-component* stock solutions (Re-Ir-Pt-Pd-Ru) were added to the dissolved sample aliquot to create an artificial 0.5 ppm solution but with an otherwise carbonatite matrix. This meant the column calibrations could be carried out on a carbonatite matrix but with HSE concentrations that facilitated concentration measurements.

3.7.5.1. Anion column calibration

Carbonatites have a different rock matrix compared to mafic and ultramafic samples. In order to verify the effectiveness of the anion columns for a carbonatite matrix, two different amounts of *Bio-Rad AG1 X8* 200-400# resin (1 cm^3 and 2 cm^3) were used. Furthermore, relative to the published elution scheme (*e.g.* Rehkämper and Halliday, 1997; Pearson and Woodland, 2000; Meisel et al., 2001; Chu et al., 2015), an additional 5 ml of acid was used at the end of every collection step for Re-Ir-Ru-Pt and also for Pd (*c.f.* Table 3.7), in case the resin behaved differently compared to mafic and ultramafic rocks. Re-Ir-Ru-Pt were collected in 1 ml fractions and Pd was collected in 2 ml fractions, which were then analysed using a *Thermo Scientific XSeries 2* ICP-MS in order to establish an elution profile for each element. To determine the yield of the columns, a 10% aliquot of the original solution was analysed together with a 10% aliquot of fraction A4 and a 5% aliquot of fraction A6 (*c.f.* Table 3.7). After the 0.5 ppm HSE doped 16462 was processed through the column, a column blank was

carried out following the column cleaning to see whether the resin could be re-used. The blank acids were run through the columns using the same recipe as for column A and the appropriate combined fraction was collected for analysis.

Table 3.7 **Recipe for anion column calibration to separate Re-Ir-Pt-Ru from Pd and to remove Zr-Hf interferences.**

ANION COLUMNS		Cut Nr.	Test A	Cut Nr.	Test B	Volume collected
Resin amount			1		2	
Resin cleaning	10 ml MQ					Waste
	10 ml 6M HNO_3					
	10 ml conc. HNO_3					
	2 ml MQ					
	10 ml conc. HCl					
	2 ml MQ					
Equilibration	2 ml 1M HCl					
	2 ml 0.5M HCl					
Load sample	**10 ml 0.5M HCl + sample**	A1	A1	B1	B1	1 x 10 ml
Wash-In	**5 ml 1M HCl**	A2-a	A2	B2-a	B2	1 x 10 ml
	5 ml 1M HCl	A2-b		B2-b		
	2 ml 0.8M HNO_3	A3-a	A3	B3-a	B3	1 x 4 ml
	2 ml 0.8 M HNO_3	A3-b		B3-b		
Collect Re-Ir-Pt-Ru	**10 ml conc. HNO_3**	A4-a	A4	B4-a	B4	20 x 1 ml
	5 ml conc. HNO_3	A4-b		B4-b		
	5 ml conc. HNO_3	A4-c		B4-c		
Wash	**2 ml MQ**	A5	A5	B5	B5	1 x 2 ml
Collect Pd	**15 ml conc. HCl**	A6-a	A6	B6-a	B6	20 x 2 ml
	10 ml conc. HCl	A6-b		B6-b		
	10 ml conc. HCl	A6-c		B6-c		
	5 ml conc. HCl	A6-d		B6-d		

Results Anion column calibration

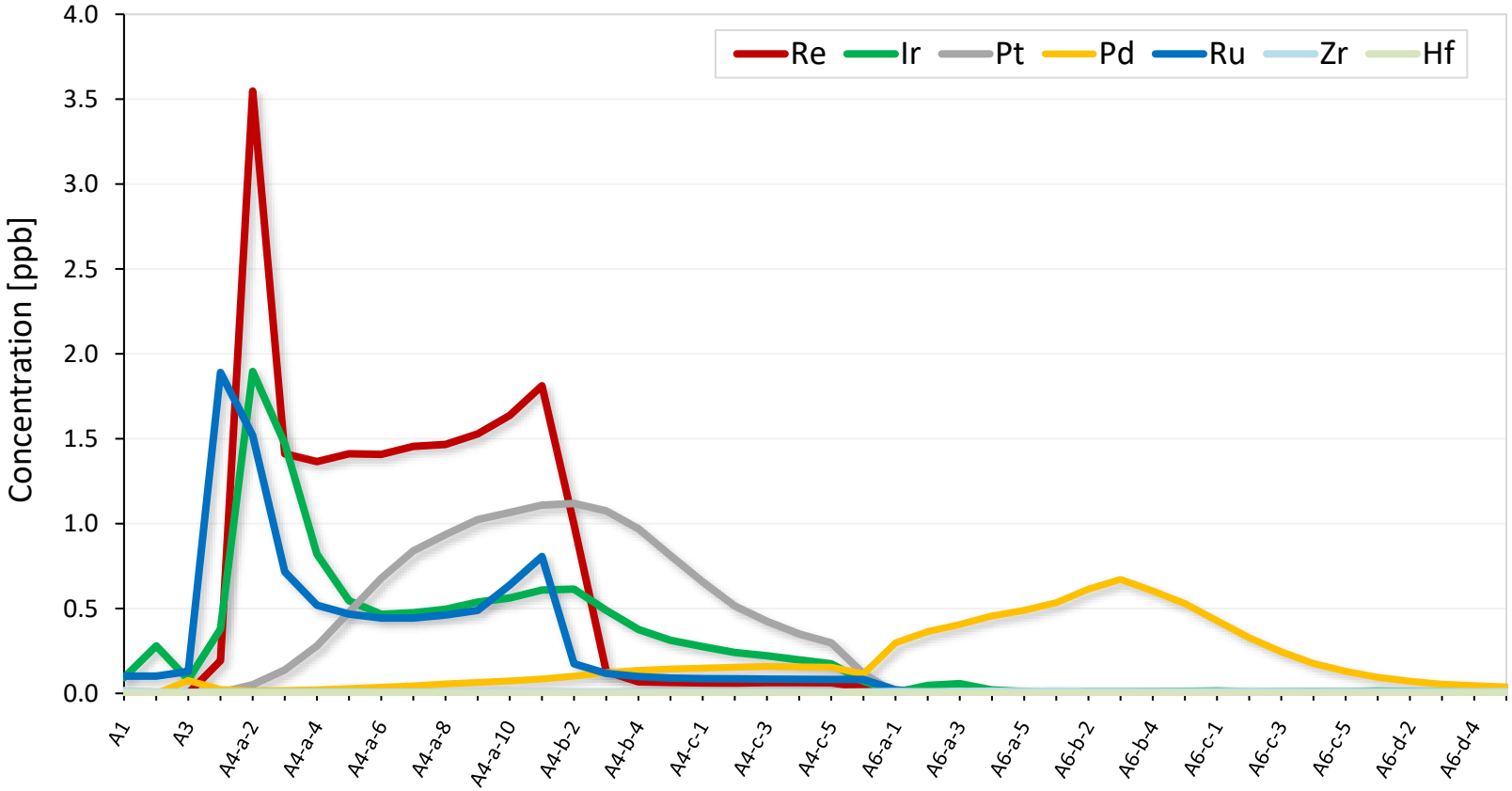

Figure 3.10 **Results from the Anion column calibration A (1 cm^3 of resin) plotted as concentration vs. collected fraction. An additional 5 ml (A4-c) is needed to release larger quantities of Pt and Ir compared to silicate rocks, which are usually only collected in fractions A4-a to A4-b.**

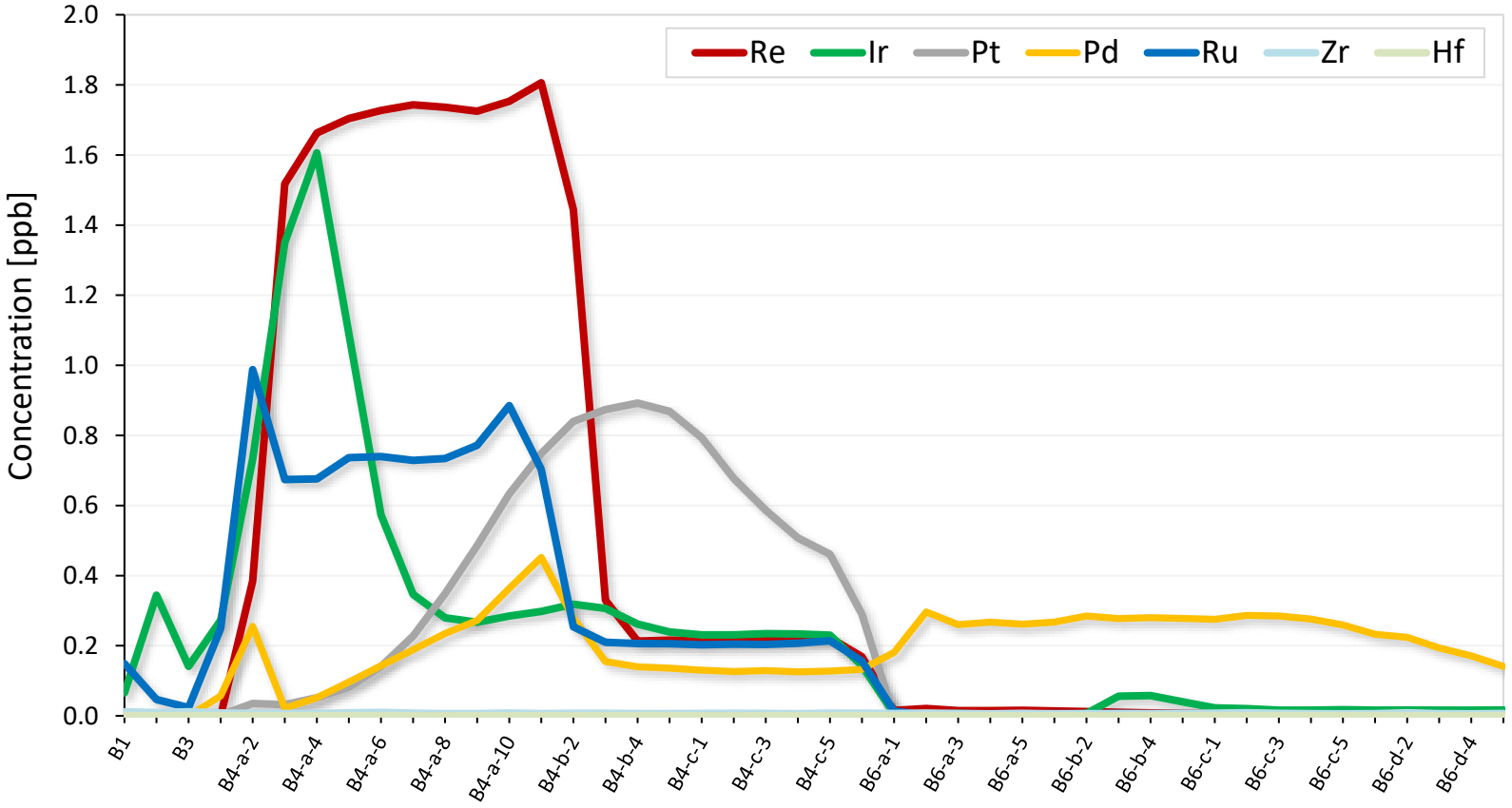

Figure 3.11 **Results from the Anion column calibration B (2 cm^3 of resin) plotted as concentration vs. collected fraction. Palladium (yellow) is eluted throughout the whole spectrum of collected fractions, although it should only be eluted from B6-a-1 onwards.**

Figure 3.10 shows the results from the Anion column calibration using 1 cm^3 of *Bio-Rad AGI X8* 200-400# resin. Fraction A5 forms the wash step between the elution of Re-Ir-Pt-Ru and Pd. Rhenium, Ir and Ru all start to elute from the column in the first and second collected fraction (A4-a-1 and A4-a-2) and continue to elute until fraction A4-c-5. Pt shows a broad peak between fractions A4-a-2 and A4-c-5 with a peak that is slightly later than that of Re-Ir-Ru. Pd also forms a smooth and wide peak with the majority being eluted after fraction A6-a-1. A small amount of Pd is eluted in the last 10 ml (A4-c-1 to A4-c-5) of the Re-Ir-Pt-Ru elution steps. However, for 2 cm^3 of resin, Pd is eluted throughout all fractions (*c.f.* Figure 3.11, B4-a-1 to B6-d-5), clearly showing that the higher amount of resin does not produce satisfying separation of the Pd fraction. Furthermore, using 2 cm^3 of resin also leads to lower yields for Ir, Pt and Pd compared to the use of 1 cm^3 of resin (*c.f.* Table 3.8). Considering the extremely low HSE contents of carbonatites (*c.f.* appendix Table 10.35), good yields are very important. The yield for Re and Ru is very similar, with the elution in 2 cm^3 of resin being more evenly distributed (Figure 3.11). It appears that the additional 5 ml of conc. HNO_3 for the Re-Ir-Pt-Ru elution for 1 cm^3 is necessary, as significant amounts of Pt are still eluted in those last 5 ml (A4-c-1 to A4-c-5). For Pd the additional 5 ml of conc. HCl were also included in the new final recipe (*c.f.* appendix Table 10.6), as minor amounts of Pd were still eluted in those last 10 ml (Figure 3.10), slightly increasing the yield. It turns out that column A containing 1 cm^3 of *Bio-Rad AGI X8* resin provided a better recovery compared to column B which had double the amount of resin. Thus 1 cm^3 of resin will be used for further purification.

Table 3.8 Yields from Anion column calibration for 1 cm^3 and 2 cm^3 of resin. The yields were calculated assuming that the doped solution had 500 ppb PGEs.

	Re	Ir	Pt	Pd	Ru
1 cm^3 resin	75.20%	44.60%	51.30%	52.60%	37.20%
2 cm^3 resin	76.30%	37.55%	37.15%	39.98%	39.17%

The column blank run for the *Bio-Rad AGI X8* 200-400# resin used for column calibration revealed that there is still a noteworthy amount of PGEs (*e.g.* up to ~55 ng of Pt following a sample that contained approximately 5000 ng) present on the resin. Thus, cleaning of the resin as described in the appendix (Table 10.6) is not sufficiently removing the PGEs from the previous sample indicating that the resin should not be re-used. Nevertheless, it should also be noted that HSE concentrations in the HSE doped sample 16462 are not representative of carbonatite concentrations.

3.7.5.2. LN-spec column calibration

Another 16462 sample solution was prepared and loaded onto an anion column containing 1 cm^3 of resin. The fractions containing the elements of interest (as per the elution profile in Figure 3.10) were collected and dried down and re-dissolved in 1M HCl, ready to be loaded onto an LN-spec column for calibration. For the LN-spec column calibration the column was filled with 1 cm^3 of *Eichrom LN-resin.* Fractions were collected in 1 ml portions (*c.f.* Table 3.9) and 100 µl of the initial sample solution was aliquoted and analysed to determine the yield of the column.

Table 3.9 Recipe for LN-spec column calibration for further purification of the sample material.

LN-spec columns		Cut Nr.	Test C	Volume collected
Resin amount			1	
Resin cleaning	4 ml MQ			Waste
	4 ml 6M HCl			
	4 ml 6M HCl			
	4 ml 2M HF			
	4 ml 6M HCl			
	4 ml 2M HF			
	4 ml MQ			
Equilibration	4 ml 1M HCl			
Load AND collect Pd	**1 ml 1M HCl**	C1	C1	1 ml
Collect Pd	**4 ml 1M HCl**	C2-a	C2	4 x 1 ml
	4 ml 1M HCl	C2-b		4 x 1 ml
Load AND collect Re-Ir-Pt-Ru	**1 ml 1M HCl**	C3	C3	1 ml
Collect Re-Ir-Pt-Ru	**5 ml 1M HCl**	C4-a	C4	5 x 1 ml
	5 ml 1M HCl	C4-b		5x 1 ml
Wash	**4 ml 2M HF**	C5	C3	4 ml
Cleaning	4 ml 2M HF			Waste
	4 ml 6M HCl			
	4 ml 2M HF			
	4 ml 6M HCl			
	4 ml 2M HF			
	4 ml 6M HCl			

Results LN-spec column calibration

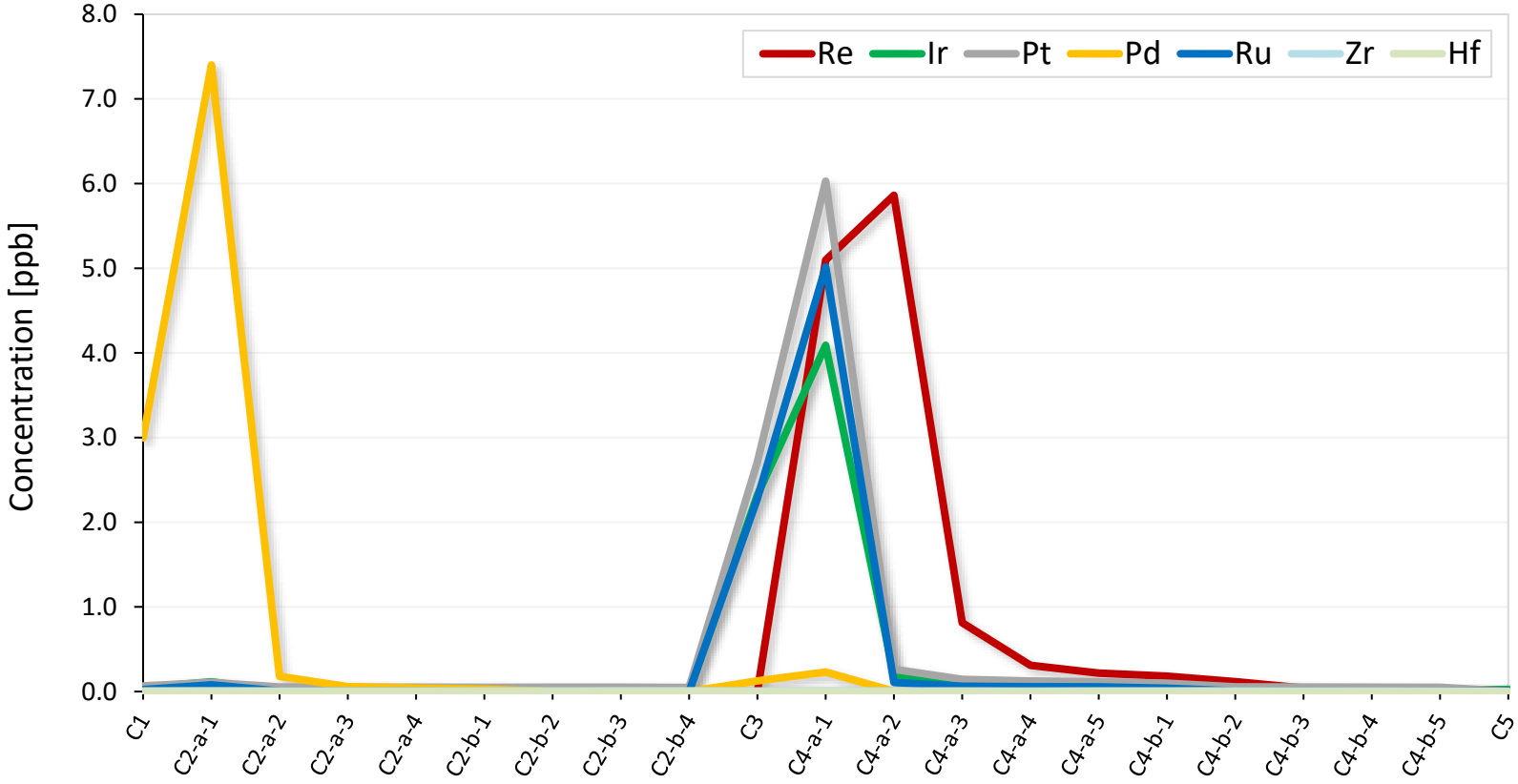

Figure 3.12 **Results from the LN-spec column calibration plotted as concentration vs. collected fraction. Peaks for Re-Ir-Ru-Pt are overlapping, with more Re being eluted in C4-a-2 to C4-a-5. All the Pd is eluted in the first 2 ml.**

Figure 3.12 shows the results from the LN-spec column calibration. As observed for the Anion column calibration, the LN-spec columns elute the HSEs in the same fractions for carbonatites as for silicate matrices (Chu et al., 2015). However, only 1 cm^3 of *Eichrom LN-resin* instead of 2 cm^3 (Chu et al., 2015) was used. Furthermore, an additional 2 ml of 1M HCl is needed to elute all the Re (C4-b-1 and C4-b-2) and to increase the yield (*c.f.* Table 3.10). Other than that, no addition of acids is needed to elute the elements of interest (Re-Ir-Ru-Pt-Pd). Therefore, the final column procedure differs from the published method only in terms of the amount of resin and the Re-Ir-Ru-Pt elution step (additional 2 ml, *c.f.* appendix Table 10.7).

Table 3.10 Yields from LN-spec column calibration for 1 cm^3 of resin. The yields were calculated from analysing the loaded solution as well as the collected fractions.

Re	Ir	Pt	Pd	Ru
96.4%	96.1%	100%	89.5%	97.8%

The *Eichrom LN-resin* was tested for re-use by analysing a blank that was processed following the post calibration clean-up. The blank showed that the amount of PGEs left on the resin is minor (*e.g.* up to ~0.2 ng of Pd following a sample that contained approximately 2600 ng Pd). Therefore, the resin can be re-used. However, blanks need to be tested regularly to ensure the quality of the resin.

3.7.6. Element 2 (SF-ICP-MS)

Highly siderophile element concentrations were analysed using a *Thermo Scientific™ ELEMENT 2™* ICP-MS. An *ESI SSI* spray chamber combined with a PFA 50 nebuliser was used for better signal stability. Oxide formation rates were estimated by running a 10 ppb Ce solution and monitoring the counts on ^{140}Ce and $^{140}Ce^{16}O$. Oxide formation rates were typically 4-5%. For correction of isobaric interferences for Pd analyses, a 1 ppb Mo, 1 ppb Cd and 1 ppb mixed Y+Zr standard were analysed at the start and the end of the measurement. To correct for isobaric interferences on Ir and Pt, a 1 ppb Hf standard solution was analysed at the start and end of the analyses, typically yielding around 3% HfO contribution. To quantify the mass bias, a 1 ppb mixed HSE solution (Re-Ir-Pt-Pd-Ru) was analysed at the start, throughout and at the end of the run. Sample analyses were bracketed by wash solutions to correct for the instrument's background.

3.7.7. Triton (N-TIMS)

Osmium was measured using a *Triton Plus™* Negative Thermal Ionisation Mass Spectrometer (N-TIMS). Due to its high electron affinity, Osmium was analysed as the negatively ionised OsO_3^- species. Samples were loaded onto a Pt-filament in 0.5 µl 9M UpA HBr together with 0.3-0.5 µl activator solution (Na(OH) and $Ba(OH)_2$). Filaments were heated up to 700-830°C with a current of 850 to 930 mA. Osmium was measured using the axial SEM detector in peak hopping mode (*c.f.* Table 3.11). Darknoise levels were between 0.0013 and 0.006 cps. Reference material DROsS (load size: 10 pg) was measured once to several times per day (⌀0.160546±0.000174 2SD; n=40) to ensure instrument performance. Isobaric element interference corrections were applied following the approach of Luguet et al. (2008).

Table 3.11 Method file used for analysing $^{187}Os/^{188}Os$ using the axial SEM detector in peak hopping mode (Luguet et al., 2008).

SEM Center cup mass	Integration time [s]	Idle time [s]
$^{192}Os^{16}O_3$	2.097	1
$^{190}Os^{16}O_3$	2.097	0.8
$^{189}Os^{16}O_3$	1.049	0.8
$^{188}Os^{16}O_3$	4.194	0.8
$^{187}Os^{16}O_3$	8.389	0.8
$^{186}Os^{16}O_3$	0.262	0.8
$^{185}Re^{16}O_3$	2.097	0.8

3.7.8. Blank contribution and data interpretation

Total procedural blanks are highly variable for Ir (<0 to 121 ppt), Ru (13.7 to 58.2 ppt), Pt (2.2 to 30.2 ppt) and Pd (9.9 to 1294 ppt), while for Os (0.09 to 2.19 ppt) and Re (<0 to 1.9 ppt) they are quite constant (*c.f.* Figure 3.13 and appendix Table 10.4). Cross-contamination from carbonatite samples as source of high blanks can be neglected, as HSEs in carbonatites are generally low in concentration (*c.f.* Chapter 6.1.1) and can even be lower than the highest blanks (*e.g.* for Pd TPBs: 577 and 1294 ppt, samples from same batch: 250 to 670 ppt). In general, carbonatites have very low IPGE (Os, Ir and Ru) concentrations (*c.f.* appendix Table 10.35), which are prone to be affected stronger by blank corrections than the PPGEs (Pt and Pd) and Re.

The reasons for high blanks could include contamination from beakers or Carius tubes. Although, Carius tubes are single-use only and pre-cleaned, they are known to generate variable Pt-blanks (*e.g.* Pearson and Woodland, 2000; Rehkämper et al., 1998). Nevertheless, Pt-blanks from this study are generally low (max. 30.2 ppt) and not as variable as for *e.g.* Pd (*c.f.* Figure 3.13).

Savillex Teflon beakers are re-used and were used for different unknown samples prior to this project. From a large supply of beakers, the visibly cleanest and newest beakers were selected and cleaned several times before being used for carbonatite samples. This does not exclude the possibility of beakers being the reason for high and variable blanks.

Additionally, high blanks could be caused by the instrument during analyses. The *Element 2* ICP-MS is used for several elemental analyses and concentrations. This could result in the release of HSEs (without Os) sticking to the spray chamber or cones, leftover from previous high-level samples.

Each batch contains at least one but often two blanks. By comparing the blanks from all batches (n=9, Figure 3.13), outliers (*e.g.* Pd 577 and 1294 ppt or Ir 121 ppt) were rejected and only the leftover "realistic" blanks were used to determine the detection limit. Data interpretation needs to be carried out with care, as it is not clear as to the cause of the high blanks. And although samples are generally low and corrected for the corresponding blank, there is still a chance of contamination of the samples.

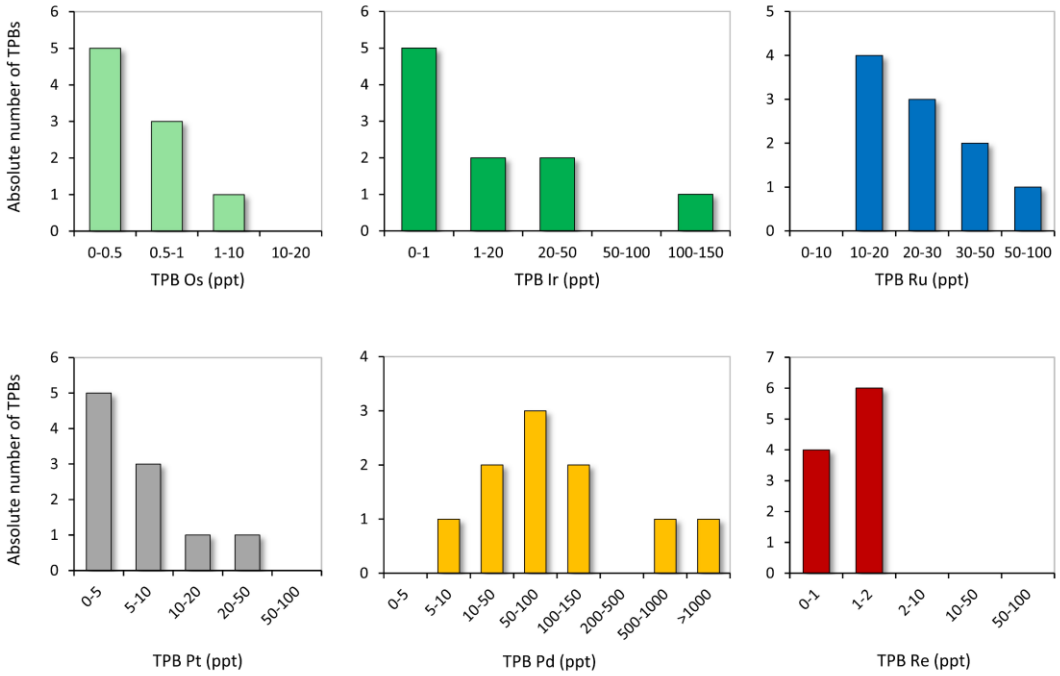

Figure 3.13 **Distribution of total procedural blanks (TPB) for all HSEs analysed using the Carius tube method (n=10).**

USGS reference material BHVO-2 (Hawaiian basalt) and COQ-1 (calciocarbonatite from Oka) were analysed multiple times in order to monitor digestion and sample preparation techniques as well as access precision and accuracy (*c.f.* appendix Table 10.36). The HSE data for BHVO-2 shows a large spread, particularly for Pt (6 to 17.3 ppb) and Os (58 to 548 ppt). Additionally, the last analysis of BHVO-2 yields much higher concentrations in HSE compared to the previous four analyses (*e.g.* average Os previous analyses: 58 to 131 ppt, Os last analysis: 548 ppt). The $^{187}Os/^{188}Os$ isotope signatures are also variable ($^{187}Os/^{188}Os$: 0.1323 to 0.1615) in this study but on average (0.1475) matching the values in published studies (0.1461 to 0.1496, Chu et al., 2015; Meisel and Moser, 2004a). Five analyses of BHVO-2 yielded $^{187}Os/^{188}Os$ ratios of 0.1475±0.02, 185±409 ppt Os, 80±11 ppt Ir, 274±73 ppt Ru, 10.3±9.4 ppb Pt, 3.1±1.2 ppb Pd and 563±30ppt Re (*c.f.* Table 10.36).

Meisel and Moser (2004b) list a few arguments for poor precision and accuracy observed in reference materials, including spectral interferences, contamination, sample size, incomplete digestion, analyte loss or blank contribution. Sample heterogeneity caused by random distribution of trace phases containing HSEs can also lead to data spread (*e.g.* Luguet and Reisberg, 2016) and could for instance explain the higher concentration for the last of the measurements of BHVO-2 as described above.

For COQ-1, all HSEs are variable (Ir: 3.2 to 14 ppt, Ru: <23.2 to 73 ppt, Pt: 14 to 50 ppt, Pd: 237 ppt to 4.6 ppb), with Os (4.6 to 6.7 ppt) and Re (1 to 1.4 ppb) showing the least variation.

Three analyses of COQ-1 yielded $^{187}Os/^{188}Os$ ratios of 5.6±2.1, 3.3±1 ppt Os, 8.4±11 ppt Ir, 31±61ppt Ru, 28±38 ppt Pt, 1.7±5 ppb Pd and 1.2±0.4 ppb Re (*c.f.* Table 10.36). As discussed in chapter 3.1, carbonatites are difficult samples to dissolve. Thus, digestion and dissolution problems in addition to the arguments mentioned before (Meisel and Moser, 2004b) might be responsible for the observed data spread. The variation in concentrations observed for the reference materials underlines the caution with which the interpretation of the carbonatite data from this study needs to be treated.

Chapter 4 : Major and trace elements

4.1. Whole-rock major elements

Following the classification diagram of Woolley and Kempe (1989), the majority of samples from this study can be classified as calciocarbonatites (*c.f.* Figure 4.1), while three samples can be defined as magnesiocarbonatites (91/66 - C2, GGU 252874 and GGU 253528) and two samples (19781 duplicated and 91/62 - C4) lie in the field of ferrocarbonatites. However, samples 19781 and 91/62 - C4 contain large quantities of magnetite and although appearing to be in the ferrocarbonatite field, they are more likely calcio- or magnesiocarbonatites, respectively, with FeO + Fe_2O_3 and MnO contents being influenced by the presence of magnetite (*c.f.* 19781 and 91/62 -C4 in Table 2.1).

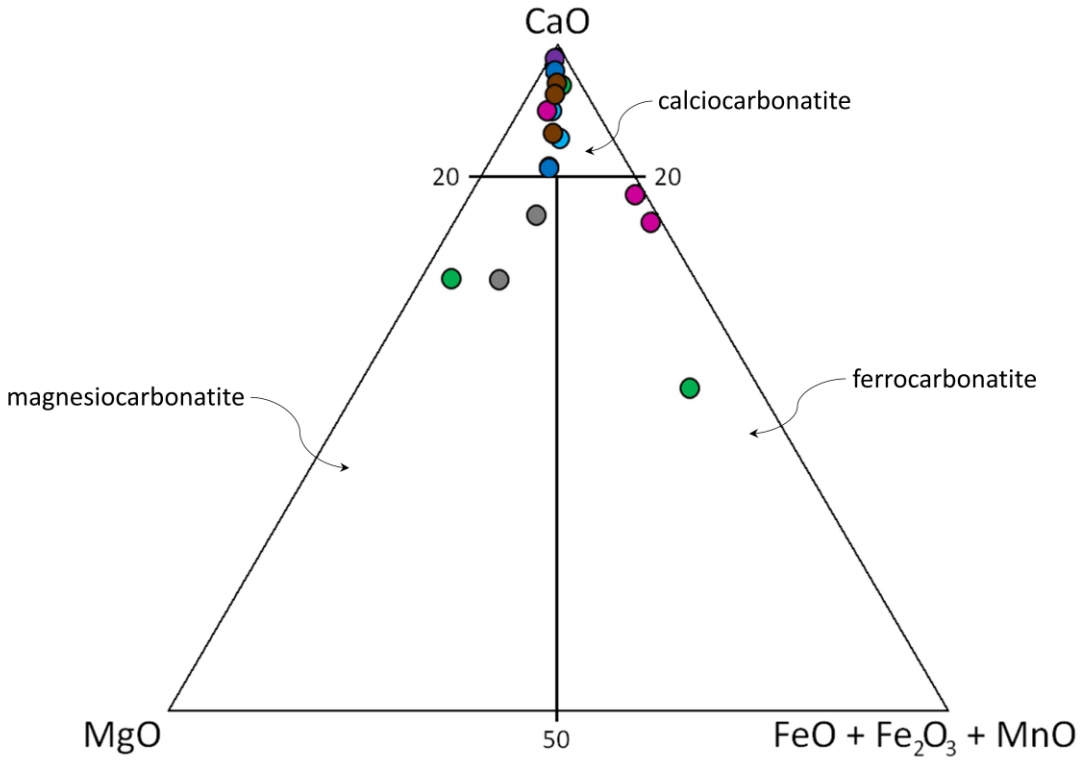

Figure 4.1 Major element data from this study plotted on the discrimination diagram for carbonatites with SiO_2 <20% using wt.% of major oxides (Woolley and Kempe, 1989).

The loss on ignition (LOI) corrected major element data was recalculated to 100% and is given in appendix Table 10.17. The LOI for carbonatites falls within the range of 28.3 wt.% and 43.6 wt.%, with the only exception being sample 91/62 – C4, with an LOI of 8.9 wt.%. This latter sample contains only ~30% carbonate and ~25% magnetite (Fe_2O_3: 28.74 wt.%), while other samples typically contain ~90% carbonate (*c.f.* Table 2.1). Sample 91/62 – C4 further contains a high proportion of apatite (*c.f.* Table 2.1), which is reflected in the P_2O_5 content (19.35 wt.%, *c.f.* bottom left Figure 4.2). For the other samples, P_2O_5 contents lie between 0.01 and 5.57 wt.%, dependent on the amount of apatite or other phosphate phases (*e.g.* monazite) present.

The amount of SiO_2 is low in all samples (0.13 to 1.87 wt.%) except for samples from Tupertalik, where SiO_2 is as high as 7.66 wt%. SiO_2 shows no clear correlation with MgO (R^2 = 0.238), Fe_2O_3 (R^2 = 0.0003) or CaO (R^2 = 0.118; *c.f.* top row Figure 4.2). The Al_2O_3 content is also low and generally varies between 0.15 wt.% (BM.1998,P18(44)) and 1.42 wt.% (GGU 252874). Except for samples 19781 (Fe_2O_3: 11.52 wt.%) and 91/62 – C4, all carbonatites have relatively low Fe_2O_3 contents (0.16 to 4.35 wt.%). Calcium is the major oxide in nearly all carbonatites (33.3 to 55.6 wt.%). The Na_2O content of all carbonatites, except those from Oldoinyo Lengai, typically lies either around 0.01 to 0.17 wt.% or is below detection limit. The same can be observed for the K_2O content, which is the highest for BM.2004,P12(132) from Oldoinyo Lengai (6.14 wt.%), but much lower (0.02 to 0.38 wt.%) for all other carbonatite samples from this study. In general, no correlation is observed for plots of CaO vs. P_2O_5 (R^2 = 0.044) or K_2O (R^2 = 0.057) but there is a light negative correlation for most samples between MgO and CaO (R^2 = 0.475; *c.f.* bottom row Figure 4.2). The MnO contents typically lie between 0.08 and 0.38 wt.%, though sample 19781 is higher (1.76 wt.%). The amount of MgO is higher in the magnesiocarbonatite 91/66 - C2 from Jacupiranga (17.16 wt.%) and GGU 252874 from Tupertalik (14.06 wt.%), while for all other samples it ranges between 0.21 and 8.77 wt.%.

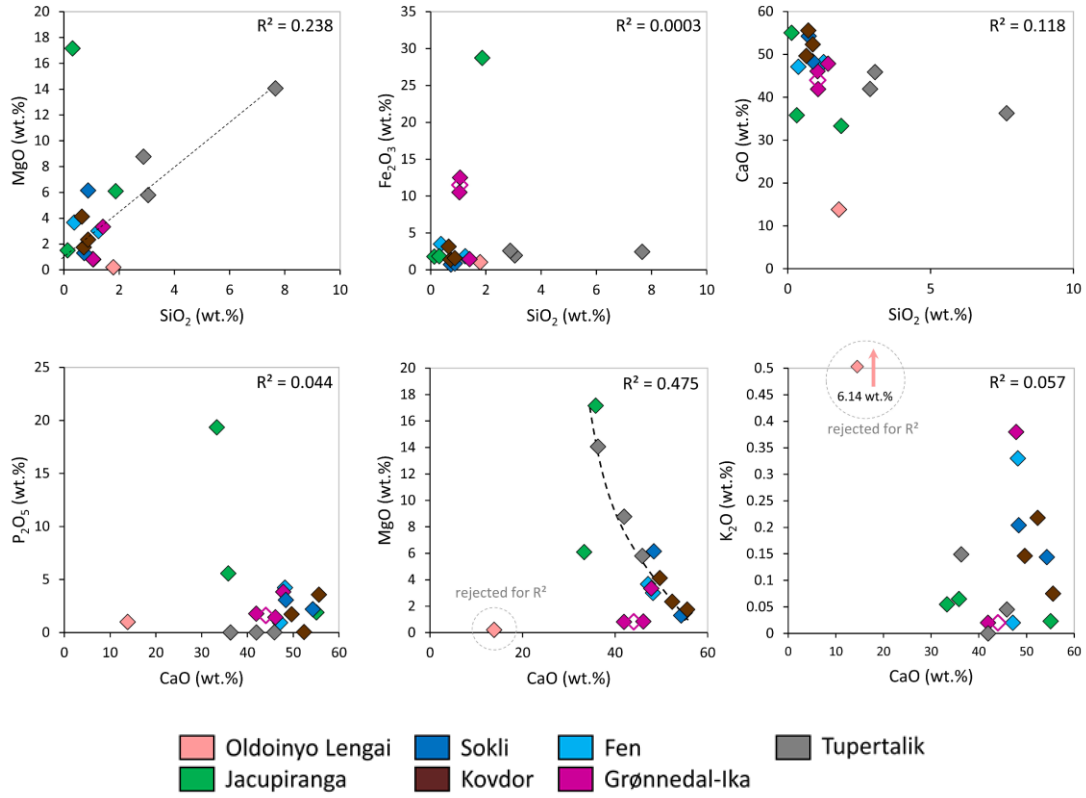

Figure 4.2 **Major element compositions of carbonatites from different localities. Filled symbols represent single analysis, while the unfilled diamond reflects the average of the two adjacent replicates. For K_2O, one of the Grønnedal-Ika samples was below the detection limit, the average thus only shows variation in CaO and not K_2O.**

4.2. Percentage of carbonate vs. non-carbonate fractions

Samples were divided into two fractions for trace element analysis (*c.f.* Chapter 3.5.2, 3.6.2 and 3.6.8), those being "carbonate" and "non-carbonate" fractions. The carbonate fraction contains mineral phases that can be dissolved in 6 M HCl (*e.g.* calcite, dolomite, ankerite, siderite etc.) while the residual non-carbonate fraction typically consists of phases such as pyrochlore, monazite, magnetite, hematite, sulphide, fluorite, baddeleyite, perovskite, silicates, apatite etc. The proportions of carbonate and non-carbonate fractions are illustrated in the form of pie diagrams in Figure 4.5 and are also given in Table 4.1. The carbonate fraction typically makes up ~90-98% of the whole-rock, while the non-carbonate fraction only contributes 2-10%.

Table 4.1 **Proportions of carbonate and non-carbonate fractions for 18 samples from the global study calculated from weighing samples before and after decarbonisation. C: carbonate; NC: non-carbonate.**

Sample name	C (%)	NC (%)
COQ-1	90.7	9.3
LI 23/02/08	91.5	8.5
LI 23/02/08 (repl)	91.1	8.9
Average	**91.3**	**8.7**
BM.2004.P9(9)	27.5	72.5
BM.2004.P9(9) (repl)	26.6	73.4
Average	**27.0**	**73.0**
J1-C1	98.3	1.7
91/66 - C2	95.5	4.5
91/66 - C2 (repl)	97.1	2.9
Average	**96.3**	**3.7**
91/60 - C5	97.7	2.3
BM.1998,P18(119)	88.3	11.7
BM.1998,P18(229)	94.0	6.0
BM.2000,P11(22)	92.7	7.3
BM.2000,P11(22) (repl)	94.3	5.7
BM.2000,P11(22) (repl)	85.9	14.1
Average	**91.0**	**9.9**
BM.2000,P14(24)	97.0	3.0
BM.2000,P14(25)	93.9	6.1
4808	96.7	3.3
10160	96.7	3.3
16462	95.3	4.7
16462 (repl)	96.3	3.7
Average	**95.8**	**4.2**
19780	67.1	32.9
19780 (repl)	67.4	32.6
Average	**67.2**	**32.8**
19781	81.4	18.6
GGU 252833	85.7	14.3
GGU 252874	71.8	28.2

4.3. Trace elements for whole-rock, carbonate and non-carbonate fractions

Whole-rock trace element analyses are given both as those from general trace element analyses (*c.f.* Chapter 3.5.1) and using the final method (*c.f.* Chapters 3.5.2 and 3.6.8), while carbonate and non-carbonate results are only given for samples that were treated using the final method (*c.f.* Chapters 3.5.2 and 3.6.8) and where both fractions were weighed prior to further chemical treatment.

Whole-rock spider diagrams

Trace element data used for whole-rock spider diagrams can be found in the appendix Table 10.18.

The trace element concentrations of carbonatites are generally enriched compared to the primitive mantle (Sun and McDonough, 1989). However, sample ASS-1 (Assynt) is depleted in Rb (0.06 ppm), Th (0.02 ppm), U (0.01 ppm), Nb (0.28 ppm) and Zr (0.09 ppm), and samples J1-C1 (Jacupiranga), 19781 and 25810 (Grønnedal-Ika), BM.1998,P18(183) (Sokli), BM.2000,P14(24) and BM.2000,P14(25) (Kovdor) are depleted in Zr (0.29 to 3.42 ppm) compared to the primitive mantle (*c.f.* Figure 1.2). Carbonatites generally show a negative Zr and Hf anomaly compared to the other trace elements. Nevertheless, samples 91/62 - C4, BM.1998,P18(229) and BM.2000,P11(22) are more enriched in Zr (555 ppm, 288 ppm and 402 ppm, respectively) compared to the other samples and do not possess a significant negative anomaly. The Zr/Hf ratios vary from 22 (BM.1998,P18(183)) to 88 (LI 23/02/08) and the average, considering all carbonatites, is ~52. Furthermore, all samples show a positive Ba anomaly (89 to 7075 ppm). Samples from Oldoinyo Lengai are significantly more enriched in Ba (6000 to 7075 ppm) compared to other samples (Ba: 89 to 2200 ppm).

While the shape and slope of the carbonatite trace elemental patterns are similar for La, Ce and from Pr to Lu, there is larger variation between Th (0.017 to 206 ppm) and Ta (0.06 to 332 ppm). Samples from the same locality generally possess concentrations within a similar order of magnitude, except for said elements between Th and Ta, which show no systematic pattern. Most samples show a positive Sr anomaly (~2200 to 27,000 ppm), though some (*e.g.* 19777: ~27,000 ppm) more prominently than others. Furthermore, samples from Oldoinyo Lengai and sample 4808 show a positive Pb anomaly (73 to 96 ppm), although samples from all other localities show a negative Pb peak. Samples from Fen show a positive U anomaly (~81 to 240 ppm) together with single samples from other localities (*e.g.* 19781 or 91/66 - C2), while most of the other samples either show a negative U anomaly (*e.g.* 19781: ~15 ppm

or 91/66 - C2: ~78 ppm) or no anomaly at all (*e.g.* 91/60 - C5 or BM.2000,P11(23)). All samples from Fen have peaks at Ta, while samples from Grønnedal-Ika and Oldoinyo Lengai have negative anomalies (*c.f.* Figure 4.3) and Kovdor samples show no strong Ta anomaly at all. In general, it can be seen that samples from Grønnedal-Ika are most enriched for trace elements La to Lu, while Fen is more enriched for Rb to Ta. For Kovdor samples, the magnesiocarbonatites (BM.2000,P11(29) and BM.2000,P11(42)) are less enriched in trace elements than the calciocarbonatites (*c.f.* Figure 4.3).

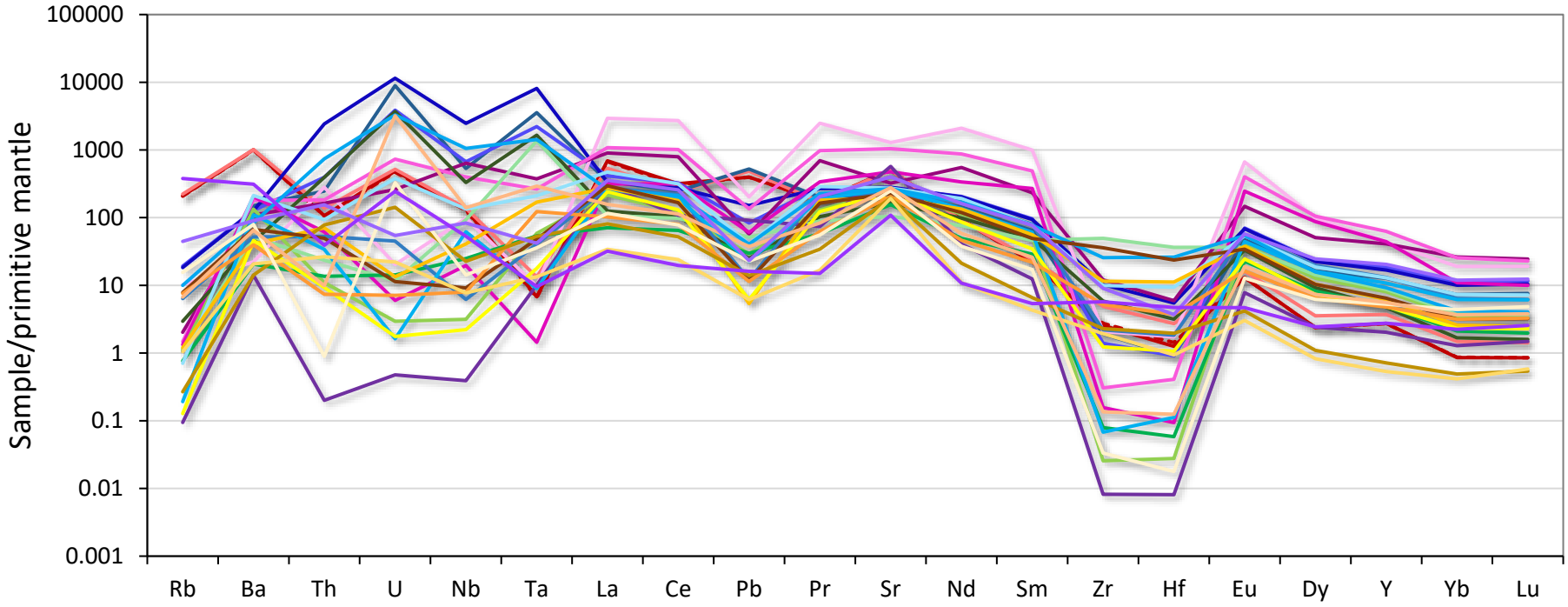

Figure 4.3 **Primitive mantle (Sun and McDonough, 1989) normalised spider diagram. For legend, please refer to Table 4.2.**

REE element patterns of whole-rock, carbonate and non-carbonate fractions

The primitive mantle normalised rare earth element (REE) patterns (Figure 4.4) all show an enrichment in the light REE (LREE), observed for all, whole-rock, carbonate and non-carbonate fractions of the samples analysed here (La_N/Lu_N = ~2.9 to ~2300; *c.f.* Figure 4.4). Whole-rock concentrations vary from 30 up to 3000 times higher for La (20 to 2000 ppm) and from 0.6 to 30 times higher for Lu (0.04 to 1.8 ppm) compared to the primitive mantle. The shapes of the patterns for whole-rock trace element analyses (top Figure 4.4) are similar and samples are generally reproducible (*c.f.* solid and dashed lines top Figure 4.4). Whole-rock samples from Tupertalik show a depletion in La and Ce compared to the other LREE, creating a bulge between Pr to Sm. Whole-rock Oldoinyo Lengai samples have a steeper slope from La to Lu, which can also be observed – although not as distinct – for two samples from Kovdor (BM.2000,P11(42) and BM.2000,P11(29)). Those two samples from Kovdor together with one sample from Fogo (BM.2004,P9(9)) have the lowest abundance in REE, while whole-rock samples from Grønnedal-Ika are most enriched in REE (*c.f.* Table 10.19 and top Figure 4.4).

For carbonate fractions, the REE slope looks similar to that of whole-rock analyses (*c.f.* centre and top Figure 4.4). Again, samples from Grønnedal-Ika are most enriched in REE, varying only minimal amongst each other (*e.g.* La: 900 to 1000 ppm; Lu: 2.3 to 3 ppm). In general, the primitive mantle normalised REE patterns of the whole-rock and carbonate fractions are very similar. If comparing the two diagrams sample by sample, it appears that the carbonate patterns mimic those of the whole-rock, except for BM.2004,P9(9) from Fogo, which has lower abundances of REE in the whole-rock than the carbonate fraction.

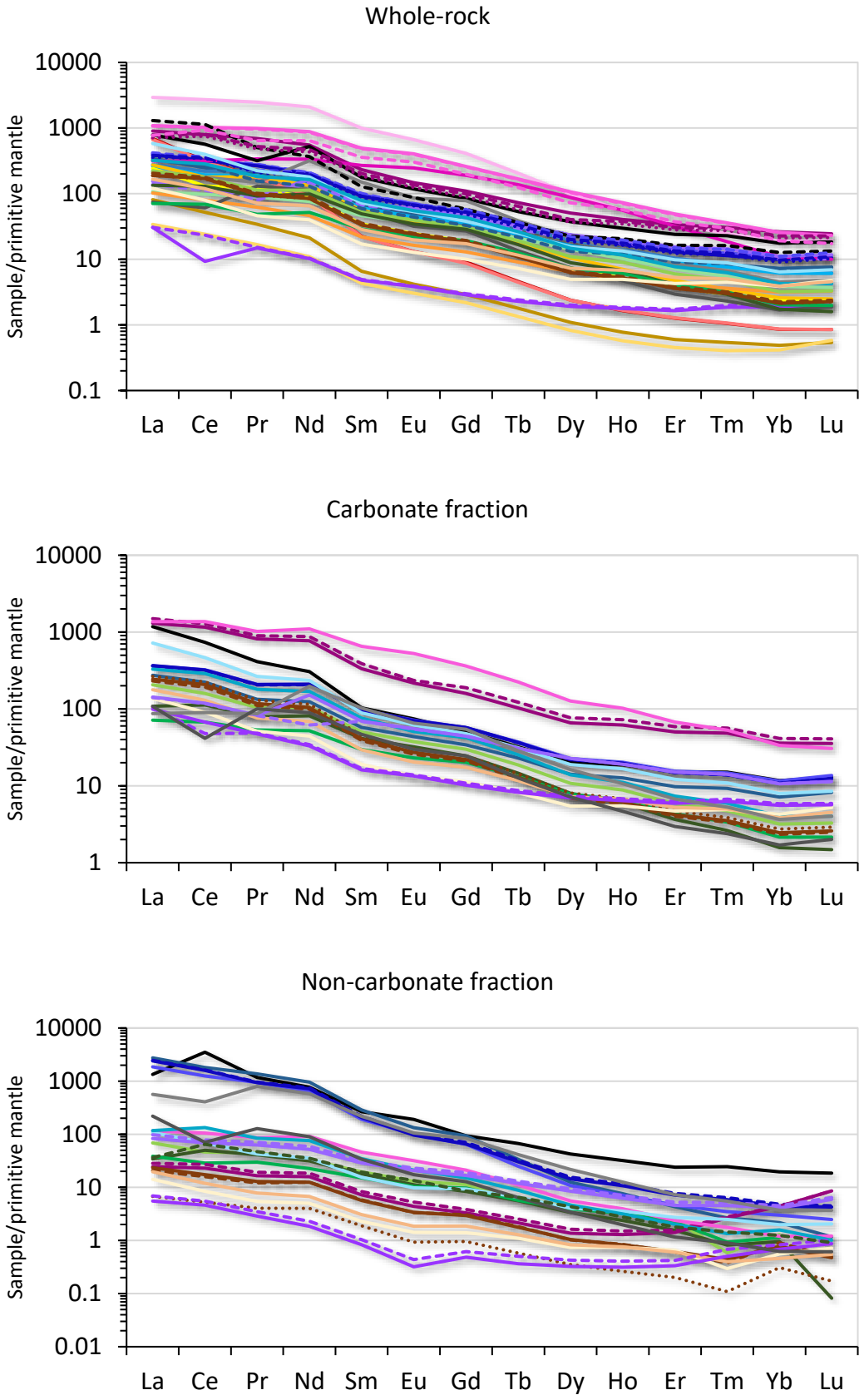

Figure 4.4 **Rare earth element patterns of samples from different localities normalised to primitive mantle (Sun and McDonough, 1989). From top to bottom: whole-rock, carbonate fractions and non-carbonate fractions. Dashed and dotted lines: replicates of the same sample. Legend on the next page (Table 4.2).**

Table 4.2 Colour codes for all samples analysed in this study.

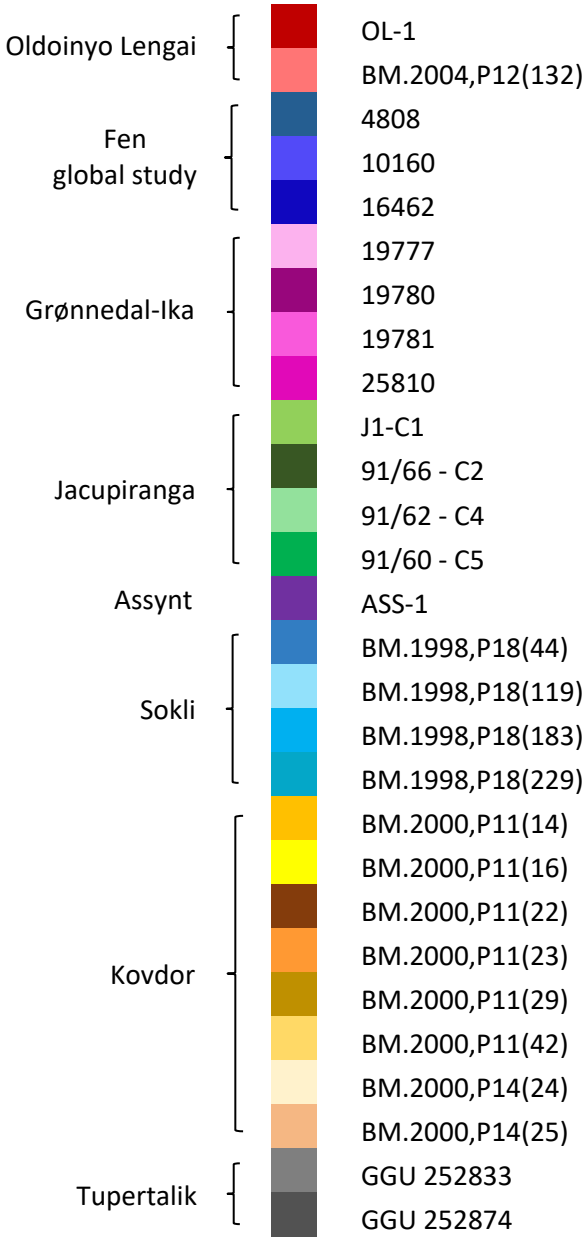

The primitive mantle normalised REE patterns for the non-carbonate fractions vary more than the whole-rock and carbonate REE patterns (*c.f.* bottom to centre and top Figure 4.4). In particular the heavy REE are more variable in concentration and the patterns do not show the same shape as those for whole-rock and carbonate fraction. For example, sample 19780 from Grønnedal-Ika is not only less enriched in REE, but also shows a negative slope from La to Er and a positive slope from Tm to Lu. This is also be observed for sample BM.2004,P9(9) from Fogo. The most enriched samples for non-carbonate fractions are from Fen as well as sample COQ-1. The negative slope of Fen samples is steeper than for the other samples. Replicated samples are reproducible, except for Lu in sample 91/66– C2, which shows a

larger variation (Lu: 0.006 to 0.1 ppm). Tupertalik samples again show a slightly lower abundance of Ce, thus creating a "kink" in the pattern.

In general, considering each fraction, samples from the same locality show similar primitive mantle normalised REE patterns. The only exception is Fogo, where the two samples analysed have a larger variation in concentration of REEs (*e.g.* non-carbonate LI 23/02/08 La: 67 ppm; BM.2004,P9(9) La: 5 ppm). This could be due to the fact, that sample BM.2004,P9(9) has a larger proportion of non-carbonate minerals, which might show different REE abundances (*c.f.* Table 2.1).

Distribution of Lu-Hf, Sm-Nd and Rb-Sr in whole-rock, carbonate and non-carbonate fractions

Parent and daughter isotopes can show variations in their elemental distribution in carbonate and non-carbonate fraction (*c.f.* Bizimis et al., 2003) and were investigated in more detail for Lu-Hf, Sm-Nd and Rb-Sr to illustrate which fraction controls each element (Figure 4.5, Figure 4.6 and Figure 4.7). Only samples for which all considered elements are above detection limit (*c.f.* appendix Table 10.23, Table 10.24 and Table 10.25) were used for Figure 4.5, Figure 4.6 and Figure 4.7. It is clear, that for the majority of samples the carbonate fraction accounts for most of the Lu (~80%), while the non-carbonate fraction contains only little Lu (Figure 4.5). Conversely, the non-carbonate fraction is the main host for Hf, accounting for at least 90% of the whole-rock Hf budget. This shows that Lu and Hf are fractionated at the carbonate/non-carbonate scale. In contrast, for Sm and Nd (Figure 4.6), both elements behave in an identical manner between carbonate and non-carbonate fraction. For some samples both, Sm and Nd, are dominated by the carbonate fraction (*e.g.* 19780, 19781, BM.1998,P18(119), BM.2000,P14(24), BM.2000,P14(25); 70-98%), while for others more Nd or Sm are found in the non-carbonate fraction (*e.g.* COQ-1, 16462 and GGU 252833; ~70%). However, there is no fractionation of Sm and Nd between carbonate and non-carbonate fraction. Rubidium and Sr show similar behaviour to Lu and Hf. Rubidium is controlled by the non-carbonate fraction for most samples (60-98%, Figure 4.7); The only exceptions being samples BM.2000,P14(24) and BM.2000,P14(25), in which the carbonate fraction accounts for most of the Rb (~80%). Unlike Rb, Sr is almost entirely controlled by the carbonate fraction (~90%). Again, we see a fractionation of Rb from Sr at the carbonate/non-carbonate scale.

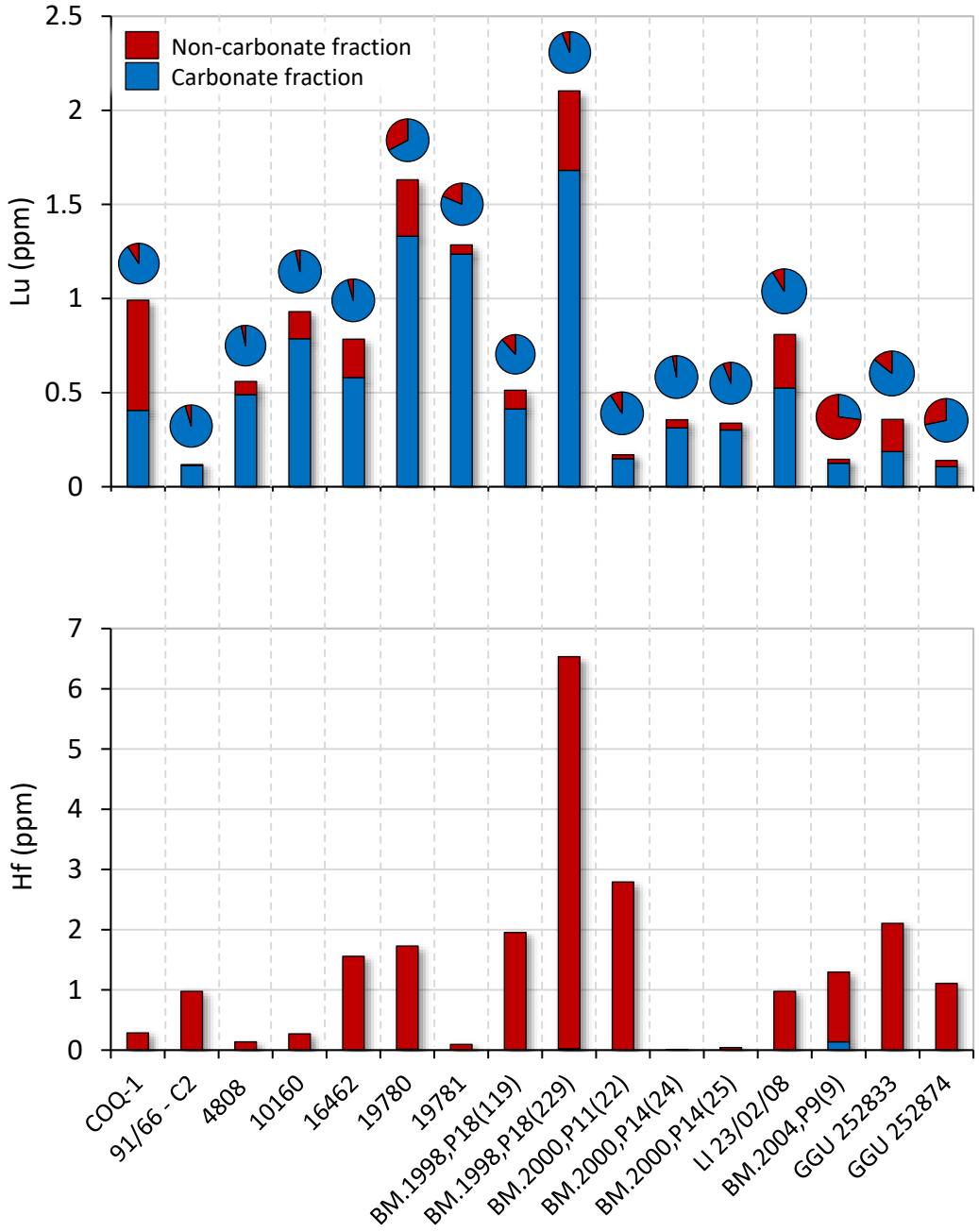

Figure 4.5 **Diagrams showing the distribution and concentration of Lu (top) and Hf (bottom) in carbonate (blue) and non-carbonate (red) fraction for different samples. Pie diagrams (top) show the percentage of carbonate to non-carbonate fraction in the whole-rock (Table 4.1). Samples 16462, 19780, BM.2000,P11(22), LI 23/08/02 and BM.2004,P9(9) represent averages of replicate analyses. Carbonate and non-carbonate fractions were calculated from the whole-rock concentration based on the percentages of the sum of concentrations of carbonate and non-carbonate fraction.**

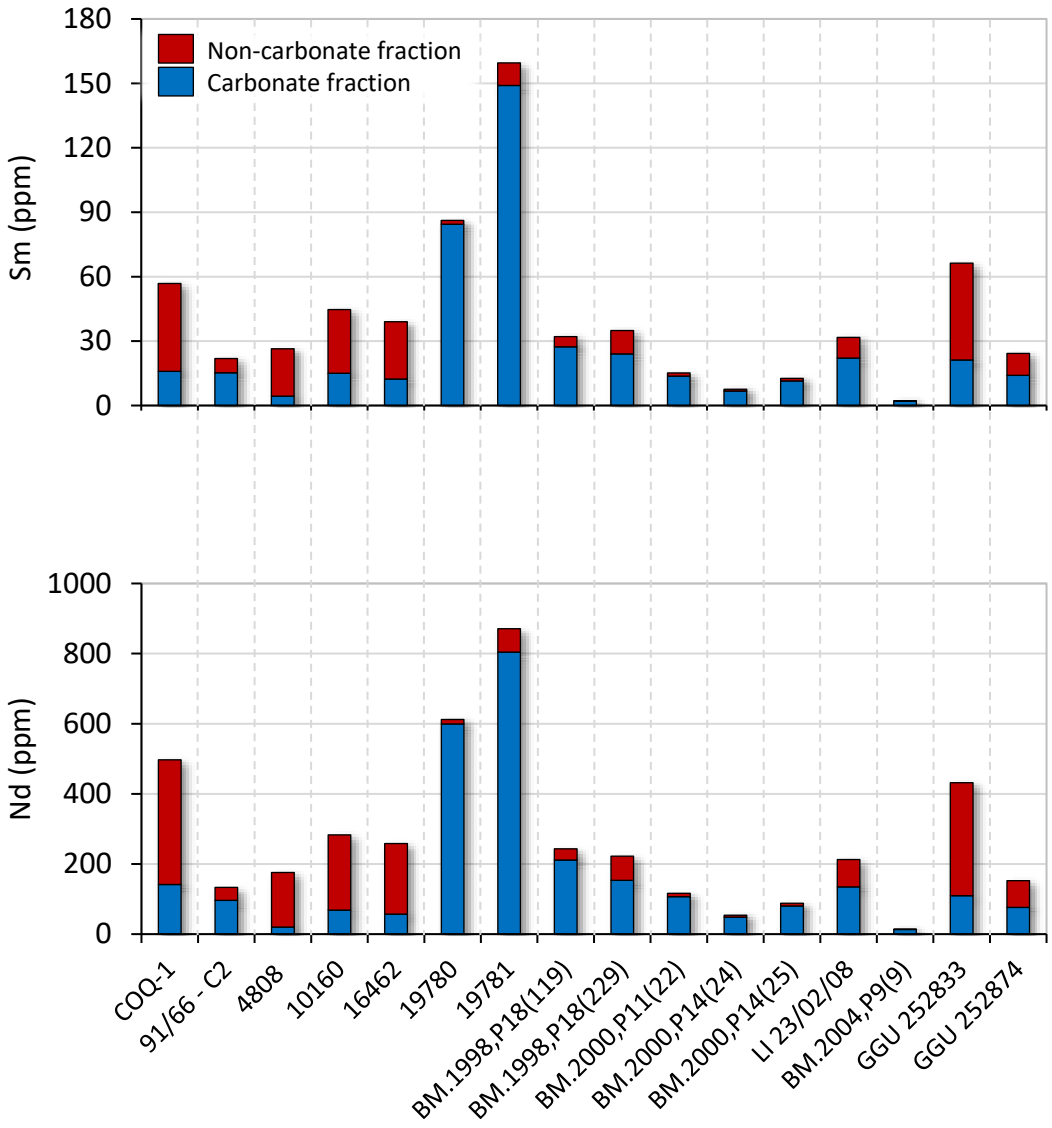

Figure 4.6 **Diagrams showing the distribution and concentration of Sm (top) and Nd (bottom) in carbonate (blue) and non-carbonate (red) fraction for different samples. Samples 16462, 19780, BM.2000,P11(22), LI 23/08/02 and BM.2004,P9(9) represent averages of replicate analyses. Carbonate and non-carbonate fractions were calculated from the whole-rock concentration based on the percentages of the sum of concentrations of carbonate and non-carbonate fraction.**

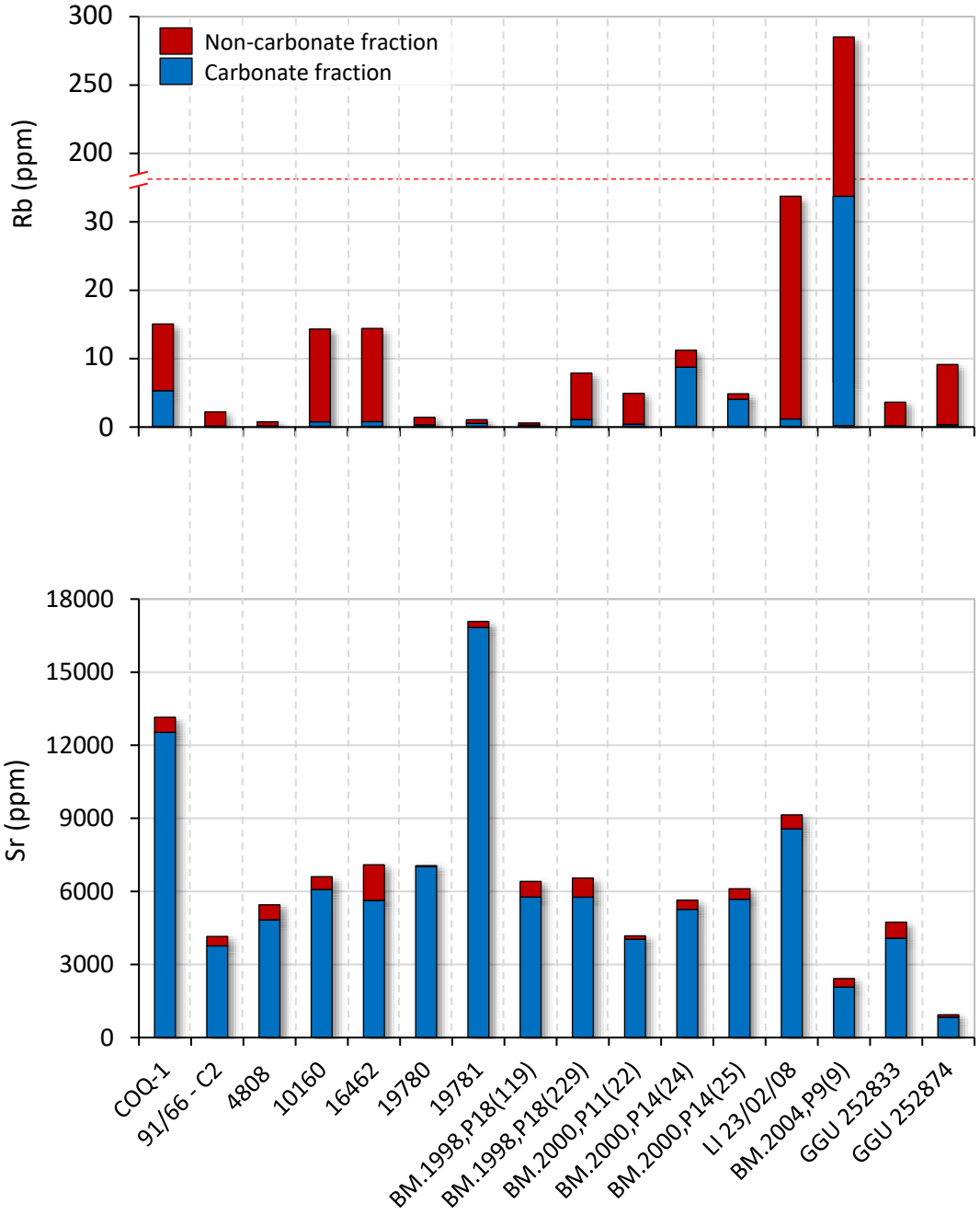

Figure 4.7 **Diagrams showing the distribution and concentration of Rb (top) and Sr (bottom) in carbonate (blue) and non-carbonate (red) fraction for different samples. Samples 16462, 19780, BM.2000,P11(22), LI 23/08/02 and BM.2004,P9(9) represent averages of replicate analyses. Carbonate and non-carbonate fractions were calculated from the whole-rock concentration based on the percentages of the sum of concentrations of carbonate and non-carbonate fraction.**

Chapter 5 : Lithophile element isotope studies (Lu-Hf, Sm-Nd and Rb-Sr)

The lithophile element isotope study has been carried out on whole-rock samples as well as on the carbonate and non-carbonate fractions of carbonatites of varying composition and age. The aim of this study is to ascertain more information on the source of carbonatites and to better understand their petrogenetic history. By analysing Lu-Hf, Sm-Nd and Rb-Sr isotopes in whole-rock, carbonate and non-carbonate fractions, the effect of elemental fractionation between the fractions (*c.f.* Chapter 4.3) is examined at the isotope level, thus addressing topics such as isotopic disequilibrium or secondary overprinting of isotope signatures.

5.1. Results

Hafnium and Nd data is presented in standard epsilon (ε) notation ($\varepsilon = ((D_{sample}/D_{chondrite}) - 1) \times 10{,}000$) and age corrected εHf and εNd values and errors were calculated using the approach of Ickert (2013) using values of CHUR from Bouvier et al. (2008) as reference values. All isotope data is given in the appendix in Table 10.32, Table 10.33 and Table 10.34.

5.1.1. Implications from combined Hf-Nd isotope signatures

It is clear from trace element analysis of the various carbonatite fractions that Lu is predominantly hosted in the carbonate phases whilst Hf is hosted in the non-carbonate phases (*c.f.* Chapter 4.3). Lu/Hf ratios for the carbonate fractions are significantly higher than for non-carbonate fractions as would be expected. The carbonate fraction tends to have correspondingly radiogenic $^{176}Hf/^{177}Hf_m$ (*c.f.* Table 10.32). If carbonate and non-carbonate fractions were derived from the same mantle source and were hence in isotopic equilibrium, their age corrected isotopic signatures should be the same, assuming the age of crystallisation is known. To re-phrase this, the slope of a regression line between carbonate and non-carbonate fractions on a $^{176}Lu/^{177}Hf$ vs. $^{176}Hf/^{177}Hf$ isochron plot (*c.f.* Figure 5.1), should yield a similar age to that determined by other means. Whole-rock results were not used for isochron plots as they were analysed as a separate dissolution, while carbonate and non-carbonate fraction results come from a single dissolution. The calculated Lu-Hf ages are compared to the published ages in Table 5.1. Not all samples have a calculated age, because for some samples either the carbonate or non-carbonate fraction did not yield isotope data. It is clear from Table 5.1 that the calculated Lu-Hf ages do not agree with the published ages. For Fogo, one age is negative, while the other age is half as old as the published age (*c.f.* Table 5.1). Samples from Jacupiranga yield ages between 47 and 85.3 Ma, younger than that

published (130 Ma, Amaral, 1978). The two samples from Sokli vary from one another (318 and 179 Ma), but sample BM.1998,P18(119) appears to be close to the published age (318 and 360 Ma, respectively). Samples from Kovdor vary from the published age by more than 100 Ma. However, all Kovdor ages calculated by the two-point Lu-Hf isochrons are similar to one another and only vary by a maximum of 32 Ma (209 to 241 Ma). Fen samples show a similar behaviour, they are relatively reproducible between different samples (363 to 375 Ma), but one replicate of sample 16462 is ~70 Ma older (430 Ma) than the other samples from Fen. Nevertheless, none of the four samples have the same age as that published (539 Ma) by Andersen and Taylor (1988). Replicate analyses of sample 19780 from Grønnedal-Ika yield reproducible Lu-Hf ages (796 and 807 Ma) but vary by ~500 Ma from the published age. Sample 19781 yields a much older age of 1401 Ma that is closer to the published Rb-Sr age of 1299 Ma (Blaxland et al., 1978). The Lu-Hf age for Tupertalik is less than half the published U-Pb age (1408 vs. 3007 Ma, Bizzarro et al., 2002).

Table 5.1 **$^{176}Lu/^{177}Hf$-$^{176}Hf/^{177}Hf$ ages calculated from regression lines defined by the carbonate and non-carbonate fractions of each sample or combined samples (Tupertalik) compared to published ages. Ages were calculated using Isoplot 4 (Ludwig, 2010).**

Locality	Sample name	Lu-Hf age (Ma)	Literature age (Ma)	Method for literature ages
Fogo	LI 23/02/08	<0	4	K-Ar biotite (Madeira et al., 2005)
	BM.2004.P9(9)	2.3 ±2.2		
Jacupiranga	J1-C1	69 ±10	130	K-Ar (Amaral, 1978)
	91/66 - C2	85.3 ±7.7		
	91/60 - C5	47 ±16		
Sokli	BM.1998,P18(119)	318 ±20	360	Rb-Sr and K-Ar phlogopite, U-Pb pyrochlore (Kononova and Shanin, 1971; Vartiainen and Woolley, 1974)
	BM.1998,P18(229)	179 ±12		
Kovdor	BM.2000,P11(22)-1	241 ±33	376	U-Pb (Amelin and Zaitsev, 2002)
	BM.2000,P11(22)-2	235 ±57		
	BM.2000,P11(22)-3	209 ±33		
	BM.2000,P14(24)	224 ±100		
	BM.2000,P14(25)	224 ±17		
Fen	4808	363 ±41	539	WR Pb-Pb (Andersen and Taylor, 1988)
	10160	375 ±35		
	16462-1	430 ±24		
	16462-2	370 ±19		
Grønnedal-Ika	19780-1	807 ±40	1299	Rb-Sr (Blaxland et al., 1978)
	19780-2	796 ±28		
	19781	1401 ±120		
Tupertalik	Tupertalik all	1408 ±580	3007	U-Pb baddeleyite (Bizzarro et al., 2002)

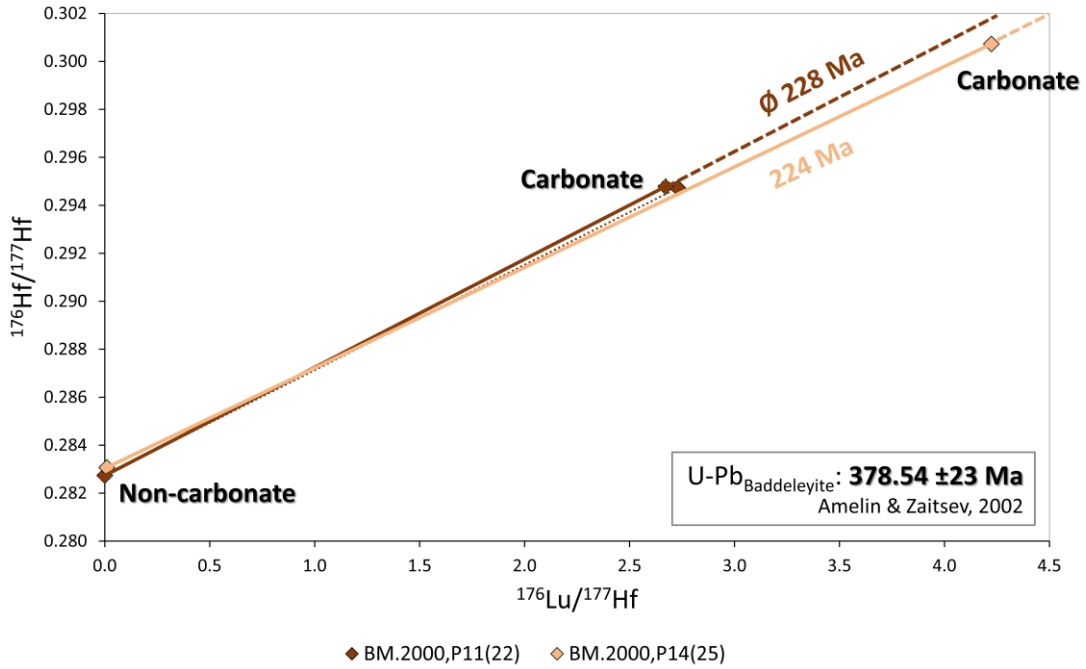

Figure 5.1 **$^{176}Hf/^{177}Hf$ vs. $^{176}Lu/^{177}Hf$ for two samples from Kovdor. Ages calculated from the slope of each two-point-regression-line are given next to the regression lines. The age calculated from sample BM.2000,P11(22) is an average age of three replicates of the same sample. Ages were calculated using Isoplot 4 (Ludwig, 2010).**

That the Lu-Hf ages in Table 5.1 do not agree with the various published ages for carbonatites in this study may reflect one, or more, of the following factors:

- The carbonate and non-carbonate fractions were never in isotopic equilibrium.
- The Lu-Hf isotope system does not date the same event as that derived from other isotope systems (Table 5.1).
- The Hf isotope or parent/daughter ratio of either or both fractions have been disturbed.
- Our measurement of the Hf isotope and/or the parent/daughter ratio are analytically compromised.

For Sm-Nd isotopes, isochron ages could not be determined using the carbonate and non-carbonate fractions, as measured $^{143}Nd/^{144}Nd$ ratios are isotopically identical (*e.g.* J1-C1 $^{143}Nd/^{144}Nd_{carbonate}$: 0.512639 ±0.000006 2SD, $^{143}Nd/^{144}Nd_{non\text{-}carbonate}$: 0.512655 ±0.000016 2SD; Table 10.33). Additionally, Sm and Nd are not strongly fractionated between the carbonate and non-carbonate fraction as is the case for Lu and Hf (*c.f.* Figure 4.5 and Figure 4.6).

εHf_t versus εNd_t

Figure 5.2 shows the age corrected (t) εHf vs. εNd for whole-rock, carbonate and non-carbonate fractions of carbonatites of which parent isotope ratios were analysed with a *CETAC Aridus™* desolvator (*c.f.* Chapter 3.5.2 and 3.6.8). Earlier analyses, where the parent isotope ratios were measured in wet plasma mode, can be found in Table 10.32 and Table 10.33, but are not plotted or described in the section below because of strong influence by isobaric interferences (*c.f.* Chapter 3.6.11 and 3.5.2). Parent isotope ratios of samples from Oldoinyo Lengai were only analysed in wet plasma mode. However, because Oldoinyo Lengai is a present day carbonatite, no age correction is necessary and thus the measured $^{176}Hf/^{177}Hf$ and $^{143}Nd/^{144}Nd$ expressed in ε-notation were also plotted in Figure 5.2 and are further described in the section below.

Whole-rock

Whole-rock samples from Sokli and Fogo, two whole-rock samples from Kovdor and one from Jacupiranga plot on the mantle array (εNd_t: 1.5 to 8; εHf_t: 6 to 9). In contrast, the remaining samples from Fen, Grønnedal-Ika, Jacupiranga, Kovdor, Oka, Oldoinyo Lengai and Tupertalik plot below the mantle array (εNd_t: 0 to 4; εHf_t: -1400 to 4). Samples from Fen fall onto the HIMU field for εNd_t (~4) with larger variations in εHf_t (-33 to 4), while samples from Oldoinyo Lengai (εNd_t: 0.4 to 0.7; εHf_t: -17 to -6.5) and Tupertalik (εNd_t: 0 to 0.6; εHf_t: -11 to -9) are close to bulk silicate earth (BSE) for εNd_t. Samples from Jacupiranga and Grønnedal-Ika fall between BSE and HIMU for εNd_t (0.4 to 2.6) and again show larger variation for εHf_t (-174 to 4). Whole-rock samples from Sokli, Kovdor, Oka and Fogo plot between the HIMU and DMM end-members when only considering εNd_t (5.3 to 8). Hence, for εNd_t the values appear reasonable, while for εHf_t most samples either fall below the mantle array (*e.g.* 16462 εHf_t: -33 and 91/60-C5 εHf_t: -48) or for some samples (*e.g.* J1-C1 εHf_t: -174/$^{176}Hf/^{177}Hf_t$: 0.277798, and BM.2000,P14(24) εHf_t: -1400/$^{176}Hf/^{177}Hf_t$: 0.243235) even below the initial of the solar system ($^{176}Hf/^{177}Hf$: 0.279811, Bouvier et al., 2008). In general, there is only minor variation in εNd_t (*e.g.* for Kovdor up to 3.5 ε-units), while εHf_t is highly variable (*e.g.* for Kovdor samples up to ~1400 ε-units).

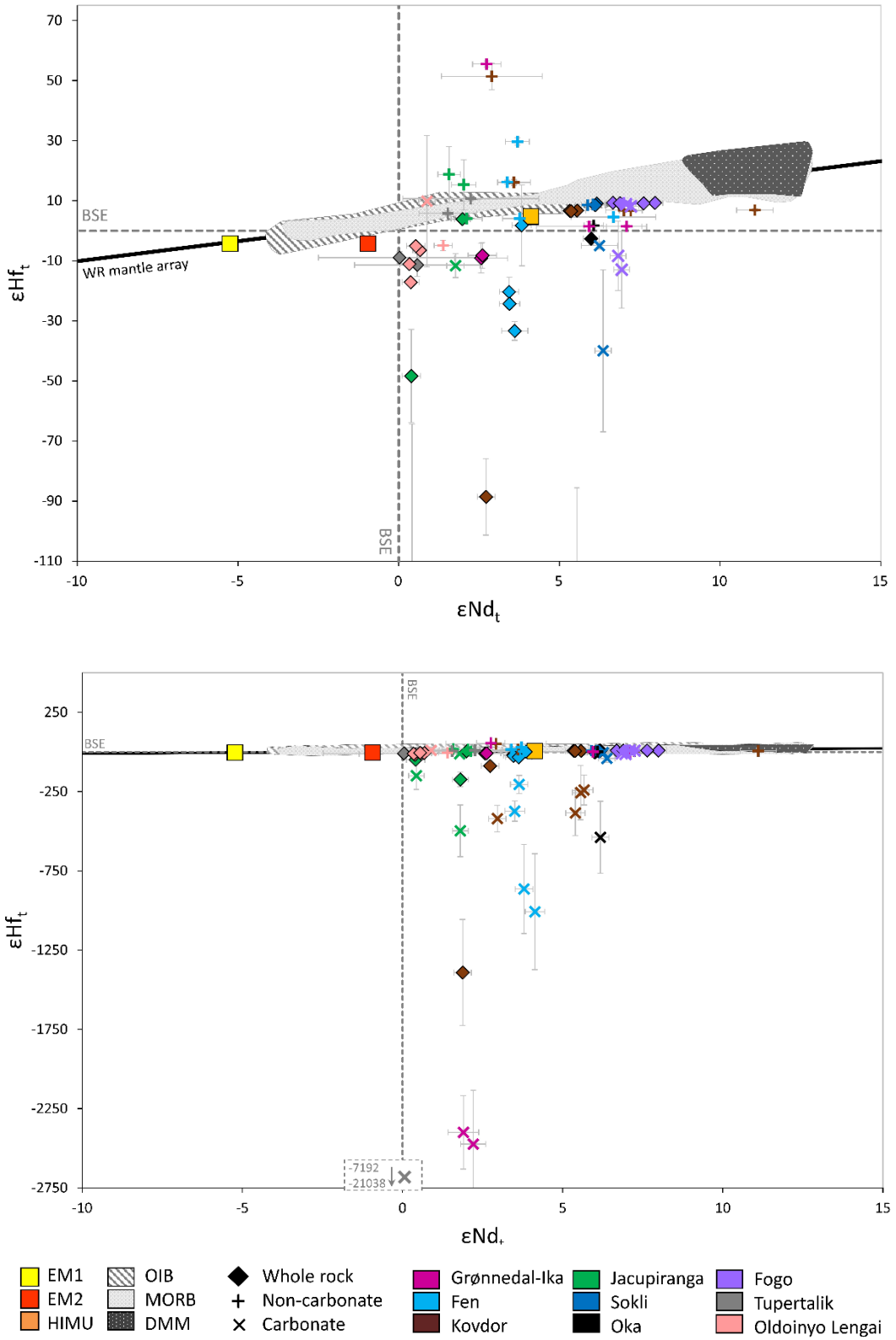

Figure 5.2 **Age corrected εHf vs. εNd for whole-rock, carbonate and non-carbonate fractions of carbonatites from different localities. Parent isotope ratios were determined by Q-ICP-MS in combination with a *CETAC Aridus™* desolvator. A detailed description of the chemical procedure is described in Chapter 3.6.8. Whole-rock mantle array: εHf = 1.33 εNd + 3.19 (Vervoort et al., 1999); Bulk silicate Earth (BSE)/Chondritic uniform reservoir (CHUR): Bouvier et al. (2008); Ocean island basalt (OIB) & mid-ocean ridge basalt (MORB): (Nowell et al., 1998; Salters and Hart, 1991; Stille et al., 1986); Enriched mantle 1 (EM1), enriched mantle 2 (EM2), high μ (HIMU) & depleted MORB mantle (DMM): Zindler and Hart (1986).**

Non-carbonate fraction

Compared to the whole-rock results (εHf_t: -1400 to 9), the non-carbonate fractions show considerably less variation in εHf_t (-5 to 55). All samples plot either on (*e.g.* Tupertalik εNd_t: 1.5 to 2.3; εHf_t: 6 to 11; Sokli εNd_t: ~6; εHf_t: ~9; Fogo εNd_t: ~7; εHf_t: ~9) or close to (above εNd_t: ~1.6 to 3.7, εHf_t: 15 to 55; and below εNd_t: 1.4 to 11, εHf_t: -7 to -5) the mantle array. The variation in εNd_t for the majority of localities studied is limited to just 5 εNd-units. Kovdor, however, exhibits slightly more variation at 8.4 εNd-units. The variation in εHf_t for non-carbonate fractions is up to six times greater compared to εNd_t but does not exceed 54 εHf-units (*e.g.* non-carbonate fractions Grønnedal-Ika).

Carbonate fraction

The variation in εNd_t values for the carbonate fraction is very similar to the whole-rock and non-carbonate fractions (εNd_t: 0.4 to 6.4; *c.f.* Figure 5.2). However, the carbonate fractions exhibit an extreme variation in εHf_t (-21,000 to -5). As mentioned previously, the carbonate fractions tend to have higher Lu/Hf ratios, thus evolving to more radiogenic signatures over time than the low Lu/Hf ratios in the non-carbonate fraction. Nevertheless, an age correction should result in a value close to or on the mantle array. In this case all but two (BM.2004,P12(132) and BM.2004.P9(9)) carbonate fractions plot below the mantle array. The variation in εHf_t at each locality reaches a maximum for the oldest samples from Tupertalik with ~21,000 ε-units variation across both carbonate and non-carbonate fractions. For the next oldest samples from Grønnedal-Ika, the variation reaches around 2400 ε-units, while for younger samples from *e.g.* Fen (~1000 ε-units), Kovdor (~1400 ε-units) and Jacupiranga (~500 ε-units) the variation tends to be "smaller" than for the very old samples. Most of the carbonate fractions plot far below the mantle array ($^{176}Hf/^{177}Hf_t$ GGU 252874: 0.078849 to 91/60 - C5: 0.27846) as well as below the initial $^{176}Hf/^{177}Hf$ of the solar system (0.279811, Bouvier et al., 2008). However, samples from Fogo (21 εHf-units) and Sokli (35 εHf-units) do not show as large a variation as from the other localities. Here, the carbonate fractions plot relatively close to the mantle array (Fogo εNd_t: ~7, εHf_t: -13 to 8; Sokli εNd_t: ~6, εHf_t: -40 to -5). The zero age samples from Oldoinyo Lengai plot on the mantle array (εNd_t: 1, εHf_t: 10). However, in general, age corrected εHf for carbonate fractions are unrealistic (<initial of solar system).

5.1.2. Implications from Sr-Nd isotope signatures

The large variations between whole-rock, carbonate and non-carbonate fractions observed for Hf isotopes, are not observed for Sr and Nd isotopes. Compared to Lu-Hf isotopes, Sm/Nd ratios are not fractionated strongly between carbonate and non-carbonate fractions (Non-carbonate Sm/Nd: 0.09 to 0.22, carbonate Sm/Nd: 0.12 to 0.37; *c.f.* Figure 4.6). The Rb/Sr ratio shows larger fractionation between the two fractions (Non-carbonate Rb/Sr: 0.0008 to 1.03, carbonate Rb/Sr: 0.00005 to 0.016), with Rb predominantly residing in the non-carbonate fraction and Sr in the carbonate fraction (*c.f.* Figure 4.7). However, for Rb-Sr isotopes the fractionation is not as strong as observed for Lu-Hf (Non-carbonate Lu/Hf: 0.0003 to 0.42, carbonate Lu/Hf: 0.83 to 195). Figure 5.3 shows the εNd_t vs. initial $^{87}Sr/^{86}Sr$ for whole-rock, carbonate and non-carbonate fractions of the carbonatites from this study. Most samples show a limited variation in Sr and plot around a value of 0.703, though errors on $^{87}Sr/^{86}Sr_t$ ratios are large due to the uncertainty on the parent isotope ratio determined by Q-ICP-MS. Whole-rock samples and carbonate fractions from the same localities plot very close to one another for both Nd and Sr. However, non-carbonate fractions from Fen are highly variable for $^{87}Sr/^{86}Sr_t$ (0.7002-0.7089) but similar for εNd (3.4-6.7). Non-carbonate fractions from BM.2000,P11(22) from Kovdor are highly variable in terms of $^{87}Sr/^{86}Sr_t$ (0.7000-0.7114), although considering all fractions of all Kovdor samples, Kovdor samples plot around 0.703-0.704. Samples from Tupertalik are generally less radiogenic in terms of Sr isotope composition (0.701), samples from Oldoinyo Lengai are similar to the value of bulk silicate Earth (0.7045, DePaolo and Wasserburg, 1976) and most samples from Jacupiranga plot above bulk silicate Earth and are separated into two groups. This grouping is associated with the emplacement sequences, the later sequences (91/62 - C4 and 91/60 - C5) are in the more radiogenic group (0.706), while the earlier sequences (J1-C1 and 91/66 - C2) are slightly less radiogenic (0.705) for $^{87}Sr/^{86}Sr_t$. For Grønnedal-Ika, most samples (19777, 19781 and 25810) are characterised by $^{87}Sr/^{86}Sr_t$ ratios of 0.703 while sample 19780 plots at >0.7035. Reference fields for mantle sources (HIMU, DMM and EM1) were plotted as present day (Figure 5.3) and are thus not necessarily representative of older samples from *i.e.* Tupertalik or Grønnedal-Ika. Nevertheless, most samples from Grønnedal-Ika and Fen plot in between BSE and HIMU, with Fen plotting closer to the HIMU end-member. Samples from Oka, Sokli and Fogo plot in between the HIMU and DMM end-member. For Kovdor, sample BM.2000,P11(22) and replicate analyses plot close to the HIMU field, while the other two samples (BM.2000,P14(24) and BM.2000,P14(25)) are in between BSE and HIMU. Samples from Tupertalik can be found on or close to BSE for εNd_t but lower than BSE

for $^{87}Sr/^{86}Sr_t$. Sample ASS-1 (εNd_t: -1.4, $^{87}Sr/^{86}Sr_t$: 0.7049) is close to BSE but moving towards the EM1 end-member (*c.f.* Figure 5.3).

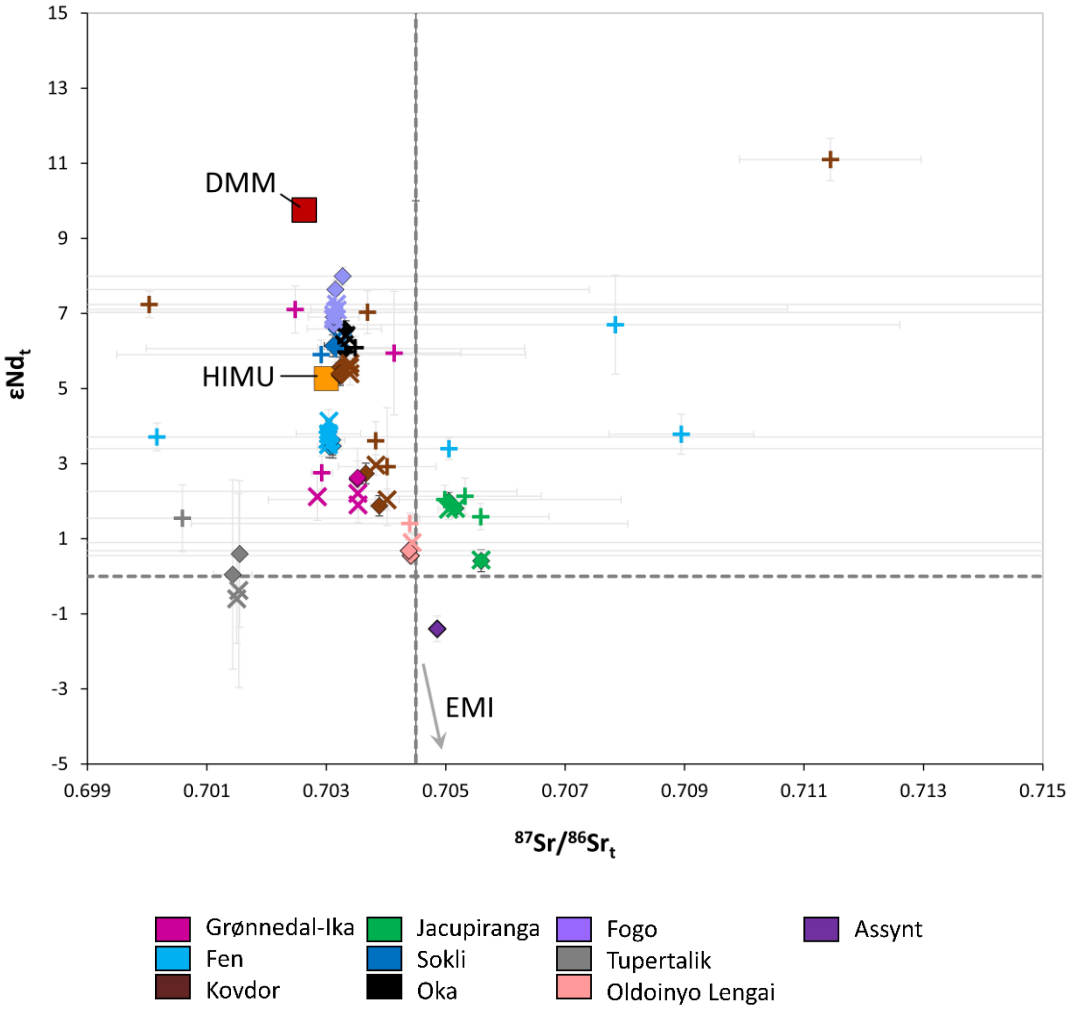

Figure 5.3 **Age corrected εNd vs. $^{87}Sr/^{86}Sr$ for whole-rock, carbonate and non-carbonate fractions of carbonatites from different localities. Bulk silicate Earth (BSE): Bouvier et al., 2008; DePaolo and Wasserburg, 1976; high μ (HIMU): Zindler and Hart (1986); depleted MORB mantle (DMM): Su and Langmuir (2003); Workman and Hart (2005).**

5.2. Discussion

5.2.1. Isotopic equilibrium

Based on Sr, Nd and Hf isotope arguments, Bizimis et al. (2003) suggest that carbonate and non-carbonate fractions in many carbonatites are not in isotopic equilibrium.

Table 5.2 **Table showing the $^{176}Lu/^{177}Hf$ ratios in carbonate fractions measured by Bizimis et al. (2003) compared to what the $^{176}Lu/^{177}Hf$ ratio of the carbonate fraction would need to be to produce the measured $^{176}Hf/^{177}Hf$ ratios of the carbonate fraction using the initial $^{176}Hf/^{177}Hf$ ratio of the non-carbonate fraction as initial ratio of the carbonate fraction.**

Locality	$^{176}Lu/^{177}Hf_{needed}$	$^{176}Lu/^{177}Hf_{measured\ in\ C\ fraction}$
Sukulu	1.40	1.95
Bukusu	1.36	7.27
Oka	7.39	4.36
Chilwa Island	3.08	3.37
Spitzkop	2.79	16.75
Deerdepoort	0.03	0.11

Discrepancies between ages from our study and the published ages described in chapter 5.1.1 could point towards isotopic disequilibrium between carbonate and non-carbonate fractions, but they could also simply be caused by disturbance of the parent/daughter ratio or measured $^{176}Hf/^{177}Hf$ isotope ratios of one or both fractions. Bizimis et al. (2003) base their disequilibrium conclusions on age corrected isotope ratios. However, if their measured $^{176}Hf/^{177}Hf$ or their parent/daughter isotope ratios were compromised, then age corrected $^{176}Hf/^{177}Hf$ ratios would not be representative.

Table 5.2 shows the measured $^{176}Lu/^{177}Hf$ ratios of the carbonate fractions (Bizimis et al., 2003) compared to the $^{176}Lu/^{177}Hf$ ratios required to age correct measured $^{176}Hf/^{177}Hf$ ratios of the carbonate fraction to match the $^{176}Hf/^{177}Hf_t$ ratios of the non-carbonate fractions. In doing this, it is assumed that the non-carbonate fraction is representative of the carbonatite source and is not consisting of xenocrysts. Similar to calculations carried out for samples from this study (Table 3.6), there is a mismatch between the measured and required $^{176}Lu/^{177}Hf$ ratios (*e.g.* Spitzkop $^{176}Lu/^{177}Hf_{required}$: 2.79 versus $^{176}Lu/^{177}Hf_{measured\ in\ C\ fraction}$: 16.75), suggesting that the parent/daughter ratio in the carbonate fraction was compromised. This raises the question as to whether carbonate and non-carbonate fractions are truly in isotopic disequilibrium or whether the carbonate fraction was overprinted.

If both carbonate and non-carbonate fractions were in isotopic equilibrium, then the calculated age based on those two fractions should reflect the “true” age. For many of the samples examined here this is clearly not the case (*c.f.* Table 5.1).

However, the published ages are mostly based on single mineral phases. Thus, it cannot be ruled out that any difference in age is a consequence of *i.e.* different closure temperatures. The mismatch between Lu-Hf derived ages and published ages do not provide definitive evidence for isotopic disequilibrium although they are strongly indicative of such.

If published ages are used to correct isotopic signatures of Hf, both carbonate and non-carbonate fractions should yield the same initial ratio if they are from the same source and in isotopic equilibrium. Figure 5.2 together with numerical results from Table 10.32 again show that this is not the case for most samples (exception: BM.2004.P9(9) from Fogo). In fact, the age corrected $^{176}Hf/^{177}Hf$ ratios of many carbonate fractions are below the initial $^{176}Hf/^{177}Hf$ of the solar system (0.279811, Bouvier et al., 2008). This is obviously unrealistic and can only happen if 1) Lu was added at a later stage, 2) Hf was removed at a later stage and/or 3) the age of the carbonatite is not correct. Of those three options, number 1) and 2) are more likely. The variation and shift of whole-rock $^{176}Hf/^{177}Hf_t$ ratios towards unrealistic values is caused by the carbonate fraction, which dominates the whole-rock composition (*c.f.* Table 4.1) and additionally hosts extremely radiogenic Hf isotopes (*c.f.* Chapter 5.1.1 and Table 10.32); and although the Hf budget is controlled by the non-carbonate fraction (*c.f.* Figure 4.5), the non-carbonate fraction only constitutes a small proportion of carbonatites and thus only contributes little to the whole-rock signature (*c.f.* Table 4.1 and Table 2.1). The only exception is one sample from Fogo (BM.2004,P9(9)), where all three fractions appear to be in isotopic equilibrium with one another. However, this sample consists of 73% of non-carbonate fraction (*c.f.* Table 4.1) and it is questionable whether this can even be considered a carbonatite. Nevertheless, the other Fogo sample (LI 23/02/08) is isotopically identical for Hf and Nd for whole-rock and non-carbonate fractions and only differs for the carbonate fraction. For Sr and Nd isotopes, isotopic disequilibrium is not as clear. While non-carbonate fractions from Fen, Kovdor and from sample BM.2004.P9(9) are very variable in $^{87}Sr/^{86}Sr_t$, carbonate and whole-rock as well as non-carbonate fractions from the other localities have the same isotopic signature for each locality. The carbonate fraction controls the Nd and Sr budget and dominates the whole-rock. Thus, it is expected that whole-rock and carbonate fraction are isotopically identical or at least similar. The variation of the non-carbonate fraction shows that for Nd and Sr there is also observable isotopic disequilibrium between carbonate and non-carbonate fractions. Bizimis et al. (2003) explain the isotopic disequilibrium as a consequence of sampling xenocrysts during ascent. Those xenocrysts are thought to be part of the non-carbonate fraction, while the carbonate fraction is thought to be pristine and reflecting the carbonatitic source.

5.2.2. Carbonatite source information

As described in chapter 1.2, the source and genesis of carbonatites is poorly understood and highly debated. Their source is thought to be either mantle plume induced (*e.g.* Bell, 2001; Bell et al., 2004; Holm et al., 2006; Jones et al., 2013), a mixed HIMU-EM1 component (*e.g.* Bell and Blenkinsop, 1987a, 1987b; Bell and Simonetti, 1994; Simonetti et al., 1997), a depleted mantle source (*e.g.* Andersen, 1987; Pearce et al., 1997), a mantle source containing a recycled component (*e.g.* Bizzarro et al., 2002; Doucelance et al., 2010), or even a source showing a DUPAL anomaly (*e.g.* Hart, 1984; Huang et al., 1995). Almost all carbonatite samples from this study plot below the mantle array for εHf_t versus εNd_t (*c.f.* Figure 5.2). The great variation in εHf_t is mostly caused by the carbonate fraction (and some whole-rock samples) and indicates open system behaviour and/or isotopic disequilibrium, especially for fractions lower than the initial of the solar system ($^{176}Hf/^{177}Hf_t$: 0.279811, Bouvier et al., 2008). The fact that $^{176}Lu/^{177}Hf$ ratios would need to be so low or even unrealistic (<0, Table 3.6) for age-corrected $^{176}Hf/^{177}Hf$ ratios to fall onto the mantle-array shows the extent to which the Lu-Hf system has been disturbed. One way to explain this discrepancy between mantle array and carbonate/whole-rock fractions would be that the carbonatite source lies below the mantle array. A reservoir with a composition below the mantle array was suggested by Nowell et al. (1998, 1999, 2004) for kimberlites and lamproites which are thought to be genetically related (*e.g.* Tappe et al., 2008), as well as for carbonatites (Bizzarro et al., 2002) and mafic alkalic rocks of the Kaapvaal craton (Janney et al., 2002). However, even for age corrected $^{176}Hf/^{177}Hf$ ratios to fall below the mantle array, the pristine $^{176}Lu/^{177}Hf$ ratios need to be higher than the ones calculated in Table 3.6, but at the same time lower than many of the measured $^{176}Lu/^{177}Hf$ (Table 3.6 and appendix Table 10.32) to avoid unrealistic/implausible $^{176}Hf/^{177}Hf$ initial ratios.

Changes in the $^{176}Lu/^{177}Hf$ and $^{176}Hf/^{177}Hf$ ratios by secondary processes could provide an alternative explanation for unrealistic age corrected $^{176}Hf/^{177}Hf$ ratios, in which case it would be impossible to constrain useful source information unless the processes overprinting the samples can be understood and quantified. Nevertheless, there are many samples that could give realistic values if it is assumed that a carbonatite source plots below the mantle array. For example, samples from Oldoinyo Lengai, Fogo (except for carbonate fractions from sample LI 23/02/08) as well as whole-rock and non-carbonate fractions from Sokli could reveal source information. For those samples, the different fractions possess similar isotope information suggesting isotopic equilibrium between them.

All three localities are thought to originate from a mantle plume (Holm et al., 2006; Jones et al., 2013; Marty et al., 1998). Bizimis et al. (2003) suggest that the non-carbonate fraction represents an assemblage of xenocryst, which will ultimately affect the whole-rock signature. If the non-carbonate fraction, which dominates the Hf budget, is an assemblage of xenocrysts then this would lead to erroneous conclusions about the nature of the Hf isotope composition of the carbonatitic source. Nevertheless, the isotopic composition of the non-carbonate fractions of Oldoinyo Lengai, Sokli and Fogo are in equilibrium with their corresponding whole-rock and carbonate fraction signatures, suggesting that they originated from the same source. For Oldoinyo Lengai, all three lithophile isotope systems agree and place the source close to bulk silicate Earth for Sr, Nd and Hf, but one that is displaced below the mantle array (εHf_t: ~-5.8, εNd_t: ~0.7) in the Hf-Nd isotope space. For Sokli (εHf_t: ~8.5, εNd_t: ~6) and Fogo (εHf_t: ~9, εNd_t: ~7), this source would be close to the mantle array for Hf and in between the HIMU and DMM end-members for Nd. This can also be observed for Nd-Sr isotopes (Figure 5.3 and appendix Table 10.33 and Table 10.34), though influence by a HIMU source can only truly be identified using Pb isotopes. This mixing of the HIMU and DMM end-members has already been observed for intermediate aged volcanic rocks from Santo Antão, Cape Verde (2 to 0.3 Ma) using Pb-Nd-Sr isotopes (Holm et al., 2006).

When adding the carbonate fractions from Sokli and sample LI 23/02/08 to this source interpretation, it can be seen that the carbonate fractions are lower in εHf_t than the whole-rock and non-carbonate fractions and thus do not match the same source, at least not for Hf. In fact, most of the carbonate fractions from this global study yield lower εHf_t than their corresponding whole-rock and non-carbonate fractions or are even unrealistically low (<initial of solar system), and thus do not reveal useful source information contrary to the conclusions of Bizimis et al. (2003). On the other hand, most non-carbonate fractions of other localities (*e.g.* Fen, Jacupiranga) are higher in εHf_t than the whole-rock and plot on or above the mantle array. Their close position to the mantle array (Figure 5.2) would suggest a mantle origin. From Figure 5.3, it can be observed that, in particular, the non-carbonate fractions of samples from Fen and Kovdor are highly variable in $^{87}Sr/^{86}Sr_t$ and samples (including all fractions) from Kovdor and Grønnedal-Ika are additionally variable in εNd_t, suggesting that they were either not derived from the same source or contaminated. Demaiffe et al. (2001) simply suggest that mixing (depleted mantle + mantle plume component) and sampling of different magma batches may explain the different geochemical and isotopic signatures within one locality, while it could also simply be a consequence of magma differentiation (*e.g.* Le Bas, 1981) and/or secondary processes.

As described above and based on Hf isotopes, Bizzarro et al. (2002) suggested the presence of a hidden mantle reservoir (Blichert-Toft and Albarède, 1997), also discussed by Nowell et al. (1998, 1999, 2004) as a source for kimberlites, which could also represent a common reservoir from which carbonatites were generated. Similar to Nowell et al. (1999), Bizzarro et al. (2002) suggest a deep seated very old (at least 3 Ga) and unradiogenic mantle source consisting of a recycled fertile lithospheric component. Nowell et al. (2004) discuss the possibility of ancient recycled oceanic crust stored in the deep Earth as being partly responsible for the isotopic signatures observed in kimberlites. For comparison, they review HIMU basalts, which show negative εHf coupled with radiogenic εNd (Ballentine et al., 1997; Chauvel et al., 1992) the source of which is thought to be influenced by oceanic crust (*e.g.* Day et al., 2010; Hofmann, 1997). Samples from Fen, for instance plot onto or close to the HIMU field for Sr-Nd-Hf isotopes (*c.f.* Figure 5.2 and Figure 5.3), suggesting that they might have too been influenced by oceanic crust. Although, the data of Bizzarro et al. (2002) suggests a similar source of carbonatites as for kimberlites, Nowell et al. (2004) outline that the carbonatite data of Bizzarro et al. (2002) needs to be treated with caution due to the possibility of post-crystallisation disturbance of the Tupertalik carbonatite. Considering the extreme εHf_t values of the carbonate fraction (*e.g.* εHf_t: -21,000) of Tupertalik, evidence for this disturbance is clear. This applies to most of the samples from this study. However, the fact that carbonatites tend to plot below the mantle array would suggest a similar source for carbonatites from this study as that suggested by Nowell et al. (1998, 1999, 2004) and Bizzarro et al. (2002). Present day samples from Oldoinyo Lengai could also support the existence of this hidden reservoir (Figure 5.2).

In contrast, Bizimis et al. (2003) suggest that a carbonatitic source must be short-lived in the mantle and that there are two stages of carbonatite formation; the first being direct melting as a mantle plume crosses the lherzolite + CO_2 + H_2O solidus and the second being plume induced melting of a metasomatized lherzolite. The latter was also suggested by Doucelance et al. (2010) for oceanic carbonatites from Cape Verde and Fuerteventura, suggesting that the metasomatic agent was influenced by subducted and recycled material. This study shows extreme $^{176}Hf/^{177}Hf_t$ compositions, which are not representative of any terrestrial source. As outlined before, this is especially the case for the carbonate fraction, which was originally thought to reveal source information (Bizimis et al., 2003). This leads to the need for a more detailed investigation of the non-carbonate fraction and the comprising minerals: Are minerals present in the non-carbonate fraction xenocrysts (Bizimis et al., 2003) or are they magmatic and therefore reveal information on the carbonatite source?

On a plot of age corrected $^{176}Hf/^{177}Hf$ versus published age (Figure 5.4), the lowest $^{176}Hf/^{177}Hf_t$ of the non-carbonate fraction for each carbonatite locality follow the evolution line of CHUR. Non-carbonate fractions with elevated $^{176}Hf/^{177}Hf_t$ mostly fall in between the evolution curves of CHUR and DMM, with the exceptions of sample BM.2000,P14(24), 4808 and 19781, which plot above the DMM evolution curve. While the non-carbonate fractions from this study mostly follow CHUR and DMM evolution, non-carbonate fractions analysed by Bizimis et al. (2003) scatter strongly (*c.f.* Figure 5.4). Kimberlites are thought to be genetically related to carbonatites and were thus plotted for reference. Young whole-rock kimberlites as well as zircons from kimberlites (Gaffney et al., 2007; Nowell et al., 2004) show a larger scatter in $^{176}Hf/^{177}Hf_t$, too, while the older whole-rock kimberlites are similarly close to CHUR evolution. In contrast, zircons and baddeleyites from carbonatites (Bizzarro et al., 2002) all plot around the CHUR evolution line with minimal scattering. Detrital zircons (Bodet and Schärer, 2000; Cina et al., 2009; He et al., 2013; Iizuka et al., 2017, 2015, 2013, 2010; Wang et al., 2011, 2009; Yang et al., 2009; Zhang et al., 2012) are thought to be representative of the continental crust and show large scattering from below CHUR evolution up to DMM evolution. Variation of non-carbonate fractions from single localities (*e.g.* from the CHUR evolution up to more radiogenic $^{176}Hf/^{177}Hf_t$ values of *i.e.* 0.28355 for sample 19781) could be explained by 1) re-equilibration or contamination with the carbonate fraction, which tends to be considerably more radiogenic than the non-carbonate fraction (*c.f.* Table 10.32), 2) sampling of xenocrysts with radiogenic εHf from the lithospheric mantle (*e.g.* Simon et al., 2002; Pearson and Nowell, 2003; Nowell et al., 2004), 3) crustal contamination, as detrital zircons fall into a similar range of $^{176}Hf/^{177}Hf_t$ identified in many non-carbonate fractions from this study and the study by Bizimis et al. (2003), and/or 4) influence of inclusions found in minerals of the non-carbonate fraction (*e.g.* 4808 and BM.2000,P14(24), *c.f.* Table 2.1). However, for the three samples plotting above the DMM evolution curve (BM.2000,P14(24), 4808 and 19781), it is most likely that they are affected by mineral inclusions, or influenced by the carbonate fraction, either through re-equilibration or because they were not fully decarbonated during dissolution. Together with the low signal intensities on ^{179}Hf during analyses of those three samples (*c.f.* Figure 5.4), their $^{176}Hf/^{177}Hf_t$ ratios bear greater uncertainties and are thus less reliable than for the other samples.

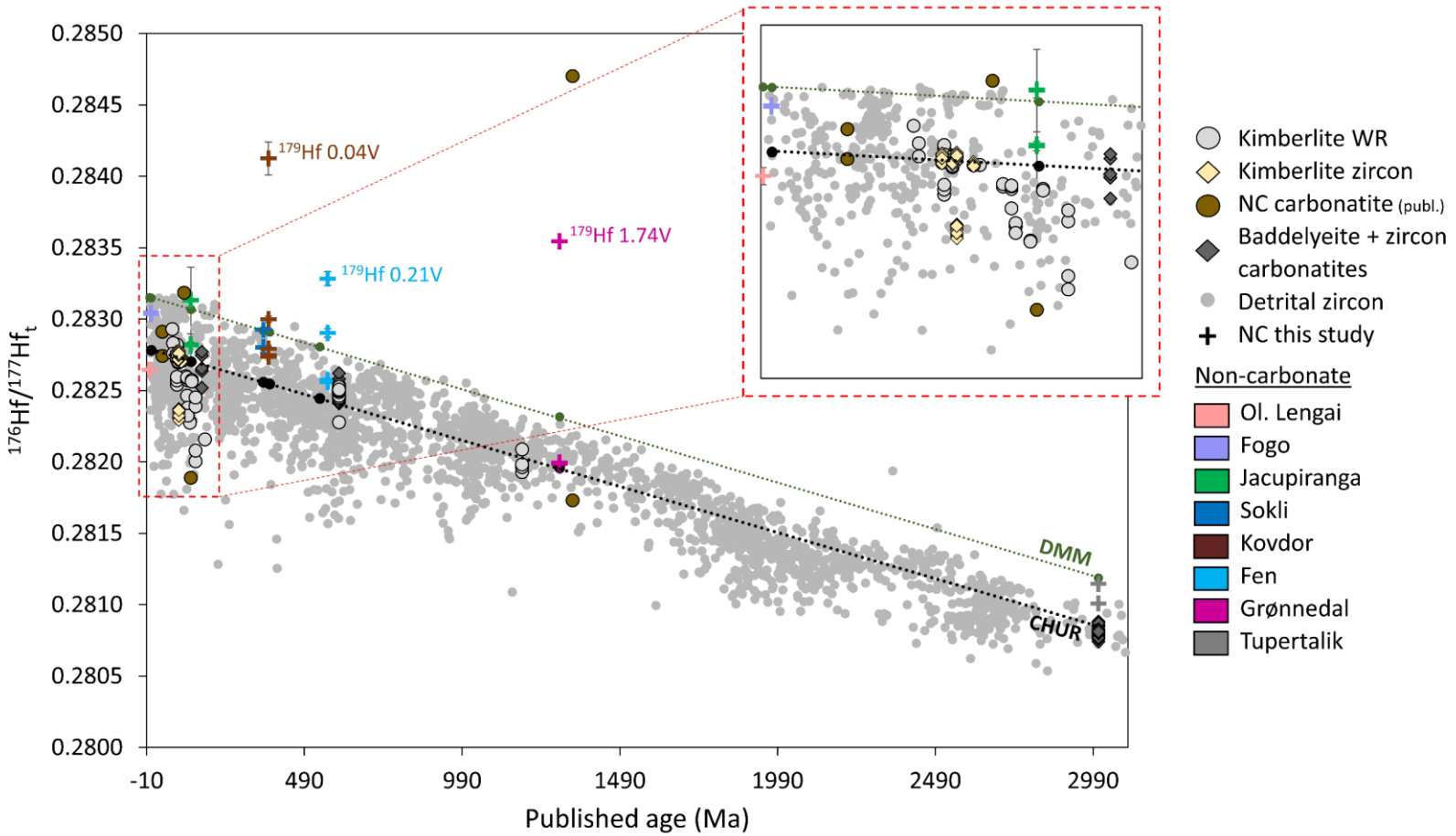

Figure 5.4 **Age corrected $^{176}Hf/^{177}Hf$ of NC fractions plotted versus published age. CHUR evolution: Bouvier et al. (2008), kimberlite whole-rock: Gaffney et al., (2007); Nowell et al. (2004), kimberlite zircon: Nowell et al. (2004), non-carbonate (NC) carbonatites: Bizimis et al. (2003),baddeleyite+zircon carbonatites: Bizzarro et al. (2002), detrital zircons: Bodet and Schärer (2000); Cina et al. (2009); He et al. (2013); Iizuka et al. (2017, 2015, 2013, 2010); Wang et al. (2011, 2009); Yang et al. (2009); Zhang et al. (2012).**

Nevertheless, the fact that the least radiogenic non-carbonate fractions from each locality in this study as well as baddeleyites and zircons from additional carbonatites (Bizzarro et al., 2002) plot close to CHUR evolution, would suggest that the Hf isotopic composition of the carbonatite source has remained quite homogeneous over the last 3 Ga. Thus, non-carbonate fractions close to CHUR evolution possibly carry source information of carbonatites and are not xenocrysts and not strongly overprinted by post melting/emplacement processes.

Baddeleyite and zircons have Lu/Hf ratios close to zero (*e.g.* $^{176}Lu/^{177}Hf$ of Tupertalik and Sarfartoq: 0 to 0.00002, Bizzarro et al., 2002) and thus their Hf isotope composition is invariant. Hence, age corrections will bear no to minor uncertainties, making baddeleyite and zircons more reliable tracers for the Hf isotope composition of the carbonatite source. Furthermore, compared to the non-carbonate fraction, there is only limited variation in Hf isotopic signatures of baddeleyite and zircon.

For age corrected $^{143}Nd/^{144}Nd$ isotopes plotted versus the published ages (Figure 5.5), the non-carbonate fractions from this study also plot close to the CHUR evolution curve. This also applies to non-carbonate fractions from Bizimis et al. (2003) and suggests that the carbonatite source is not only relatively homogeneous for Hf isotopes, but also for Nd isotopes.

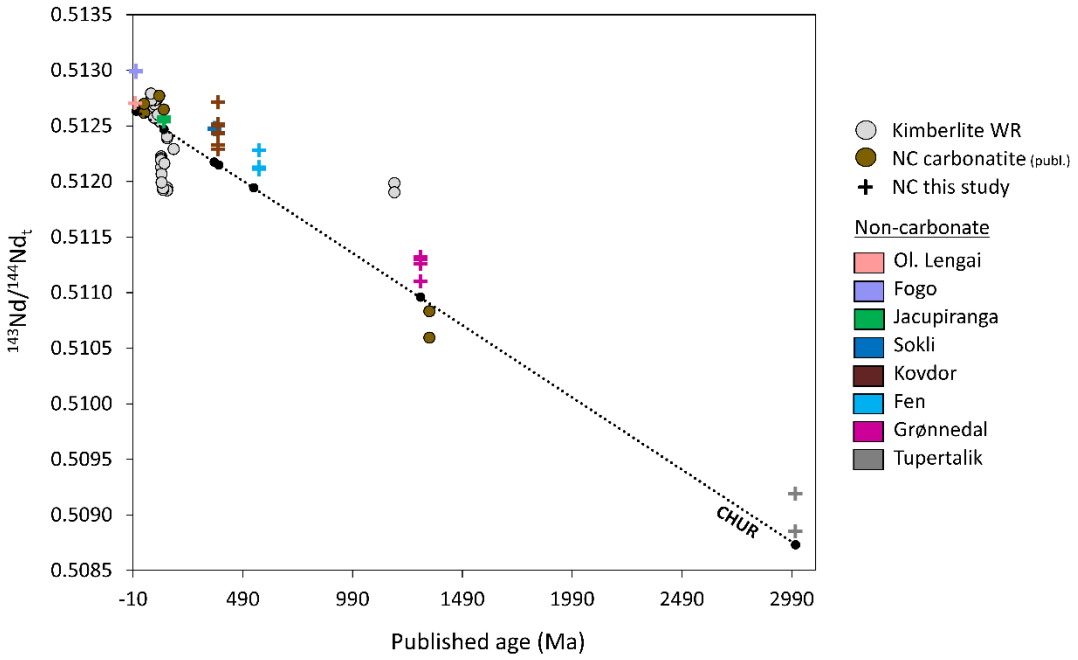

Figure 5.5 **Age corrected $^{143}Nd/^{144}Nd$ of NC fractions plotted versus published age. CHUR evolution: Bouvier et al. (2008), kimberlite whole-rock: Nowell et al. (2004), non-carbonate (NC) carbonatites: Bizimis et al. (2003).**

The only conclusion that can be made with any certainty is that the whole-rock signatures of carbonatites need to be treated with extreme caution, as non-carbonate and carbonate fractions are not in isotopic equilibrium, due to secondary overprinting of the carbonate fraction. This effect can be greater the older the samples are, as shown by mostly unaffected isotopic signatures from Oldoinyo Lengai versus strong disequilibrium between the different fractions from Tupertalik. This suggests that the Hf isotopic signature of the carbonate fraction does not reveal useful source information, at least not for samples older than present day.

5.2.3. Processes overprinting carbonatites

Several studies have already pointed to post-magmatic processes overprinting carbonatites (*e.g.* Andersen, 1984; Smith et al., 2018; Zaitsev and Keller, 2006). The open system behaviour observed for carbonate fractions as well as some whole-rock samples from this study indicates that these samples have also experienced post-magmatic alteration. Processes such as fluid induced subsolidus re-equilibration (diffusion), exsolution, recrystallisation, hydrothermal modification/crystallisation as well as tectonic mobilisation (Chakhmouradian et al., 2016b, 2016a) are all potential mechanisms that could result in open system behaviour. Generally, only small numbers of carbonatites can even be considered pristine and elemental exchange during hydrothermal processes and recrystallisation of carbonates can lead to isotopic exchange (Chakhmouradian et al., 2016b). Lutetium and Hf are fractionated at the scale of carbonate and non-carbonate fraction. Thus, if a more soluble mineral like calcite (*e.g.* Brantley, 2008) interacts and/or reacts with infiltrating fluids or simply recrystallises due to metamorphic processes, it can change its elemental composition, thus increasing for instance the Lu/Hf ratio by incorporating more Lu or by loss of Hf. If this process occurs at a later stage, the calcite will not have enough time to develop the corresponding radiogenic signature, thus when age correcting there will be a mismatch between the parent and daughter isotope ratios resulting in overcorrected $^{176}Hf/^{177}Hf$ ratios if Lu/Hf is too high.

Carbonatites located in tectonically active regions or particularly old carbonatites are likely to be more affected than younger carbonatites (Chakhmouradian et al., 2016b). For example, the older Greenland samples from Tupertalik experienced metamorphic overprinting dated to 2650 Ma (Larsen and Rex, 1992). The Fen complex lies close to and might have been influenced by the younger Palaeozoic Oslo rift. Samples from Jacupiranga are thought to be influenced by crustal processes (Santos and clayton, 1995), while younger samples from Fogo have not experienced major overprinting and the present day samples from Oldoinyo Lengai

have experienced no metamorphism but strong alteration due to the properties of natrocarbonatites (*c.f.* Zaitsev and Keller, 2006). To determine by how much the Lu/Hf ratio would need to be increased to create radiogenic signatures as observed for carbonate fractions from Tupertalik, those carbonate fractions together with the carbonate fractions of Oldoinyo Lengai were used for calculations: Tupertalik and Oldoinyo Lengai fall onto the same area on the εNd_t versus εHf_t plot and thus it is assumed that the isotopic composition of Oldoinyo Lengai could reflect that of Tupertalik at the time of eruption. Additionally, Oldoinyo Lengai is a carbonatite of zero age and it is thus believed that it reflects a representative value of a carbonatite unaffected by hydrothermal or metamorphic processes. If we now take the $^{176}Hf/^{177}Hf_m$ ratio alongside the $^{176}Lu/^{177}Hf_m$ ratio of the carbonate fraction of Oldoinyo Lengai and calculate the $^{176}Hf/^{177}Hf$ ratio after 357 Ma (metamorphic event occurred 2650 Ma years ago, age of Tupertalik 3007 Ma), we obtain a $^{176}Hf/^{177}Hf_{met}$ ratio of 0.283216. If we now take the measured $^{176}Hf/^{177}Hf$ ratio of the carbonate fraction of Tupertalik (0.46884) and assume that the $^{176}Hf/^{177}Hf_{met}$ is the initial of that value, we can now calculate what the Lu/Hf needs to be to create a value that becomes substantially radiogenic over 2650 Ma. The Lu/Hf ratio needed would be 3.66, which is approximately 160× higher than the initial value of 0.023. If we take the more radiogenic sample from Tupertalik (0.755442), the Lu/Hf value increases to 9.31, which is around 400× higher. This means the process needs to enrich Lu/Hf in the carbonate fraction by 160 and 400 times. However, those are the values we would need to correct back to something more realistic. The measured Lu/Hf ratios for those two samples from Tupertalik were much higher with 6.75 and 18.45, respectively.

Processes enriching HREE such as Lu, were described by Smith et al. (2018), who showed that during alteration of monazite to apatite, REEs are mobilised, causing light to medium REEs to be leached and HREE to be added. They suggested that this type of alteration is likely linked to a late magmatic stage or metasomatic addition of REE. However, this cannot apply to the carbonatites of this study, as the HREE show no general enrichment (*c.f.* Figure 4.4). Additionally, if this process would have occurred during a late magmatic stage, the samples would have developed a corresponding radiogenic $^{176}Hf/^{177}Hf$ signature and age corrections should result in more realistic values. And although apatite is one of the major minerals found in carbonatites (*c.f.* Table 2.1), it is considered a phase that resides in the non-carbonate fraction. Thus, if this process was responsible for Lu-enrichment, we would rather expect to see it in the non-carbonate and not the carbonate fraction.

A study on trace element behaviour in relation to Lu-Hf and Sm-Nd isotope systematics during metamorphic dehydration/hydration (Martin et al., 2010) found that Lu can be mobile while Hf can be immobile during fluid circulation/exchange. However, this study addresses amphibolite facies conditions which cannot necessarily be applied to overprinting of carbonatites. In a study of hydrothermal modification of zircons, Zhu et al. (2017) describe a change of the Lu/Hf ratio of hydrothermal (and pre-magmatic) zircons, that becomes 10x higher than volcanic zircons due to hydrothermal activity. They explain this as being due to addition of Lu rather than loss of Hf, as they observe a positive correlation of Lu with the Lu/Hf ratio and no correlation for Hf with Lu/Hf. Their zircons have almost uniform $^{176}Hf/^{177}Hf$ ratios with varying Lu/Hf ratios, showing that hydrothermal activity has only a minor effect on the isotopic composition of Hf. Although, Zhu et al. (2017) performed their study on zircons and not on whole-rock samples or mineral assemblages, their work nevertheless shows that hydrothermal activity can change the Lu/Hf ratio without affecting the Hf isotopic signature. However, in our study there is no linear relationship between Lu and Lu/Hf or Hf and Lu/Hf (Figure 5.6). However, there is a negative exponential relationship between Hf and Lu/Hf (Figure 5.6). When considered on a log/log plot of Hf versus Lu/Hf (Figure 5.7), it is clear that the non-carbonate fraction shows high Hf-concentrations and low Lu/Hf ratios, while the carbonate fraction shows the opposite trend. The whole-rock samples are scattered in between carbonate and non-carbonate fractions. This exponential relationship and clear separation of carbonate from non-carbonate fractions can simply be explained by fractionation of Hf between the different fractions, which is also supported by the distribution of Lu and Hf observed in Figure 4.5. Although, fractionation of Hf between carbonate and non-carbonate fractions is likely responsible for the exponential trend, there is still the possibility of loss of Hf contributing to the low Lu/Hf ratios.

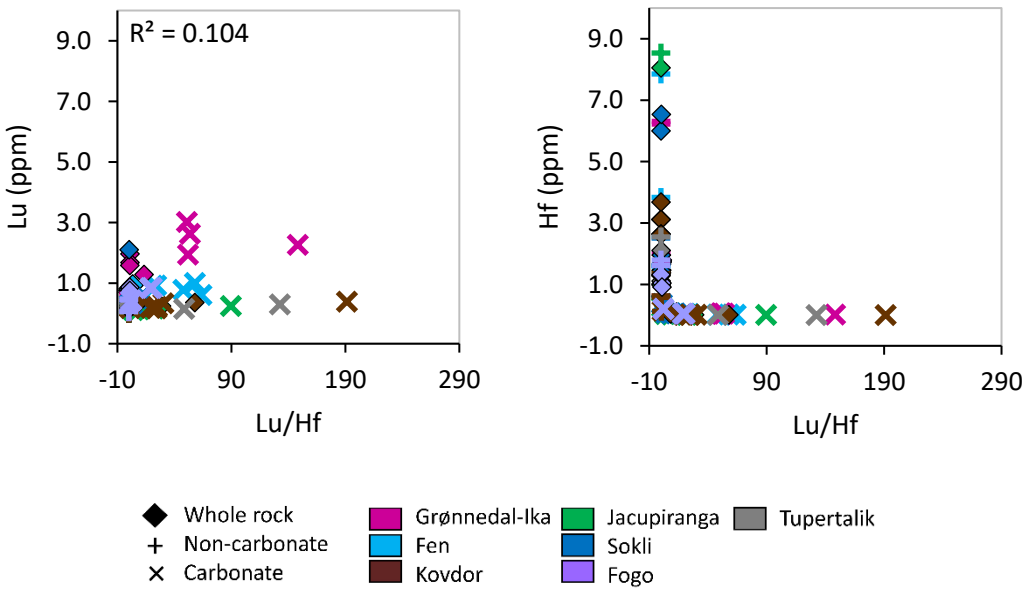

Figure 5.6 **Lu versus Lu/Hf (left) and Hf versus Lu/Hf (right). There is no clear correlation visible for Lu vs. Lu/Hf and a negative exponential correlation for Hf vs. Lu/Hf.**

That there is no clear linear relationship between Lu and Lu/Hf shows that addition of Lu cannot be the sole process responsible for the high Lu/Hf ratios. Although, there might have been several processes responsible for changing the Lu/Hf ratios not necessarily following a linear relationship. For example, there might have been hydrothermal addition of Lu followed by metamorphic overprinting and/or recrystallisation.

Lutetium and Sr both positively correlates with Nd for carbonate and whole-rock fractions (Figure 5.8). This indicates that the processes affecting the Lu budget could also account for Nd and Sr, although they do not affect Sr or Nd to the same extent. In contrast, the non-carbonate fractions show no correlation between Lu and Nd or Sr and Nd, which would suggest that the non-carbonate fraction has either not been affected by the same processes or could also mean that the non-carbonate fractions contain xenocrysts.

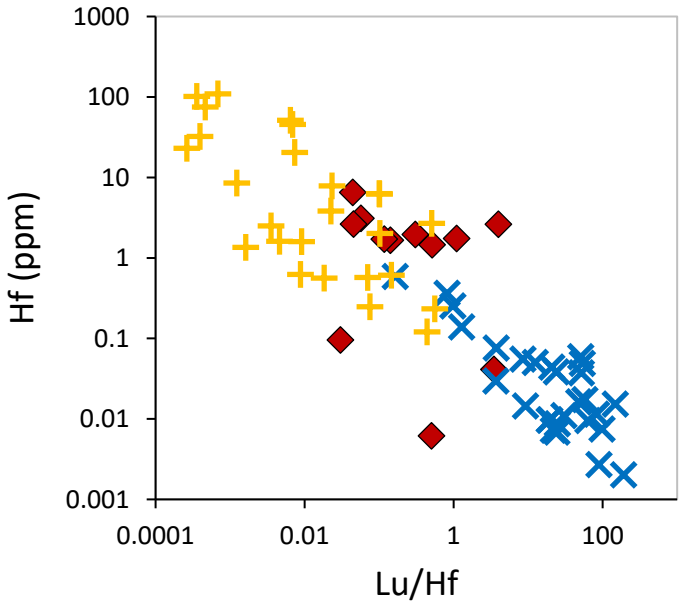

Figure 5.7 **Log/log plot of Hf versus Lu/Hf for whole-rock (red), carbonate (blue) and non-carbonate (yellow) fractions.**

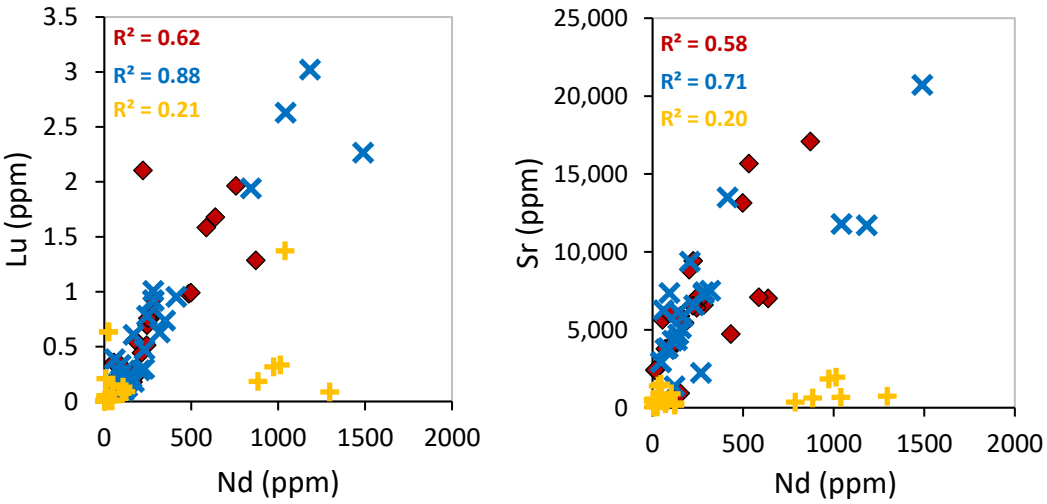

Figure 5.8 **Lu versus Nd (left) and Sr versus Nd (right) for whole-rock (red), carbonate (blue) and non-carbonate (yellow) fractions showing a positive correlation for carbonate and whole-rock fractions.**

The carbonate fraction dominates the Lu budget and contains negligible Hf (~0.01 to 2.5% of the whole-rock). Carbonates are more soluble than many phases present in the non-carbonate fraction (*e.g.* Brantley, 2008). If there were to be one or several events causing dissolution and precipitation processes, they are more likely to affect the carbonates, which again appear to be more likely to incorporate Lu and not the relatively immobile Hf into their crystal lattice. On the other hand, those processes may also decrease the amount of Lu, which could explain why there is no linear relationship of Lu and Lu/Hf. It remains unclear which processes have affected the samples from this study. However, there is no doubt that the carbonate fraction and thus most whole-rock samples have experienced extensive secondary alteration and thus cannot be used for determining the carbonatitic source. Strontium and Nd isotopes might be more robust, where due to the substantial enrichment of those elements in most samples, secondary processes will not have the same effect. Nevertheless, it cannot be said with certainty whether Nd and Sr have been affected as strongly as Hf. Though, the correlation of Lu and Sr with Nd would suggest that all of these elements are coupled, suggesting both Nd and Sr isotopes have also been affected.

5.3. Conclusions

The global study of lithophile element isotope compositions of carbonatites from different localities, tectonic settings and of different ages, has led to the following conclusions:

- Lu, Sm, Nd and Sr are predominantly hosted by the carbonate fraction, while Hf and Rb are largely hosted in the non-carbonate fraction.
- Whole-rock isotope signatures cannot be used to constrain source information and carbonatite source investigations need to be carried out on the mineral scale.
- The Lu-Hf isotope system has been disturbed and decoupled from the Sm-Nd and Rb-Sr isotope systems.
- Most carbonatites have experienced extensive secondary alteration
    - Lutetium and Hf show open system behaviour for carbonate fractions, resulting in Lu/Hf ratios that do not account for the measured $^{176}Hf/^{177}Hf$ ratios and which are thus responsible for implausible age corrected $^{176}Hf/^{177}Hf$ ratios (<initial of solar system).
    - The carbonate fraction is strongly affected by secondary processes and thus does not carry useful source information unless these can be quantified and accurately corrected for. It is unclear which processes lead to changes in the Lu/Hf ratio.
- Young carbonatite samples provide more reliable isotopic information on the carbonatitic source since the isotope compositions are immune from the problems associated with alteration and application of age corrections. Oldoinyo Lengai samples suggest the source is close to bulk silicate Earth for Nd and Sr isotopes, but displaced below the Nd-Hf isotope mantle array, thus, supporting a potential hidden mantle reservoir (Nowell et al., 2004, 1999, 1998; Bizzarro et al., 2002). Fogo samples appear to have a Hf-Nd-Sr isotope source composition between the HIMU and DMM end-member.
- The initial Hf and Nd isotope composition of the non-carbonate fractions are characterised by a relatively limited range and plot close to the CHUR evolution curve. This suggests that the carbonatite source could have remained close to chondritic and relatively homogeneous over ~3 Ga.
- Differences in the isotopic signatures of samples and their carbonate and non-carbonate fractions from one locality are likely caused by their unique mode of minerals, which again can be either related to magmatic differentiation (Le Bas, 1981), different local sources affected by mixing in the mantle (Demaiffe et al., 2001), sampling of xenocrysts or local secondary overprinting.

Chapter 6 : Highly siderophile elements and Re-Os isotope study

Highly siderophile element abundances and $^{187}Os/^{188}Os$ isotope signatures in whole-rock carbonatites are examined in this section. The HSEs are thought to be mainly hosted by base metal sulphides in Earth's upper mantle (*e.g.* Mitchell and Keays, 1981; Luguet and Reisberg, 2016). Thus, BMS petrography was studied together with the whole-rock HSE and $^{187}Os/^{188}Os$ isotope signatures found in carbonatites, with the aim of providing insights into the origin of the BMS (mantle vs. crustal/hydrothermal) as well as the conditions under which they have formed. Combined with the knowledge obtained from the lithophile element isotope study in Chapter 5, the aim is to better understand carbonatite petrogenesis.

6.1. Results

6.1.1. Whole-rock highly siderophile element abundances

Whole-rock HSE abundances for natrocarbonatites (OL-1 and BM.2004, P12(13)) from this study range from <0.9 to 1.15 ppt Os, 1.8 to 11 ppt Ir, <23.2 to 55 ppt Ru, 82 ppt to 8.9 ppb Pt, <121 ppt to 4.9 ppb Pd, and 7.8 to 10.2 ppb Re; for magnesiocarbonatites (91/66 – C2, 91/60 – C5 and GGU 252874) from <0.9 to 4.8 ppt Os, <1 to 1.7 ppt Ir, <23.2 ppt Ru, <12.7 to 47 ppt Pt, <121 to 167 ppt Pd, and 20 to 45.5 ppt Re; and for calciocarbonatites (remaining samples appendix Table 10.35) from <0.9 to 12.6 ppt Os, <1 to 38 ppt Ir, <23.2 to 85 ppt Ru, <12.7 to 160 ppt Pt, <121 to 958 ppt Pd, and 3.2 ppt to 1.8 ppb Re (*c.f.* Table 10.35). Hence, when taking into account all samples, whole-rock HSE abundances range between <0.9 ppt and 10.2 ppb equivalent to 0.0003 to 29 times the HSE abundances of the primitive upper mantle (PUM, Becker et al., 2006; Figure 6.1).

Samples from Oldoinyo Lengai have the highest abundance in Re (7.8 and 10.2 ppb) followed by sample 4808 from Fen (1.8 ppb), all being higher than PUM (0.35 ppb; Becker et al., 2006). The remaining samples are generally one to three orders of magnitude lower in Re compared to PUM. Those latter range between 3.2 ppt (GGU 252833) and 206 ppt (J1-C1 and ASS-1).

While Pt and Pd for one Oldoinyo Lengai sample (OL-1; 8890 and 4926 ppt, respectively) are close to PUM (Pt: 7600 ppt and Pd: 7100; Becker et al., 2006), they are lower (Pt: 82.4 ppt) or below detection limit (bdl) for the other sample (BM.2004,P12(132)) from Oldoinyo Lengai. Variation between those two samples can also be observed for Ir (10.6 and 1.8 ppt), Ru (55.4 ppt and bdl), and Os (bdl and 1.2 ppt). Samples from Fogo are bdl for Ir, similar in

Pd (187 and 258 ppt) and Os (2.5 and 2.3 ppt) but differ for Re (9.3 and 17.8 ppt), Ru (bdl and 84.8 ppt) and Pt (78.6 and 46.4 ppt).

For samples from Jacupiranga, the calciocarbonatite (J1-C1) is higher in Re (206 ppt) than the other three carbonatites (magnesiocarbonatites: 45.5 and 36.8 ppt, magnetite carbonatite 48.3 ppt). In contrast, the magnetite carbonatite (91/62 - C4) is higher in Pt (125 ppt) compared to the other Jacupiranga samples (47.7, 47.1 and 23.8 ppt). For Ru all samples except the calciocarbonatite (J1-C1, 27.3 ppt) are below detection limit (bdl), while for Os all but one magnesiocarbonatite (91/60 - C5, 4.8 ppt) are bdl. For Ir, the two magnesiocarbonatites (91/66 - C2 and 91/60 - C5) have 1.15 and 1.69 ppt, while the other two samples are bdl.

Carbonatites from the Kola Peninsula (Sokli and Kovdor) vary between 11.7 ppt (BM.2000,P11(22)) and 159 ppt (BM.1998,P18(183)) for Re. Except for sample BM.1998,P18(229) (6.4 ppt), all Kola samples are bdl for Ir. For Ru all Kola samples but BM.2000,P11(22) (30.5 ppt) are bdl. Platinum is either bdl (BM.1998,P18(44) and BM.2000,P14(24)) or varies between 40.7 and 159.5 ppt. Osmium is bdl for all Kola samples except BM.1998,P18(183) (3.5 ppt). For Pd, only samples BM.1998,P18(229) and BM.2000,P11(22) are above detection limit (665 and 583 ppt, respectively).

Sample 4808 from Fen is not only high in Re but is the highest in Os (12.6 ppt) from all the carbonatites but still much lower than PUM (3900 ppt; Becker et al., 2006). However, Ir and Pd are bdl, while for the other Fen sample (16462), Ir is the highest of all analysed carbonatites (38.2 ppt) and Pd is also at the higher end of the spectrum (958 ppt). Nevertheless, 16462 is lower in Re (138 ppt) and Os (1.46 ppt) and similar in Ru (41 ppt) compared to sample 4808 (40 ppt).

Samples from Grønnedal-Ika differ from each other for all HSEs; while sample 19781 is below detection limit for Ir, Ru, Pt and Os, sample 19780 is only bdl for Ru and above detection limit for all other elements (Ir: 10.6 ppt, Pt: 42 ppt, Os: 1.2 ppt). For Re and Pd both samples give reasonable numbers (Re: 15 ppt for 19780 and 6.5 ppt for 19781, Pd: 171 ppt for 19780 and 311 ppt for 19781). The oldest samples from Tupertalik are bdl for Ir, Ru, Pt and Pd and only give reasonable numbers for Re (3.2 and 19.6 ppt) and Os (3.9 and 1.6 ppt).

When taking into account all carbonatite samples, the average values for HSEs of carbonatites are as follows: 1) Os: 3.3 ppt, 2) Ir: 9.2 ppt, 3) Ru: 46.5 ppt, 4) Pt: 695 ppt, 5) Pd: 795 ppt and 6) Re: 1041 ppt.

The CI-chondrite normalised HSE patterns of carbonatites from this study show the typical melt-like positive slope from Os to Re (Figure 6.1) with suprachondritic Re_N/Os_N ranging from 10 to 105,000. As reference for typical melt patterns, OIB (alkali basalt, Day et al., 2010) and MORB (sample Ridelante DR 10; Bézos et al., 2005; Gannoun et al., 2007) were also plotted. The slope of HSE patterns for carbonatites is steeper than OIB with a general enrichment in Pt, Pd and Re and a depletion in Os, Ir and Ru. Additionally, HSEs in carbonatites are less abundant than in OIB (*e.g.* Os two orders of magnitude lower, Ir one order of magnitude lower), while Re is more abundant (*c.f.* average carbonatite pattern, Figure 6.1). In contrast, the MORB pattern more closely resembles the patterns of most carbonatites, showing similarly low concentrations in *i.e.* Pt (MORB: 53 ppt, Bézos et al., 2005; carbonatites: 27 to 160 ppt, excl. OL-1) and Ru (MORB: 61 ppt, carbonatites: 27 to 85 ppt). Sample OL-1 from Oldoinyo Lengai shows a steeper HSE pattern compared to the other carbonatites as well as MORB and OIB, raising the average value in Pt (695 ppt), which otherwise is not as high (24 to 159 ppt, n = 13) for the other carbonatites.

Samples from Fen, Assynt and Oldoinyo Lengai show the highest Re_N/Os_N ratios (Fen: 1122 and 1686, Assynt: 2134, Oldoinyo Lengai: 105,000), while for the other localities Re_N/Os_N varies between 10 (GGU 252833) and 148 (19780). Os_N/Ir_N ratios for most samples are subchondritic and vary from 0.04 to 0.61, while for sample 91/60 - C5 it is suprachondritic (Os_N/Ir_N: 2.66). For Pd_N/Pt_N ratios, most samples are suprachondritic (5.61 to 37), while sample OL-1 (Pd_N/Pt_N: 0.85) is subchondritic, though close to chondritic. Except for samples 19781 (Pd_N/Re_N: 3.21), BM.2000,P11(22) (Pd_N/Re_N: 3.32) and LI 23/02/08 (Pd_N/Re_N: 2.06), Pd_N/Re_N ratios are subchondritic (0.03 to 0.77) to chondritic (BM.2004.P9(9), 0.97). There is no systematic of normalised HSE ratios (Re_N/Os_N, Os_N/Ir_N, Pt_N/Pd_N, Re_N/Pd_N) with age or composition identifiable.

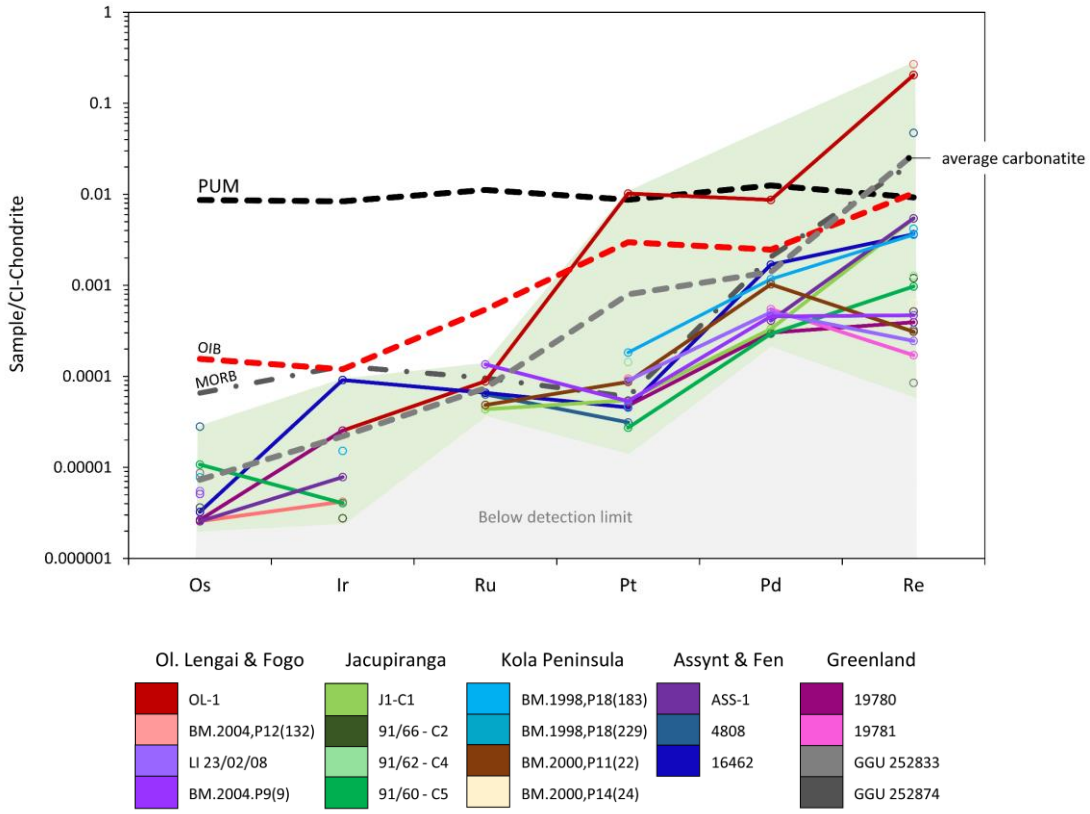

Figure 6.1 **CI-chondrite (Fischer-Gödde et al., 2010; Horan et al., 2003) normalised HSE patterns of carbonatites from different localities. Grey field: below detection limit, pale green field: field of all carbonatites from this study. Average carbonatite (grey dashed line) calculated from all plotted carbonatite patterns, PUM = primitive upper mantle (Becker et al., 2006), OIB = ocean island basalt (Day et al., 2010), MORB = mid-ocean ridge basalt (Bézos et al., 2005; Gannoun et al., 2007) Left to right: increasing incompatibility.**

Figure 6.2 shows the different highly siderophile elements plotted against one another and Figure 6.3 shows Os, Ir, Ru, Pt, Pd and Re plotted versus CaO. There is no observed correlation between Os and Ir (R^2 = 0.069), Pt and Ir (R^2 = 0.14), Pd and Pt (R^2 = 0.0003) or Pd and Re (R^2 = 0.031) and no correlation between HSEs and the CaO content (R^2 = 0.004 to 0.26).

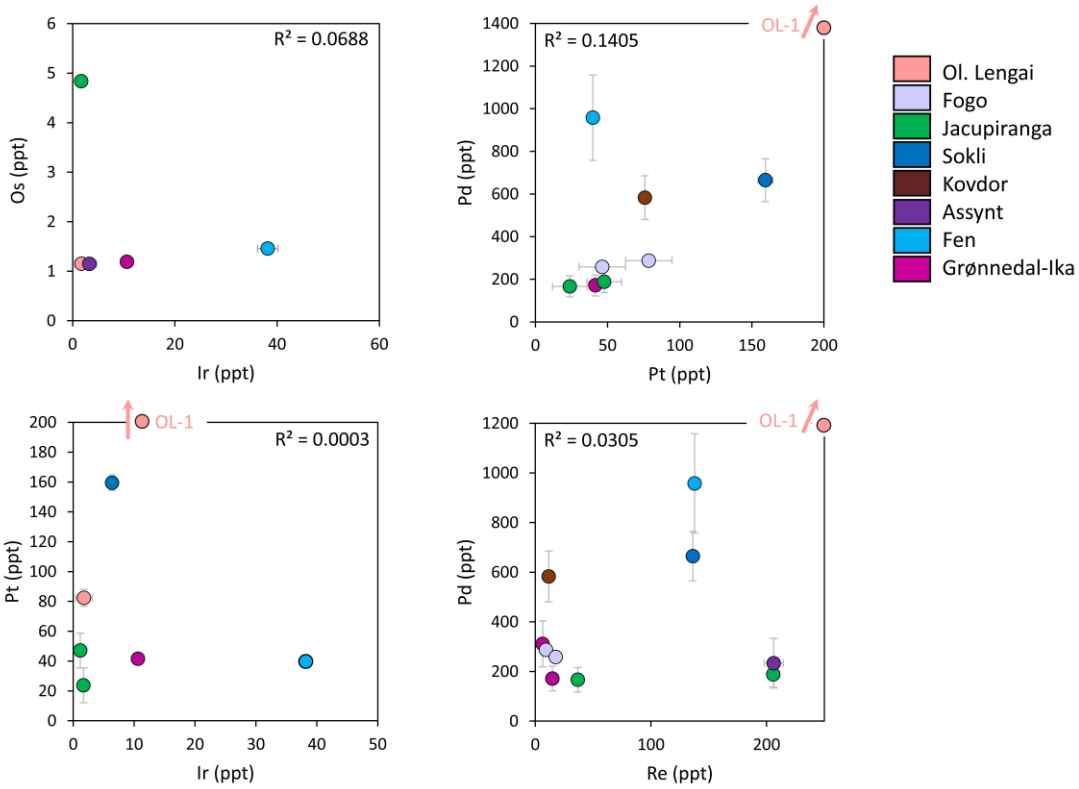

Figure 6.2 **Binary HSE variations in carbonatites. If no error is indicated, it is smaller than the symbol.**

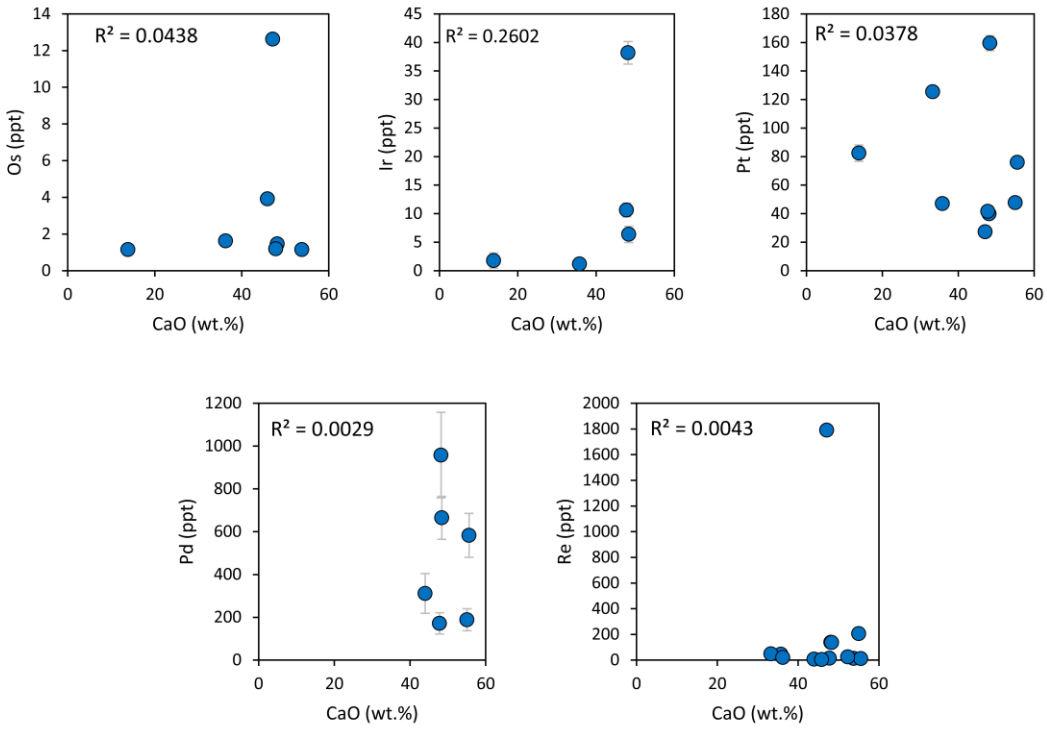

Figure 6.3 **HSE concentrations versus CaO. Blue circles represent all carbonatite samples from this study. CaO was determined semi-quantitively and no error given. For HSE errors are smaller than the symbols if not indicated.**

6.1.2. Whole-rock $^{187}Os/^{188}Os$ signatures

Measured (m) $^{187}Os/^{188}Os$ are all radiogenic and range for magnesiocarbonatites (91/66 - C2, 91/60 - C5 and GGU 252874) between 0.3705 and 47.6. Natrocarbonatites OL-1 and BM.2004,P12(132) have $^{187}Os/^{188}Os_m$ of 0.1636 and 0.2623, respectively. $^{187}Os/^{188}Os_m$ ratios in calciocarbonatites (remaining samples, *c.f.* appendix Table 10.35) range between 0.1477 and 55.6. The initial $^{187}Os/^{188}Os$ for all samples at time of eruption (t) are either radiogenic or negative (Figure 6.4 and appendix Table 10.35). For samples with Os concentrations below detection limit, age corrections could not be applied and thus only measured $^{187}Os/^{188}Os$ were plotted (Figure 6.4) and will be further described. The youngest samples from Oldoinyo Lengai (present day) and Fogo (4 Ma) are the least radiogenic (0.1636, 0.2623 and 0.3367, 0.1477, respectively), while samples from Assynt, Fen and Tupertalik show the highest $^{187}Os/^{188}Os_m$ ratios from this study (55.6, 48.66 and 47.64, respectively). The $^{187}Os/^{188}Os_m$ ratios do not correlate with age or tectonic setting and the $^{187}Os/^{188}Os_m$ of carbonatites from a given locality are very variable (*e.g.* Jacupiranga: 9.69, 0.8569, 1.54 and 0.3705; Fen: 48.66 and 5.77; Tupertalik: 0.6551 and 47.64, Figure 6.4). Re/Os ratios, considering all localities, vary between 0.82 (Tupertalik) and ~8850 (Oldoinyo Lengai). Again, samples from the same locality show large variations (*e.g.* Fen: 142 and 94, Tupertalik: 0.82 and 12).

There is no correlation for measured $^{187}Os/^{188}Os$ versus Os ($R^2 = 0.0905$) or versus Re ($R^2 = 0.0075$), though the four samples from Jacupiranga show a regression of 0.9967 mainly controlled by sample J1-C1 which shows a much higher $^{187}Os/^{188}Os$ ratio and Re concentration (Figure 6.5). Furthermore, there is no correlation between measured $^{187}Os/^{188}Os$ versus Re/Os ($R^2 = 0.006$) and versus Pd/Ir ($R^2 = 0.078$, Figure 6.5) when considering all samples.

Calculated T_{MA} model ages vary between 0.19 Ma and >Earth (appendix Table 10.35) and do not reflect the ages of the carbonatites from the literature (*e.g.* Oldoinyo Lengai: 0 Ma vs. T_{MA} = 0.19 Ma; Fen: 539 Ma, Andersen and Taylor (1988) vs. T_{MA} = 757 and 4210 Ma). However, for sample BM.1998,P18(44) from Sokli the T_{MA} age (349 Ma) is close to the published age (360 Ma, Vartiainen and Woolley, 1974 and references therein), while the T_{MA} of sample BM.1998,P18(183) from Sokli it is too young (44 Ma) compared to the published age.

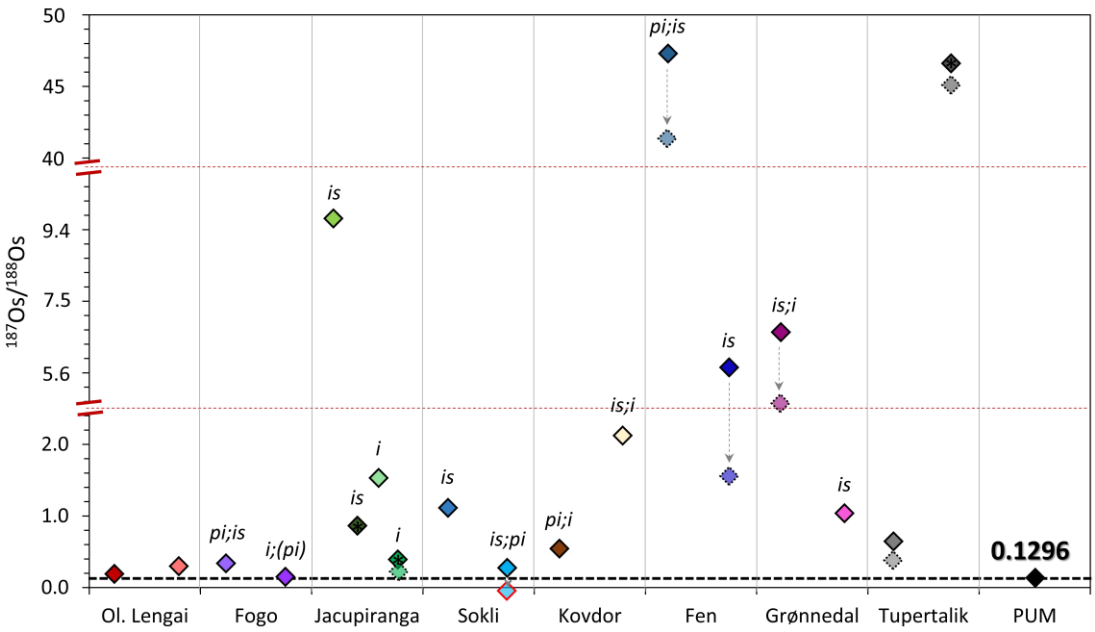

Figure 6.4 **$^{187}Os/^{188}Os$ ratios plotted versus localities. Diamonds with solid outlines show the measured $^{187}Os/^{188}Os$ ratios. Transparent diamonds with dashed outlines represent age corrected $^{187}Os/^{188}Os$ ratios. Age corrections for samples from Oldoinyo Lengai and Fogo are not resolvable on this scale. Diamonds with red outlines represent negative values. Sample age increases from left to right (present day, 4 Ma, 131 Ma, 360 Ma, 376 Ma, 539 Ma, 1299 Ma, 3007 Ma). Black dashed line: primitive upper mantle (PUM, Becker et al., 2006). Stars highlight the magnesiocarbonatites. pi: pseudo-included BMS, i: included BMS, is: interstitial BMS. Errors are smaller than the symbols.**

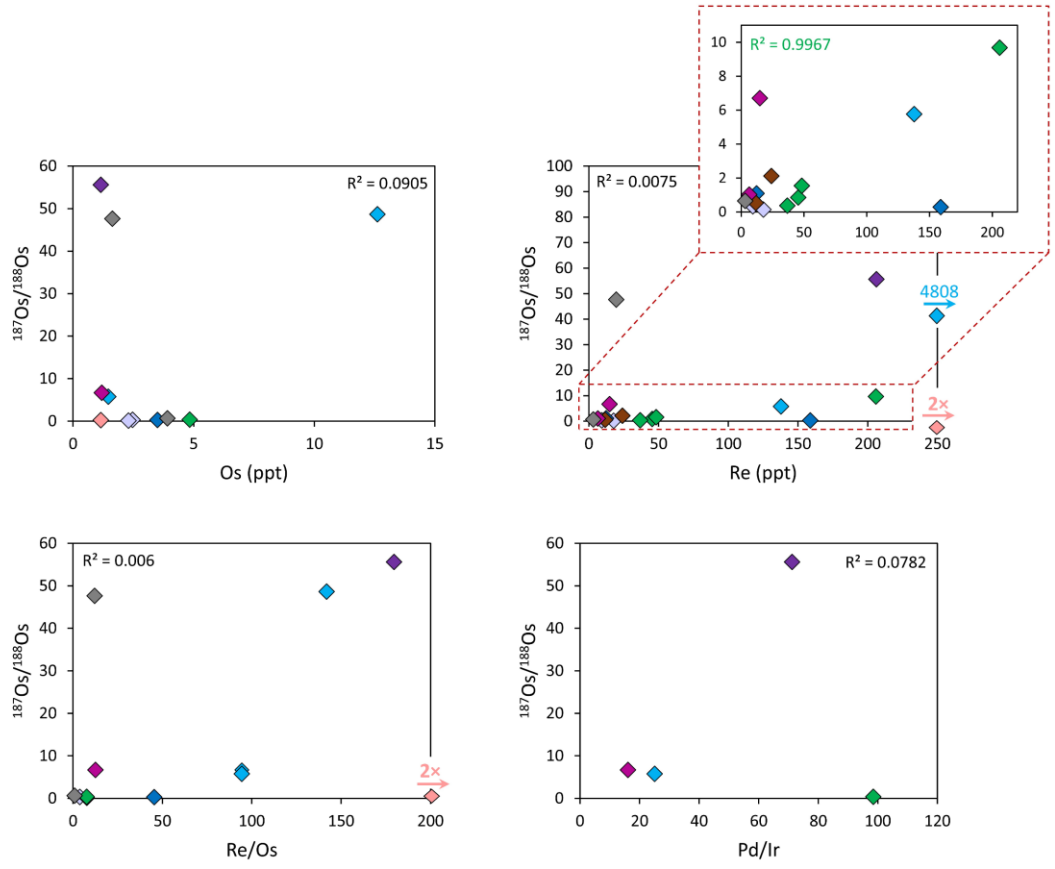

Figure 6.5 **Measured $^{187}Os/^{188}Os$ versus Re, Os, Re/Os and Pd/Ir. Errors are smaller than the symbols.**

6.1.3. Base metal sulphides (BMS)

Base metal sulphides (BMS) are a common accessory phase in carbonatites (*c.f.* Table 2.1 and Table 6.1). They represent from 0.02% up to 2% of the carbonatite modal abundance. These percentages reflect estimates based on surface areas of selected carbonatite thin sections (samples 19780, 19781, BM.2000,P11(22) and 16462). The number of BMS present in all carbonatite samples from this study are given in Table 6.1 together with their composition, habit, size, distribution within the sample, condition and mineral phases they are found to be associated with. Pyrite and pyrrhotite are the most common BMS found in carbonatites, though sphalerite can also be found included in pyrite (*c.f.* Table 10.11). The composition of the BMS is based on elemental analyses, thus it cannot be excluded that some of the pyrite might be marcasite. Most BMS in carbonatites from this study are present as interstitial grains or pseudo-inclusions (*c.f*. Table 6.1), though some samples only have included BMS (*e.g.* 91/62 – C4 and 91/60 – C5). Figure 6.6 shows back-scattered electron images of BMS from samples 19780, 19781 and 16462. While BMS from sample 16462 are large (up to 4000 µm) and mostly unaltered, BMS from 19780 and 19781 are much smaller (100-200 µm and 20-30 µm, respectively) and strongly altered (*c.f.* Figure 6.6).

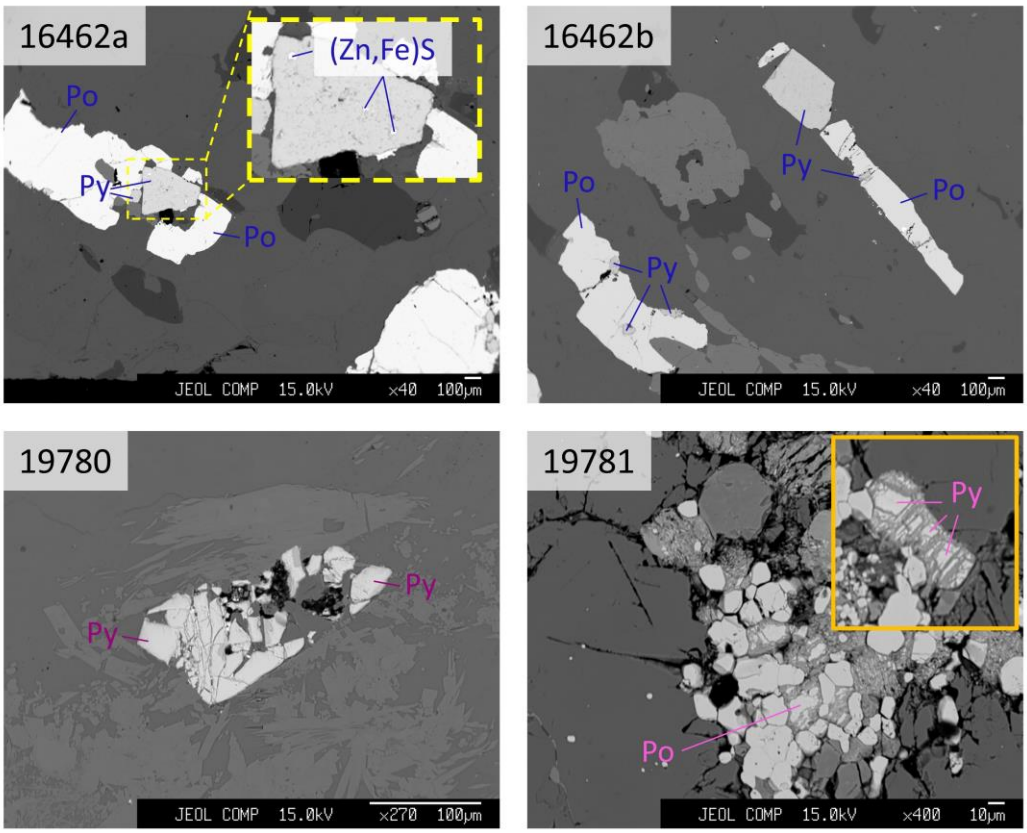

Figure 6.6 **Back-scattered electron images of BMS from Fen (top row) and Grønnedal-Ika (bottom row). Py = pyrite, po = pyrrhotite.**

Table 6.1 **Base metal sulphide petrography of samples relevant for highly siderophile element and Re-Os chemistry. Pi: pseudo-inclusions, i: inclusions, is: interstitial; Samples analysed by microprobe show mineral compositions (py: pyrite, po: pyrrhotite, sph: sphalerite), while samples characterised by reflected light microscopy were only identified as either homogeneous (ho, single BMS phase) or heterogeneous (he, multiphase BMS) grains.**

Sample name	#	Type	Composition	Habit	Size range (µm)	Distribution in thin section	Condition	Associated with
LI 23/02/08	12	pi; is	ho	rounded; tabular; irregular	<100	random	altered	carbonate, phlogopite
BM.2004.P9(9)	>30	i; (pi)	ho	rounded; irregular	10-20	random	altered	carbonate, (Fe-oxide)
J1-C1	3	is	ho	elongated; subrounded	300-6000	random	Porous texture, fractured, smaller grains fresher	carbonate, apatite
91/66 - C2	21	is	ho	elongated; angular	300-3000	locally oriented	relatively fresh, slightly fractured	carbonate, apatite
91/62 - C4	16	i	ho	equant; elongated	200	Only in one Fe-oxide	very altered, fractured, porous texture	Fe-oxides
91/60 - C5	2	i	ho	rounded	10	random	relatively fresh	carbonate
BM.1998,P18(44)	>30	is; pi	he	elongated; irregular; equant	300-1800	random	first type: strongly altered, porous texture, second type: relatively fresh, irregular grains	carbonate, apatite, phlogopite
BM.1998,P18(183)	19	is	he	striated; irregular; elongated	50-2000	random	partly fresh, small fractures, partly altered, porous texture	carbonate
BM.1998,P18(229)	>30	is; pi	ho	subhedral; elongated; striated	100-1500	even	Porous texture, some fresh, some altered	carbonate, apatite, pyrochlore,

Table 6.1 (continued)

Sample name	#	Type	Composition	Habit	Size range (µm)	Distribution in thin section	Condition	Associated with
BM.2000,P11(22)	10	pi; i	ho	striated; irregular; elongated	50-400	random, more and larger in apa-ol-rich section	Slightly altered, rarely stretch marks	carbonate, apatite, olivine, Fe-oxides
BM.2000,P14(24)	14	is; i	he	elongated; irregular	50-2500	random, oriented	fractured textures,	phlogopite, carbonate
4808	>30	pi; is	he	elongated; angular;	2000-4000	random	altered, fractured, partly porous texture,	carbonate
16462	10	is	po, py, sph	po: elongated, py: equant; irregular	up to 4000	random	po: relatively fresh, py: porous texture	carbonate, apatite
19780	10	i; is	py	rounded; angular; subhedral	100-200	random	fractured	carbonate, amphibole
19781	2	is	po, py	tabular	20-30	random	strongly altered	Fe-oxides, carbonate, apatite
Oldoinyo Lengai	>30	is	ho	irregular	10-600	even	altered, porous texture	unknown

6.2. Discussion

6.2.1. BMS as hosts of HSEs in carbonatites

Highly siderophile elements exhibit chalcophile behaviour in Earth's upper mantle (*e.g.* Mitchell and Keays, 1981) and thus base metal sulphides (BMS) are thought to control the whole-rock HSE budget (*e.g.* Luguet and Reisberg, 2016 and references therein). However, HSE are not exclusively chalcophile as they can exhibit siderophile behaviour in *i.e.* platinum group minerals (PGM, Luguet et al., 2007, 2003; Peregoedova et al., 2004; O'Driscoll and González-Jiménez, 2016). Nevertheless, other phases such as silicates and oxides (1.7% to ~33% in carbonatites excl. BM.2004,P9(9), Table 4.1) can additionally minorly contribute to the HSE budget (*e.g.* Burton et al., 1999; Mitchell and Keays, 1981). The modal abundance of base metal sulphides in four samples (BM.2000,P11(22), 19780, 19781 and 16462) was used together with the corresponding whole-rock highly siderophile element abundances to calculate the concentrations of HSEs in their BMS assemblages, assuming that the BMS account for ~100% of the HSEs. To simplify calculations, it was assumed that BMS also account for all the Re, although Re could additionally be hosted by other phases, *i.e.* silicates (*e.g.* Burton et al., 1999) in carbonatites. The results are given in the appendix (Table 10.37) and Figure 6.7. Results were compared to BMS from gabbros and gabbroic eclogites (Dale et al., 2009), because there is no HSE data available for BMS of carbonatites. As was shown in Chapter 5, carbonatites were likely affected by several post-magmatic processes, thus carbonatites needed to be compared to rocks with equally low HSE abundances that were also affected by post-emplacement processes (in this case subduction metamorphism, Dale et al., 2009).

The mass balance calculations from the appendix (Table 10.35) mostly match the concentration ranges for pyrite, pyrrhotite and pentlandite in gabbros and gabbroic eclogites given by Dale et al. (2009) (Figure 6.7). Compared to the published data (Os: 1 to 204 ppb, Dale et al., 2009) the calculated Os concentrations (100 ppt to 1.9 ppb) are lower. They are below the BMS fields for sample 16462 (100 ppt), BM.2000,P11(22) (600 ppt) and 19780 (600 ppt) and at the lower boundary of pyrite for 19781 (1.9 ppb). In contrast, Ir is at the lower end of the range of pyrite (1 to 192 ppb, Dale et al., 2009) for sample 16462 (2.2 ppb), and within the pentlandite (4 to 23 ppb, Dale et al., 2009) and pyrite range for sample 19780 (5.6 ppb). Ruthenium is variable (1.5 to 102 ppb) for the samples from this study and falls within range of BMS (3 to <524 ppb) from Dale et al. (2009) for samples from Grønnedal-Ika (10 and 102 ppb) but below the range for samples 16462 (2.4 ppb) and BM.2000,P11(22) (1.5 ppb). For Pt both samples from Grønnedal-Ika (20.8 and 21.9 ppb) are within the range of

pyrite (4 to 167 ppb, Dale et al., 2009), while the sample from Kovdor (2.3 ppb) is closer to pyrrhotite (<2 to 6 ppb, Dale et al., 2009). Palladium concentrations are within the range of pyrrhotite (15 to 67 ppb, Dale et al., 2009) for samples BM.2000,P11(22) (29.1 ppb) and 16462 (56.3 ppb), and slightly higher for sample 19780 (90.2 ppb). In contrast, Pd is strongly enriched and resembling pentlandite concentrations (226 ppb to 1.98 ppm) for sample 19781 (1.56 ppm). Pd-enrichment can a feature of pentlandite (Dale et al., 2009) or could also be caused by platinum group minerals (*e.g.* O'Driscoll and González-Jiménez, 2016). Unfortunately, no pentlandite or PGMs were identified in any of the studied samples, though PGMs usually occur in micro-sizes (*e.g.* 1 to 5 µm, Luguet et al., 2007) difficult to identify by optical examination. A study by Rudashevsky et al. (2004) on BMS in the Kovdor carbonatite found Pt- (*e.g.* isoferroplatinum, Table 10.1) and Pd-rich PGMs (*e.g.* mertieite, Table 10.1), showing that PGMs can be present in carbonatites. Rhenium concentrations in BMS from Dale et al. (2009) range from 2 and 41 ppb. Samples 16462 (8.1 ppb), 19780 (7.8 ppb) and 19781 (32 ppb) fall within that range of Re, but BM.2000,P11(22) is far lower (<450 ppt) than BMS from Dale et al. (2009).

Rudashevsky et al. (2004) described pyrrhotite as the major BMS found in Kovdor carbonatites and the pattern of sample BM.2000,P11(22) does agree with pyrrhotite concentrations (Dale et al., 2009) for Pt and Pd, however not for Ru and Re, which are too low. For sample 16462 the CI-chondrite normalised HSE pattern resembles that of pyrrhotite for Pt, Pd and Re, but is closer to pyrite for Ir and Ru. Microprobe analyses of sample 16462 showed that most BMS in this sample are either pyrrhotite or pyrite (*c.f.* Table 10.11), matching the observed pattern if not taking into account Os. Mismatch between carbonatitic BMS patterns and BMS of gabbros and gabbroic eclogites can have several reasons; For instance, it should be considered that BMS could be of secondary origin (*i.e.* hydrothermal), leading to different fractionation of the HSEs (dependent on *i.e.* the composition of the hydrothermal fluid) compared to primary BMS. Metasomatism could further lead to enrichment and/or depletion of HSEs, which depends on the degree of S-saturation of the percolating melt/fluid as well as the melt/rock ratio (*e.g.* Ackerman et al., 2009; Alard et al., 2000; Harvey et al., 2015). Additionally, other phases such as PGMs could contribute to the HSE budget, though, PGMs are rare and are usually found in *i.e.* rocks stripped by BMS (*e.g.* Luguet et al., 2007). Thus, it remains questionable whether or to which extent PGMs contribute to the HSE budgets in carbonatites. Nonetheless, close match of the calculated HSE concentrations in carbonatitic BMS to the concentrations of BMS from gabbros and

gabbroic eclogites suggest that BMS could be the main hosts for HSEs in carbonatites and thus whole-rock results should be representative of BMS.

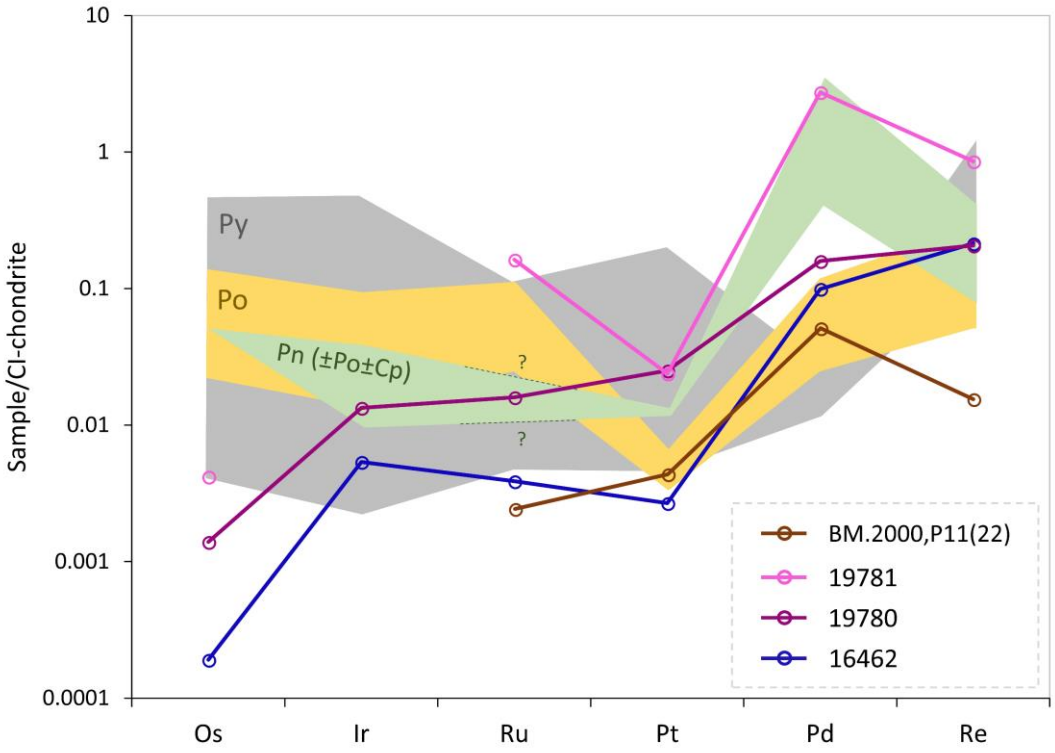

Figure 6.7 **Calculated CI-chondrite normalised (Fischer-Gödde et al., 2010; Horan et al., 2003) highly siderophile element patterns for base metal sulphide assemblages of two samples from Grønnedal-Ika (19781 and 19780) one sample from Kovdor (BM.2000,P11(22)) and one sample from Fen (16462). The concentrations were calculated by estimating the modal abundance of base metal sulphides in whole-rock samples and using the whole-rock highly siderophile element abundances (Table 10.35). Fields for pyrite (py), pyrrhotite (po) and pentlandite (pn) ±pyrrhotite ±chalcopyrite (cp) are from Dale et al. (2009). Ru for the pn ±po ±cp field below detection limit, Ir and Pt were connected, and Ru is thus not representative.**

6.2.2. Conditions of BMS evolution

Pyrite (or marcasite) and pyrrhotite are the major BMS in carbonatites (*c.f.* Table 10.11). Pyrite is often associated with hydrothermal activity (*e.g.* Murowchick and Barnes, 1986; Reich et al., 2013) but can also be of magmatic origin (*e.g.* Cafagna and Jugo, 2016), while marcasite is thought to precipitate from low temperature acidic aqueous solutions (*e.g.* Allen et al., 1914, 1912; Murowchick and Barnes, 1986). Pyrite and pyrrhotite together with the presence of magnetite and/or hematite as well as emplacement temperatures of the carbonatite bodies were plotted in Figure 6.8 to determine the sulphur (fS_2) and oxygen fugacity (fO_2). The approximate conditions in which BMS in samples from this study have formed can be seen in Table 6.2. The stability fields of pyrite, pyrrhotite, magnetite and hematite in a log(fS_2) versus log(fO_2) plot vary with temperature (*c.f.* Figure 6.8, Mitchell and

Krouse, 1975). Where a large temperature range for single localities was given, two temperatures were plotted as end-members (Figure 6.8; Fen, Oka and Jacupiranga). Evaluation of Figure 6.8 yields log(fS_2) values between -13 and 1 and between ΔFMQ -1 and +3 for log(fO_2) as conditions in which BMS in carbonatites have formed. For fO_2, this is within the range or slightly more oxidising (*e.g.* Jacupiranga, Kovdor and Fen at ΔFMQ+3) of the upper mantle fO_2 (ΔFMQ±2) as was derived from spinel peridotites (*e.g.* McCammon and Kopylova, 2004; Frost and McCammon, 2008 and references therein). In the review on the redox state of Earth's mantle, Frost and McCammon (2008) describe that shifts to more oxidising conditions can be caused by either a long residence time in the lithosphere, close relation to subduction zones or can be caused by *i.e.* metasomatism (McCammon et al., 2001). More reducing conditions are thought to indicate that samples are linked to the asthenosphere. Using the estimates from Figure 6.8 we obtain a log(fO_2) for Oka carbonatites ranging between -27 and -23 (ΔFMQ +1) for a temperature of 450°C. For a temperature of 700°C, which is at the upper end of the temperature range given in Table 6.2, log(fO_2) is at around -15 (= FMQ), which agrees with estimates of oxygen fugacity of Oka carbonatites from Friel and Ulmer (1974). Rudashevsky et al. (2004) suggest that pyrrhotite and PGMs found in Kovdor carbonatites have crystallised at high temperatures (1190°C, Skinner et al., 1976) from a S-rich fluid which separated from the carbonatitic melt. This is based on microprobe analyses and textural relationships between BMS and carbonate phases, *i.e.* BMS pockets in carbonate-rich areas of the thin section and BMS inclusions in calcite. The high crystallisation temperature would suggest that log(fS_2) and log(fO_2) obtained from Figure 6.8 were underestimated for crystallisation of pyrrhotite. Pyrite accompanied by magnetite at Kovdor crystallised at a later stage, partly replacing pyrrhotite (Rudashevsky et al., 2004) suggesting that log(fS_2) and log(fO_2) conditions (Figure 6.8 and Table 6.2) for those two mineral phases could still be representative. Pyrrhotite to pyrite/marcasite transformation has been experimentally shown under hydrothermal conditions (up to 220°C) by Qian et al. (2011) and has also been described during low temperature (<200°C) hydrothermal alteration of primary pyrrhotite-pentlandite-chalcopyrite to pyrite-millerite-chalcopyrite on the example of the Grasvalley-Norite-Pyroxenite-Anorthosite member from the Bushweld Complex, South Africa (Holwell et al., 2017). Additionally, re-equilibration of BMS can occur down to <200°C during cooling (Craig and Kullerud, 1969; Gitlin, 1985; Kullerud, 1970).

This raises the question whether carbonatitic BMS represent the stage of formation or rather of later re-equilibration. Extent of re-equilibration or whether emplacement temperatures given for the carbonatites are representative of BMS crystallisation remains unclear.

Table 6.2 **Ranges for log(fO_2) and log(fS_2) for carbonatites of different localities defined by Figure 6.8 (Mitchell and Krouse, 1975) using published emplacement temperatures (T) and petrography of the samples. Po: pyrrhotite, py: pyrite, Mt: magnetite. ΔFMQ calculations are based on Myers and Eugster (1983).**

Locality	logfO_2	logfS_2	T (°C)	Petrography	References
Oldoinyo Lengai	ΔFMQ -1 to +2	-6 to -5	491-519	po + Mt	Krafft and Keller, 1989; Mattsson et al., 2018
Jacupiranga	ΔFMQ +1 to +3	-5 to 1	446-692	py + po + Mt	Gomide et al., 2013; Haynes et al., 2003
Oka	ΔFMQ +1 to FMQ	-8 to 1	443-771	py + Mt	Haynes et al., 2003; Mitchell and Krouse, 1975 and references therein
Kovdor	ΔFMQ +1 to +3	-5 to -4	452-651	po + py + Mt	Ivanyuk et al., 2017; Rudashevsky et al., 2004
Fen	ΔFMQ +1 to FMQ	-13 to -8	280-380	po + py + Mt	Jennings and Mitchell, 1969
	ΔFMQ +3	-2 to 0	600-700		Friedrichsen, 1968

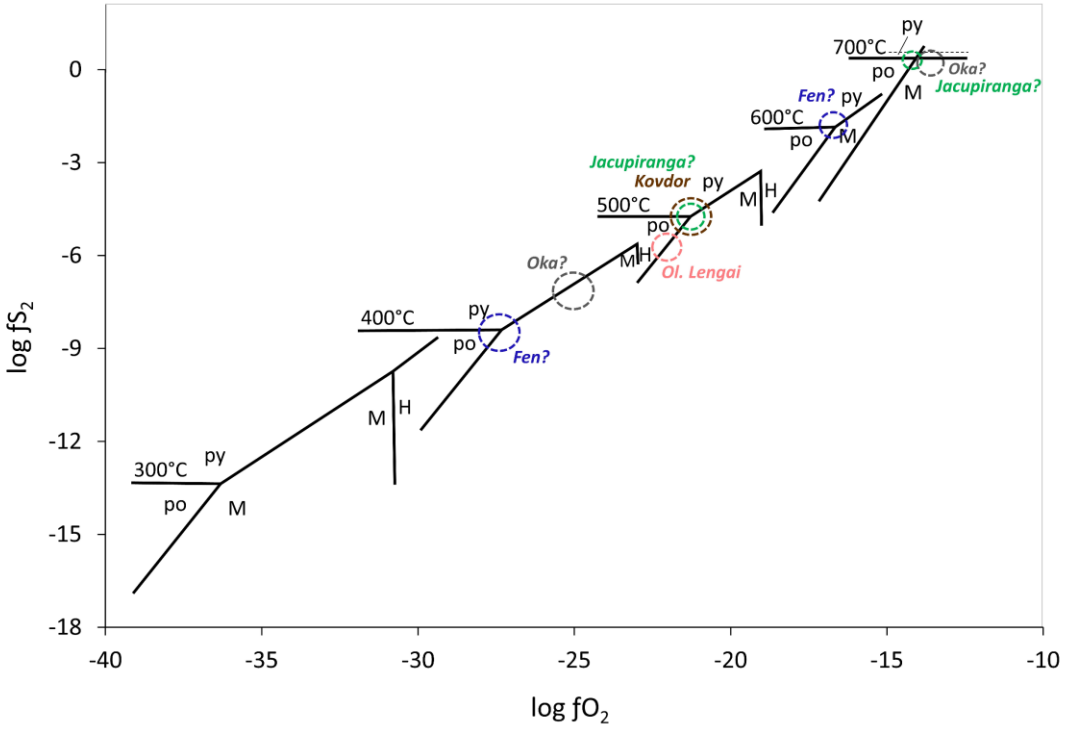

Figure 6.8 **log(fS_2) versus log(fO_2) for different temperature ranges showing the relative stability fields of pyrite (py), pyrrhotite (po), magnetite (M) and hematite (H) (Mitchell and Krouse, 1975). Coloured dashed circles represent the estimated position of samples from Oldoinyo Lengai, Jacupiranga, Oka, Kovdor and Fen based on their mineral assemblages and estimated temperatures (*c.f.* Table 6.2). Two areas are given for Fen, Oka and Jacupirana, as there are two different temperature ranges given for the emplacement of those carbonatites (Friedrichsen, 1968; Gomide et al., 2013; Haynes et al., 2003; Jennings and Mitchell, 1969; Mitchell and Krouse, 1975).**

6.2.3. Implications from HSE abundances and Re-Os isotope systematics on carbonatite evolution

There is currently no study that has focussed on both highly siderophile element and Re-Os isotope signatures in carbonatites. One study by Cheng et al. (2003) addresses PGE abundances in carbonatites from the Maoniuping REE deposit. However, their PGE concentrations are one to three orders of magnitude higher than observed for carbonatites from this study. Cheng et al. (2003) did not undertake Re-Os isotope measurements and they interpret the high PGE abundances as being due to the metasomatic interaction of primary magnesiocarbonatites with harzburgite in the upper mantle. In contrast a study by Escrig et al. (2005) analysed Re-Os isotopes of two carbonatite samples from Fogo (Cape Verde) for the purpose of excluding them as potential contaminants of Fogo basalts. A similar study was carried out on two carbonatites from Fuerteventura (Widom et al., 1999) but PGE abundances were not measured. Nevertheless, both Re-Os studies found that $^{187}Os/^{188}Os$ signatures of carbonatites are radiogenic ($^{187}Os/^{188}Os_m$ 0.1924 to 0.6138) combined with low Os concentrations (4.7 to 22.9 ppt), which is also observed in carbonatites from this study. Except for sample 91/60 - C5 (Os_N/Ir_N = 2.66), all samples show a depletion of Os relative to Ir (Os_N/Ir_N = 0.04 to 0.61). A substantial depletion in Os concentrations could be explained by 1) Os was removed by a process that did not affect Ir to create Os_N/Ir_N <1 (Chondrite Os/Ir = 1.07, Fischer-Gödde et al., 2010; PUM Os_N/Ir_N.= 1.04, Becker et al., 2006), 2) Ir was added by a process that did not affect Os, or 3) the use of an imperfectly matching spike for carbonatites together with very low abundances in HSEs has perturbed the results and created a mismatch between Os and the other HSEs that is of analytical nature. On the other hand, for many samples Ir is below detection limit, and thus it is unclear whether the low Os_N/Ir_N ratios are truly a common feature of carbonatites.

The often unrealistic (>Earth) T_{MA} model ages and their disagreement with published ages (*c.f.* Chapter 6.1.2) combined with unrealistic and inconsistent initial $^{187}Os/^{188}Os$, as well as no clear correlation between the HSEs (*c.f.* Figure 6.2), HSEs vs. CaO, and measured $^{187}Os/^{188}Os$ vs. HSEs, indicates that there has been disturbance of both Re-Os isotopes and the HSE abundances.

Mavrogenes and O'Neill (1999) investigated the solubility of sulphide in mafic magmas by examining their dependency on pressure, temperature and oxygen fugacity. They found that sulphur contents at sulphide saturation (SCSS) decrease exponentially with pressure, while the temperature effect is small and SCSS insensitive to fO_2. Thus, melts at higher depths are

S-saturated and potentially evolve into S-undersaturated melts during ascent. Hence, in order to arrive at the surface saturated in S and to precipitate BMS, the melt would either need to assimilate S during ascent or be driven to S-saturation by fractional crystallisation of silicate phases. If carbonatites have formed at great depths in Earth's mantle, they will have reached S-undersaturation on their way towards the surface and are thus prone to re-equilibrate with the surrounding mantle and carry mixed signatures of the mantle column. Jorgenson (2017) addresses sulphur solubility of carbonatites and found that carbonatites show one order of magnitude higher sulphur solubility compared to silicate melts (Liu et al., 2007) at pressures of 1 and 2 GPa. Thus, they are theoretically more likely to dissolve S present in the mantle column and inherit the HSE and Re-Os signatures of the mantle they percolated. Though, if carbonatites are S-saturated at their source and retain S-saturation during ascent, BMS with the signature of the source might crystallise from a sulphur-rich melt that exsolves from the carbonatite melt (*e.g.* Guzmics et al., 2012). Alternatively, Day (2013, and references therein) describes the process of crystal-liquid fractionation involving the segregation of sulphides. In this model it is proposed that a S-undersaturated melt that reaches S-saturation by crystal fractionation will then start segregating a sulphide liquid with low Re/Os ratios, leaving behind a residual melt with high Re/Os ratios and low compatible HSE abundances. One genesis model of carbonatites (*c.f.* Chapter 1.2) involves fractional crystallisation as main mechanism creating carbonatitic melts (*e.g.* Gittins, 1989; Gittins and Jago, 1998; Watkinson and Wyllie, 1971; Weidendorfer et al., 2016). Thus, if carbonatites have evolved by fractional crystallisation (*c.f.* Table 1.1), high Re/Os ratios and low compatible HSE abundances could theoretically originate from this process. However, if Re-Os isotopic signatures and HSE abundances observed in carbonatites were derived from this fractional crystallisation process, then the melt must have either resided in the mantle long enough or Re/Os ratios must have been high enough to produce the extremely radiogenic $^{187}Os/^{188}Os$ signatures observed in some samples in this study. For example, it would take ~3.7 Ga to produce the initial $^{187}Os/^{188}Os$ ratio of sample 4808 (42.6) when using the corresponding measured $^{187}Re/^{188}Os$ ratio of 671 (*c.f.* Table 10.35). Alternatively, if we assume 10 Ma as residence time of the carbonatite melt in the mantle, the $^{187}Re/^{188}Os$ ratio would need to be as high as ~260,000 to produce the initial $^{187}Os/^{188}Os$ of sample 4808. Jones et al. (2013) argue that due to the high infiltration rates of carbonatites (Hammouda and Laporte, 2000), carbonatites should have short residence times in the mantle, which is thought to prevent strong chemical interaction (Dalou et al., 2009). Short residence times would contradict the hypothesis of a long-lived carbonatite melt in the mantle.

Alternatively, carbonatites could have sampled a high Re/Os metasomatic reservoir, relative to chondritic compositions (*e.g.* Escrig et al., 2005 and for lamprophyres Gan and Huang 2017). Peucker-Ehrenbrink et al. (2012) reported Re/Os ratios of oceanic crust that could be as high as 30,000. Osmium concentrations in oceanic crust vary between 0.4 and 276 ppt, with an average value of 27 ppt (Peucker-Ehrenbrink et al., 2012). MORB glasses, yield similarly low Os concentrations ranging from 0.18 to 140 ppt and high $^{187}Re/^{188}Os$ ratios (30 to ~8000, Gannoun et al., 2007). If oceanic crust with high Re/Os and low Os concentrations was subducted and recycled in the mantle, there could be a long-lived high Re/Os metasomatic reservoir in the mantle (*e.g.* Gan and Huang, 2017) developing radiogenic Os signatures, which could have been sampled by *e.g.* S-undersaturated carbonatitic magmas. Such a long-lived high Re/Os reservoir as a source of carbonatitic melts was suggested by Polák et al. (2016) for carbonatites from Sevattur, India. However, if the melts are derived from or chemically modified by such a source region, there should be a consistent signature within each outcrop. Instead, carbonatites from one locality differ strongly in their Re-Os isotopic signatures (*c.f.* chapter 6.1.2). Also, there are samples for which age-corrections result in negative values, indicating that the Re/Os ratio is too high for the given $^{187}Os/^{188}Os$ signature (*c.f.* appendix Table 10.35), which taken together with the arguments above suggests open system behaviour. However, it remains unclear which processes have led to the signatures observed in carbonatites.

As already described in chapter 5.2, Lu-Hf isotope systematics have been influenced by processes such as metamorphism (*e.g.* Tupertalik, Larsen and Rex, 1992) and/or post-magmatic/hydrothermal alteration, also leading to open system behaviour. These processes could have resulted in depletion and re-enrichment events (*e.g.* Hf loss and/or Lu addition) that could have also influenced the Re-Os isotope system as well as HSE abundances. Differences in isotopic signatures within one locality and between carbonate and non-carbonate fractions for Lu-Hf isotopes were explained by either magmatic differentiation (*e.g.* Le Bas, 1981), different sources in the mantle (*i.e.* sampling of xenocrysts) and/or local post-magmatic overprinting. Effects of magmatic differentiation would only become evident for samples from Jacupiranga, as each sample represents one emplacement sequence (J1-C1: calciocarbonatite from sequence C1, sample 91/66 - C2: magnesiocarbonatite from sequence C2, 91/62 - C4: calciocarbonatite from sequence C4 and 91/60 - C5: magnesiocarbonatite from sequence C5, *c.f.* Chapter 1.1). Magnesiocarbonatites from Jacupiranga have less radiogenic $^{187}Os/^{188}Os$ (0.8569 and 0.3705) than the calciocarbonatites (9.69 and 1.54), but there is no systematic when considering the order of emplacement (C1,

C2, C4, C5). It remains unclear as to the cause of less radiogenic $^{187}Os/^{188}Os$ ratios of magnesiocarbonatites from Jacupiranga, as this cannot be observed for *i.e.* the magnesiocarbonatite from Tupertalik (GGU 252874), which is highly radiogenic ($^{187}Os/^{188}Os$: 47.64). There is also no systematic in HSE abundances when considering the order of emplacement sequences for Jacupiranga carbonatites. This suggests that magmatic differentiation is not responsible for observed $^{187}Os/^{188}Os$ signatures and HSE abundances. Thus, the most likely scenario for explaining the observed extreme and variable Re-Os isotope signatures is post-magmatic alteration or crustal contamination. Contamination by oceanic crust has shown to result in high Re/Os and $^{187}Os/^{188}Os$ signatures as was observed in OIBs (*e.g.* Reisberg et al., 1993). Crustal contamination effects are for example quantified by using $^{187}Os/^{188}Os$ isotopes combined with lithophile isotope systems such as Rb-Sr or Sm-Nd (*e.g.* Day, 2013). However, Sr and Nd concentrations in carbonatites are high (Sr: ~900 to 27,000 ppm, Nd: ~15 to 2840 ppm, *c.f.* Table 10.23 and Table 10.26) and thus insensitive to contamination by crustal material (*i.e*. continental crust Sr: 330 ppm, Nd: 27 ppm, Wedepohl, 1995 and references therein). Thus, it is difficult to quantify to which extent crustal assimilation contributed to Re-Os isotope systematics and HSE abundances for samples from this study. Though for example, a study by Lee et al. (2006) found that there was no crustal contamination detected in the Kovdor carbonatite complex. However, Kovdor samples show high $^{187}Os/^{188}Os$ ratios, suggesting that crustal contamination is probably not responsible for the observed $^{187}Os/^{188}Os$ isotope signatures and HSE abundances.

A study by Xiong and Wood (1999) found that oxidising fluids can efficiently mobilise Re at high temperatures, high salinity and low sulphur contents and precipitate them when, *e.g.* mixed with fluids containing reduced S. Mobility of Re has also been suggested during subduction metamorphism (*e.g.* Dale et al., 2007) or hydrothermal overprinting (*e.g.* Walker et al., 1989; Marcantonio et al., 1993b, 1993a). Nevertheless, not only Re can be mobilised but also Os was found to become mobile in hydrothermal environments (*e.g.* under amphibolite facies conditions, Walker et al., 1989; in hydrothermal fluids, Marcantonio et al., 1993a; or mobile as Na-(Os)-rich complex, Barkov et al., 2008). Thus, the observed Re/Os ratios as well as Re-Os isotope systematics could be due to overprinting by hydrothermal fluids. Additionally, a lot of BMS from this study have porous textures (*c.f.* Table 6.1), which was also observed in hydrothermal BMS (*e.g.* Wohlgemuth-Ueberwasser et al., 2015). Sphalerite, which was found included in pyrite in sample 16462 (*c.f.* Figure 6.6), is typically associated to hydrothermal activity (*e.g.* Barnes, 1997) and would suggest that both, pyrite and sphalerite, are of hydrothermal and not of magmatic origin.

Base metal sulphides in carbonatites from this study can mostly be found as interstitial grains or pseudo-inclusions and are only rarely found as inclusions (*e.g.* 91/62 – C4, 91/60 – C5 and 19780). Sample BM.2000,P11(22) has BMS which are either included or pseudo-included in other mineral phases and the $^{187}Os/^{188}Os$ signature of that sample is less radiogenic (0.5383) than for the other Kovdor sample (2.119), which additionally has interstitial BMS (*c.f.* Table 6.1 and Figure 6.4). This can also be observed for the two calciocarbonatites from Jacupiranga, where sample 91/62 – C4 with included BMS is less radiogenic ($^{187}Os/^{188}Os$: 1.54) than J1-C1 ($^{187}Os/^{188}Os$: 9.689) with only interstitial BMS. For magnesiocarbonatites from Jacupiranga, sample 91/60 – C5 with included BMS is also less radiogenic ($^{187}Os/^{188}Os$: 0.3705) than the second sample 91/66 – C2 with only interstitial BMS ($^{187}Os/^{188}Os$: 0.8569). Carbonate is often the phase containing included BMS and in the lithophile element isotope study (*c.f.* Chapter 5), carbonate phases are thought to be more affected (*e.g.* recrystallised) by post-magmatic alteration than the non-carbonate phases (*e.g.* magnetite, apatite, phlogopite). Thus, although samples with included BMS appear to be less radiogenic than those with interstitial grains, the type of occurrence of BMS (inclusion, pseudo-inclusion or interstitial) is not necessarily an indicator of the degree of overprinting.

Carbonatites have very low HSE abundances, with Os being the least abundant of the HSEs. Hence, only minor modification by *i.e.* mobilisation of HSEs can disturb the Re-Os isotope systematics and can additionally lead to fractionation of the HSEs (*cf*. Day, 2013). Nevertheless, CI-chondrite normalised HSE patterns of carbonatites show the typical melt-like pattern. Therefore, overprinting must have either yielded similar HSE fractionation as that observed during melting, or the disturbance was so minor that it only influenced the Re-Os isotopes and not the other HSE abundances. Young carbonatites (*e.g.* Oldoinyo Lengai and Fogo) as well as some older carbonatites (*e.g.* from Jacupiranga and Sokli) show radiogenic signatures that are not too far from enriched mantle sources such as HIMU ($^{187}Os/^{188}Os$ = 0.15, Hanyu et al., 2011). These signatures might be realistic, but this does not exclude that those carbonatites might still show mixed signatures of the mantle column and/or signatures caused by different extents of post-magmatic alteration or contamination. Hence, source information cannot be reliably obtained from Re-Os isotopes or HSE abundance; at least not from the whole-rock results from samples presented in this study.

6.3. Conclusions

As was already shown in Chapter 5, carbonatites have experienced a complex petrological history. The study on highly siderophile elements and Re-Os isotope systematics has led to the following conclusions:

- Base metal sulphides are likely the main host for highly siderophile elements in carbonatites. However, this needs to be confirmed by analysing single BMS grains.
- BMS from carbonatites in this study are mostly found as interstitial grains or pseudo-inclusions. The most common phases are pyrrhotite and pyrite of which the latter can be of mantle- and/or hydrothermal origin.
- The conditions of BMS formation in carbonatites from this study range from log(fS_2) of -13 to 1 and log(fO_2) ΔFMQ -1 to +3. However, it remains unclear whether they are representative of carbonatite formation or rather of late stage re-equilibration.
- Whole-rock highly siderophile element abundances range from <0.9 to 12.6 ppt Os, <1 to 38 ppt Ir, <23.2 to 84.8 ppt Ru, <12.7 ppt to 8.9 ppb Pt, <120.9 ppt to 4.9 ppb Pd and 3.2 ppt to 10 ppb Re; yielding a typical melt-like CI-chondrite normalised pattern with a positive slope from Os to Re (Re_N/Os_N = 10 - 105,000).
- Whole-rock Re-Os isotope systematics show open system behaviour:
    - $^{187}Os/^{188}Os_m$ signatures are highly variable and range from close to PUM and enriched mantle values of 0.1636 to highly radiogenic values of 55.6 with Re/Os ratios varying from 0.82 to 8800 showing no systematic variation with age or tectonic setting.
    - Age corrected $^{187}Os/^{188}Os$ ratios are either negative or remain radiogenic and are highly variable within one locality.
    - T_{MA} model ages do not match the published ages and are often implausible (>Earth).
- It cannot be excluded that the high Re/Os ratios and low HSE abundances observed in carbonatites originate from either fractional crystallisation processes and/or a high Re/Os source in the mantle. However, observed highly radiogenic $^{187}Os/^{188}Os$ ratios and implausible T_{MA} model ages cannot be explained by either of the two. Thus, the HSE abundances and Re-Os isotope systematics of carbonatites from this study must have either been contaminated during ascent and/or overprinted by post-magmatic alteration events (*e.g.* hydrothermal activity)
- The nature of the processes overprinting carbonatites remains unknown and cannot be determined from whole-rock measurements.

Chapter 7 : Case study – The Fen complex

The global lithophile element isotope study, HSE abundances and $^{187}Os/^{188}Os$ isotope study of carbonatites provide an overview on processes affecting carbonatites and have also addressed possible source information that can be obtained. The Fen case study aims to address the source and petrogenesis of the Fen complex by combining field evidence with a Lu-Hf, Sm-Nd and Rb-Sr isotope study on whole-rock, carbonate, non-carbonate and single mineral fractions and by combining this information with HSE abundances and a $^{187}Os/^{188}Os$ isotope study on whole-rock carbonatites.

7.1. Introduction to the Fen complex

The Fen complex is part of the *Gea Norvegica Geopark* and is located near the village Ulefoss, close to the late Palaeozoic alkaline Oslo Rift in the Nome municipality, Telemark in Norway. It lies adjacent to the shores of lake Norsjø and covers an area of 4.5 km². The Fen complex consists of alkaline rocks and carbonatites, with the latter making up almost 60% of the surface area of the complex (Andersen, 1987). The emplacement of the complex is thought to be related to the opening of the Proto-Atlantic and subsequent extensional tectonic activity (Dahlgren, 1994). It was at Fen where the term "carbonatite" was first introduced by Brøgger and Goldschmidt (1918) and published by Brøgger (1921) when discovering that the Fen limestone was of magmatic origin. This gave rise to a controversy caused by Bowen's counter-thesis which suggested that the carbonates in Fen are metasomatic, re-melted and recrystallized carbonates rather than magmatic carbonates (Bowen, 1924). The whole alkaline complex intrudes Precambrian Telemark gneisses (Lie and Østergaard, 2011) and carbonatite emplacement occurred at 539±14 Ma determined by Andersen and Taylor (1988) using whole-rock Pb-Pb chronology. Brøgger (1921) suggested that the origin of the Fen complex started with violent explosive volcanism creating a vent that was infilled by the magmatic assemblage now found in the Fen complex. This theory was based on the shape of the complex as well as comparison to the nearby diatreme that produced the porphyritic "Sannaite" (Brøgger, 1921). The Fen complex consists of several types of carbonatite including søvite (calcite carbonatite), rauhaugite (dolomite carbonatite), ankerite carbonatite and silicocarbonatite. The alkaline and ultramafic rocks are melteigite, ijolite, urtite, fenite, vipetoite, hollaite, phonolite and damtjernite (also damkjernite). Alteration of ankerite carbonatite has produced a rock type known as rødberg (=redrock), which was mined for iron from 1652 to 1927 (Andersen, 1984; Brøgger, 1921). The sequence of emplacement and formation of the rocks in the Fen complex is thought to be as follows:

1. Ijolite-melteigite; 2. Søvite 3. Rauhaugite 4. Damtjernite; 5. Ankerite carbonatites; and 6. Rødberg (Griffin and Taylor, 1975).

7.2. Collaboration with Telemark Fylkeskommune

The field work in the Fen carbonatite complex in Norway involved a collaboration with Sven Dahlgren, who is the regional geologist for Telemark Fylkeskommune (Telemark County Municipality). This collaboration included an organised tour around Fen's geology, a presentation on the complex, and sampling in the Tufte tunnel, Cappelen quarry and melteigite type-locality.

7.3. Outcrop descriptions

During the field work, 14 outcrops were visited (*c.f.* Figure 7.1 and Table 7.1). The outcrops included the most common geological sequences of the Fen complex such as the carbonatites but also the associated alkaline silicate rocks and the fenite aureole surrounding the complex. Short outcrop descriptions based on the field notes and personal communication by Sven Dahlgren are given in this chapter.

Table 7.1 **GPS coordinates of outcrops visited during the field trip. Coordinates are given in WGS84 coordinate system. Waypoint numbers were allocated by the GPS device.**

Waypoint #	Outcrop name	Latitude	Longitude
26	Holla church ruin	59.270987	9.273884
27	Naturminne Melteigite	59.263712	9.270117
28	Fenite	59.258314	9.262097
29	Cappelen quarry	59.281938	9.285629
30	Deformed Søvite dike	59.282292	9.289068
31	Entrance Tufte tunnel	59.280835	9.278285
32	Søvite quarry	59.281831	9.283165
33	Rødberg near mines	59.276753	9.301991
34	Ankeritised Damtjernite	59.269063	9.299477
35	Weathered Rauhaugite	59.26699	9.301015
36	Silicocarbonatite	59.278577	9.271461
37	Phonolite dikes	59.303109	9.258026
38	Sannaite 1	59.254276	9.252549
39	Sannaite 2	59.254493	9.252282
42	Melteigite	59.256213	9.271755

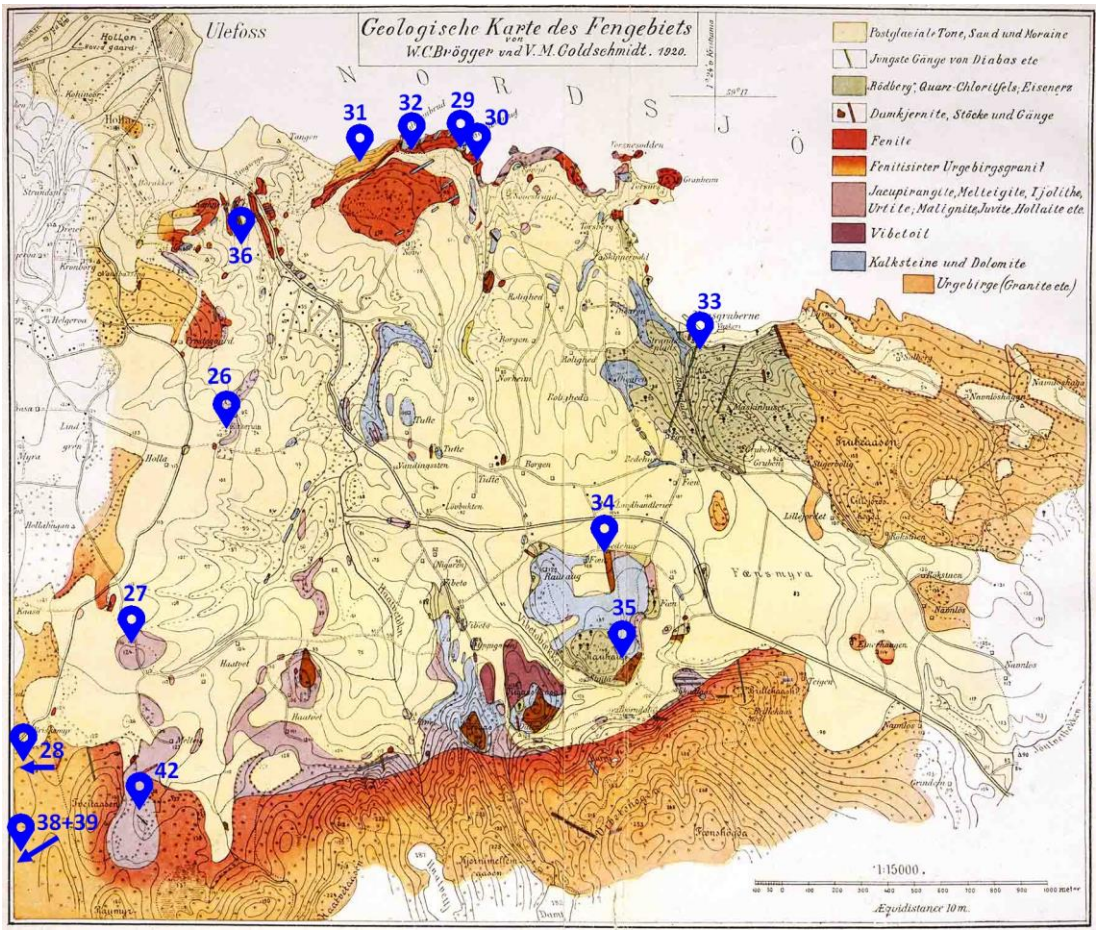

Figure 7.1 Geological map of the Fen complex (Brøgger, 1921) showing the GPS waypoints and corresponding numbers for each outcrop. Legend entries translated from German from top to bottom: 1. Postglacial clay, sand and moraine; 2. Youngest dikes of diabas etc.; 3. "Rødberg", quartz-chlorite bedrock; Iron ore,; 4. Damtjernite, sills and dikes; 5. Fenite; 6. Fenitised bedrock granite; 7. Jacupirangite, melteigite, ijolite, urtite, malignite, juvite, hollaite etc.; 8. Vibetoite; 9. Limestone and dolomite; 10. Bedrock (granite etc.).

7.3.1. WP26. Holla church ruin – An overview

The Holla church ruin dates back to the 12th century and uses local rocks in its walls. The window and doorways are made of Fen søvite. The position of this ruin provides an overview over the Fen complex:

Figure 7.2 View of the Fen complex towards NNE; yellow: Fen complex, red: Fen iron mines, blue: late Carboniferous to Cretaceous basalts, and purple: Proterozoic plutons from the Oslo rift.

It is clear from Figure 7.2 that geological exposures of the complex are rare. The actual volcanic edifice of the Fen volcano is not visible anymore due to erosion in the late Precambrian (estimated 2 km erosion per 30 Ma, personal communication Sven Dahlgren). Furthermore, the complex is now covered by a thick deposit of Holocene post-glacial clay. General uplift in the region caused by the retreating ice-shield has resulted in further erosion and material deposition from the surrounding hills into the valley (Brøgger, 1921; personal communication Sven Dahlgren and Gea Norvegica Geopark: http://www.geoparken.com).

7.3.2. WP27. Naturminne melteigite

The relatively small (ca. 5x2 m) *Naturminne* located near the Melteig farm consists mainly of melteigite, which is an intrusive rock that is part of the ijolite series. Melteigite comprises pyroxene and nepheline, with pyroxene being the dominant phase (60% to 90%, mindat.org). At this locality large nepheline veins (ca. 10 cm wide) can be found.

7.3.3. WP28. Fenite

The fenite surrounds the Fen complex like an aureole (*c.f.* Figure 7.1). Fenite is named after the Fen complex (Brøgger, 1921; Elliott et al., 2018) and is the product of reaction between highly alkaline fluids/carbonatite melts and bedrock. In Fen it shows a green-blue tinge caused by aegirine and arfvedsonite. Within a few cm, the bedrock gneiss can be strongly fenitised (blue) to less fenitised (light coloured, *c.f.* Figure 7.3). The outcrop visited lies at the southern border of the Fen complex and fluids released during melteigite and ijolite emplacement are responsible for the fenitisation here (*c.f.* Figure 7.1; personal communication Sven Dahlgren). Additional to the fenite, fragments of fenite breccias and

younger phonolite dikes can be seen (*c.f.* Figure 7.3) crosscutting the older fenites. The breccias contain bedrock gneiss and phonolite fragments in an aegirine-augite matrix. Phonolites within the fenite zones have been altered, made visible by the presence of albite as consequence of Na-mobilisation during the fenitisation process (personal communication Sven Dahlgren).

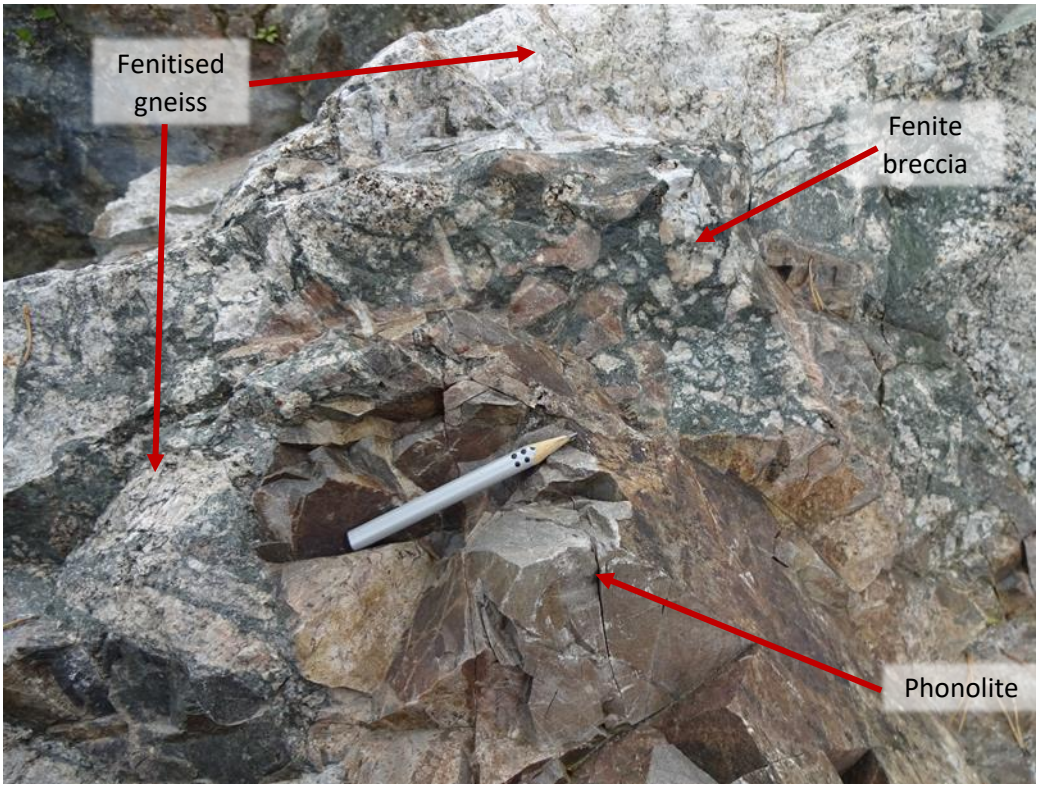

Figure 7.3 **Fenitised gneiss fragment including phonolite dike and fenite breccia within a centimetre scale.**

7.3.4. WP29. Cappelen quarry

The Cappelen quarry is the type locality for søvite which was named by Brøgger and Goldschmidt after the nearby Søve farm in 1918. Brøgger and Goldschmidt further discovered that carbonatites are igneous at this quarry. It was mined for Niobium (Mitchell, 2015) in the 1950s and was later extended into an underground mine (Tufte) where it was mined until 1965 (Gea Norvegica Geopark: http://www.geoparken.com). Carbonatite at the Cappelen quarry is present as large dikes that crosscut fenitised ijolite/melteigite (*c.f.* Figure 7.4). The dikes contain bedrock xenoliths, which was one of the observations used by Brøgger and Goldschmidt to classify the carbonate rocks as igneous (personal communication Sven Dahlgren; Brøgger and Goldschmidt, 1918). The main mineralogy of the søvite consists of calcite, magnetite, amphibole, apatite, base metal sulphides and pyrochlore, of which

pyrochlore is the Nb-bearing phase. Geiger counter measurements of the fenite (0.3 µS/h), søvite (0.5 µS/h) and hydrothermal veins (2 µS/h) show stronger radioactive decay in the hydrothermal veins, caused by enrichment in Th (mobile XRF: 550 ppm Th). Samples CQW-1 and CQW-2 were collected from large loose blocks at the western end of this locality (outside the sampling restrictions). The samples were chosen and sampled away from ankerite and hydrothermal veins, which tend to have a large altering influence on the søvites. CQW-1 is a phlogopite-bearing søvite and is likely to be fresher and more representative of a sparsely affected carbonatite compared to the amphibole-bearing sample CQW-2.

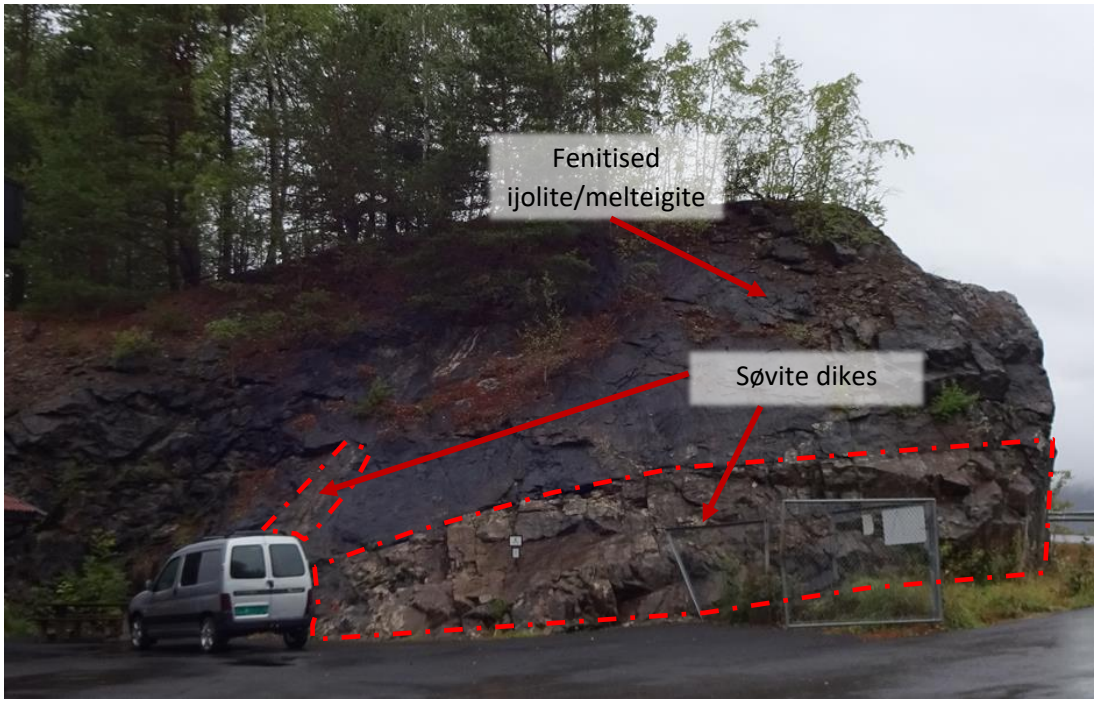

Figure 7.4 Naturminne Cappelen quarry with light coloured søvite dikes (red dashed line) crosscutting blueish fenitised ijolite/melteigite.

7.3.5. WP30. Deformed søvite dike

Just a few hundred metres southeast from Cappelen quarry, at the shore of lake Norsjø, is a deformed carbonatite dike that has intruded the ultramafic Damtjernite. Damtjernite is an ultramafic lamprophyre associated with diatreme volcanism (*e.g.* Brøgger, 1921; Dahlgren, 1994). At this outcrop carbonatite and damtjernite magmatism alternate, visible as carbonatite dikes crosscutting damtjernite and damtjernite dikes crosscutting the carbonatites (*c.f.* Figure 7.5).

Figure 7.5 Alternating magmatic events between damtjernite (black) and carbonatite melts (white). Left: deformed carbonatite dike crosscutting damtjernite, right: horizontal damtjernite dike crosscutting the deformed carbonatite. Handlense for scale.

The deformation is unlikely to be tectonic but rather is thought to be associated with emplacement of the magma. The emplacement of both melts is thought to be genetically linked and because the damtjernite crosscuts an already deformed carbonatite, it is thought that the deformation is the product of previous injection of the carbonatite melt into the damtjernite ("toothpaste injection"). Additionally, an ankerite breccia – similar to the fenite breccia – can be found "injected" into a fenite-carbonatite assemblage (*c.f.* Figure 7.6). It is thought that the carbonatite dike found here is related to the dikes in Cappelen quarry (personal communication Sven Dahlgren).

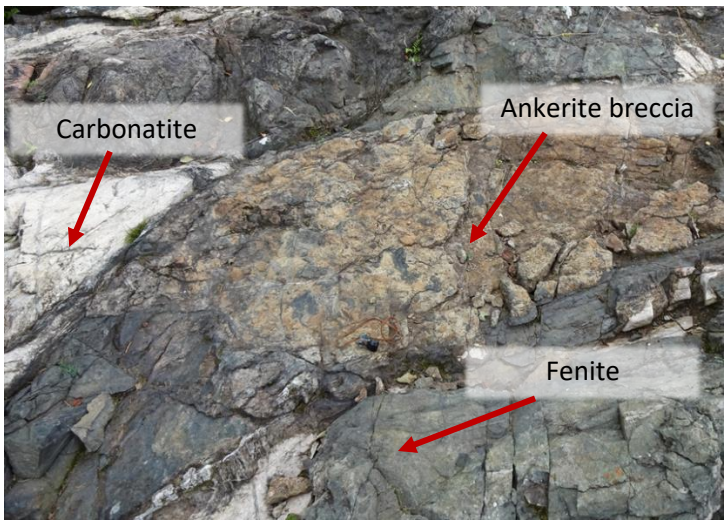

Figure 7.6 Assemblage of carbonatite, damtjernite and ankerite breccia. Handlense for scale.

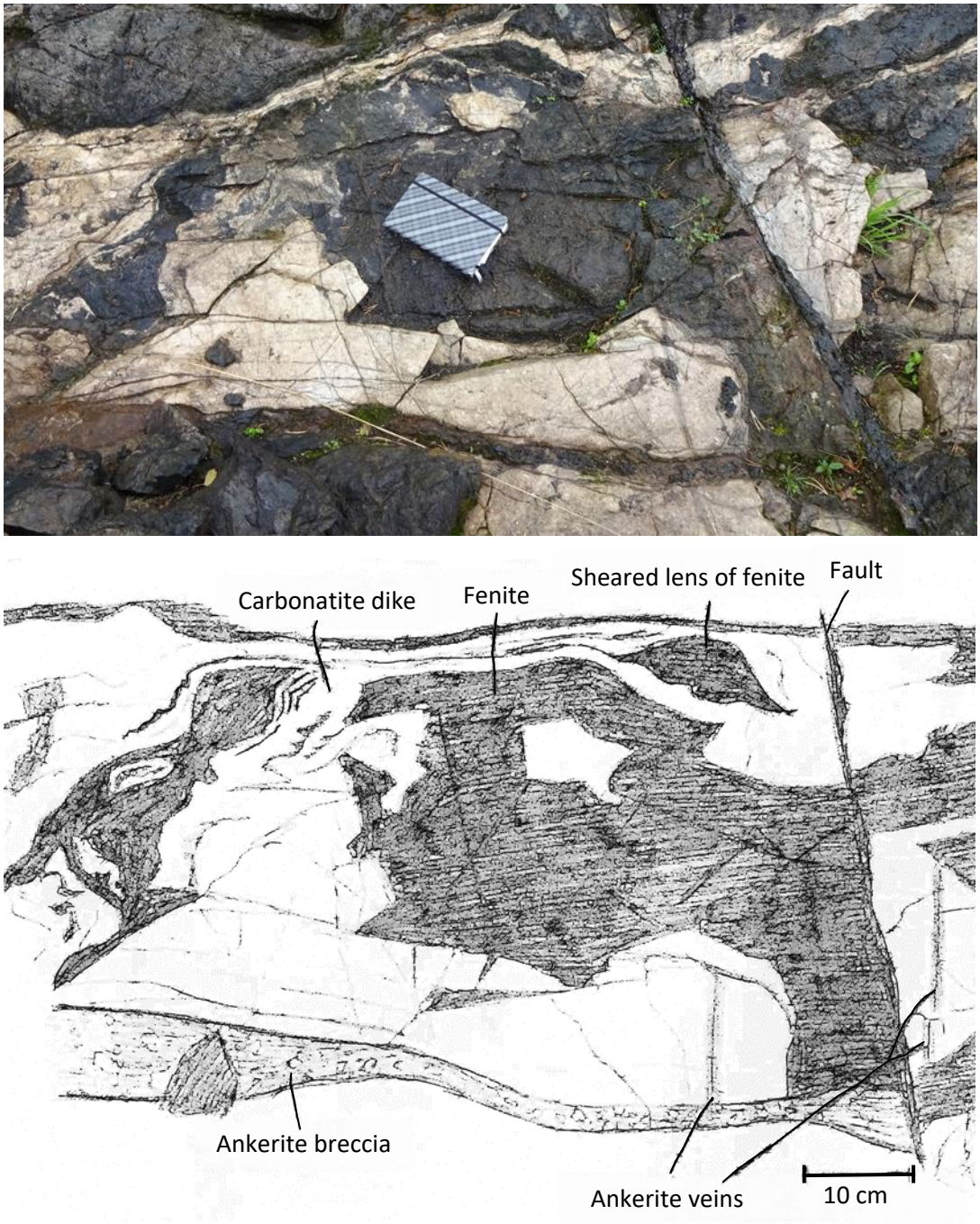

Figure 7.7 **Top: Photo of deformed carbonatite dike in fenite; bottom: matching sketch pointing out carbonatite, fenite, sheared fenite lens, ankerite breccia and veins and a fault.**

7.3.6. WP31. Entrance Tufte tunnel

The entrance to the mining tunnel belonging to Cappelen quarry mentioned in chapter 7.3.4 lies at this location. The company Norsk Hydro started investigations to mine the carbonatite dike "Hydro dike" *(c.f.* Figure 7.8 left) for phosphate for use in the production of fertiliser during the second world war. However, the carbonatite was eventually mainly mined for Niobium (Gea Norvegica Geopark: http://www.geoparken.com).

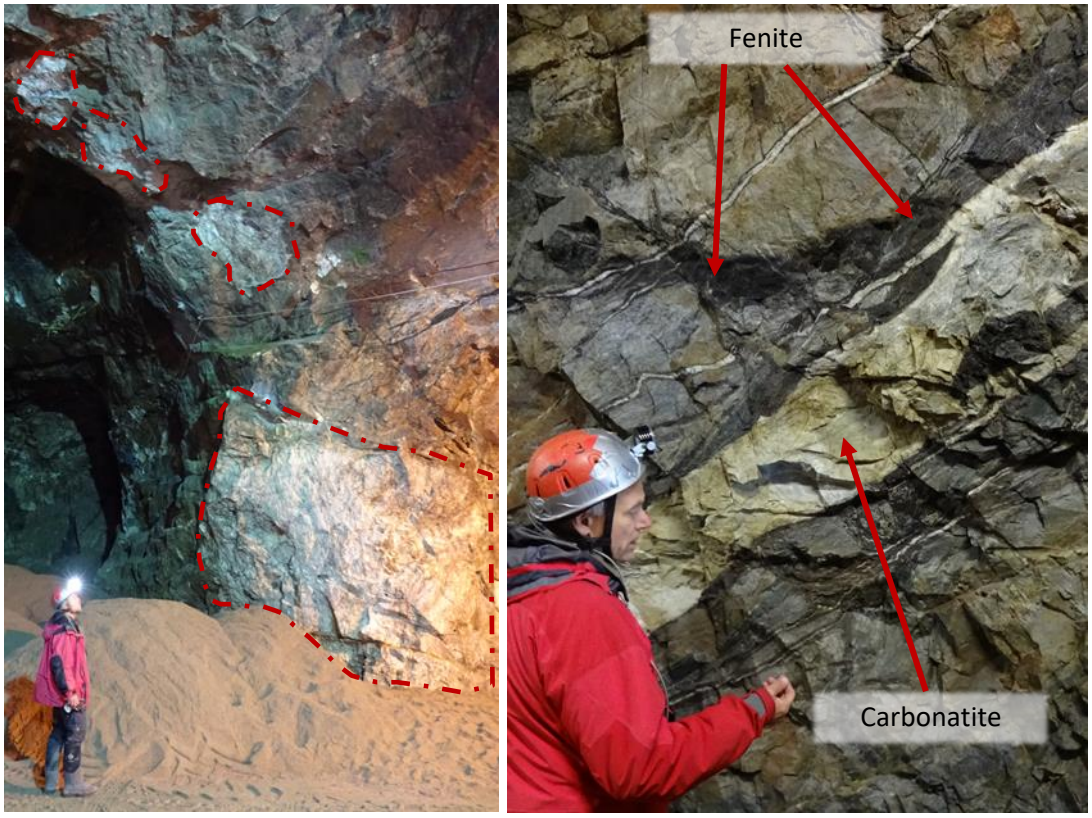

Figure 7.8 **Insights from the transport tunnel/Tufte, left: Hydro dike søvite (red dashed lines), right: søvite dike (white) with cm-scale fenitisation (black) visible at the immediate contact of carbonatite and gneiss.**

The transport tunnel for the former mine is still intact – though closed for the general public – and the Telemark County Municipality, under instruction of regional geologist Sven Dahlgren, decided to clean the tunnel walls to expose further outcrops for Scientific research. The cleaning exposed a lot of dikes and textures, such as small scale fenitisation (*c.f.* Figure 7.8 right), fenitised granite-gneiss showing albitisation, phonolite dikes, rødberg, ankeritic veins, a large sulphide vein and carbonatite dikes of different compositions (dolomitic, ankeritic and calcitic). The small scale fenitisation is due to carbonatite emplacement, while the large scale fenitisation is a result of ijolite emplacement (personal communication Sven Dahlgren; Brøgger, 1921). Samples were taken from the freshest søvite dike (THY = Hydro

dike), a dolomite carbonatite dike on the east side 51.5 m into the tunnel (TS 51.5 m E), an ankerite carbonatite on the east side 498 m into the tunnel (TS 498 E) and from an about 1 m wide sulphide vein on the west side 531 m into the tunnel (TS 531 W). For the sulphide vein it is unclear whether it is related to the carbonatite emplacement or the later Oslo rift. A more altered carbonatite body further inside the tunnel is thought to be of the same origin as sample 4808 (global study).

7.3.7. WP32. Søvite quarry

Next to the Entrance of the Tufte tunnel lies an old quarry that contains an artificially cleaned outcrop showing a carbonatite dike crosscutting fenite that contains fragments of ijolite and melteigite. The outcrop has experienced strong alteration visible in strongly altered veins as well as chlorite and muscovite crystallisation.

Figure 7.9 Small exposure of a carbonatite dike in fenite in the old Søvite quarry.

7.3.8. WP33. Rødberg near mines

This outcrop lies along the main road and can be found close to the nearby iron mines. The rock mined for is rødberg (=redrock). Andersen (1986) describes the composition of rødberg as hematite-calcite-dolomite carbonatite. It is thought that rødberg is a product of extensive ankerite carbonatite alteration caused by groundwater-derived hydrothermal fluids; During this process immobile phases such as Fe and Th as well as further insoluble phases are enriched by dissolving the carbonate and other soluble phases (Andersen, 1984). This enrichment becomes detectable when using a Geiger counter on the various stages of altered rock; while the ankerite carbonatite detects 1.5 µS/h, the more hematised ankerite

carbonatite shows 3.6-4.5 µS/h and deep red rødberg 9-14 µS/h. This is mainly due to the enrichment of the Th by selective dissolution as described above.

7.3.9. WP34. Ankeritised damtjernite

Near the road is an exposure of damtjernite containing phlogopite, calcite, apatite, magnetite, Cr-spinel, perovskite, olivine and clinopyroxenes. The phlogopite is present as large crystals and megacrysts together with mantle xenoliths (personal communication Sven Dahlgren). The damtjernite furthermore shows ankeritic alteration, visible as ankerite veins, which suggests that the damtjernite is older than the carbonatite emplacements in Fen. Gravimetric measurements yielded a heavy gravimetric anomaly below the Fen complex; It is suggested that this anomaly is due to the presence of damtjernite (Ramberg, 1973).

7.3.10. WP35. Weathered rauhaugite

At this outcrop an Fe-dolomite carbonatite called rauhaugite is exposed. Rauhaugite is prone to substantial alteration, which is visible as a 20 cm thick weathering horizon of soil on top of the outcrop. Furthermore, the outcrop is strongly fractured and shows a thin red film of iron-oxide on the usually beige dolomite carbonatite. Red iron-rich veins in between dolomite crystals also show strong oxidation. The alteration observed is thought to be responsible for density loss of rauhaugite (personal communication Sven Dahlgren).

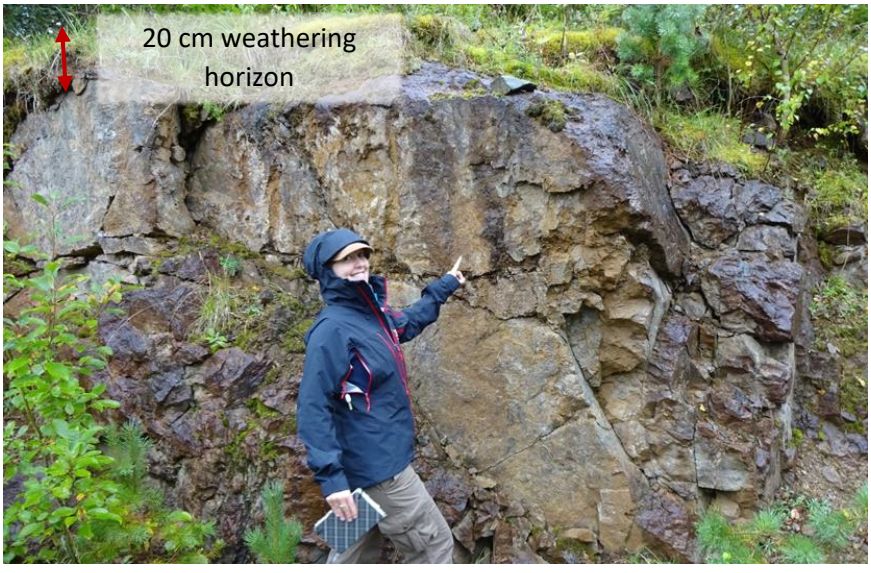

Figure 7.10 **Characteristic red colour of a weathered rauhaugite with iron-oxide coating.**

7.3.11. WP36. Silicocarbonatite

This outcrop of silicocarbonatite is very small (2x2 m) and can be found near the town hall greenspace in Ulefoss. It is not well exposed and covered in bushes. The surface is weathered and due to restriction, hammering to expose a fresh surface is not permitted. The occurrence of silicocarbonatite is minor compared to the other types of carbonatites found in Fen, however, it is thought that the silicocarbonatite is texturally and mineralogically related to the ijolite-melteigite series (Brøgger, 1921).

7.3.12. WP37. Phonolite dikes

Outside the actual area of the Fen complex and thus not visible on the map (Figure 7.1) there are a number of phonolite and damtjernite dikes as well as several smaller carbonatite dikes that crosscut the bedrock granite gneiss. The phonolite dikes have large K-feldspar and altered nepheline phenocrysts and show a 5 cm chilled margin towards the gneiss. The carbonatite dikes, however, are only 3-4 cm thick, seldom thicker, and very weathered. Damtjernite dikes reach a thickness of up to 50 cm. Nearby there is a thicker carbonatite dike with a damtjernite core (*c.f.* Figure 7.11).

Figure 7.11 **Left: small, strongly weathered carbonatite dike (red dashed line) in bedrock gneiss; right: larger carbonatite dike (red dashed line) with damtjernite core (orange dashed line) in bedrock gneiss.**

7.3.13. WP38+39. Sannaite

The sannaite is part of a larger diatreme body. The exposure is poor due to vegetation and the dimensions of the diatreme can only be mapped using magnetic anomalies (personal communication S. Dahlgren). Sannaite is a porphyritic igneous rock (Brøgger, 1921) that contains gneissic xenoliths, and Ti-amphibole and phlogopite xenocrysts of up to 5 cm (*c.f.* Figure 7.12).

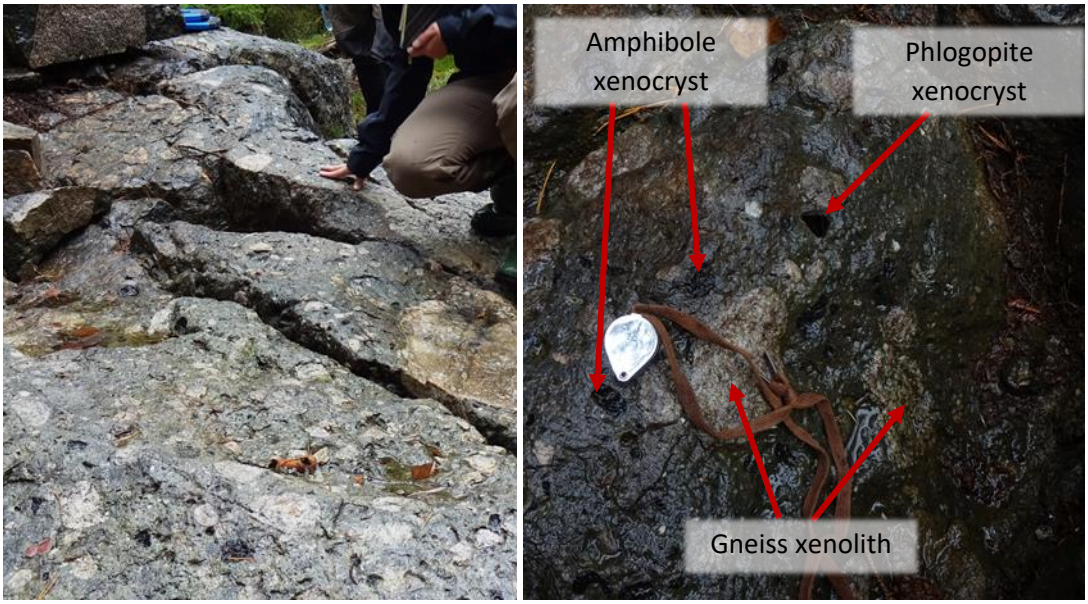

Figure 7.12 Left: Fractured sannaite outcrop with clearly visible light-coloured gneiss xenoliths; right: Sannaite showing amphibole and phlogopite xenocrysts and gneiss xenoliths.

7.3.14. WP42. Melteigite

This locality near the Melteig family farm is the type locality for melteigite. However, urtite and ijolite are also present. Melteigite, urtite and ijolite show different modal abundances of nepheline and pyroxene (Urtite: 70-90% nepheline; ijolite: 50% nepheline; melteigite: 30% nepheline, Bergstøl and Svinndal, 1960), but all belong to the same group of pyroxene-nepheline rocks. Outcrops and loose sample material are very heterogeneous showing cumulate and pegmatitic structures (*c.f.* Figure 7.13) of nepheline and pyroxene (aegirine-augite) and minor amounts of biotite. Urtite, ijolite and melteigite are often associated and can be found alternating on a cm scale (*c.f.* Figure 7.13). This makes it difficult to choose a representative sample. However, in the southern part of the melteigite complex, samples appear to be less altered (fresh grey nepheline) and more homogeneous. Sample MTGS (ijolite) was thus sampled from this area and was taken from a loose block that appeared to be homogeneous and showed no cumulate textures.

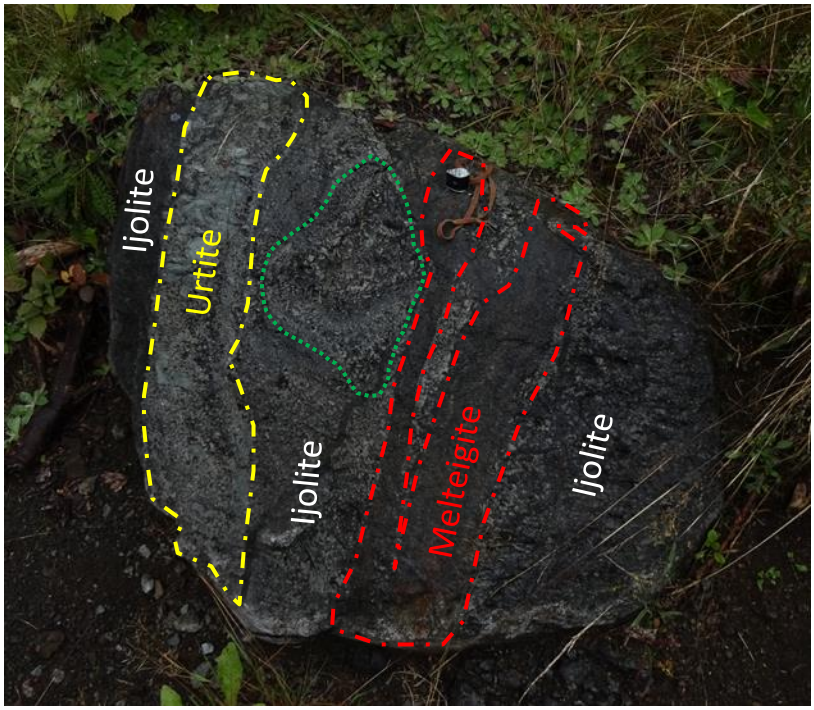

Figure 7.13 **Large boulder showing the heterogeneity of the ijolite series at the melteigite type locality. Within a few centimetres ijolite (white), urtite (yellow) and melteigite (red) alternate. The green dashed line further highlights a pegmatitic sequence within the ijolite.**

7.4. Results

7.4.1. Trace elements for whole-rock, carbonate, non-carbonate and mineral fractions

REE element patterns of whole-rock, carbonate, non-carbonate fractions and mineral separates

The same LREE enrichment (primitive mantle normalised) observed for carbonatites from the global study (*c.f.* Figure 4.4), can be seen for samples from Fen (Figure 7.14). Light rare earth elements are enriched in all fractions (*e.g.* La: 50 to 2000 ppm = 30 to 2000 times primitive mantle), but less enriched for HREE (*e.g.* Lu: 0.06 to 1.36 ppm = 0.6 to 11 times primitive mantle). Sample replicates are highly reproducible, with the exception of the non-carbonate fraction of THY, where the replicate analysis is slightly lower in concentration for the LREE (*e.g.* La: 1500 versus 830 ppm) and slightly higher for the HREE (*e.g.* Lu: 0.27 versus 0.45 ppm).

The whole-rock REE patterns of the case study are all similar to one another, except for sample TS 498 E, which is similar in the LREE concentration but lower in concentration from Sm to Lu (*e.g.* Sm: ~11 ppm versus ~30 ppm and Yb: 0.4 ppm versus ~3-4 ppm) resulting in a steeper slope. Furthermore, whole-rock samples show a positive Nd-anomaly and sample CQW-1 additionally shows a positive Pr anomaly.

The REE pattern of the carbonate fraction mimics the whole-rock pattern but does not show the anomalies in Pr and Nd as distinctly as the whole-rock samples. For the non-carbonate fraction the LREE are more variable (*e.g.* La, one order of magnitude) than for whole-rock or carbonate fractions. In general, the non-carbonate fractions show higher concentrations of REE (*e.g.* La: 100 to 2000 ppm) compared to the carbonate (*e.g.* La: 50 to 124 ppm) and whole-rock fractions (*e.g.* La: 60 to 106 ppm).

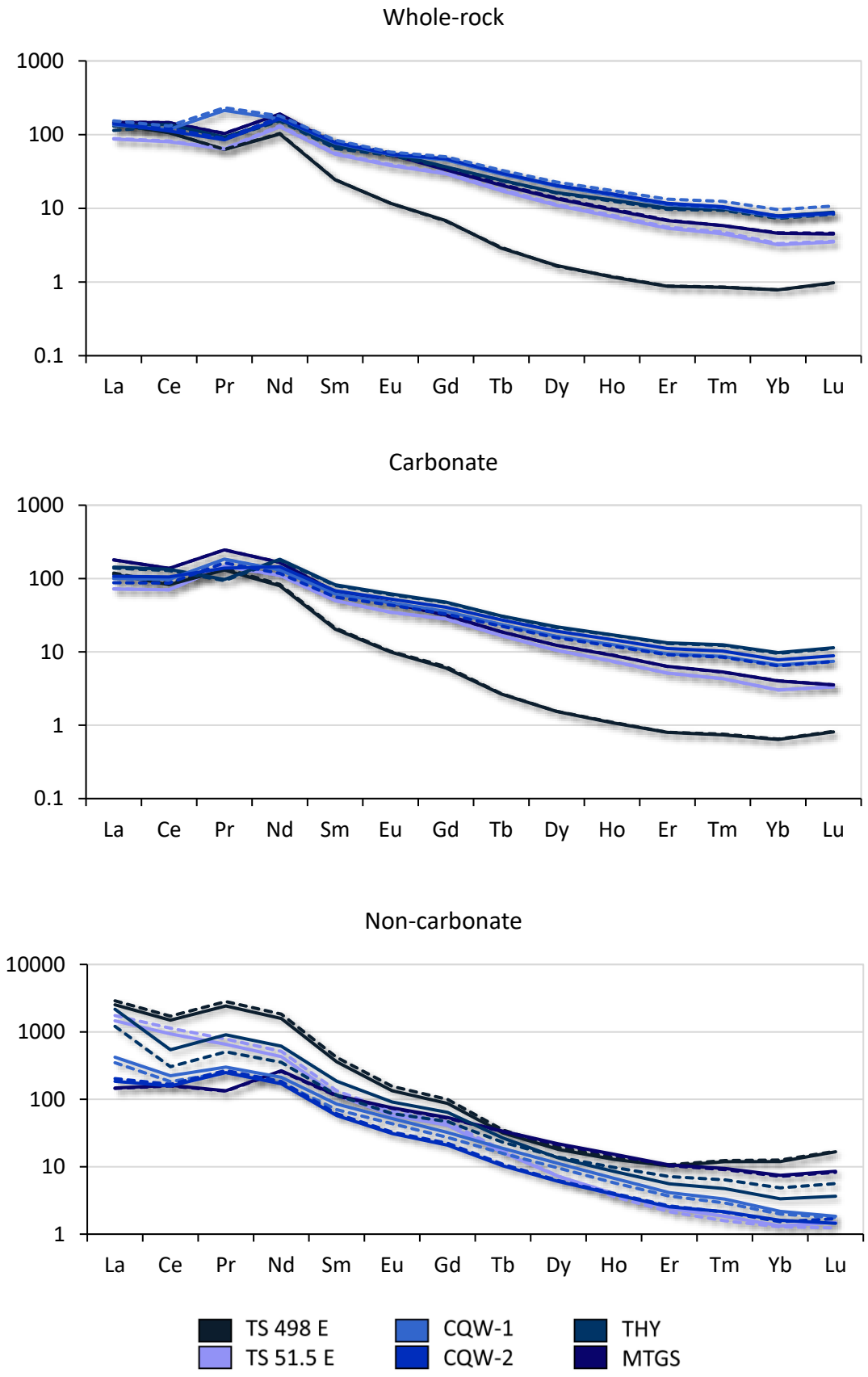

Figure 7.14 **Rare earth element patterns of whole-rock (top), carbonate (centre) and non-carbonate fractions (bottom) from Fen, Norway normalised to primitive mantle (Sun and McDonough, 1989). Dashed and dotted lines represent replicates of the same sample.**

The primitive mantle normalised REE patterns for mineral separates are similar to the patterns of whole-rock and carbonate fractions. Calcite shows very similar concentration ranges as were observed for the carbonate fraction (*e.g.* Nd: C-fraction 177 ppm, calcite 139 ppm; Lu: C-fraction 0.55 ppm, calcite 0.61 ppm). However, it does not show the anomalies that are observed for the carbonate fraction. Apatite is close to calcite for the LREE but is lower in concentration for Nd (97 ppm) to Lu (0.08 ppm), resulting in a steeper REE pattern with a negative Yb anomaly. Phlogopite and chlorite REE patterns are very similar to one another, showing a slightly steeper slope than calcite, but being almost an order of magnitude lower in concentration compared to calcite. Chlorite shows similar concentrations in LREE compared to phlogopite. Magnetite has the same pattern as phlogopite but shows overall lower concentrations in REE (*e.g.* La: ~14 ppm versus 40 ppm, Lu: 0.004 versus 0.02 ppm). Replicate analyses of the single phases are highly reproducible.

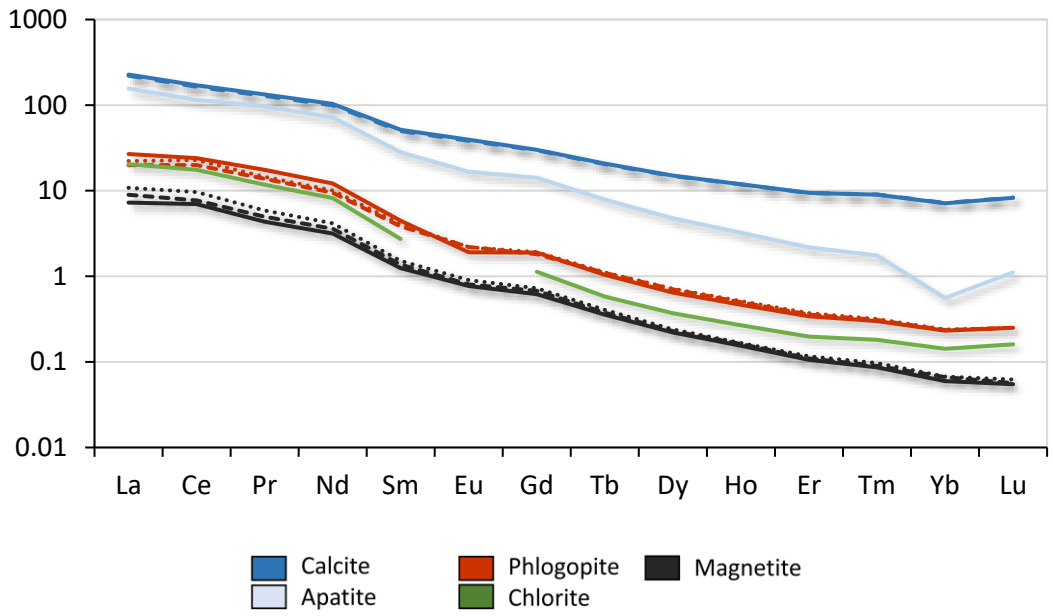

Figure 7.15 **Rare earth element patterns of mineral separates from sample CQW-1 from Fen, Norway normalised to primitive mantle (Sun and McDonough, 1989). Dashed and dotted lines represent replicates of the same sample.**

Distribution of Lu-Hf, Sm-Nd and Rb-Sr in carbonate and non-carbonate fractions and mineral separates

Table 7.2 **Proportions of carbonate and non-carbonate fractions for 6 samples from the Fen case study calculated from weighing samples before and after decarbonisation. C: carbonate; NC: non-carbonate.**

Sample name	C (%)	NC (%)
TS 51.5 E	98.5	1.5
TS 51.5 E (repl)	98.8	1.2
Average	**98.6**	**1.4**
TS 498 E	97.9	2.1
TS 498 E (repl)	97.9	2.1
Average	**97.9**	**2.1**
MTGS	57.0	43.0
MTGS (repl)	54.4	45.6
Average	**55.7**	**44.3**
THY	98.2	1.8
THY (repl)	96.2	3.8
Average	**97.2**	**2.8**
CQW-1	90.2	9.8
CQW-1 (repl)	88.3	11.7
Average	**89.2**	**10.8**
CQW-2	86.5	13.5
CQW-2 (repl)	87.1	12.9
Average	**86.8**	**13.2**

Figure 7.16, Figure 7.17 and Figure 7.18 show the elemental distribution of Lu, Hf, Sm, Nd, Rb and Sr in the carbonate and non-carbonate fractions of the samples from Fen. For most carbonatite samples, Lu is dominantly hosted by the carbonate fraction (~80%) and Hf by the non-carbonate fraction (~99%, Figure 7.16) as already observed for carbonatites from the global study (*c.f.* Figure 4.5). Although, Lu is also present in the non-carbonate fraction (up to 20%). For the ijolite (MTGS) and one carbonatite sample (TS 498 E), Lu (~70%) and Hf (~99%) are both largely hosted by the non-carbonate fraction. However, Lu is also present in the carbonate fraction of MTGS. Except for the latter samples, Lu and Hf are fractionated at the carbonate to non-carbonate scale. For the ijolite sample, the proportion of non-carbonate fraction in the whole-rock (44.3%, Table 7.2 and Figure 7.16) is much higher than for carbonatite samples (1.4% to 13.2%, Table 7.2 and Figure 7.16).

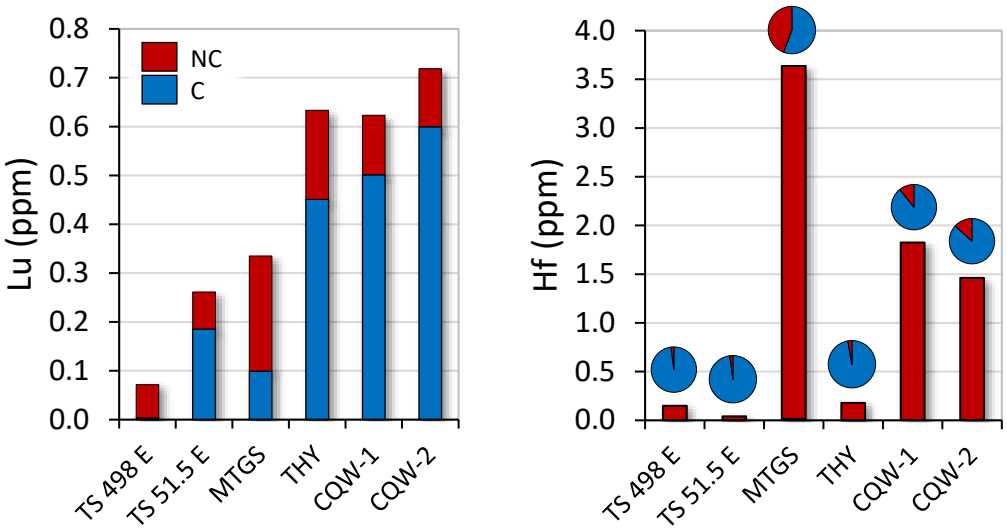

Figure 7.16 **Diagrams showing the distribution and concentration of Lu (left) and Hf (right) in carbonate (blue) and non-carbonate (red) fraction for different samples from Fen, Norway. Pie diagrams (right) show the percentage of carbonate to non-carbonate fraction in the whole-rock (Table 7.2). All samples represent averages of duplicate analyses. Carbonate and non-carbonate fractions were calculated from the whole-rock concentration based on the percentages of the sum of concentrations of carbonate and non-carbonate fraction.**

Like the samples described in the global study (Figure 4.6), the carbonatites and the ijolite sample show no elemental fractionation of Sm from Nd between the carbonate and non-carbonate fractions. Both Sm and Nd are distributed similarly between the fractions but are slightly more enriched in the non-carbonate fraction (~60%), as was observed for samples from the global study (*c.f.* Figure 4.6).

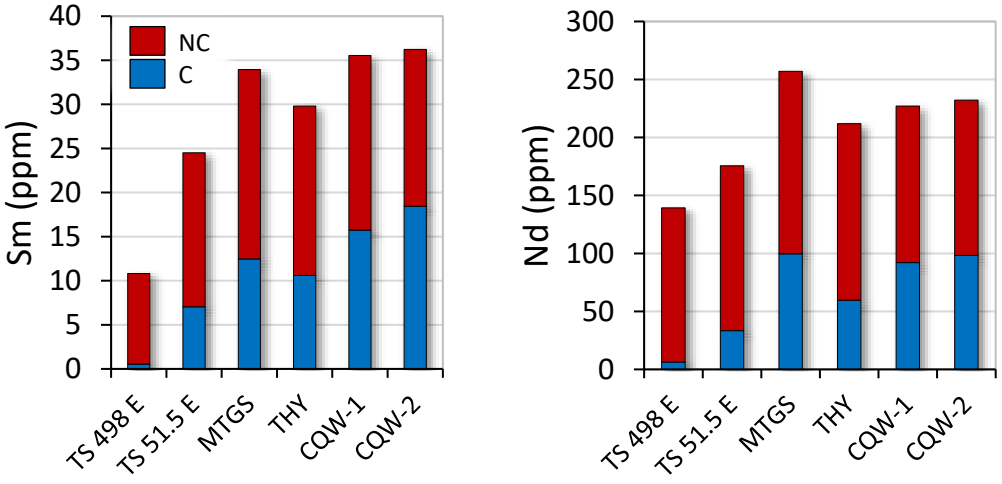

Figure 7.17 **Diagrams showing the distribution and concentration of Sm (left) and Nd (right) in carbonate (blue) and non-carbonate (red) fraction for different samples from Fen, Norway. All samples represent averages of duplicate analyses. Carbonate and non-carbonate fractions were calculated from the whole-rock concentration based on the percentages of the sum of concentrations of carbonate and non-carbonate fraction.**

The non-carbonate fraction generally accounts for most of the Rb in the whole-rock (*c.f.* Figure 4.7), which is also observed for carbonatites from Fen (60-99%; Figure 7.18). However, for the ijolite sample, most of the Rb resides in the carbonate fraction (~60%), although a large portion can be also found in the non-carbonate fraction. Strontium is clearly controlled by the carbonate fraction (~70-90%), which indicates elemental fractionation of Rb from Sr between carbonate and non-carbonate fraction.

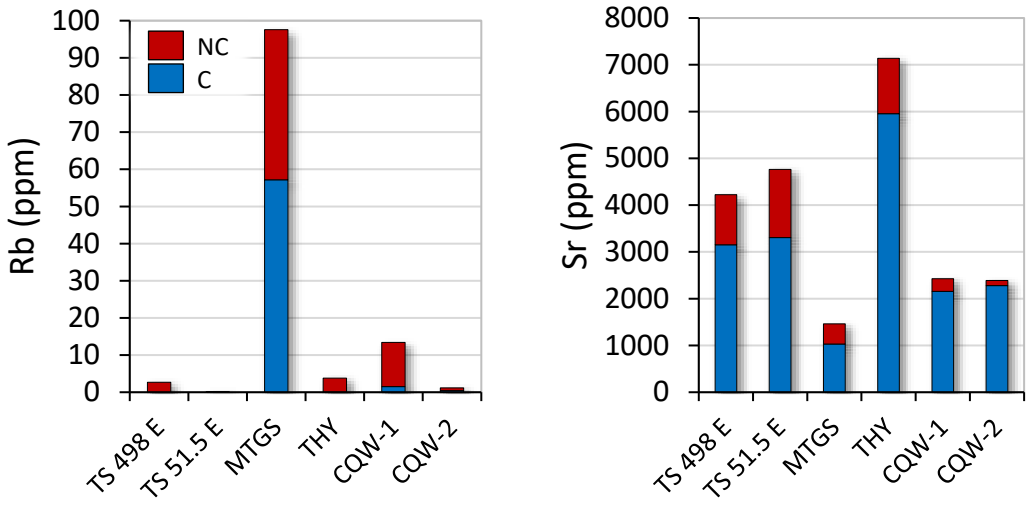

Figure 7.18 **Diagrams showing the distribution and concentration of Rb (left) and Sr (right) in carbonate (blue) and non-carbonate (red) fraction for different samples from Fen, Norway. All samples represent averages of duplicate analyses. Carbonate and non-carbonate fractions were calculated from the whole-rock concentration based on the percentages of the sum of concentrations of carbonate and non-carbonate fraction.**

The distribution of Lu, Hf, Sm, Nd, Rb and Sr in the different mineral fractions is shown as percentage of the whole-rock elemental abundance in Figure 7.19 and in Table 7.3. Samarium and Nd are both dominantly hosted in calcite (58% and 53%, respectively), but also in apatite (32% and 36%, respectively). The distribution of these elements is almost identical between the different mineral fractions and there is no clear elemental fractionation. In contrast the majority of Rb resides in either phlogopite or chlorite (~50% each) with hardly any Rb in the other minerals (<1%). Strontium, in contrast, predominantly resides in calcite (91%) and only minor amounts can be found in apatite, phlogopite and chlorite. A similar distribution is observed for Lu (calcite: 84%), although apatite controls a larger proportion of Lu (11%) than Sr (5%). Hafnium is dominantly hosted in apatite (77%), but can also be found in magnetite, phlogopite and chlorite, with only traces in calcite (0.2%).

Table 7.3 **Distribution of Sm, Nd, Rb, Sr, Lu and Hf in mineral fractions from sample CQW-1 given in %.**

Mineral fraction	Sm	Nd	Rb	Sr	Lu	Hf
Calcite	58.2	53.4	0.01	91.4	84.0	0.2
Phlogopite	4.7	5.2	50.1	2.5	2.5	5.1
Magnetite	1.6	1.8	0.1	0.3	0.6	10.4
Apatite	32.4	35.5	0.3	4.5	11.3	77.3
Chlorite	3.1	4.1	49.5	1.3	1.6	7.0

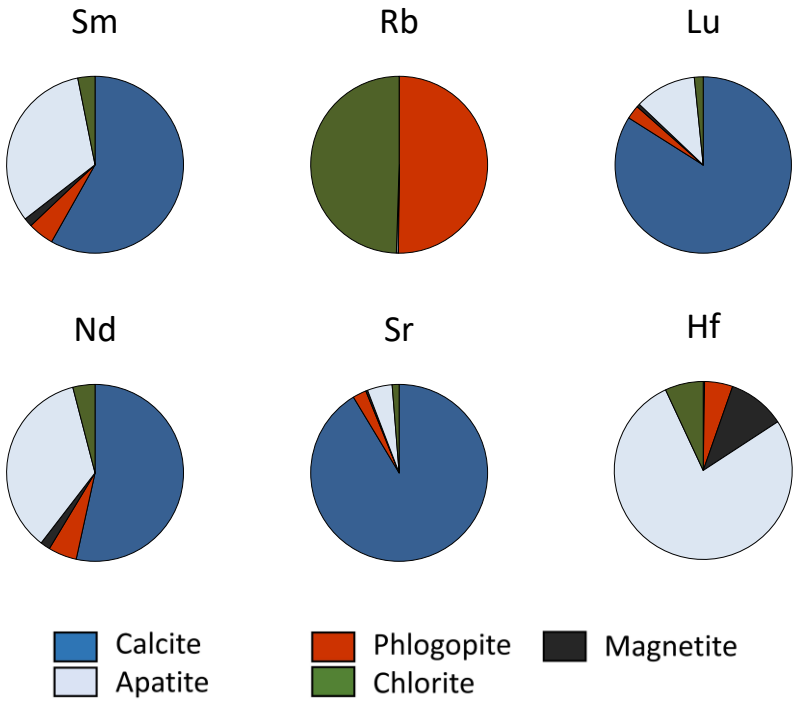

Figure 7.19 **Distribution of relative abundances of Lu, Hf, Sm, Nd, Rb and Sr in % in the different mineral fractions picked from whole-rock sample CQW-1.**

7.4.2. Hf-Nd-Sr isotope systematics

Figure 7.20 shows the age corrected (t) εHf plotted versus εNd for the six samples from the Fen carbonatite. Each sample was duplicated to monitor reproducibility. Error bars for εHf_t are large as consequence of the elemental measurements to determine the $^{176}Lu/^{177}Hf$ ratio from trace element concentrations and are not representative of the errors obtained for $^{176}Hf/^{177}Hf$ (appendix Table 10.38). There is little variation observable for Nd isotopes (εNd_t 3.2 to 4.2) but, as observed for the global study (*c.f.* chapter 5.1.1), substantial Hf isotope variation (all fractions considered: >900 εHf-units). Whole-rock samples range between εHf_t -33 and 1.6, while carbonate fractions range from εHf_t -966 to -8.3 and non-carbonate fractions range between εHf_t -0.5 and 10.5 (*c.f.* appendix Table 10.38).

For Hf isotopes, except for samples TS 51.5 E and THY, all whole-rock samples plot close to or onto bulk silicate Earth and just below the HIMU field. Non-carbonate fractions plot around the HIMU field within the mantle array for both Hf and Nd isotopes. In contrast, the carbonate fractions of all samples plot far below the mantle array (εHf_t <0) and for some samples (THY, CQW-1 and one replicate of CQW-2) even below the initial of the solar system ($^{176}Hf/^{177}Hf$: 0.279811 Bouvier et al., 2008) for Hf isotopes.

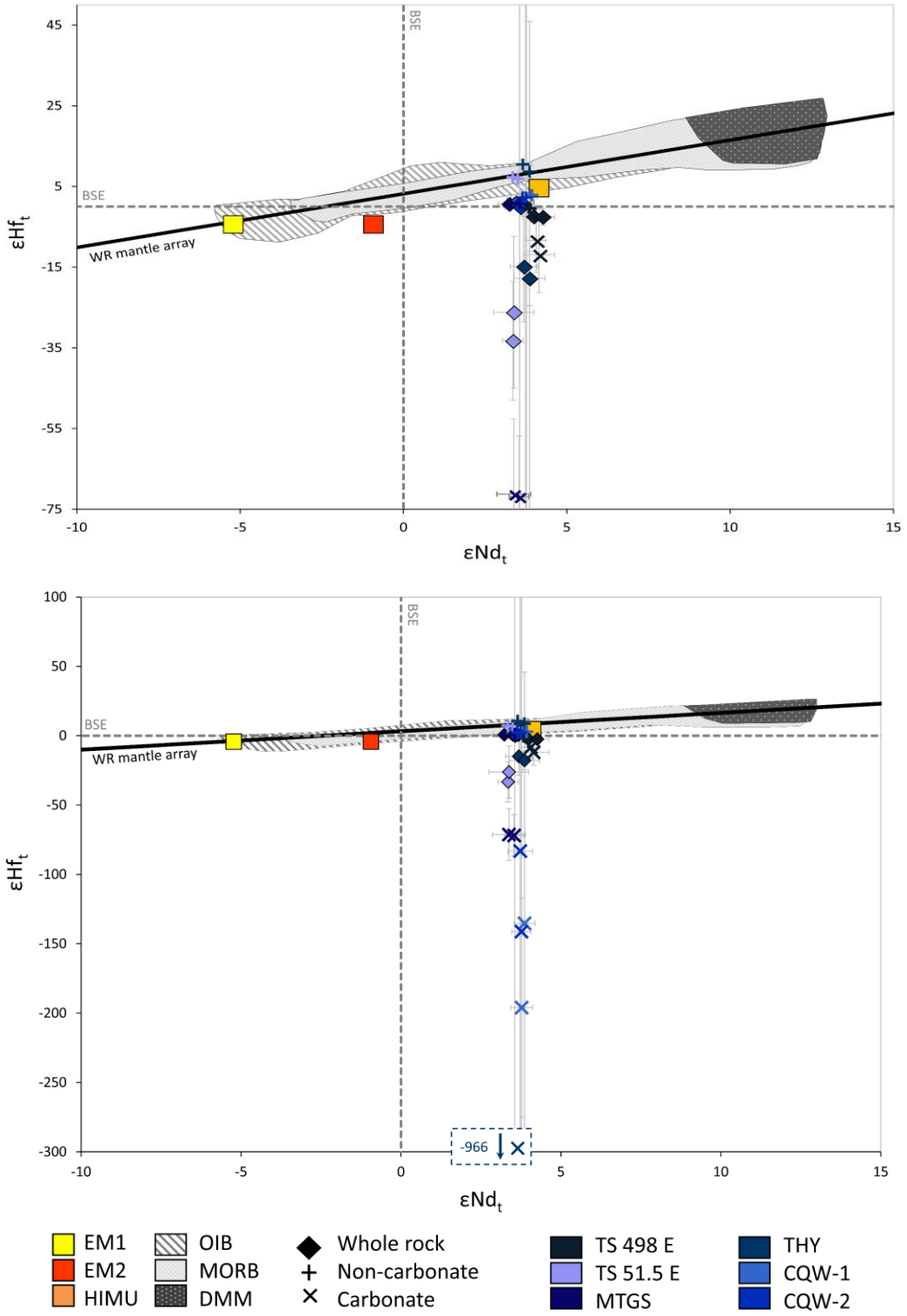

Figure 7.20 **Age corrected εHf vs. εNd for samples from the Fen case study in two different scales. ε values and errors calculated using Ickert (2013). Error bars represent a combination of the uncertainty of age, the parent-ratio analyses as well as the $^{176}Hf/^{177}Hf$ determined by ICP-MS. Whole-rock mantle array: εHf = 1.33 εNd + 3.19 (Vervoort et al., 1999); Bulk silicate Earth (BSE): Bouvier et al., 2008; Jacobsen and Wasserburg, 1980; Mid-ocean ridge basalt (MORB) and ocean island basalt (OIB): Nowell et al., 1998; Salters and Hart, 1991; Stille et al., 1986; EM1, EM2, HIMU and DMM: Zindler and Hart, 1986.**

Figure 7.21 shows εHf_t versus εNd_t for whole-rock, carbonate and non-carbonate fractions as well as for the mineral fractions phlogopite, magnetite, apatite and chlorite of sample CQW-1. For calcite, Hf analyses were below detection limit and thus are not illustrated (*c.f.* appendix Table 10.38). In chapter 7.4.1, it was shown that Hf in sample CQW-1 is mainly controlled by apatite, which is considered to be part of the non-carbonate fraction. Apatite plots below the mantle array with εNd_t of 3.5 identical to the whole-rock of CQW-1. Although apatite plots below the mantle array (εHf_t: -8.3), within the 2SD error it also plots in the same range as the whole-rock and non-carbonate fraction (εHf_t: 1.4 and 2.9, respectively). Magnetite and phlogopite plot on the mantle array (εNd_t: 3.5 to 4.8; εHf_t: 3.6 to 8.9) and within 2SD error to the non-carbonate fraction and the HIMU end-member. In contrast, chlorite plots at εNd_t of 14.6, but with identical εHf_t as average phlogopite (5.3).

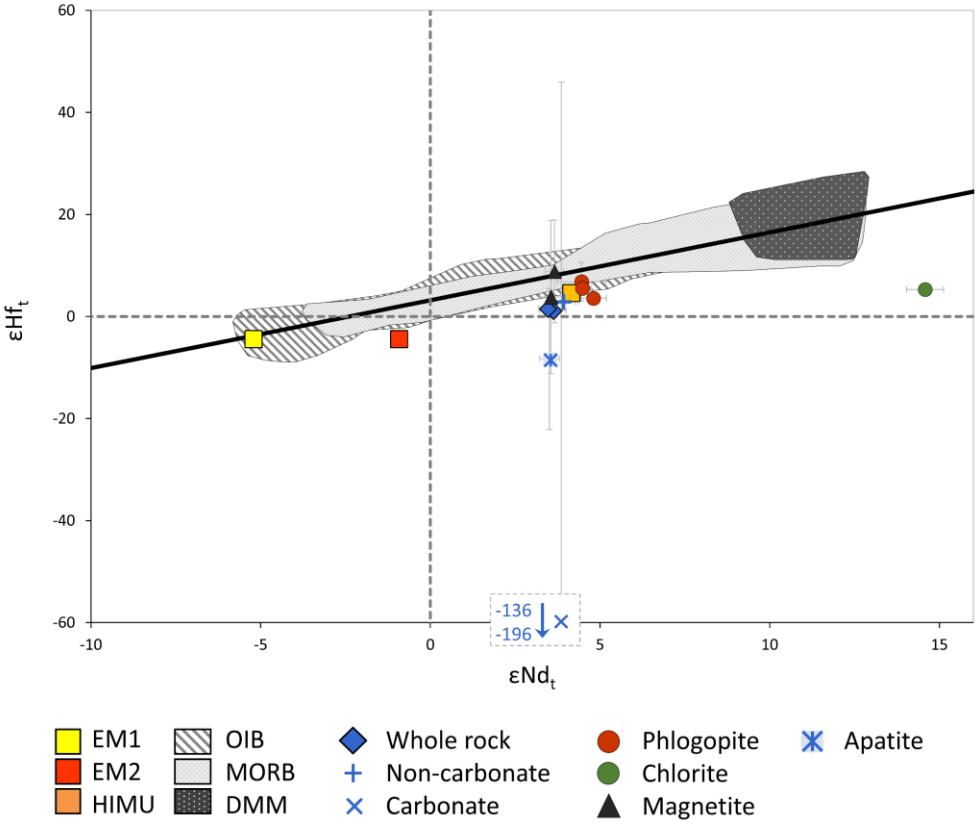

Figure 7.21 **Age corrected εHf vs. εNd for whole-rock, carbonate and non-carbonate fractions and mineral separates from sample CQW-1 from Fen, Norway. ε values and errors calculated using Ickert (2013). Error bars represent a combination of the uncertainty of the age, the parent-ratio analyses as well as the $^{176}Hf/^{177}Hf$ determined by ICP-MS, the latter having almost no influence. Whole-rock mantle array: εHf = 1.33 εNd + 3.19 (Vervoort et al., 1999); bulk silicate Earth (BSE): Bouvier et al., 2008; Jacobsen and Wasserburg, 1980; mid-ocean ridge basalt (MORB) and ocean island basalt (OIB): Nowell et al., 1998; Salters and Hart, 1991; Stille et al., 1986; EM1, EM2, HIMU and DMM: Zindler and Hart, 1986.**

When calculating ages from two-point age regression defined by carbonate and non-carbonate fraction in a $^{176}Hf/^{177}Hf$ vs. $^{176}Lu/^{177}Hf$ plot (*c.f.* Table 7.4), it is clear that the ages calculated in this study (205 to 483 Ma) do not match the age published (539 Ma) by Andersen and Taylor (1988). However, samples TS 498 E, CQW-1 and CQW-2 are very similar to one another (467, 463 and 483 Ma), while TS 51.5 E differs strongly (205 Ma) from the published age and the ages calculated for the other samples. However, this latter sample also has the largest error on the calculated age (205 ±650).

Table 7.4 **$^{176}Lu/^{177}Hf$-$^{176}Hf/^{177}Hf$ ages calculated from regression lines defined by the carbonate and non-carbonate fractions of each sample compared to the published age. Ages were calculated using Isoplot 4 (Ludwig, 2010).**

Sample name	in Ma	Literature age (Ma)	Method
TS 498 E	467 ±39	539	WR Pb-Pb (Andersen and Taylor, 1988)
TS 51.5 E	205 ±650		
THY	430 ±90		
CQW-1	463 ±24		
CQW-2	483 ±85		
MTGS	395 ±17		

Compared to the εHf_t versus εNd_t plot, εNd_t vs. $^{87}Sr/^{86}Sr_t$ shows less variation (Figure 7.22). All whole-rock, carbonate and most non-carbonate fractions of the Fen samples are isotopically indistinguishable for Nd and Sr isotopes. As described previously, εNd_t only varies by ~1 ε-unit and has an average value of 3.7 ±0.2, while the average value for $^{87}Sr/^{86}Sr_t$ is 0.70308 ±0.0016. The Fen samples, thus fall below the HIMU end-member ($^{87}Sr/^{86}Sr_t$: 0.703; εNd_t: 5.3, Zindler and Hart, 1986). Non-carbonate fractions from samples TS 498 E and THY are higher (THY: 0.7067) or lower (TS 498 E: 0.6956) in $^{87}Sr/^{86}Sr_t$ compared to the other samples and fractions. However, for sample TS 498 E and THY this is only the case for one of the two replicates. This variation in $^{87}Sr/^{86}Sr_t$ for the non-carbonate fraction has been observed previously for non-carbonate fractions from Fen samples from the global study (*c.f.* Figure 5.3).

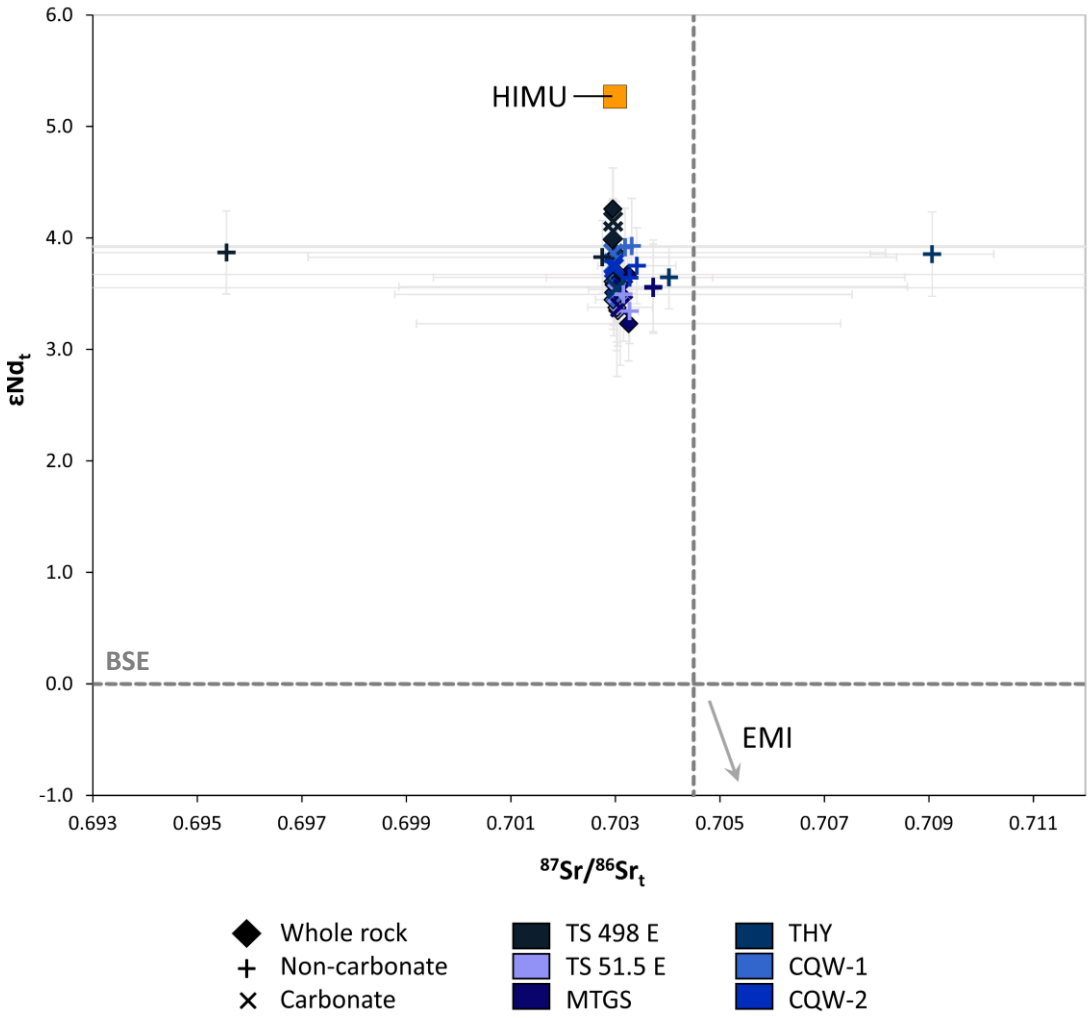

Figure 7.22 **Age corrected εNd vs. $^{87}Sr/^{86}Sr$ for whole-rock, carbonate and non-carbonate fractions of carbonatites from Fen, Norway. Bulk silicate Earth (BSE): Bouvier et al., 2008; DePaolo and Wasserburg, 1976; high μ (HIMU): Zindler and Hart (1986).**

In the εNd_t versus $^{87}Sr/^{86}Sr_t$ diagram for mineral separates from sample CQW-1 (Figure 7.23), calcite, apatite and magnetite show a similar range ($^{87}Sr/^{86}Sr_t$: 0.70294 to 0.70304; εNd_t: 3.5 to 4.6) as observed for whole-rock, carbonate and non-carbonate fractions (Figure 7.22) just below the HIMU end-member. Phlogopite is slightly lower in $^{87}Sr/^{86}Sr_t$ (0.70236) compared to the other fractions (0.703) and is not as reproducible as *i.e.* magnetite (phlogopite: 0.70236 ± 0.00069 2SD; magnetite: 0.70303 ± 0.00002 2SD), though errors on Sr isotopes are large. In contrast, chlorite (εNd_t: 14.6; $^{87}Sr/^{86}Sr_t$: 0.710) plots far away from any other fractions of sample CQW-1 (εNd_t: 3.8; $^{87}Sr/^{86}Sr_t$: 0.703).

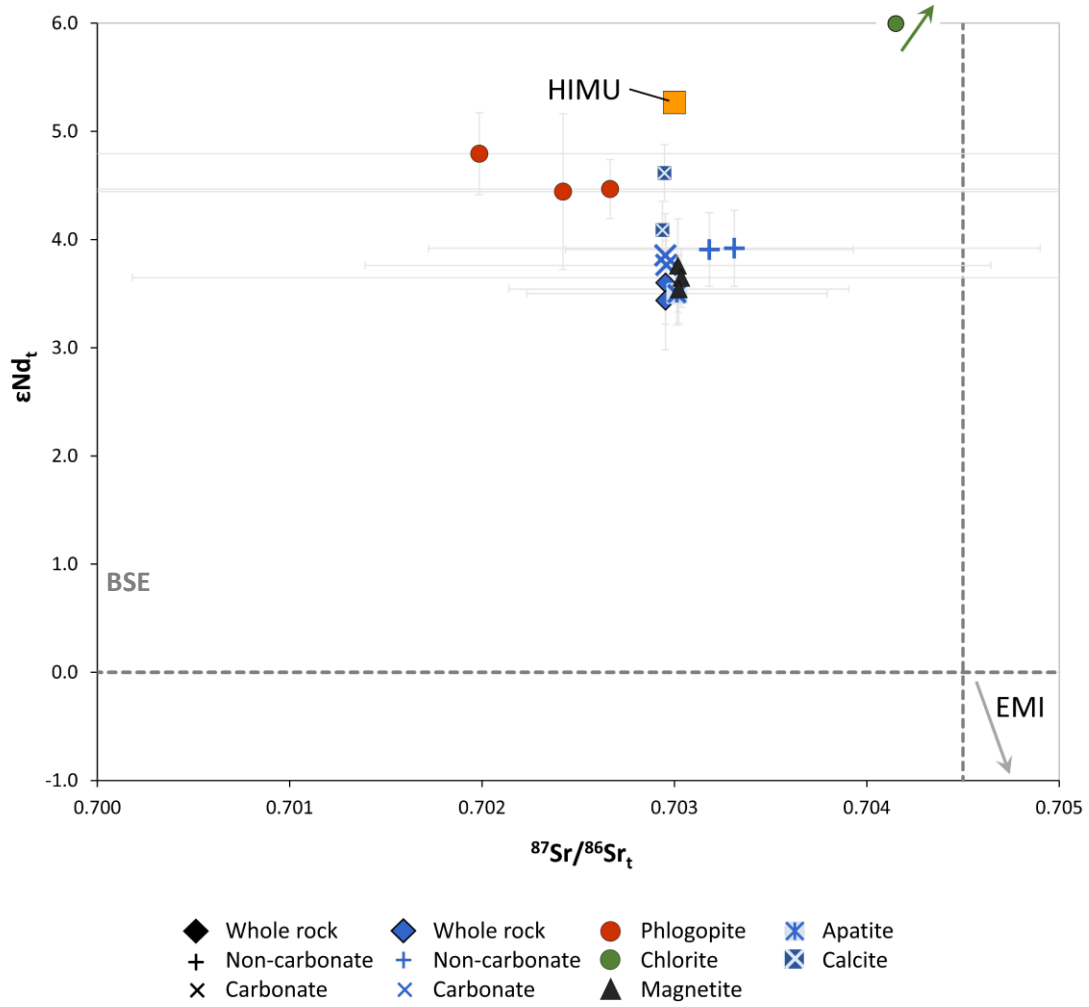

Figure 7.23 **Age corrected εNd vs. $^{87}Sr/^{86}Sr$ for whole-rock, carbonate and non-carbonate fractions and mineral separates of sample CQW-1 from Fen. Bulk silicate Earth (BSE): Bouvier et al., 2008; DePaolo and Wasserburg, 1976; Fields for mid-ocean ridge basalt (MORB), Ocean island and continental basalt were adopted from White (2013) and references within.**

7.4.3. Whole-rock highly siderophile elements and Re-Os isotope systematics

Whole-rock HSE and Re-Os isotope data are given in the appendix in Table 10.41 and are illustrated in Figure 7.24 and Figure 7.25.

For samples from Fen carbonatites, HSE abundances fall within a similar range as carbonatites from the global study with concentrations ranging from <0.9 to 4.4 ppt Os, <1 to 5.5 ppt Ir, <23.2 to 46.8 ppt Ru, <12.7 to 43.12 ppt Pt, <120.9 to 670 ppt Pd and 58.4 to 626 ppt Re, approximately 0.0008 to 1.9 times the concentrations of the primitive upper mantle (PUM, Becker et al., 2006). However, compared to the global study, all carbonatites from Fen show a depletion in Pt (average carbonatite: 695 ppt, average Fen_{global}: 33 ppt; average Fen_{case}: bdl). Ijolite sample MTGS falls within the same concentration range as Fen carbonatites from the global study for Pt (43 ppt). Osmium concentrations for the case study samples either vary between 3.3 ppt (TS 498 E) and 4.4 ppt (CQW-1), or are below detection limit (TS 51.5 E; MTGS). In contrast, Fen samples from the global study yielded concentrations of 1.5 ppt (16462) and 12.6 ppt (4808). Iridium is below detection limit for all case study samples except for TS 498 E (5.5 ppt). Ruthenium concentrations (38 to 47 ppt) are almost identical to the average carbonatite from the global study (47 ppt), except for MTGS, where it is bdl. Palladium concentrations are again mostly below detection limit, except for samples CQW-2 (670 ppt) and TS 498 E (247 ppt), of which CQW-2 is close to the average carbonatite. Magnesiocarbonate TS 51.5 E and ijolite MTGS show the lowest abundances in Re (58 and 86 ppt, respectively), while all other carbonatite samples from Fen range between 495 and 626 ppt, which is in a similar order of magnitude as OIB (390 ppt, Day et al., 2010) and PUM (350 ppt, Becker et al., 2006) and in between the two Fen samples from the global study (138 and 1790 ppt). Replicate analyses of sample CQW-1 are reproducible for all HSEs, except for Ru (45, 46.8 and 37.6 ppt), where the third replicate is slightly lower (*c.f.* appendix Table 10.41).

CI-chondrite normalised HSE patterns from Fen (Figure 7.24) are mostly incomplete due to many elements (*e.g.* Ir, Pt and Pd) being below detection limit. However, taking into account the Fen samples from the global study, an area for Fen carbonatites can be drawn (pale blue field, Figure 7.24). It shows the typical melt-like pattern (Re_N/Os_N = 1639 to 1819) as observed for carbonatites from the global study (grey dashed line) and OIB (Day et al., 2010), though with the previously described negative Pt-anomaly.

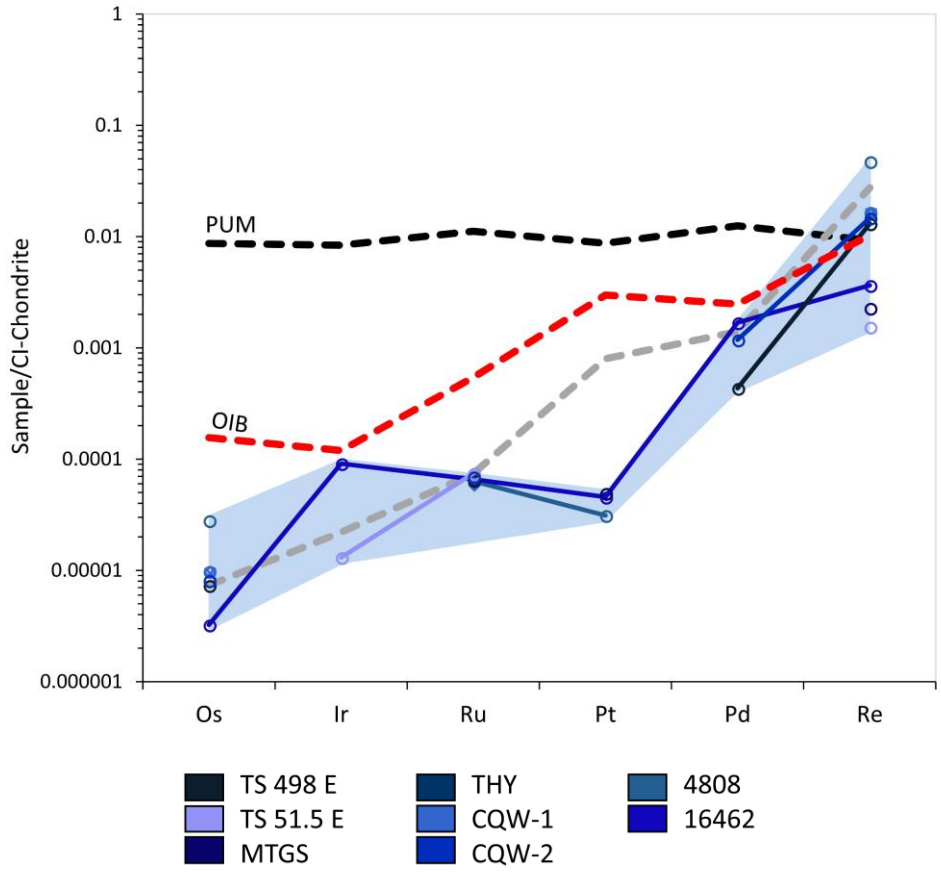

Figure 7.24 **CI-chondrite (Fischer-Gödde et al., 2010; Horan et al., 2003) normalised HSE patterns of carbonatites from the Fen carbonatite complex. Pale blue field: field of all carbonatites from Fen. Average carbonatite (grey dashed line) calculated from carbonatites of the global study (*c.f.* chapter 6.1.1), PUM = primitive upper mantle (Becker et al., 2006), OIB = ocean island basalt (Day et al., 2010). Left to right: increasing incompatibility.**

Compared to the global study, most carbonatite samples from Fen show even more radiogenic age corrected $^{187}Os/^{188}Os$ ratios (*e.g.* 196.7 to 259.1) up to 2000 times the value of PUM (0.1296,Becker et al., 2006). Age corrections are only minor (*c.f.* Figure 7.25), although Re/Os ratios are high (652 to 724). For samples TS 51.5 E (magnesiocarbonatite) and MTGS (ijolite), Os was below detection limit, but measured $^{187}Os/^{188}Os$ ratios were also both highly radiogenic (22.68 and 16.38). Both calciocarbonatites (CQW-1 and CQW-2) show similar isotopic signatures ($^{187}Os/^{188}Os_m$: 203 to 266) to the ankerite carbonatite TS 498 E ($^{187}Os/^{188}Os_m$: 239), while the magnesiocarbonatite TS 51.5 E ($^{187}Os/^{188}Os_m$: 22.7) and ijolite MTGS ($^{187}Os/^{188}Os_m$: 16.4) vary strongly from the other three samples. Replicate analyses of CQW-1 are reproducible for Os concentrations (4.39 ±0.12 ppt 2SD) but show variation in the measured and age corrected $^{187}Os/^{188}Os$ ratios (measured: 223.9 ±44 and age corrected: 217.9 ±44 2SD). T_{MA} model ages (appendix Table 10.41) are all implausible (>Earth).

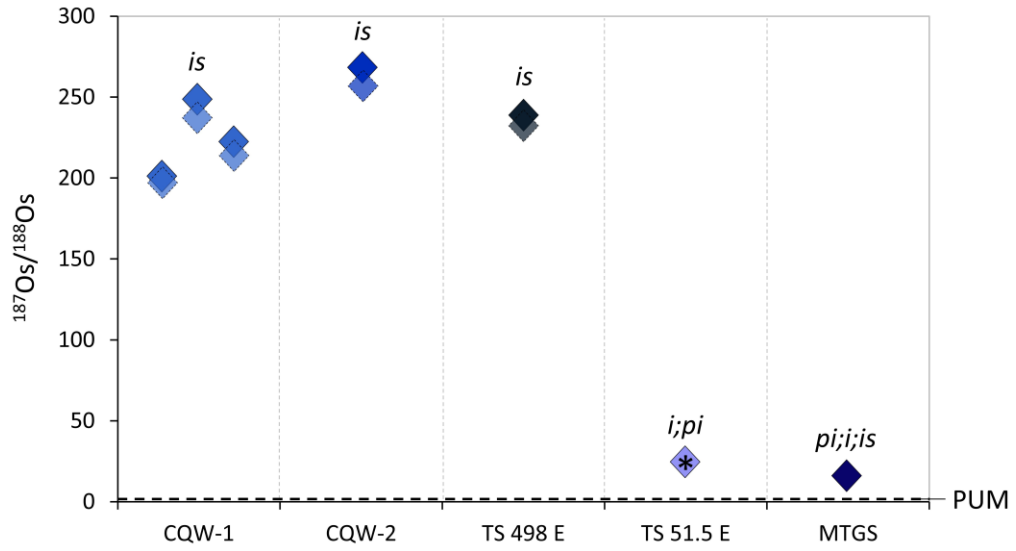

Figure 7.25 **Whole-rock $^{187}Os/^{188}Os$ ratios for samples from the Fen carbonatite case study. Diamonds with solid outlines show the measured $^{187}Os/^{188}Os$ ratios. Transparent diamonds with dashed outlines represent the age corrected $^{187}Os/^{188}Os$ ratios. Plot shows all data, although for TS 51.5 E and MTGS, Os was below detection limit (appendix Table 10.41). PUM = primitive upper mantle (Becker et al., 2006). Star highlights the magnesiocarbonatite. pi: pseudo-included BMS, i: included BMS, is: interstitial BMS. Errors are smaller than the symbols.**

7.4.4. Base metal sulphides

Base metal sulphides in Fen carbonatites as well as the ijolite MTGS are common accessory minerals with variable abundances (*c.f.* Table 7.5). Except for BMS from samples MTGS and TS 51.5 E, all BMS show alteration to a different extent, ranging from porous textures to strongly fractured, often accompanied by transformation to Fe-oxide (Figure 7.26). This was also observed for BMS from Fen samples from the global study (*c.f.* Table 6.1). While sample 16462 from the global study has both pyrrhotite and pyrite, only pyrite was found and analysed in sample CQW-1 (*c.f.* appendix Table 10.11). BMS in Fen samples are mainly interstitial grains, though sample TS 51.5 E only has included and pseudo-included BMS, and MTGS has all three types.

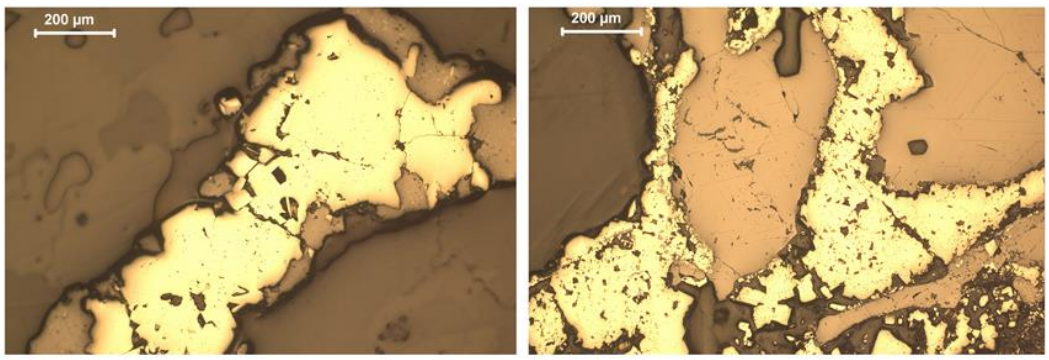

Figure 7.26 **Reflected light image of interstitial pyrite associated to magnetite/Fe-oxides found in sample CQW-1.**

Table 7.5 **Base metal sulphide petrography of samples from the Fen carbonatite case study. Pi: pseudo-inclusions, i: inclusions, is: interstitial Samples analysed by microprobe show mineral compositions (py: pyrite), while samples characterised by reflected light microscopy were only identified as either homogeneous (ho, single BMS phase) or heterogeneous (he, multiphase BMS) grains.**

Sample name	#	Type	Composition	Habit	Size range (µm)	Distribution in thin section	Condition	Associated with
CQW-1	>10	is	py	irregular	200-2000	random	porous, altered	Fe-oxides, carbonate
CQW-2	>20	is	ho	elongated; irregular	up to 4000	relatively even	very altered	Fe-oxides, apatite
TS 498 E	>30	is	ho	rounded; equant; irregular; tabular	up to 2,500	relatively even	porous, fractured	Carbonate
TS 51.5 E	15	i; pi	ho	rounded; angular	20-50	random	relatively fresh, slightly porous	Carbonate
MTGS	>30	pi; i; is	ho	rounded; elongated; tabular	≤10	random	relatively fresh	pyrochlore, pyroxene, phlogopite, in altered matrix

7.5. Discussion

7.5.1. Combined lithophile and siderophile element perspective of Fen carbonatite genesis

As was described in chapters Chapter 5 and Chapter 6, post-magmatic alteration can have major effects on isotopic signatures of carbonatites. Like carbonatites from the global lithophile element study (*c.f.* Chapter 5), Fen carbonatites show open system behaviour resulting in isotopic disequilibrium between carbonate and non-carbonate fractions for Lu-Hf isotopes. This is reflected in isochron ages that do not match published age data, and εHf_t values for the carbonate fraction that are implausibly low (<the initial of the solar system, *e.g.* Bouvier et al., 2008).

For Hf isotopes, whole-rock fractions from CQW-1, CQW-2, TS 498 E, MTGS and non-carbonate fractions are all similar to one another and plot close to, though mostly below, the HIMU field. This can also be observed for combined Nd and Sr isotopes (Figure 7.22) and agrees with findings from Fen samples from the global study suggesting influence by a HIMU source. A study by Andersen and Taylor (1988) on Pb isotopes, finds that Fen carbonatites show extreme $^{206}Pb/^{204}Pb$ ratios between 18.91 and 226.26, many of which are falling within the HIMU range (>19.5 *e.g.* Stracke et al., 2005; Zindler and Hart, 1986) suggesting the possibility of a HIMU source affecting the carbonatite source. Though, based on the analysis of country rocks, Andersen and Taylor (1988) explain the observed Pb isotope signature as being derived from a crustal source rather than a mantle source.

Andersen (1988) suggests that for Fen there is no primitive carbonatite magma but rather that each different carbonatite forms by slightly different processes that are linked to other rock types such as ijolite, syenite or nephelinite. Ijolite sample MTGS is isotopically identical to the carbonatites. This would suggest that they were either derived from the same source and/or overprinted by the same processes and would partly support Andersen's hypothesis (link of silicate to carbonatite rock). However, all carbonatites from Fen are isotopically identical, suggesting that there is one source for both carbonatites and ijolite. Nevertheless, to confirm this, further investigations of related silicate rocks are required.

Although fractionation of Lu from Hf between carbonate and non-carbonate fraction in ijolite sample MTGS is not as substantial as that observed for carbonatites, εHf_t values still show very low age corrected values for the carbonate fraction of that sample (~-71). However, the most extreme εHf_t values were observed for the carbonate fraction of sample THY (~-950) and are similar to the carbonate fraction of sample 4808 (-1000) from the global study.

Sample 4808 comes from a strongly altered area of the carbonatite complex (*c.f.* chapter 7.3.6). The only type of mica found in this sample was chlorite (*c.f.* Table 2.1), which is considered a secondary mineral (*e.g.* De Kimpe, 1987). Due to the similarly extreme εHf_t of the carbonate fractions of THY and 4808, it is assumed that sample THY has experienced similar alteration to sample 4808. If extreme εHf_t are an indicator for the degree of overprinting, then sample TS 498 E appears to be the least affected sample, followed by MTGS and the samples from Cappelen quarry (CQW), while samples THY and TS 51.5 E (whole-rock) would be more strongly affected. However, this is not reflected in the degree of alteration observed in thin sections, where TS 498 E shows stronger evidence for alteration than some of the other samples (*c.f.* Table 2.1). This suggested εHf_t indicator is also only partly reflected in the calculated isochron ages (*c.f.* Table 7.4), where sample TS 51.5 E yields the least plausible age (205 Ma), while THY (430 Ma) and the other samples (395 to 483 Ma), though still too low, are closer to the published age (539 Ma, Andersen and Taylor, 1988). When adding Re-Os isotope signatures to the picture, the observed signatures do not match the findings for the alteration series suggested using Hf isotopes, where TS 51.5 E is the most overprinted sample. In fact, samples CQW-1, CQW-2 and TS 498 E, which for Hf are thought to be less affected, have the most radiogenic $^{187}Os/^{188}Os$ signatures. This would suggest that Hf isotopes are no clear indication for the degree of post-magmatic overprinting. Though, the form of alteration affecting the lithophile isotope systems might not affect the Re-Os isotopes to the same extent and vice versa.

Strongly radiogenic $^{187}Os/^{188}Os$ signatures in chapter 6.2.3 were mostly linked to post-magmatic alteration, further demonstrated by often unrealistic T_{MA} model ages, inconsistent $^{187}Os/^{188}Os$ ratios at time of eruption and the presence of sphalerite and porous pyrite. The HSE abundances show typical melt-like patterns, suggesting that whatever overprinted the Re-Os isotopes has either caused similar fractionation of HSEs as observed during melting or suggests that the HSEs have not been affected as strongly by post-emplacement processes as Re-Os isotopes. Samples with the least radiogenic Os isotope signatures of this study are magnesiocarbonatite TS 51.5 E and ijolite sample MTGS. In those samples, BMS are present as inclusions compared to the other samples where only interstitial BMS and pseudo-inclusions were found. Though, as was discussed in chapter 6.2.3, the type of occurrence of BMS (inclusion, pseudo-inclusion or interstitial) is not necessarily an indicator of the degree of overprinting. Thus, the less radiogenic character of TS 51.5 E and MTGS might also be due to their whole-rock major element composition and the way these compositions are affected by overprinting compared to *i.e.* calciocarbonatites.

Nevertheless, for Os isotopes all samples found at Fen are highly radiogenic ($^{187}Os/^{188}Os_m$: 16.4 to 259) and often more radiogenic than most samples from the global study. While sample 16462 from the global study contains pyrrhotite and pyrite, sample CQW-1 only contains pyrite. A sample taken from the massive sulphide vein crosscutting the Fen carbonatite (*c.f.* chapter 7.3.6) comprises only pyrite and Fe-oxides (appendix Table 10.11). It is possible that the formation of this vein coincides with overprinting of the Fen carbonatites and might thus be responsible for the extreme $^{187}Os/^{188}Os$ ratios observed. To confirm this, Os isotope investigations of the sulphide vein are required. Not only the sulphide vein but also hydrothermal as well as ankeritic alteration veins can be found throughout the whole Fen carbonatite complex (*e.g.* chapters 7.3.5, 7.3.6, 7.3.7,7.3.9 and 7.3.10) delivering field evidence for syn- or post-magmatic chemical modification of Fen carbonatites. As was mentioned in chapter 6.2, Re as well as Os can be mobilised during hydrothermal alteration, which is possibly responsible for observed isotopic signatures at Fen.

As outlined in chapter 5.2, the work of Chakhmouradian et al. (2016) highlights the importance of evaluating post-magmatic processes in order to understand carbonatite evolution and to avoid misinterpretations. This was also stressed much earlier by Andersen (1984), who although only working with the extreme example of transformation from ferrocarbonatite to rødberg, implied that other carbonatites might have suffered similar alteration. At Fen, he suggested that meteoric water circulating through a thermal anomaly induced a hydrothermal cell, and that this was the responsible agent for post-magmatic alteration. As also noted before by Gittins (1979), hydrothermal fluids can result in elemental partitioning by *e.g.* carbonate dissolution and recrystallisation, leading to disequilibrium on the whole-rock scale (Andersen, 1984).

Strontium and Nd concentrations in carbonatites are very high (*e.g.* appendix Table 10.23, Table 10.26 and Table 10.30) and post-magmatic alteration should only have minor influence on the isotopic signature unless the overprinting fluid was dramatically enriched in those elements. When considering data from Fen and the global study, the non-carbonate fractions tend to show more variable Sr isotopes, while Nd is largely constant; Though, errors on age corrected Sr isotopes are large. In chapter 5.2 variation in isotopic signatures of the non-carbonate fraction was explained by the non-carbonate fraction being contaminated by either the carbonate fraction, crustal material or by xenocrysts. The carbonate fraction cannot be responsible for the observed variation, as no carbonate fraction shows this offset in Sr isotopes. Thus, the variation is likely caused by either crustal contamination or by

sampling of xenocrysts. Because the carbonate and not the non-carbonate fraction controls the Sr budget (*c.f.* Figure 4.7 and Figure 7.18), the non-carbonate fraction is potentially more prone to be affected by overprinting. However, it remains unclear which exact process is responsible for the variation in Sr isotopes of the non-carbonate fraction.

Andersen (1987) described the evolution of carbonatites at Fen as a seven stage history: 1) Partial melting of the mantle source resulting in depletion; 2) Introduction of CO_2 and re-mobilisation of LREE by metasomatism; 3) Partial melting of the metasomatized mantle lherzolite; 4) Chemical exchange of the melt with the upper mantle resulting in further LREE enrichment as well as transfer of volatiles; 5) Liquid immiscibility and/or fractional crystallisation in the crust producing silicate and carbonatite melts; 6) Evolution of carbonatitic melts with different compositions within the crust accompanied by crustal contamination; and 7) Post-magmatic alteration. Interaction between carbonatite and crustal/country rocks during emplacement or during post-magmatic alteration at Fen has later also been suggested *i.e.* based on Pb isotopes (Andersen and Taylor, 1988).

Although, post-magmatic alteration appears to be the main reason for the observed isotopic variation and open system behaviour for both lithophile and siderophile element systems, the carbonatites from Fen may still have been influenced by processes such as assimilation of mantle or contamination by crustal material as well as fractional crystallisation or immiscibility processes prior to emplacement (*e.g.* Andersen, 1987). However, this will be difficult to identify based on the isotope systems considered here as the likelihood of all those processes affecting the samples to a different extent makes it almost impossible to distinguish them apart, at least at the whole-rock/carbonate/non-carbonate scale.

7.5.2. Implications from mineral separates

As was shown in chapters Chapter 5 and Chapter 6 and discussed previously (*e.g.* Andersen, 1987, 1984; Bizimis et al., 2003; Chakhmouradian et al., 2016b, 2016a), interpretation of data based on whole-rock or even carbonate and non-carbonate scale can lead to wrong interpretation of the carbonatite source due to disequilibrium phenomena (*c.f.* Chapter 5.2.1). Whole-rock samples comprise an assemblage of minerals and thus only represent a mixed signature; For instance, carbonate and non-carbonate fraction are not isotopically identical for age corrected Lu-Hf isotopes and will both contribute to the isotopic signature of the whole-rock (*c.f.* chapters 5.2). Thus, mineral separates might reveal more information on the nature of carbonatites.

Mineral separates from sample CQW-1 show only minor variation. Errors for εHf_t on apatite and magnetite are large, due to low Lu concentrations (appendix Table 10.31). Magnetite is considered to be one of the earlier phases to crystallise and can be present in form of chemically and morphologically different phases in carbonatite magmas sensitive to changes in carbonatite evolution (*e.g.* Lee et al., 2005; Reguir et al., 2008; Ripp et al., 2006). Within error all analysed magnetite are isotopically identical to the whole-rock and non-carbonate fractions of CQW-1 for Hf-Nd-Sr isotopes.

Apatite falls below the mantle array but, within error, also lies within the lower magnetite fraction (εHf_t: 3.8, εNd_t: 3.5) and whole-rock (εHf_t: 1.4, εNd_t: 3.5) in the Hf-Nd space. Based on the study of fluid inclusions in apatite (Andersen, 1986b) it was suggested that apatite phenocrysts in søvite and dolomite-carbonatite formed in equilibrium with the carbonatite magma and are thus, together with calcite, dolomite and pyrochlore, part of the original phenocryst assemblage of the melt. To confirm the isotopic signature of apatite and use it for source interpretation, more analyses would need to be undertaken. Unfortunately, interpretation on that one data point is not reliable.

For the Nd-Sr isotope space, chlorite plots far from the bulk silicate Earth and the other minerals. Because chlorite is considered a secondary mineral (*e.g.* De Kimpe, 1987), it cannot be used for source interpretation. However, transformation from *i.e.* phlogopite to chlorite (*c.f.* Table 2.1) might be detected by comparing the isotopic signatures of both minerals.

Phlogopite is lower in $^{87}Sr/^{86}Sr_t$ and similar in εNd_t to calcite. The offset in Nd observed for phlogopite could be a result of initial transformation into chlorite. However, this does not apply to the offset in Sr, which moves towards lower $^{87}Sr/^{86}Sr_t$, while chlorite shows higher $^{87}Sr/^{86}Sr_t$ (0.710). For the example of Alnö Island in Sweden, Hode Vuorinen and Skelton (2004) argue that silicate minerals such as pyroxene or phlogopite were assimilated from wall-rocks and are not derived from the carbonatite magma itself. In contrast, at Jacupiranga, Brod et al. (2001) describe primary magmatic phlogopites associated with the carbonatite melt that developed independently of the phlogopites found in associated silicate rocks. The isotopic variation between phlogopite and the other mineral fractions is so minor and errors on Sr isotopes so large, that it cannot be said with certainty whether the isotopic composition of phlogopite has been influenced by *i.e.* an adjacent wall-rock, has been altered or whether within error it is identical with the other fractions. Further investigations are required.

Calcite, apatite and magnetite possess similar $^{87}Sr/^{86}Sr_t$ compositions (0.7029-0.7030), while for Nd isotopes calcite together with phlogopite are both slightly higher (4.1 to 4.8) than the

other fractions excluding chlorite (εNd_t: 3.4 to 3.9). Calcite is a primary mineral phase in carbonatites. However, it commonly dissolves and re-crystallises (*e.g.* Andersen, 1984; Chakhmouradian et al., 2016a) and as discussed earlier (Chapter 7.5.1) this can result in disequilibrium in the whole-rock isotopic signature. Unfortunately, the calcite analysed here had too little Hf to be analysed for $^{176}Hf/^{177}Hf$, and for Nd and Sr there is no evidence for re-equilibration likely due to the high concentration of both elements (Nd: ~145 ppm, Sr: ~8000 ppm, Table 10.31). Nevertheless, the carbonate fraction of CQW-1 falls far below the mantle array for Hf isotopes and as calcite is the major constituent, it is expected that it would also show similarly low initial Hf isotope signatures.

The close match of magnetite with apatite and calcite for Nd and Sr isotopes would suggest that they have crystallised from the same melt. When considering Hf isotopes, phlogopite is isotopically similar to magnetite, while for Sr isotopes phlogopite has lower $^{87}Sr/^{86}Sr_t$. Nevertheless, the close fit of all fractions, except chlorite, to one another and to the HIMU end-member would suggest that they are derived from the same source, which in return might have been influenced by a HIMU source. However, this would need to be verified using Pb isotopes on the mineral separates.

7.6. Conclusions

Study of the Fen samples has led to the following conclusions:

- For all samples from Fen, Sm and Nd are almost equally distributed between carbonate and non-carbonate fraction. When only considering the carbonatites, Lu and Sr are dominated by the carbonate fraction, while Hf and Rb are dominated by the non-carbonate fraction and for ijolite MTGS, Lu and Hf are dominated by the non-carbonate, and Rb and Sr by the carbonate fraction.
- For mineral separates Hf is mainly controlled by apatite, Lu and Sr by calcite, Rb by phlogopite and chlorite, and Sm and Nd by calcite and apatite.
- As observed for the global study, carbonate and non-carbonate fractions are not in isotopic equilibrium due to open system behaviour of the carbonate fraction.
- Magnetite, apatite and calcite are in isotopic equilibrium for Nd and Sr isotopes. Phlogopite shows a larger variation in Sr isotopes but is most likely in equilibrium with magnetite, apatite and calcite. Within error, magnetite, apatite and phlogopite are in isotopic equilibrium for Hf isotopes, suggesting the same source for all mineral fractions.
- Samples from Fen have experienced strong post-magmatic alteration:

- Lu-Hf isotopes show open system behaviour that results in incongruous Lu/Hf ratios leading to overcorrected and unrealistic $^{176}Hf/^{177}Hf_t$ (<initial of solar system, Bouvier et al., 2008) for the carbonate fraction and consequently very low $^{176}Hf/^{177}Hf_t$ for many whole-rock samples.
- Re-Os isotope systematics show open system behaviour with $^{187}Os/^{188}Os_t$ ratios as extreme as 260 and T_{MA} model ages >Earth. Samples that have BMS inclusions are less radiogenic than samples with interstitial grains or pseudo-inclusions.
- The 1 m wide sulphide vein, strongly altered rocks such as rødberg as well as hydrothermal and ankerite veins found throughout the Fen complex provide field evidence for extensive post-magmatic alteration.

The study of whole-rock, carbonate and non-carbonate fractions combined with different mineral fractions could be explained by the following modified history of genesis of the Fen carbonatites as was first suggested by Andersen (1987):

1) Partial melting of a CO_2 and volatile-rich mantle source with a HIMU component
2) Separation of carbonatitic melt from silicate melt by fractional crystallisation and/or liquid immiscibility
3) Crystallisation of phenocrysts in carbonatite melt (*e.g.* apatite, phlogopite and magnetite)
4) Chemical exchange with uppermost mantle and/or crust affecting BMS and residual carbonatite melt
5) Emplacement of carbonatite and release of fluids and volatiles during cooling (fenitisation)
6) Post-magmatic alteration by hydrothermal events overprinting both lithophile (carbonate fraction) and siderophile (BMS) isotope systems

Chapter 8 : Summary and overall conclusion

8.1. Summary

This thesis contains major, trace element, ultra-trace element (highly siderophile elements) as well as lithophile (Lu-Hf, Sm-Nd and Rb-Sr) and chalcophile (Re-Os) isotope data on a suite of 39 carbonatites and associated rocks (ijolite, BMS vein) from ten different localities ranging in age from present day (Oldoinyo Lengai, Tanzania) to 3007 Ma (Tupertalik, Greenland), covering natrocarbonatites, calciocarbonatites, magnesiocarbonatites and ankerite carbonatites.

Major mineral phases in carbonatites from this study are carbonate, magnetite, phlogopite/mica and apatite, while single samples also contain arfvedsonite (19780), clinopyroxene (*e.g.* LI 23/02/08), olivine (*e.g.* 91/62 – C4), nyerereite and gregoryite (OL-1 and BM.2004,P12(132)). Minor and accessory phases include base metal sulphides, chlorite, pyrochlore, zircon and spinel.

The CaO content in carbonatites from this study is typically around 50 wt.% for calciocarbonatites and 35 to 40 wt.% for magnesiocarbonatites (MgO: 9-17 wt.%). Fe_2O_3, P_2O_5 and SiO_2 vary depending on the modal abundances of magnetite, apatite and silicate phases (*e.g.* pyroxene or amphibole). The natrocarbonatite analysed for whole-rock major elements consists of 31 wt.% Na_2O, 14 wt.% CaO and 6 wt.% K_2O.

Most whole-rock carbonatites from this study show a distinct negative Zr and Pb anomaly and are highly variable in Th, U, Nb and Ta concentrations. Primitive mantle normalised REE patterns are all enriched in the light REE (up to 3000× primitive mantle), resulting in a negative slope from La to Lu (La_N/Lu_N = ~2.9 to ~2300). This is also reflected in the REE pattern of the carbonate and non-carbonate fractions.

Carbonatites from this study have been separated into carbonate fraction (phases that can be dissolved in 6 M HCl, ~90% of the whole-rock) and non-carbonate fraction (*e.g.* magnetite, mica, BMS, apatite, ~10% of the whole-rock). Our investigations show that Lu, Sm, Nd and Sr are mainly hosted by the carbonate fraction of carbonatites, while Hf and Rb are mainly controlled by the non-carbonate fraction, leading to a potential decoupling of the Rb-Sr and Lu-Hf isotope systems over time

8.1.1. Lithophile element isotope study

From 39 samples, 24 carbonatites from ten different localities were selected for measurement of the lithophile element isotope systematics. The εHf_t values for whole-rock carbonatites range from 9 to <initial of the solar system ($^{176}Hf/^{177}Hf$: 0.279811, Bouvier et al. (2008)) which is also observed for the carbonate fraction (-5 to <initial of the solar system). In contrast, the non-carbonate fraction yields more plausible εHf_t values ranging from 1.4 to 56. This, together with a mismatch between Lu-Hf isochron ages and published ages, points towards open system behaviour of the Lu-Hf isotope system for the carbonate fraction. Thus, whole-rock samples, which are dominated by the carbonate fraction, are not representative of the carbonatite source for Lu-Hf isotopes. Samples from one locality show variable Lu-Hf and Sm-Nd isotopic signatures, which could be a consequence of the mineralogy resulting from magmatic differentiation (*e.g.* Le Bas, 1981), different sources in the mantle (Demaiffe et al., 2001), and/or local secondary overprinting. Young samples from Oldoinyo Lengai and Fogo could reveal more reliable source information due to their immunity regarding age corrections, while older samples are more prone to be affected by post-magmatic processes (*e.g.* Tupertalik, Larsen and Rex, 1992). The fact that most carbonatites plot below the mantle array in the Hf-Nd isotope space, suggests that the presence of a hidden mantle reservoir (Nowell et al., 2004, 1999, 1998; Bizzarro et al., 2002) is possible. This is especially the case for young samples or for those samples of which the isotope information of whole-rock, carbonate and non-carbonate fractions are in agreement. For Nd and Sr isotopes, the variation is not as strong as that observed for Lu-Hf, and Nd and Sr isotopes of the carbonatites are within the range of, or close to, known mantle reservoirs (*e.g.* DMM, Su and Langmuir (2003); Workman and Hart (2005), or HIMU, Zindler and Hart (1986)). Though the non-carbonate fractions of *i.e.* Fen and Kovdor are more variable for Sr isotopes, which could be a consequence of *i.e.* sampling of xenocrysts (Bizimis et al., 2003). Nevertheless, based on the close fit of many non-carbonate fractions to CHUR and DMM evolution, it is though that the Hf isotopic signatures of the non-carbonate fractions could record source information which in return reflect a carbonatite source that remained uniform with time. Nonetheless, the Lu-Hf isotope system appears to be decoupled from the Sm-Nd and Rb-Sr isotope systems and it is uncertain to what extent the two latter isotope systems were affected by processes overprinting Lu-Hf isotopes. In general, the nature of the processes overprinting carbonatites remain unclear, however, it is obvious that samples from this study have experienced substantial post-magmatic perturbation.

8.1.2. Highly siderophile elements and Re-Os isotope systematics

Of the original 39 carbonatite samples, 20 samples from ten localities were analysed for Re-Os isotopes and HSE abundances. Highly siderophile elements are likely to be mainly hosted by base metal sulphides in carbonatite samples. Base metal sulphides found in carbonatites are mostly interstitial grains or pseudo-inclusions and are made up of pyrrhotite, pyrite or sphalerite, of which the latter two often show porous textures and are thought to originate hydrothermally (*e.g.* Wohlgemuth-Ueberwasser et al., 2015). The conditions in which BMS in carbonatites have formed vary between log(fS_2) values of -13 and 1 and between ΔFMQ -1 and +3 for log(fO_2). CI-chondrite normalised HSE patterns show a positive slope from Os to Re (Re_N/Os_N = 10 - 105,000), with HSE concentrations ranging between <0.9 and 12.6 ppt Os, <1 and 38 ppt Ir, <23.2 and 85 ppt Ru, <12.7 ppt and 8.9 ppb Pt, <121 ppt and 4.9 ppb Pd and from 3.2 ppt to 10.2 ppb Re. $^{187}Os/^{188}Os$ signatures are all radiogenic and vary strongly between different localities but also within each locality. They range from 0.1636 to 48.66 and there is no systematic variation with age or tectonic setting, though the natrocarbonatites ($^{187}Os/^{188}Os_m$: 0.1636 and 0.2623) and carbonatites with BMS present as inclusions ($^{187}Os/^{188}Os_m$: 0.3705 to 1.54) tend to be less radiogenic than carbonatites with only interstitial BMS ($^{187}Os/^{188}Os_m$: up to 48.66). The measured $^{187}Os/^{188}Os$ at time of eruption are either negative or radiogenic with minimal change compared to the measured $^{187}Os/^{188}Os$ (*e.g.* $^{187}Os/^{188}Os_m$: 48.66; $^{187}Os/^{188}Os_t$: 42.6). The T_{MA} model ages either do not reflect the published ages or are older than Earth. These observations lead to the conclusion that HSE abundances and Re-Os isotope systematics result from open system behaviour, caused by contamination during ascent and/or by post-magmatic alteration, *i.e.* hydrothermal activity.

8.1.3. Fen case study

During a field campaign to the Fen carbonatite complex in Norway, seven samples were collected of which six were analysed for Lu-Hf isotopes and five for Re-Os isotopes and HSE abundances. Mineral separation was carried out for sample CQW-1, for which calcite, phlogopite, magnetite, apatite and chlorite were picked. Whole-rock samples, carbonate and non-carbonate as well as mineral separates were analysed for Lu-Hf, Sm-Nd and Rb-Sr isotopes, and Re-Os isotope measurements were carried out on the whole-rock samples. For Lu-Hf isotopes, εHf_t values possess a similar range (10.5 to <initial of the solar system, Bouvier et al., (2008)) as that observed for the global study. The $^{187}Os/^{188}Os$ isotope ratios of the Fen carbonatites are extremely radiogenic (up to 265.7). Again, isochron ages for Lu-Hf isotopes point towards open system behaviour indicated by isotopic disequilibrium between

carbonate and non-carbonate fraction. Whole-rock T_{MA} model ages (>Earth) for whole-rock samples and εHf_t values (<initial of the solar system) for carbonate fractions provide further evidence for open system behaviour. When only considering mineral separates, Lu, Sm, Nd and Sr are mainly hosted by calcite, while nearly all Rb resides in either chlorite or phlogopite. Apatite dominates the Hf abundance but is also responsible for a large proportion of the Sm and Nd. On the whole-rock, carbonate and non-carbonate scale both, Sm and Nd, appear to be dominantly hosted by the non-carbonate fraction, although the carbonate fraction still contains a sufficient amount (~30%) of both elements. The Nd isotopes for whole-rock, carbonate and non-carbonate fractions yield similar values ($^{143}Nd/^{144}Nd_t$: 0.512119 ±0.00004 2SD, n=36) for Fen samples as observed from the global study ($^{143}Nd/^{144}Nd_t$: 0.512126 ±0.00002 2SD, n=11) and show no evidence of isotopic disequilibrium. For Sr isotopes, for the majority of samples the whole-rock, carbonate and non-carbonate fractions are in isotopic equilibrium. For Sr and Nd isotopes, all mineral fractions, except chlorite ($^{87}Sr/^{86}Sr_t$: 0.710194; $^{143}Nd/^{144}Nd_t$: 0.512684), yield similar $^{87}Sr/^{86}Sr_t$ (0.702892 ±0.00064 2SD, n=15) and $^{143}Nd/^{144}Nd_t$ values (0.512141 ±0.00004 2SD, n=15). However, there is slightly more variation for Sr isotopes in phlogopite (0.70236 ± 0.00069 2SD). For Hf isotopes in the mineral separates, there is more variation (εHf_t: -8.3 to 8.9) than observed for Nd or Sr isotopes, which is likely of analytical nature. Based on a study by Andersen (1987) and observations from the Fen case study, a multi-stage genesis was suggested to explain the observed isotopic signatures at Fen, involving: 1) Partial melting of a mantle source rich in CO_2 and volatiles, likely consisting of a HIMU component, 2) Fractional crystallisation and/or liquid immiscibility of carbonatite from silicate melt, 3) A first generation of phenocryst crystallisation in the carbonatite melt (*e.g.* apatite, phlogopite and magnetite), 4) Assimilation of mantle or crust during ascent, 5) Fenitisation, and 6) Post-magmatic alteration. Post-magmatic alteration is thought to be responsible for the open system behaviour observed for Lu-Hf and Re-Os isotopes. Visible alteration in thin sections (*e.g.* TS 498 E and CQW-2, Table 2.1) and field evidence in form of hydrothermal (sulphide) and ankerite veins as well as local extensive alteration to rødberg confirms secondary alteration of the complex.

8.2. Overall conclusion

This thesis presents the first combined Lu-Hf, Sm-Nd, Rb-Sr and Re-Os isotope study, together with highly siderophile element abundances in carbonatites of different age, composition and tectonic environment. The global study together with the case study carried out at the Fen carbonatite complex have led to the following concluding remarks:

- For Lu-Hf isotope studies, whole-rock samples are best dissolved in a HF-HNO_3 mixture (1:3). When samples are diluted for trace element aliquoting, a *10,000 ppm ROMIL PrimAg® Mono-Component Al-Solution* is added to suppress formation of fluorites (*e.g*. Tanaka et al., 2003), before the samples are passed through columns. Alternatively, carbonate and non-carbonate fractions can be chemically separated and treated differently to prevent formation of fluorites. By diluting Ca-rich samples (whole-rock and carbonate fraction) further and passing each sample through four (Sr-spec), two (cation) and one final (anion) chromatographic columns, the amount of sample matrix is reduced, and yields are improved.
- Lu, Sm, Nd and Sr are hosted by the carbonate fractions of carbonatites, while Hf and Rb reside in the non-carbonate fraction.
    - For samples from Fen, Sm and Nd are both dominated by the non-carbonate fraction, although the carbonate fraction still holds a large proportion of both elements.
    - Calcite controls Lu and Sr, while phlogopite and chlorite together account for most of the Rb. Hafnium is mainly controlled by apatite, though apatite and calcite together control Sm and Nd concentrations.
- Base metal sulphides (BMS) are likely to be the main host for HSEs in carbonatites.
    - They are mostly made up of pyrrhotite, pyrite ± sphalerite.
    - They are usually found as interstitial grains or pseudo-inclusions and sometimes as inclusions in *i.e.* carbonate or magnetite.
    - The porous texture of pyrite and inclusions of sphalerite could indicate a secondary, *i.e.* hydrothermal, origin (*e.g.* Barnes, 1997; Wohlgemuth-Ueberwasser et al., 2015).
- Re-Os isotope systematics in whole-rock carbonatites show open system behaviour and have either been contaminated during ascent and/or overprinted by post-emplacement processes (*e.g.* hydrothermal activity).

- Due to open system behaviour, Lu-Hf isotopes in the carbonate and non-carbonate fractions of carbonatites are not in equilibrium, and thus neither whole-rock nor carbonate fractions can be used to determine source information.
    - Present day and young carbonatites (*e.g.* Oldoinyo Lengai and Fogo) will be less influenced by post-emplacement radiogenic ingrowth. Additionally, age-corrections applied to daughter-isotope ratios will only be minor. So although it cannot be excluded that young samples have undergone secondary overprinting, the effect on the isotope ratios will only be minor, and thus they are more likely to reflect a source composition than older samples which have undergone regional metamorphism (*e.g.* Tupertalik, Larsen and Rex, 1992).
    - The source for Oldoinyo Lengai is close to that of the bulk silicate Earth for Nd and Sr, but displaced below the Hf-Nd mantle array for Hf isotopes, which could support the presence of a hidden mantle reservoir (Nowell et al., 2004, 1999, 1998; Bizzarro et al., 2002).
    - For Fogo the source is between the HIMU and DMM end-member for Hf-Nd-Sr isotopes.
- Post-magmatic alteration is most likely responsible for observed open system behaviour in both whole-rock Re-Os and in whole-rock/carbonate fractions for Lu-Hf isotopes. The extent to which highly siderophile element abundances, Re-Os isotopes and Lu-Hf isotopes were affected by secondary overprinting remains difficult to quantify.
- The non-carbonate fraction of carbonatites is likely more reliable for determining the carbonatite source.
    - The Hf and Nd isotopic composition of the non-carbonate fractions of various aged carbonatites plot on or close to the CHUR evolution curve suggesting a carbonatite source that remained relatively homogeneous with time (~3 Ga).
- Isotopic equilibrium is observed for Nd and Sr isotope compositions of magnetite, apatite and calcite of sample CQW-1 from Fen, while phlogopite shows more variation in Sr isotopes. This variation could be due to chemical exchange of phlogopite with adjacent wall-rock or could be of analytical origin. For Hf isotopes, all analysed mineral fractions trend towards isotopic equilibrium. This suggests that the analysed mineral phases were derived from the same source, which in turn was possibly influenced by a HIMU source.

8.2.1. Petrogenetic model for global carbonatites

Figure 8.1 shows a simplified illustration of the genesis of carbonatites including different potential sources of contamination or overprinting mechanisms that could affect the Re-Os and Lu-Hf isotope systems. The model here is based on different previously suggested models for their genesis (*e.g.* Andersen, 1987; Cheng et al., 2017; Hamilton et al., 1979; Le Bas, 1981; Nelson et al., 1988; Walter et al., 2008; Watkinson and Wyllie, 1971) combined with the findings from this thesis. In this petrogenetic model, the mantle source of carbonatites could be influenced by recycled oceanic crust with high Re/Os and $^{187}Os/^{188}Os$ ratios. Partial melting produces a melt with, compared to the mantle, higher Re/Os ratios (>0.089, PUM Becker et al., 2006) and lower Lu/Hf ratios (<0.239, primitive mantle; McDonough and Sun, 1995) due to the more incompatible behaviour of Re and Hf. Crystallisation of phenocrysts could record $^{176}Hf/^{177}Hf$ and Lu/Hf ratios of the carbonatite source. During ascent, the melt could become S-undersaturated, which in turn may be balanced by either fractional crystallisation of silicates or by assimilation of BMS from the mantle column or crust. This chemical interaction with the lithosphere would then cause further metasomatism, for example, through the loss of volatiles resulting in the continued evolution of the ascending melt. Immiscible separation of carbonatite from silicate melt or fractional crystallisation could also result in the generation of alkaline silicate melts, which are commonly found associated with carbonatites. Intrusive carbonatites can be affected by crustal contamination, while extrusive carbonatites potentially entrain xenocrysts from the mantle or crust, which carry the $^{176}Hf/^{177}Hf$ and Lu/Hf ratios of their corresponding source region. Loss of volatiles during cooling and corresponding fenitisation again changes the composition of the carbonatitic melt, which, with further cooling, will crystallise the matrix with a potentially different $^{176}Hf/^{177}Hf$ and Lu/Hf composition. After emplacement, carbonatites are affected by post-magmatic alteration, for example, hydrothermal overprinting and/or re-crystallisation of minerals. Thus, Re/Os and Lu/Hf ratios increase with time, which will also affect the $^{187}Os/^{188}Os$ and $^{176}Hf/^{177}Hf$ isotope signatures. Additionally, carbonatites could inherit the isotopic signatures of the overprinting fluids.

The presented model highlights the many potential influences on carbonatite evolution and illustrates just how complex the petrological history of those unusual melts may be.

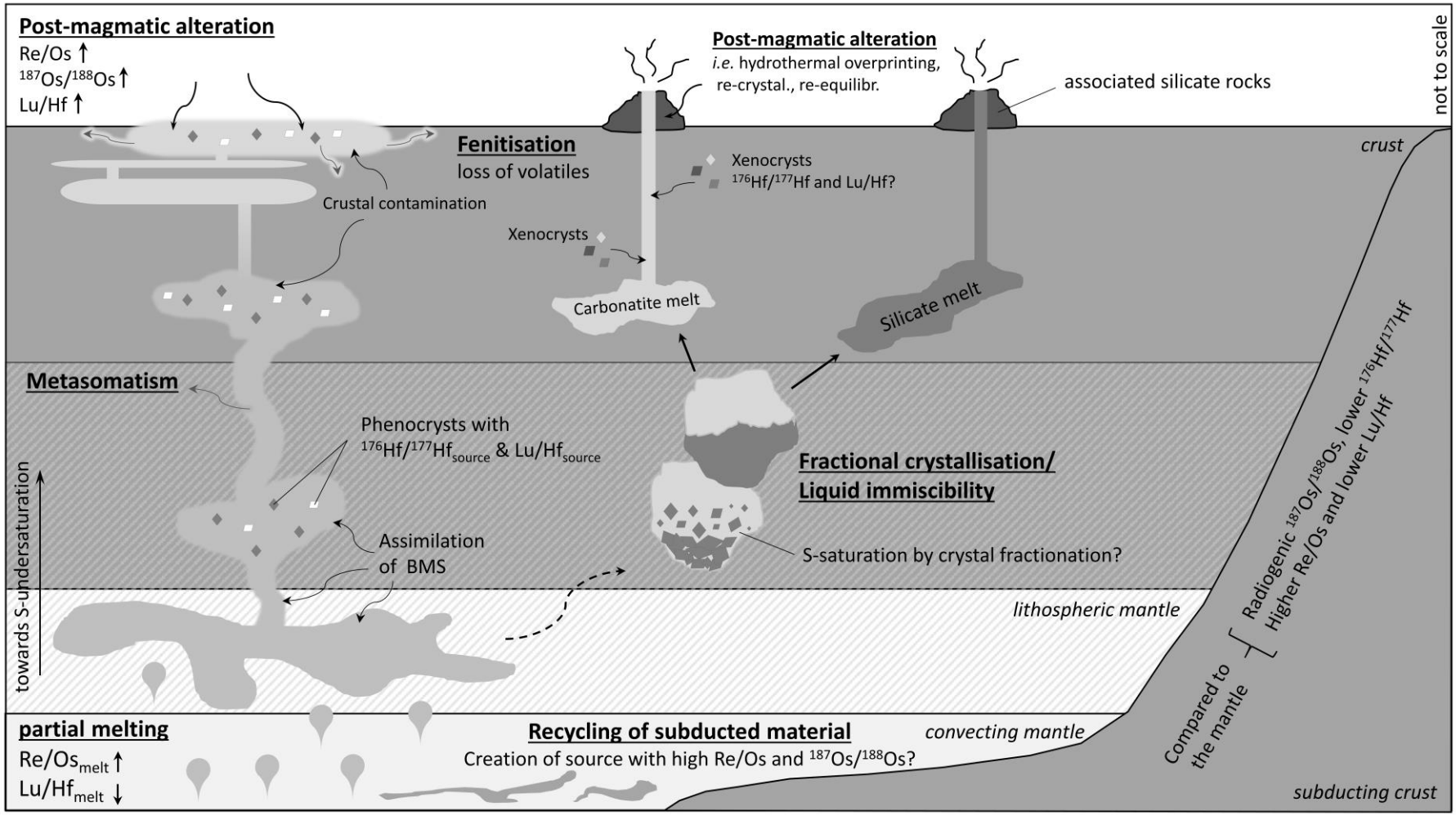

Figure 8.1 **Cartoon illustrating the complicated petrogenetic history of carbonatites. Processes were drawn as different paths, although a combination of all processes could be responsible for isotopic signatures observed at single localities.**

8.3. Outlook

This study has demonstrated the analytical challenges that emerge when working with carbonatites in the lab (*c.f.* Chapters 3.1 and 3.6). Additionally, due to strong post-emplacement overprinting, it is difficult to identify the carbonatite source or clearly trace the petrogenetic history. To better understand carbonatites, the following research topics could be addressed:

- Analyse fenites associated with carbonatite emplacement using Lu-Hf, Re-Os, Sm-Nd and Rb-Sr isotopes. The fluids overprinting the country rock are a missing component of the carbonatite melt and could reveal further information on emplacement processes.
- Analyse silicate magmas which are related to carbonatite emplacement. How have they been affected by post-emplacement processes and how do initial isotope ratios of carbonatites relate to those of the silicate rocks?
- Analyse a larger number of young carbonatites (*e.g.* from Oldoinyo Lengai or Cape Verde) as they are likely less influenced by post-emplacement processes than older carbonatites and may record clearer source information (*c.f.* Chapter 5.2.3).
- Carry out digestions with isotope dilution to analyse the $^{176}Lu/^{177}Hf$ ratio with higher accuracy. Though, this will likely not change the outcome of this study, it would be interesting to see whether more accurate results for $^{176}Lu/^{177}Hf$ ratios can be obtained.
- Measure Pb isotopes to confirm the influence of a HIMU source (*e.g.* at Fen, compare Chapter 7.4).
- Conduct experiments to prove if *i.e.* hydrothermal alteration can result in the observed isotopic and elemental signatures. Can hydrothermal fluids truly enrich Lu over Hf or Re over Os to the extent observed in this study? Is there a model that could explain the extreme isotopic signatures observed in this study?
- Conduct a more detailed study on mineral phases present in carbonatites. Different mineral phases may record different events, which could lead to a better understanding of the nature of the processes overprinting carbonatites. Additionally, this might reveal a mineral phase representative of the carbonatite source:
    - For Lu-Hf isotopes, finding and analysing zircon and baddeleyite could lead to more information on the carbonatite source (*c.f.* Chapter 5.2.2).
    - Apatite is thought to be a primary mineral in carbonatites (*c.f.* Andersen, 1986b) and is additionally a major host of Hf (*c.f.* Chapters 7.4.1 and 7.5.2). Thus,

analysing more apatite could further lead to a better understanding of the carbonatite source.

  - For Re-Os isotopes and HSE abundances, carrying out a study on single BMS from carbonatites might show whether all BMS record the same or different $^{187}Os/^{188}Os$ signatures, which in return could help identify different generations of BMS or could help to understand the processes overprinting BMS. Additionally, it could confirm BMS as the major hosts of HSE (*e.g.* Chapter 6.2.1).

- Carry out a Re-Os isotope study and investigate HSE abundances on the sulphide vein present at the Fen complex. Is the sulphide vein responsible for the extremely radiogenic $^{187}Os/^{188}Os$ ratios found at Fen? Did it affect BMS in Fen carbonatites? When did it form?
- Create a mixed HSE spike to better match carbonatite concentrations.

This study in combination with the suggested future research topics might lead to a better understanding of carbonatites and could help resolve open questions, such as source information and the nature of the processes overprinting carbonatites.

Chapter 9 : References

Ackerman, L., Walker, R.J., Puchtel, I.S., Pitcher, L., Jelínek, E., Strnad, L., 2009. Effects of melt percolation on highly siderophile elements and Os isotopes in subcontinental lithospheric mantle: A study of the upper mantle profile beneath Central Europe. Geochimica et Cosmochimica Acta 73, 2400–2414.

Akizawa, N., Miyake, A., Ishikawa, A., Tamura, A., Terada, Y., Uesugi, K., Takeuchi, A., Arai, S., Tanaka, C., Igami, Y., Suzuki, K., Kogiso, T., 2017. Metasomatic PGE mobilization by carbonatitic melt in the mantle: Evidence from sub-µm-scale sulfide–carbonaceous glass inclusion in Tahitian harzburgite xenolith. Chemical Geology 475, 87–104.

Alard, O., Griffin, W.L., Lorand, J.P., Jackson, S.E., O'Reilly, S.Y., 2000. Non-chondritic distribution of the highly siderophile elements in mantle sulphides. Nature 407, 891–894.

Allen, E.T., Crenshaw, J.L., Larsen, E.S., 1912. The mineral sulphides of iron. American Journal of Science 169–236.

Allen, E.T., Crenshaw, J.L., Merwin, H.E., 1914. Effect of temperature and acidity in the formation of marcasite (FeS2) and wurtzite (ZnS). American Journal of Science 393–421.

Amaral, G., 1978. Potassium-argon age studies on the Jacupiranga alkaline district, State of Sao Paulo, Brazil, in: Proceedings of the First International Symposium on Carbonatites. Departamento Nacional da Producdo Mineral, Brasilia, 297–302.

Amelin, Y., Zaitsev, A.N., 2002. Precise geochronology of phoscorites and carbonatites: The critical role of U-series disequilibrium in age interpretations. Geochimica et Cosmochimica Acta 66, 2399–2419.

Amundsen, H.E.F., 1987. Evidence for liquid immiscibility in the upper mantle. Nature 327, 692–695.

Andersen, T., 1988. Evolution of peralkaline calcite carbonatite magma in the Fen complex, southeast Norway. Lithos 22, 99–112.

Andersen, T., 1987. Mantle and crustal components in a carbonatite complex, and the evolution of carbonatite magma: Ree and isotopic evidence from the fen complex, southeast Norway. Chemical Geology: Isotope Geoscience section 65, 147–166.

Andersen, T., 1986a. Compositional Variation of Some Rare Earth Minerals from the Fen Complex (Telemark, SE Norway): Implications for the Mobility of Rare Earths in a Carbonatite System. Mineralogical Magazine 50, 503–509.

Andersen, T., 1986b. Magmatic fluids in the Fen carbonatite complex, S.E. Norway. Contr. Mineral. and Petrol. 93, 491–503.

Andersen, T., 1984. Secondary processes in carbonatites: petrology of “rødberg” (hematite-calcite-dolomite carbonatite) in the Fen central complex, Telemark (South Norway). Lithos 17, 227–245.

Andersen, T., Taylor, P.N., 1988. Pb isotope geochemistry of the Fen carbonatite complex, S.E. Norway: Age and petrogenetic implications. Geochimica et Cosmochimica Acta 52, 209–215.

Aspden, J.A., 1981. The Composition of Solid Inclusions and the Occurrence of Shortite in Apatites from the Tororo Carbonatite Complex of Eastern Uganda. Mineralogical Magazine 44, 201–204.

Aspden, J.A., 1980. The mineralogy of primary inclusions in apatite crystals extracted from Alnö ijolite. Lithos 13, 263–268.

Aspden, J.A., 1977. Inclusion Studies in Ijolites and Carbonatitic Rocks, with Particular Reference to the Identification of the Solid Components (PhD). University of Leicester.

Assunção, C.T., Machado, F., Gomes, R.A., 1966. On the occurrence of carbonatites in the Cape Verde Islands. Bol. Soc. Geol. Portugal 179–188.

Ballentine, C.J., Lee, D.-C., Halliday, A.N., 1997. Hafnium isotopic studies of the Cameroon line and new HIMU paradoxes. Chemical Geology 139, 111–124.

Bardina, N.Y., Popov, V.S., 1994. Fenites: systematics, formation conditions and significance for crustal magma genesis. Zapiski Vseross. Mineral. Obshcheswa 485–497.

Barker, D.S., 1989. Field relations of carbonatites, in: Bell, K. (Ed.), Carbonatites. Unwin Hyman, London, pp. 38–69.

Barkov, A.Y., Martin, R.F., LeBarge, W., Fedortchouk, Y., 2008. Grains of Pt-Fe alloy and inclusions in a Pt-Fe alloy from Florence Creek, Yukon, Canada: Evidence for mobility of Os in a Na-H2O-Cl-rich fluid. The Canadian Mineralogist 46, 343–360.

Barnes, H.L., 1997. Geochemistry of Hydrothermal Ore Deposits. John Wiley & Sons.

Barnes, S.-J., Naldrett, A.J., Gorton, M.P., 1985. The origin of the fractionation of platinum-group elements in terrestrial magmas. Chemical Geology 53, 303–323.

Beard, B.L., Johnson, C.M., 2004. Inter-mineral Fe isotope variations in mantle-derived rocks and implications for the Fe geochemical cycle. Geochimica et Cosmochimica Acta 68, 4727–4743.

Becker, H., Horan, M.F., Walker, R.J., Gao, S., Lorand, J.-P., Rudnick, R.L., 2006. Highly siderophile element composition of the Earth’s primitive upper mantle: Constraints from new data on peridotite massifs and xenoliths. Geochimica et Cosmochimica Acta 70, 4528–4550.

Bedford, C.M., 1989. The mineralogy, geochemistry, and petrogenesis of the grønnedal-íka alkaline igneous complex, south-west Greenland (Doctoral). Durham University.

Bell, K., 2001. Carbonatites: Relationships to mantle-plume activity, in: Special Paper of the Geological Society of America. 267–290.

Bell, K., Blenkinsop, J., 1987. Archean depleted mantle: Evidence from Nd and Sr initial isotopic ratios of carbonatites. Geochimica et Cosmochimica Acta 51, 291–298.

Bell, K., Castorina, F., Lavecchia, G., Rosatelli, G., Stoppa, F., 2004. Is there a mantle plume below Italy? Eos, Transactions American Geophysical Union 85, 541.

Bell, K., Farquhar, R.M., Dawson, J.B., 1973. Strontium isotope studies of alkalic rocks: the active carbonatite volcano Oldoinyo Lengai, Tanzania. Bulletin of the Geological Society of America 84, 1019–1030.

Bell, K., Rukhlov, A.S., 2004. Carbonatites from the Kola Alkaline Province: origin, evolution and source characteristics. Phoscorites and carbonatites from mantle to mine: the key example of the Kola Alkaline Province 10, 421–455.

Bell, K., Simonetti, A., 1994. Tilton and Carbonatites. EOS, Trans. Am. Geophys. Union 700.

Bergstøl, S., Svinndal, S., 1960. The Carbonatite and Per-alkaline Rocks of the Fen Area. Norges Geologiske Undersøkelse 99–110.

Bézos, A., Lorand, J.-P., Humler, E., Gros, M., 2005. Platinum-group element systematics in Mid-Oceanic Ridge basaltic glasses from the Pacific, Atlantic, and Indian Oceans. Geochimica et Cosmochimica Acta 69, 2613–2627.

Bilenker, L.D., Weis, D., Scoates, J.S., Perry, E., 2018. The application of stable Fe isotopes to magmatic sulfide systems: constraints on the Fe isotope composition of magmatic pyrrhotite. Economic Geology 113, 1181–1192.

Biondi, J.C., 2005. Brazilian mineral deposits associated with alkaline and alkaline-carbonatite complexes., in: Comin-Chiaramonti, P., Gomes, C.B. (Eds.), Mesozoic to Cenozoic Alkaline Magmatism in the Brazilian Platform. Edusp/ FAPESP, São Paulo, Brazil, 707–750.

Bizimis, M., Salters, V., Dawson, J., 2003. The brevity of carbonatite sources in the mantle: evidence from Hf isotopes. Contributions to Mineralogy and Petrology 145, 281–300.

Bizzarro, M., Simonetti, A., Stevenson, R.K., David, J., 2002. Hf isotope evidence for a hidden mantle reservoir. Geology 30, 771–774.

Blaxland, A.B., Breemen, O.V., Emeleus, C.H., Anderson, J.G., 1978. Age and origin of the major syenite centers in the Gardar province of south Greenland: Rb-Sr studies. Geological Society of America Bulletin 89, 231–244.

Blichert-Toft, J., Albarède, F., 1997. The Lu-Hf isotope geochemistry of chondrites and the evolution of the mantle-crust system. Earth and Planetary Science Letters 148, 243–258.

Bodet, F., Schärer, U., 2000. Evolution of the SE-Asian continent from U-Pb and Hf isotopes in single grains of zircon and baddeleyite from large rivers. Geochimica et Cosmochimica Acta 64, 2067–2091.

Bouvier, A., Vervoort, J.D., Patchett, P.J., 2008. The Lu–Hf and Sm–Nd isotopic composition of CHUR: Constraints from unequilibrated chondrites and implications for the bulk composition of terrestrial planets. Earth and Planetary Science Letters 273, 48–57.

Bowen, N.L., 1924. The Fen area in Telemark, Norway. American Journal of Science 1–11.

Brantley, S., 2008. Kinetics of mineral dissolution, in: Brantley, S., Kubicki, J.D., White, A.F. (Eds.), Kinetics of Water-Rock Interaction. Springer, New York, 151–210.

Breemen, O. van, Aftalion, M., Johnson, M.R.W., 1979. Age of the Loch Borrolan complex, Assynt, and late movements along the Moine Thrust Zone. Journal of the Geological Society 136, 489–495.

Brod, J.A., Gaspar, J.C., de Araújo, D.P., Gibson, S.A., Thompson, R.N., Junqueira-Brod, T.C., 2001. Phlogopite and tetra-ferriphlogopite from Brazilian carbonatite complexes: petrogenetic constraints and implications for mineral-chemistry systematics. Journal of Asian Earth Sciences 19, 265–296.

Brøgger, W., Goldschmidt, V.M., 1918. En foreløbig meddelelse om Fensfeltet. Joint meeting of the Science Society.

Brøgger, W.C., 1921. Die Eruptivgesteine des Kristianiagebietes—IV—Das Fengebiet in Telemark, Norwegen. Norske Skrifter udgit av Videnskabsselskabet i Kristiania, Mathematisk- naturvidenskapelig klasse 9, 1–408.

Bugge, J.A.., 1978. Norway, in: Bowie, S.H.U. (Ed.), Mineral Deposits of Europe, Volume 1: Northwest Europe. The Institution of Mining and Metallurgy and The Mineralogical Society, London, 199–249.

Burton, K.W., Schiano, P., Birck, J.-L., Allègre, C.J., 1999. Osmium isotope disequilibrium between mantle minerals in a spinel-lherzolite. Earth and Planetary Science Letters 172, 311–322.

Cafagna, F., Jugo, P.J., 2016. An experimental study on the geochemical behavior of highly siderophile elements (HSE) and metalloids (As, Se, Sb, Te, Bi) in a mss-iss-pyrite system at 650°C: A possible magmatic origin for Co-HSE-bearing pyrite and the role of metalloid-rich phases in the fractionation of HSE. Geochimica et Cosmochimica Acta 178, 233–258.

Canadian mines handbook, 1992. Southam Press, Ontario.

Carlson, R.W., 1994. Mechanisms of Earth differentiation: Consequences for the chemical structure of the mantle. Reviews of Geophysics 32, 337–361.

Chakhmouradian, A.R., 2006. High-field-strength elements in carbonatitic rocks: Geochemistry, crystal chemistry and significance for constraining the sources of carbonatites. Chemical Geology 235, 138–160.

Chakhmouradian, A.R., Reguir, E.P., Couëslan, C., Yang, P., 2016a. Calcite and dolomite in intrusive carbonatites. II. Trace-element variations. Miner Petrol 110, 361–377.

Chakhmouradian, A.R., Reguir, E.P., Zaitsev, A.N., 2016b. Calcite and dolomite in intrusive carbonatites. I. Textural variations. Miner Petrol 110, 333–360.

Chauvel, C., Hofmann, A.W., Vidal, P., 1992. himu-em: The French Polynesian connection. Earth and Planetary Science Letters 110, 99–119.

Cheng, X., Zhilong, H., Cong-Qiang, L., Liang, Q., Wenbo, L., Tao, G., 2003. PGE geochemistry of carbonatites in Maoniuping REE deposit, Sichuan Province, China; preliminary study. Geochemical Journal 37, 391–399.

Cheng, Z., Zhang, Z., Hou, T., Santosh, M., Chen, L., Ke, S., Xu, L., 2017. Decoupling of Mg–C and Sr–Nd–O isotopes traces the role of recycled carbon in magnesiocarbonatites from the Tarim Large Igneous Province. Geochimica et Cosmochimica Acta 202, 159–178.

Chu, Z., Yan, Y., Chen, Z., Guo, J., Yang, Y., Li, C., Zhang, Y., 2015. A Comprehensive Method for Precise Determination of Re, Os, Ir, Ru, Pt, Pd Concentrations and Os Isotopic Compositions in Geological Samples. Geostand Geoanal Res 39, 151–169.

Cina, S.E., Yin, A., Grove, M., Dubey, C.S., Shukla, D.P., Lovera, O.M., Kelty, T.K., Gehrels, G.E., Foster, D.A., 2009. Gangdese arc detritus within the eastern Himalayan Neogene foreland basin: Implications for the Neogene evolution of the Yalu–Brahmaputra River system. Earth and Planetary Science Letters 285, 150–162.

Cohen, A.S., Waters, F.G., 1996. Separation of osmium from geological materials by solvent extraction for analysis by thermal ionisation mass spectrometry. Analytica Chimica Acta 332, 269–275.

Commerce Resources Corporation, 2007. Technical Report June 2007.

Condie, K.C., 1989. Origin of the Earth's crust. Global and Planetary Change, The Long-Term Stability of the Earth System 1, 57–81.

Courtney, R.C., White, R.S., 1986. Anomalous heat flow and geoid across the Cape Verde Rise: evidence for dynamic support from a thermal plume in the mantle. Geophysical Journal of the Royal Astronomical Society 87, 815–867.

Craddock, P.R., Warren, J.M., Dauphas, N., 2013. Abyssal peridotites reveal the near-chondritic Fe isotopic composition of the Earth. Earth and Planetary Science Letters 365, 63–76.

Craig, J.R., Kullerud, G., 1969. Phase Relations in the Cu-Fe-Ni-S System and Their Application to Magmatic Ore Deposits, in: Wilson, H.D.B. (Ed.), Magmatic Ore Deposits. Economic Geology Monograph, 232–243.

Dahlgren, S., 1994. Late proterozoic and Carboniferous ultramafic magmatism of carbonatitic affinity in southern Norway. Lithos 31, 141–154.

Dale, C.W., Burton, K.W., Pearson, D.G., Gannoun, A., Alard, O., Argles, T.W., Parkinson, I.J., 2009. Highly siderophile element behaviour accompanying subduction of oceanic crust: Whole rock and mineral-scale insights from a high-pressure terrain. Geochimica et Cosmochimica Acta 73, 1394–1416.

Dale, C.W., Gannoun, A., Burton, K.W., Argles, T.W., Parkinson, I.J., 2007. Rhenium–osmium isotope and elemental behaviour during subduction of oceanic crust and the implications for mantle recycling. Earth and Planetary Science Letters 253, 211–225.

Dalou, C., Koga, K.T., Hammouda, T., Poitrasson, F., 2009. Trace element partitioning between carbonatitic melts and mantle transition zone minerals: Implications for the source of carbonatites. Geochimica et Cosmochimica Acta 73, 239–255.

Dauphas, N., Craddock, P.R., Asimow, P.D., Bennett, V.C., Nutman, A.P., Ohnenstetter, D., 2009. Iron isotopes may reveal the redox conditions of mantle melting from Archean to Present. Earth and Planetary Science Letters 288, 255–267.

Dauphas, N., Janney, P.E., Mendybaev, R.A., Wadhwa, M., Richter, F.M., Davis, A.M., van Zuilen, M., Hines, R., Foley, C.N., 2004. Chromatographic separation and multicollection-ICPMS analysis of iron. Investigating mass-dependent and -independent isotope effects. Anal. Chem. 76, 5855–5863.

Dauphas, N., John, S.G., Rouxel, O., 2017. Iron Isotope Systematics. Reviews in Mineralogy and Geochemistry 82, 415–510.

Dawson, J.B., 1989. Sodium carbonatite extrusions from Oldoinyo Lengai, Tanzania: Implications for carbonatite complex genesis, in: Bell, K. (Ed.), Carbonatites. Unwin Hyman, London, 255–277.

Day, J.M.D., 2013. Hotspot volcanism and highly siderophile elements. Chemical Geology 341, 50–74.

Day, J.M.D., Pearson, D.G., Macpherson, C.G., Lowry, D., Carracedo, J.C., 2010. Evidence for distinct proportions of subducted oceanic crust and lithosphere in HIMU-type mantle beneath El Hierro and La Palma, Canary Islands. Geochimica et Cosmochimica Acta 74, 6565–6589.

De Kimpe, C.R., 1987. Alteration of Phlogopite to Corrensite at Sharbot Lake, Ontario1. Clays and Clay Minerals 35, 150–158.

Deans, T., Garson, M.S., Coats, J.S., 1971. Fenite-type Soda Metasomatism in the Great Glen, Scotland. Nature 234, 145–147.

Demaiffe, D., Verhulst, A., Balaganskaya, E., Kirnarsky, Y., 2001. The Kovdor ultramafic, carbonatitic and alkaline complex (Kola Peninsula, Russia): evidence for multi-source evolution. Journal of African Earth Sciences 32, A15–A16.

DePaolo, D.J., Wasserburg, G.J., 1976a. Nd isotopic variations and petrogenetic models. Geophysical Research Letters 3, 249–252.

DePaolo, D.J., Wasserburg, G.J., 1976b. Inferences about magma sources and mantle structure from variations of 143Nd/144Nd. Geophys. Res. Lett. 3, 743–746.

Dixon, J.A., Collins, B.A., 1977. The carbonatite complex of North and south Ruri, in: Le Bas, M.J. (Ed.), Carbonatite-Nephelinite Volcanism. John Wiley & Sons Ltd, 169–198.

Dobson, D.P., Jones, A.P., Rabe, R., Sekine, T., Kurita, K., Taniguchi, T., Kondo, T., Kato, T., Shimomura, O., Urakawa, S., 1996. In-situ measurement of viscosity and density of carbonate melts at high pressure. Earth and Planetary Science Letters 143, 207–215.

Doucelance, R., Hammouda, T., Moreira, M., Martins, J.C., 2010. Geochemical constraints on depth of origin of oceanic carbonatites: The Cape Verde case. Geochimica et Cosmochimica Acta 74, 7261–7282.

Dowall, D.P., Pearson, D.G., Nowell, G.M., 2003. Chemical pre-concentration procedures for high-precision analysis of Hf-Nd-Sr isotopes in geological materials by plasma ionisation multi-collector mass spectrometry (PIMMS) techniques, in: Holland, J.G., Tanner, S.D. (Eds.), Plasma Source Mass Spectrometry. Special Publications of the Royal Society of Chemistry, 21–337.

Dutta, T., Kim, K.-H., Uchimiya, M., Kwon, E.E., Jeon, B.-H., Deep, A., Yun, S.-T., 2016. Global demand for rare earth resources and strategies for green mining. Environmental Research 150, 182–190.

Elliott, H.A.L., Wall, F., Chakhmouradian, A.R., Siegfried, P.R., Dahlgren, S., Weatherley, S., Finch, A.A., Marks, M.A.W., Dowman, E., Deady, E., 2018. Fenites associated with carbonatite complexes: A review. Ore Geology Reviews 93, 38–59.

Emeleus, C.H., 1964. The Grønnedal-íka Alkaline Complex, South Greenland - The Structure and Geological History of the Complex. Grønlands Geologiske Undersøgelse Bulletin 45.

Escrig, S., Doucelance, R., Moreira, M., Allègre, C.J., 2005. Os isotope systematics in Fogo Island: Evidence for lower continental crust fragments under the Cape Verde Southern Islands. Chemical Geology 219, 93–113.

Fischer-Gödde, M., Becker, H., Wombacher, F., 2010. Rhodium, gold and other highly siderophile element abundances in chondritic meteorites. Geochimica et Cosmochimica Acta 74, 356–379.

Freestone, I.C., Hamilton, D.L., 1980. The role of liquid immiscibility in the genesis of carbonatites — An experimental study. Contr. Mineral. and Petrol. 73, 105–117.

Friedrichsen, H., 1968. Sauerstoffisotopen einiger Minerale der Karbonatite des Fengebiets Süd Nowergen. Lithos 70–75.

Friel, J.J., Ulmer, G.C., 1974. Oxygen Fugacity Geothermometry of the Oka Carbonatite. American Mineralogist 59, 314–318.

Frost, D.J., McCammon, C.A., 2008. The Redox State of Earth's Mantle. Annual Review of Earth and Planetary Sciences 36, 389–420.

Gaffney, A.M., Blichert-Toft, J., Nelson, B.K., Bizzarro, M., Rosing, M., Albarède, F., 2007. Constraints on source-forming processes of West Greenland kimberlites inferred from Hf–Nd isotope systematics. Geochimica et Cosmochimica Acta 71, 2820–2836.

Gan, T., Huang, Z., 2017. Platinum-group element and Re-Os geochemistry of lamprophyres in the Zhenyuan gold deposit, Yunnan Province, China: Implications for petrogenesis and mantle evolution. Lithos 282–283, 228–239.

Gannoun, A., Burton, K.W., Parkinson, I.J., Alard, O., Schiano, P., Thomas, L.E., 2007. The scale and origin of the osmium isotope variations in mid-ocean ridge basalts. Earth and Planetary Science Letters 259, 541–556.

Gaspar, J.C., Wyllie, P.J., 1983. Magnetite in the carbonatites from the Jacupiranga Complex, Brazil. American Mineralogist 68, 195–213.

Gitlin, E., 1985. Sulfide remobilization during low temperature alteration of seafloor basalt. Geochimica et Cosmochimica Acta 49, 1567–1579.

Gittins, J., 1989. The origin and evolution of carbonatite magmas, in: Bell, K. (Ed.), Carbonatites: Genesis and Evolution. Unwin Hyman Ltd., London, pp. 580–600.

Gittins, J., 1979. Problems inherent in the application of calcite-dolomite geothermometry to carbonatites. Contr. Mineral. and Petrol. 69, 1–4.

Gittins, J., Jago, B.C., 1998. Differentiation of natrocarbonatite magma at Oldoinyo Lengai volcano, Tanzania. Mineralogical Magazine 62, 759–768.

Goldschmidt, V.M., 1937. The principles of distribution of chemical elements in minerals and rocks. The seventh Hugo Müller Lecture, delivered before the Chemical Society on March 17th, 1937. J. Chem. Soc. 0, 655–673.

Gomide, C.S., Brod, J.A., Junqueira-Brod, T.C., Buhn, B.M., Santos, R.V., Barbosa, E.S.R., Cordeiro, P.F.O., Palmieri, M., Grasso, C.B., Torres, M.G., 2013. Sulfur isotopes from Brazilian alkaline carbonatite complexes. Chemical Geology 341, 38–49.

Gorring, M.L., Kay, S.M., 2000. Carbonatite metasomatized peridotite xenoliths from southern Patagonia: implications for lithospheric processes and Neogene plateau magmatism. Contrib Mineral Petrol 140, 55–72.

Green, D.H., Wallace, M.E., 1988. Mantle metasomatism by ephemeral carbonatite melts. Nature 336, 459.

Griffin, W.L., Taylor, P.N., 1975. The Fen Damkjernite: Petrology of a “central-complex kimberlite.” Physics and Chemistry of the Earth 9, 163–177.

Gudfinnsson, G.H., Presnall, D.C., 2005. Continuous Gradations among Primary Carbonatitic, Kimberlitic, Melilititic, Basaltic, Picritic, and Komatiitic Melts in Equilibrium with Garnet Lherzolite at 3–8 GPa. J. Petrology 46, 1645–1659.

Guzmics, T., Mitchell, R.H., Szabó, C., Berkesi, M., Milke, R., Ratter, K., 2012. Liquid immiscibility between silicate, carbonate and sulfide melts in melt inclusions hosted in co-precipitated minerals from Kerimasi volcano (Tanzania): evolution of carbonated nephelinitic magma. Contrib Mineral Petrol 164, 101–122.

Halama, R., 2005. The Gronnedal-Ika Carbonatite-Syenite Complex, South Greenland: Carbonatite Formation by Liquid Immiscibility. Journal of Petrology 46, 191–217.

Hamilton, D.L., Freestone, I.C., Dawson, J.B., Donaldson, C.H., 1979. Origin of carbonatites by liquid immiscibility. Nature 279, 52–54.

Hammouda, T., Laporte, D., 2000. Ultrafast mantle impregnation by carbonatite melts. Geology 28, 283–285.

Hanyu, T., Tatsumi, Y., Senda, R., Miyazaki, T., Chang, Q., Hirahara, Y., Takahashi, T., Kawabata, H., Suzuki, K., Kimura, J.-I., Nakai, S., 2011. Geochemical characteristics and origin of the HIMU reservoir: A possible mantle plume source in the lower mantle. Geochemistry, Geophysics, Geosystems 12.

Hart, S.R., 1984. The DUPAL anomaly: A large scale isotopic mantle anomaly in the Southern Hemisphere. Nature 309.

Harvey, J., König, S., Luguet, A., 2015. The effects of melt depletion and metasomatism on highly siderophile and strongly chalcophile elements: S–Se–Te–Re–PGE systematics of peridotite xenoliths from Kilbourne Hole, New Mexico. Geochimica et Cosmochimica Acta 166, 210–233.

Hauri, E.H., Shimizu, N., Dieu, J.J., Hart, S.R., 1993. Evidence for hotspot-related carbonatite metasomatism in the oceanic upper mantle. Nature 365, 221.

Haynes, E.A., Moecher, D.P., Spicuzza, M.J., 2003. Oxygen isotope composition of carbonates, silicates, and oxides in selected carbonatites: constraints on crystallization temperatures of carbonatite magmas. Chemical Geology 193, 43–57.

He, M., Zheng, H., Clift, P.D., 2013. Zircon U–Pb geochronology and Hf isotope data from the Yangtze River sands: Implications for major magmatic events and crustal evolution in Central China. Chemical Geology 360–361, 186–203.

Heinrich, E.W., 1966. The geology of carbonatites. Rand McNally, Chicago.

Herz, N., 1977. Timing of spreading in the South Atlantic: Information from Brazilian alkalic rocks. Geological Society of America Bulletin 88, 101–112.

Hode Vuorinen, J., Skelton, A.D.L., 2004. Origin of silicate minerals in carbonatites from Alnö Island, Sweden : magmatic crystallisation or wall rock assimilation. Terra Nova 16, 210–215.

Hoernle, K., Tilton, G., Le Bas, M., Duggen, S., Garbe-Schönberg, D., 2002. Geochemistry of oceanic carbonatites compared with continental carbonatites: mantle recycling of oceanic crustal carbonate. Contributions to Mineralogy and Petrology 142, 520–542.

Hofmann, A.W., 1997. Mantle geochemistry: the message from oceanic volcanism. Nature 385, 219–229.

Högbom, A.G., 1893. Über das Nephelinsyenitgebiet auf der Insel Alnö. Geologiska Föreningen i Stockholm Förhandlingar 17, 100–160.

Holm, P.M., Wilson, J.R., Christensen, B.P., Hansen, L., Hansen, S.L., Hein, K.M., Mortensen, A.K., Pedersen, R., Plesner, S., Runge, M.K., 2006. Sampling the Cape Verde Mantle Plume: Evolution of Melt Compositions on Santo Antão, Cape Verde Islands. Journal of Petrology 47, 145–189.

Holwell, D.A., Adeyemi, Z., Ward, L.A., Smith, D.J., Graham, S.D., McDonald, I., Smith, J.W., 2017. Low temperature alteration of magmatic Ni-Cu-PGE sulfides as a source for hydrothermal Ni and PGE ores: A quantitative approach using automated mineralogy. Ore Geology Reviews 91, 718–740.

Horan, M.F., Walker, R.J., Morgan, J.W., Grossman, J.N., Rubin, A.E., 2003. Highly siderophile elements in chondrites. Chemical Geology, Highly Siderophile elements in the Earth and Meteorties: A volume in honor of john Morgan 196, 27–42.

Hu, Z., Zhang, W., Liu, Y., Chen, H., Gaschnig, R.M., Zong, K., Li, M., Gao, S., Hu, S., 2013. Rapid bulk rock decomposition by ammonium fluoride (NH4F) in open vessels at an elevated digestion temperature. Chemical Geology 355, 144–152.

Huang, W.L., Wyllie, P.J., Nehru, C.E., 1975. Subsolidus and liquidus phase relationships in the system CaO-SiO2-CO2 to 30kb with geological applications. American Mineralogist 285–301.

Huang, Y.-M., Hawkesworth, C.J., van Calsteren, P., McDermott, F., 1995. Geochemical characteristics and origin of the Jacupiranga carbonatites, Brazil. Chemical Geology 119, 79–99.

Ickert, R.B., 2013. Algorithms for estimating uncertainties in initial radiogenic isotope ratios and model ages. Chemical Geology 340, 131–138.

Iizuka, T., Campbell, I.H., Allen, C.M., Gill, J.B., Maruyama, S., Makoka, F., 2013. Evolution of the African continental crust as recorded by U–Pb, Lu–Hf and O isotopes in detrital zircons from modern rivers. Geochimica et Cosmochimica Acta 107, 96–120.

Iizuka, T., Komiya, T., Rino, S., Maruyama, S., Hirata, T., 2010. Detrital zircon evidence for Hf isotopic evolution of granitoid crust and continental growth. Geochimica et Cosmochimica Acta 74, 2450–2472.

Iizuka, T., Yamaguchi, T., Hibiya, Y., Amelin, Y., 2015. Meteorite zircon constraints on the bulk Lu−Hf isotope composition and early differentiation of the Earth. Proc Natl Acad Sci U S A 112, 5331–5336.

Iizuka, T., Yamaguchi, T., Itano, K., Hibiya, Y., Suzuki, K., 2017. What Hf isotopes in zircon tell us about crust–mantle evolution. Lithos 274–275, 304–327.

Ishikawa, A., Senda, R., Suzuki, K., Dale, C.W., Meisel, T., 2014. Re-evaluating digestion methods for highly siderophile element and 187Os isotope analysis: Evidence from geological reference materials. Chemical Geology 384, 27–46.

Ivanyuk, G., Kalashnikov, A., Pakhomovsky, Y., Bazai, A., Goryainov, P., Mikhailova, J., Yakovenchuk, V., Konopleva, N., 2017. Subsolidus Evolution of the Magnetite-Spinel-UlvöSpinel Solid Solutions in the Kovdor Phoscorite-Carbonatite Complex, NW Russia. Minerals 7, 215.

Jacobsen, S.B., Wasserburg, G.J., 1980. Sm-Nd isotopic evolution of chondrites. Earth and Planetary Science Letters 50, 139–155.

Jäger, E., 1979. The Rb—Sr Method, in: Lectures in Isotope Geology. Springer, Berlin, Heidelberg, pp. 13–26.

Janney, P.E., Le Roex, A.P., Carlson, R.W., Viljoen, K.S., 2002. A chemical and multi-isotope study of the Western Cape olivine melilitite province, South Africa: Implications for the sources of kimberlites and the origin of the HIMU signature in Africa. J. Petrol. 43, 2339–2370.

Jennings, D.S., Mitchell, R.H., 1969. An estimate of the temperature of intrusion of carbonatite at the Fen complex, S. Norway. Lithos 2, 167–169.

Johnson, C.M., Bell, K., Beard, B.L., Shultis, A.I., 2010. Iron isotope compositions of carbonatites record melt generation, crystallization, and late-stage volatile-transport processes. Miner Petrol 98, 91–110.

Jones, A.P., Genge, M.J., Carmody, L., 2013. Carbonate melts and carbonatites, in: Hazen, R.M., Jones, A.P., Baross, J.A. (Eds.), Reviews in Mineralogy & Geochemistry - Carbon in Earth. Mineralogical society of America, USA, 280–322.

Jorgenson, C., 2017. Sulphur solubility of carbonatites as a mass transfer agent in the mantle (Bachelor thesis). Dalhousie University, Halifax, NS, Canada.

Klaudius, J., Keller, J., 2006. Peralkaline silicate lavas at Oldoinyo Lengai, Tanzania. Lithos, Peralkaline RocksA special issue dedicated to Henning SørensenPERALK2005 Workshop 91, 173–190.

Kononova, V.A., Shanin, L.L., 1971. On possible application of nepheline for alkaline rock dating. Bull Volcanol 35, 251–264.

Kossert, K., Jörg, G., Gostomski, C.L. v., 2013. Experimental half-life determination of 176Lu. Applied Radiation and Isotopes, 6th International Conference on Radionuclide Metrology - Low Level Radioactivity Measurement Techniques 81, 140–145.

Krafft, M., Keller, J., 1989. Temperature measurements in carbonatite lava lakes and flows from oldoinyo lengai, Tanzania. Science 245, 168–170.

Kukharenko, A.A., 1967. Alkaline magmatic activity of eastern part of the Baltic shield. Zapiski Vserossiskogo Mineralogicheskogo Obshchetstva 96, 547–566.

Kullerud, G., 1970. Sulfide phase relations. Mineral. Soc. Ameri. Spec. Pap. 3, 199–210.

Lancelot, J.R., Allègre, C.J., 1974. Origin of carbonatitic magma in the light of the Pb-U-Th isotope system. Earth and Planetary Science Letters 22, 233–238.

Larsen, L.M., Pedersen, A.K., 1982. A minor carbonatite occurrence in southern West Greenland: the Tupertalik intrusion, in: Ellitsgaard-Rasmussen, K. (Ed.), The Geological Survey of Greenland Report No. 110. Kobenhavn, 38–43.

Larsen, L.M., Rex, D.C., 1992. A review of the 2500 Ma span of alkaline-ultramafic, potassic and carbonatitic magmatism in West Greenland. Lithos, Potassic and ultrapotassic magmas and their origin 28, 367–402.

Larsen, L.M., Rex, D.C., Secher, K., 1983. The age of carbonatites, kimberlites and lamprophyres from southern West Greenland: recurrent alkaline magmatism during 2500 million years. Lithos 16, 215–221.

Le Bas, M.J., 1989. Diversification of carbonatite, in: Bell, K. (Ed.), Carbonatites - Genesis and Evolution. Unwyn Hyman, London, 428–447.

Le Bas, M.J., 1981. Carbonatite magmas. Mineralogical Magazine 44, 133–140.

Lee, M.J., Lee, J.I., Hur, S.D., Kim, Y., Moutte, J., Balaganskaya, E., 2006a. Sr–Nd–Pb isotopic compositions of the Kovdor phoscorite–carbonatite complex, Kola Peninsula, NW Russia. Lithos, Peralkaline RocksA special issue dedicated to Henning SørensenPERALK2005 Workshop 91, 250–261.

Lee, M.J., Lee, J.I., Hur, S.D., Kim, Y., Moutte, J., Balaganskaya, E., 2006b. Sr–Nd–Pb isotopic compositions of the Kovdor phoscorite–carbonatite complex, Kola Peninsula, NW Russia. Lithos, Peralkaline Rocks 91, 250–261.

Lee, M.J., Lee, J.I., Moutte, J., 2005. Compositional variation of Fe−Ti oxides from the Sokli complex, northeastern Finland. Geosci J 9, 1–13.

Lentz, D.R., 1999. Carbonatite genesis: A reexamination of the role of intrusion-related pneumatolytic skarn processes in limestone melting. Geology 27, 335–338.

Lie, A., Østergaard, C., 2011. The Fen carbonatite complex, Ulefoss, South Norway.

Liu, Y., Samaha, N.-T., Baker, D.R., 2007. Sulfur concentration at sulfide saturation (SCSS) in magmatic silicate melts. Geochimica et Cosmochimica Acta 71, 1783–1799.

Long, K.R., Van Gosen, B.S., Foley, N.K., Cordier, D., 2010. The geology of rare earth elements. Republished from: The Principal Rare Earth Elements Deposits of the United States.

Ludwig, K.R., 2010. Isoplot/Ex Version 4.1: a Geochronological Toolkit for Microsoft Excel; Berkeley Geochronology Center Special Publication: Berkeley, CA, USA

Luguet, A., Lorand, J.-P., Seyler, M., 2003. Sulfide petrology and highly siderophile element geochemistry of abyssal peridotites: a coupled study of samples from the Kane Fracture Zone (45°W 23°20N, MARK area, Atlantic Ocean). Geochimica et Cosmochimica Acta 67, 1553–1570.

Luguet, A., Nowell, G.M., Pearson, D.G., 2008. 184Os/188Os and 186Os/188Os measurements by Negative Thermal Ionisation Mass Spectrometry (N-TIMS): Effects of interfering element and mass fractionation corrections on data accuracy and precision. Chemical Geology, Highly Siderophile Element Geochemistry 248, 342–362.

Luguet, A., Reisberg, L., 2016. Highly Siderophile Element and 187Os Signatures in Non-cratonic Basalt-hosted Peridotite Xenoliths: Unravelling the Origin and Evolution of the Post-Archean Lithospheric Mantle. Reviews in Mineralogy and Geochemistry 81, 305–367.

Luguet, A., Shirey, S.B., Lorand, J.-P., Horan, M.F., Carlson, R.W., 2007. Residual platinum-group minerals from highly depleted harzburgites of the Lherz massif (France) and their role in HSE fractionation of the mantle. Geochimica et Cosmochimica Acta 71, 3082–3097.

Madeira, J., Munhá, J., Tassinari, C.C.G., Mata, J., Brum da Silveira, A., Martins, S., 2005. K/Ar ages of carbonatites from the island of fogo (Cape Verde). IV semana de Geoquímica & VIII Congresso de Geoquímica dos Países de Língua Portuguesa 475–478.

Maitre, R.W.L., Streckeisen, A., Zanettin, B., Bas, M.J.L., Bonin, B., Bateman, P., 2002. Igneous Rocks: A Classification and Glossary of Terms: Recommendations of the International Union of Geological Sciences Subcommission on the Systematics of Igneous Rocks. Cambridge University Press.

Marcantonio, F., Reisberg, L., Zindler, A., Wyman, D., Hulbert, L., 1993a. An isotopic study of the Ni-Cu-PGE-rich Wellgreen intrusion of the Wrangellia Terrane: Evidence for hydrothermal mobilization of rhenium and osmium. Geochimica et Cosmochimica Acta 58, 1007–1018.

Marcantonio, F., Zindler, A., Reisberg, L., Mathez, E.A., 1993b. Re-Os isotopic systematics in chromitites from the Stillwater Complex, Montana, USA. Geochimica et Cosmochimica Acta 57, 4029–4037.

Mariano, A.N., 1989. Nature of economic mineralization in carbonatites and related rocks, in: Bell, K. (Ed.), Carbonatites - Genesis and Evolution. Unwin Hyman Ltd., Boston, 149–176.

Martin, C.A., Duchêne, S., Luais, B., Goncalves, P., Deloule, E., Fournier, C., 2010. Behavior of trace elements in relation to Lu–Hf and Sm–Nd geochronometers during metamorphic dehydration–hydration in the HP domain of Vårdalsneset, Western Gneiss Region, Norway. Contributions to Mineralogy and Petrology, 437–458.

Marty, B., Tolstikhin, I., Kamensky, I.L., Nivin, V., Balaganskaya, E., Zimmermann, J.-L., 1998. Plume-derived rare gases in 380 Ma carbonatites from the Kola region (Russia) and the argon isotopic composition in the deep mantle. Earth and Planetary Science Letters 164, 179–192.

Mata, J., Moreira, M., Doucelance, R., Ader, M., Silva, L.C., 2010. Noble gas and carbon isotopic signatures of Cape Verde oceanic carbonatites: Implications for carbon provenance. Earth and Planetary Science Letters 291, 70–83.

Mattsson, H.B., Balashova, A., Almqvist, B.S.G., Bosshard-Stadlin, S.A., Weidendorfer, D., 2018. Magnetic mineralogy and rock magnetic properties of silicate and carbonatite rocks from Oldoinyo Lengai volcano (Tanzania). Journal of African Earth Sciences 142, 193–206.

Mavrogenes, J.A., O'Neill, H.S.C., 1999. The relative effects of pressure, temperature and oxygen fugacity on the solubility of sulfide in mafic magmas. Geochimica et Cosmochimica Acta 63, 1173–1180.

McCammon, C., Griffin, W.L., Shee, S., O'Neill, H., 2001. Oxidation during metasomatism in ultramafic xenoliths from the Wesselton kimberlite, South Africa: implications for the survival of diamond. Contributions to Mineralogy and Petrology 141, 287.

McCammon, C., Kopylova, M.G., 2004. A redox profile of the Slave mantle and oxygen fugacity control in the cratonic mantle. Contrib Mineral Petrol 148, 55–68.

McDonough, W.F., 2003. Compositional Model for the Earth's Core. Treatise on Geochemistry 2, 568.

McDonough, W.F., Sun, S. -s., 1995. The composition of the Earth. Chemical Geology, Chemical Evolution of the Mantle 120, 223–253.

McKie, D., Frankis, E.J., 1976. Nyerereite: a new volcanic carbonate mineral from Oldoinyo Lengai, Tanzania : Zeitschrift für Kristallographie [WWW Document].

Meisel, T., Moser, J., 2004a. Platinum-Group Element and Rhenium Concentrations in Low Abundance Reference Materials. Geostandards and Geoanalytical Research 28, 233–250.

Meisel, T., Moser, J., 2004b. Reference materials for geochemical PGE analysis: new analytical data for Ru, Rh, Pd, Os, Ir, Pt and Re by isotope dilution ICP-MS in 11 geological reference materials. Chemical Geology, Highly Siderophile Element Behavior in High Temperature Processes 208, 319–338.

Meisel, T., Moser, J., Fellner, N., Wegscheider, W., Schoenberg, R., 2001. Simplified method for the determination of Ru, Pd, Re, Os, Ir andPt in chromitites and other geological materials by isotope dilution ICP-MSand acid digestion. Analyst 126, 322–328.

Mercier-Langevin, P., Houlé, M.G., Dubé, B., Monecke, T., Hannington, M.D., Gibson, H.L., Goutier, J., 2012. A Special Issue on Archean Magmatism, Volcanism, and Ore Deposits: Part 1. Komatiite-Associated Ni-Cu-(PGE) Sulfide and Greenstone-Hosted Au DepositsPreface(,). Economic Geology 107, 745–753.

Millet, M.-A., Baker, J.A., Payne, C.E., 2012. Ultra-precise stable Fe isotope measurements by high resolution multiple-collector inductively coupled plasma mass spectrometry with a 57Fe–58Fe double spike. Chemical Geology 304–305, 18–25.

Mitchell, R.H., 2015. Primary and secondary niobium mineral deposits associated with carbonatites. Ore Geology Reviews 64, 626–641.

Mitchell, R.H., Keays, R.R., 1981. Abundance and distribution of gold, palladium and iridium in some spinel and garnet lherzolites: implications for the nature and origin of precious metal-rich intergranular components in the upper mantle. Geochimica et Cosmochimica Acta 45, 2425–2442.

Mitchell, R.H., Krouse, H.R., 1975. Sulphur isotope geochemistry of carbonatites. Geochimica et Cosmochimica Acta 39, 1505–1513.

Murowchick, J.B., Barnes, H.L., 1986. Marcasite precipitation from hydrothermal solutions. Geochimica et Cosmochimica Acta 50, 2615–2629.

Myers, J., Eugster, H.P., 1983. The system Fe-Si-O: Oxygen buffer calibrations to 1,500K. Contr. Mineral. and Petrol. 82, 75–90.

Naldrett, A.J., 1997. Key factors in the genesis of Noril'sk, Sudbury, Jinchuan, Voisey's Bay and other world-class Ni-Cu-PGE deposits: Implications for exploration. Australian Journal of Earth Sciences 44, 283–315.

Nelson, D.R., Chivas, A.R., Chappell, B.W., McCulloch, M.T., 1988. Geochemical and isotopic systematics in carbonatites and implications for the evolution of ocean-island sources. Geochimica et Cosmochimica Acta 52, 1–17.

Nielsen, T.F., Veksler, I.V., 2002. Is natrocarbonatite a cognate fluid condensate? Contributions to Mineralogy and Petrology 142, 425–435.

Notholt, A.J.G., Highley, D.E., Deans, T., 1990. Economic minerals in carbonatites and associated alkaline igneous rocks. Institute of Mineralogy and Metallurgy, Transactions 99.

Nowell, G.M., Kempton, P.D., Noble, S.R., Fitton, J.G., Saunders, A.D., Mahoney, J.J., Taylor, R.N., 1998a. High precision Hf isotope measurements of MORB and OIB by thermal ionisation mass spectrometry: insights into the depleted mantle. Chemical Geology 149, 211–233.

Nowell, G.M., Pearson, D.G., Bell, D.R., Carlson, R.W., Smith, C.B., Kempton, P.D., Noble, S.R., 2004. Hf Isotope Systematics of Kimberlites and their Megacrysts: New Constraints on their Source Regions. J Petrology 45, 1583–1612.

Nowell, G.M., Pearson, D.G., Irving, A.J., Turner, S.P., 1998b. A Hf isotope study of lamproites: Implications for their origins and relationship to kimberlite. (Conference abstract), Extended Abstracts 7th International Kimberlite Conference. Cape Town.

Nowell, G.M., Pearson, D.G., Kempton, P.D., Noble, S.R., Smith, C.B., 1999. Origins of kimberlites: a Hf isotope perspective., in: Gurney, J.J., Gurney, J.L., Pascoe, M.D., Richardson, S.H. (Eds.), Proceedings 7th International Kimberlite Conference, Cape Town. Goodwood, S. Africa: National Book Printer, 616–624.

Nowell, G.M., Pearson, D.G., Parman, S.W., Luguet, A., Hanski, E., 2008. Precise and accurate 186Os/188Os and 187Os/188Os measurements by Multi-collector Plasma Ionisation Mass Spectrometry, part II: Laser ablation and its application to single-grain Pt–Os and Re–Os geochronology. Chemical Geology, Highly Siderophile Element Geochemistry 248, 394–426.

O'Driscoll, B., González-Jiménez, J.M., 2016. Petrogenesis of the Platinum-Group Minerals. Reviews in Mineralogy and Geochemistry 81, 489–578.

Ottley, C.J., Pearson, D.G., Irvine, G.J., 2003. A routine method for the dissolution of geological samples for the analysis of REE and trace elements via ICP-MS, in: Holland, J.G., Tanner, S.D. (Eds.), Special Publications. Royal Society of Chemistry, Cambridge, 221–230.

Paarma, H., 1970. A new find of carbonatite in North Finland, the Sokli plug in Savukoski. Lithos 3, 129–133.

Paarma, H., Talvitie, J., 1976. Deep fractures - Sokli carbonatite. University of Oulu, Department of Geophysics Contribution 65, 5.

Pearce, N.J.G., Leng, M.J., Emeleus, C.H., Bedford, C.M., 1997. The origins of carbonatites and related rocks from the Gronnedal-Ika Nepheline Syenite complex, South Greenland: C-O-Sr isotope evidence. Mineral. Mag. 61, 515–529.

Pearson, D.G., Nowell, G.M., 2003. Dating Mantle Differentiation: a comparison of the Lu-Hf, Re-Os &Sm-Nd isotope systems in the Beni Bousera peridotite massif and constraints on the Nd-Hf isotope composition of the lithospheric mantle. Presented at the EGS - AGU - EUG Joint Assembly, 5430.

Pearson, D.G., Woodland, S.J., 2000. Solvent extraction/anion exchange separation and determination of PGEs (Os, Ir, Pt, Pd, Ru) and Re–Os isotopes in geological samples by isotope dilution ICP-MS. Chemical Geology 165, 87–107.

Peregoedova, A., Barnes, S.-J., Baker, D.R., 2004. The formation of Pt–Ir alloys and Cu–Pd-rich sulfide melts by partial desulfurization of Fe–Ni–Cu sulfides: results of experiments and implications for natural systems. Chemical Geology, Highly Siderophile Element Behavior in High Temperature Processes 208, 247–264.

Petrov, S.V., 2004. Economic deposits associated with the alkaline and ultrabasic complexes of the Kola Peninsula, in: Wall, F., Zaitsev, A.N. (Eds.), Phoscorites and Carbonatites from Mantle to Mine: The Key Example of the Kola Alkaline Province, Mineralogical Society Series. Mineralogical Society, London, 469–490.

Peucker-Ehrenbrink, B., Hanghoj, K., Atwood, T., Kelemen, P.B., 2012. Rhenium-osmium isotope systematics and platinum group element concentrations in oceanic crust. Geology 40, 199–202.

Pineau, F., Allègre, C.J., 1972. Study and significance of the strontium-87/strontium-86 ratios in carbonatites. Comptes Rendus des Seances de l'Academie des Sciences, Serie D: Sciences Naturelles 274, 2620–2623.

Pirajno, F., 2015. Intracontinental anorogenic alkaline magmatism and carbonatites, associated mineral systems and the mantle plume connection. Gondwana Research 27, 1181–1216.

Pokhilenko, N.P., Agashev, A.M., Litasov, K.D., Pokhilenko, L.N., 2015. Carbonatite metasomatism of peridotite lithospheric mantle: implications for diamond formation and carbonatite-kimberlite magmatism. Russian Geology and Geophysics 56, 280–295.

Polák, L., Ackerman, L., Magna, T., Rapprich, V., Upadhyah, D., 2016. Highly siderophile element geochemistry of carbonatites and associated alkaline rocks from Tamil Nadu. Presented at the Goldschmidt conference, Yokohama, Japan.

Qian, G., Xia, F., Brugger, J., Skinner, W.M., Bei, J., Chen, G., Pring, A., 2011. Replacement of pyrrhotite by pyrite and marcasite under hydrothermal conditions up to 220 C: An experimental study of reaction textures and mechanisms. American Mineralogist 96, 1878–1893.

Ramberg, I.B., 1973. Gravity studies of the Fen complex, Norway, and their petrological significance. Contr. Mineral. and Petrol. 38, 115–134.

Rankin, A.H., 1977. Fluid-Inclusion Evidence for the Formation Conditions of Apatite from the Tororo Carbonatite Complex of Eastern Uganda. Mineralogical Magazine 41, 155–164.

Reguir, E.P., Chakhmouradian, A.R., Halden, N.M., Yang, P., Zaitsev, A.N., 2008. Early Magmatic and Reaction-induced Trends in Magnetite from the Carbonatites of Kerimasi, Tanzania. The Canadian Mineralogist 46, 879–900.

Rehkämper, M., Halliday, A.N., 1997. Development and application of new iondashexchange techniques for the separation of the platinum group and other siderophile elements from geological samples. Talanta 44, 663–672.

Rehkämper, M., Halliday, A.N., Wentz, R.F., 1998. Low-blank digestion of geological samples for platinum-group element analysis using a modified Carius Tube design. Fresenius J Anal Chem 361, 217–219.

Reich, M., Deditius, A., Chryssoulis, S., Li, J.-W., Ma, C.-Q., Parada, M.A., Barra, F., Mittermayr, F., 2013. Pyrite as a record of hydrothermal fluid evolution in a porphyry copper system: A SIMS/EMPA trace element study. Geochimica et Cosmochimica Acta 104, 42–62.

Reisberg, L., Zindler, A., Marcantonio, F., White, W., Wyman, D., Weaver, B., 1993. Os isotope systematics in ocean island basalts. Earth and Planetary Science Letters 120, 149–167.

Richard, P., Shimizu, N., Allegre, C.J., 1974. 143Nd/ 146Nd, a natural tracer: an application to oceanic basalts. Earth and Planetary Science Letters 31, 269–278.

Richardson, D.G., Birkett, T.C., 1996. Carbonatite-associated deposits, in: Eckstrand, O.R., Sinclair, W.D., Thorpe, R.I. (Eds.), Geology of Canadian Mineral Deposit Types. Geological Survey of Canada, Ottawa, 541–558.

Richter, F.M., Dauphas, N., Teng, F.-Z., 2009. Non-traditional fractionation of non-traditional isotopes: Evaporation, chemical diffusion and Soret diffusion. Chemical Geology, Applications of non-traditional stable isotopes in high-temperature geochemistry 258, 92–103.

Ripp, G.S., Karmanov, N.S., Doroshkevich, A.G., Badmatsyrenov, M.V., Izbrodin, I.A., 2006. Chrome-bearing mineral phases in the carbonatites of northern Transbaikalia. Geochem. Int. 44, 395–402.

Rosenberg, P.E., 1967. Subsolidus relations in the system CaCO3 - MgCO3 - FeCO3 between 350 and 550 C. American Mineralogist 52, 787–796.

Roskosz, M., Sio, C.K.I., Dauphas, N., Bi, W., Tissot, F.L.H., Hu, M.Y., Zhao, J., Alp, E.E., 2015. Spinel–olivine–pyroxene equilibrium iron isotopic fractionation and applications to natural peridotites. Geochimica et Cosmochimica Acta 169, 184–199.

Rowe, R.B., 1958. Niobium (Columbium) deposits of Canada. Geological Survey of Canada, Economic Geology Series 18, 29–31.

Rudashevsky, N.S., Kretser, Y.L., Rudashevsky, V.N., Sukharzhevskaya, E.S., 2004. A review and comparison of PGE, noble-metal and sulphide mineralization in phoscorites and carbonatites from Kovdor and Phalaborwa. 363–393.

Rudnick, R.L., McDonough, W.F., Chappell, B.W., 1993. Carbonatite metasomatism in the northern Tanzanian mantle: Petrographic and geochemical characteristics. Earth and Planetary Science Letters 114, 463–475.

Rukhlov, A., Bell, K., 2003. Depleted mantle: the story from Hf isotopes in zircon and baddeleyite from carbonatites. Presented at the EGS - AGU - EUG Joint Assembly, 13944.

Salters, V.J.M., Hart, S.R., 1991. The mantle sources of ocean ridges, islands and arcs: the Hf-isotope connection. Earth and Planetary Science Letters 104, 364–380.

Santos, R.V., clayton, R.N., 1995. Variations of oxygen and carbon isotopes in carbonatites: A study of Brazilian alkaline complexes. Geochimica et Cosmochimica Acta 59, 1339–1352.

Schrauder, M., Navon, O., 1993. Solid carbon dioxide in a natural diamond. Nature 365, 42–44.

Schuessler, J.A., Schoenberg, R., Behrens, H., Blanckenburg, F. von, 2007. The experimental calibration of the iron isotope fractionation factor between pyrrhotite and peralkaline rhyolitic melt. Geochimica et Cosmochimica Acta 71, 417–433.

Schweitzer, K.M., 2015. Highly siderophile elements (HSE) and 187Os signatures of the mantle xenoliths from the Hyblean Plateau, Sicily. Unpublished master thesis, University of Bonn, 16.

Shafiqullah, M., Tupper, W.M., Cole, T.J.S., 1970. K-Ar age of the carbonatite complex, Oka, Quebec. The Canadian Mineralogist 10, 541–552.

Shahar, A., Young, E.D., Manning, C.E., 2008. Equilibrium high-temperature Fe isotope fractionation between fayalite and magnetite: An experimental calibration. Earth and Planetary Science Letters 268, 330–338.

Simon, N.S.C., Pearson, G., Davies, G.R., 2002. The Lu-Hf isotope composition of cratonic lithosphere: Disequilibrium between garnet and clinopyroxene in kimberlite xenoliths. Geochimica et Cosmochimica Acta A717.

Simonetti, A., Bell, K., Shrady, C., 1997. Trace- and rare-earth-element geochemistry of the June 1993 natrocarbonatite lavas, Oldoinyo Lengai (Tanzania): Implications for the origin of carbonatite magmas. Journal of Volcanology and Geothermal Research 75, 89–106.

Skinner, B.J., Luce, F.D., Dill, J.A., Ellis, D.E., Hagan, H.A., Lewis, D.M., Odell, D.A., Sverjensky, D.A., Williams, N., 1976. Phase relations in ternary portions of the system Pt-Pd-Fe-As-S. Economic Geology 71, 1469–1475.

Smoliar, M.I., Walker, R.J., Morgan, J.W., 1996. Re-Os Ages of Group IIA, IIIA, IVA, and IVB Iron Meteorites. Science 271, 1099–1102.

Steiger, R.H., Jäger, E., 1977. Subcommission on geochronology: Convention on the use of decay constants in geo- and cosmochronology. Earth and Planetary Science Letters 36, 359–362.

Smith, M., Kynicky, J., Xu, C., Song, W., Spratt, J., Jeffries, T., Brtnicky, M., Kopriva, A., Cangelosi, D., 2018. The origin of secondary heavy rare earth element enrichment in carbonatites: Constraints from the evolution of the Huanglongpu district, China. Lithos 308–309, 65–82.

Stille, P., Unruh, D.M., Tatsumoto, M., 1986. Pb, Sr, Nd, and Hf isotopic constraints on the origin of Hawaiian basalts and evidence for a unique mantle source. Geochimica et Cosmochimica Acta 50, 2303–2319.

Stosch, H.-G., 2004. Einführung in die Isotopengeochemie.

Stracke, A., Hofmann, A.W., Hart, S.R., 2005. FOZO, HIMU, and the rest of the mantle zoo. Geochemistry, Geophysics, Geosystems 6.

Streckeisen, A., 1979. Classification and nomenclature of volcanic rocks, lamprophyres, carbonatites and melilitic rocks: recommendations and suggestions of the IUGS Subcommission on the Systematics of Igneous Rocks. Geology 7, 331–335.

Streckeisen, A., 1978. IUGS Subcommission on the Systematics of Igneous Rocks. Classification and Nomenclature of Volcanic Rocks, Lamprophyres, Carbonatites and Melilite Rocks. Recommendations and Suggestions., in: Neues Jahrbuch Für Mineralogie, Abhandlungen. 1–14.

Su, Y., Langmuir, C.H., 2003. Global MORB chemistry compilation at the segment scale. Department of Earth Sciences, Columbia University.

Sun, S.–., McDonough, W.F., 1989. Chemical and isotopic systematics of oceanic basalts: implications for mantle composition and processes. Geological Society, London, Special Publications 42, 313–345.

Suwa, B.K., Oana, S., Wada, H., Osaki, S., 1975. Isotope geochemistry and petrology of African carbonatites. Physics and Chemistry of the Earth 9, 735–745.

Sweeney, R.J., 1994. Carbonatite melt compositions in the Earth's mantle. Earth and Planetary Science Letters 128, 259–270.

Tanaka, R., Makishima, A., Kitagawa, H., Nakamura, E., 2003. Suppression of Zr, Nb, Hf and Ta coprecipitation in fluoride compounds for determination in Ca-rich materials. J. Anal. At. Spectrom. 18, 1458–1463.

Tappe, S., Foley, S.F., Kjarsgaard, B.A., Romer, R.L., Heaman, L.M., Stracke, A., Jenner, G.A., 2008. Between carbonatite and lamproite—Diamondiferous Torngat ultramafic lamprophyres formed by carbonate-fluxed melting of cratonic MARID-type metasomes. Geochimica et Cosmochimica Acta 72, 3258–3286.

Van Gosen, B.S., Verplanck, P.L., Long, K.R., Gambogi, J., Seal, R.R., 2014. The Rare-Earth Elements—Vital to Modern Technologies and Lifestyles.

van Straaten, P., 2002. Rocks for crops: Agrominerals of sub-Saharan Africa. ICRAF, Nairobi, Kenya.

Vartiainen, H., Paarma, H., 1979. Geological characteristics of the Sokli carbonatite complex, Finland. Economic Geology 74, 1296–1306.

Vartiainen, H., Woolley, A.R., 1974. The age of the Sokli carbonatite, Finland, and some relationships of the North Atlantic alkaline igneous province. Bulletin of the Geological Society of Finland 46, 81–91.

Veksler, I.V., Lentz, D.R., 2006. Parental magmas of plutonic carbonatites, carbonate-silicate immiscibility and decarbonation reactions: evidence from melt and fluid inclusions. Miner Assoc Can Short Course 36, 123–149.

Veksler, I.V., Nielsen, T.F.D., Sokolov, S.V., 1998. Mineralogy of Crystallized Melt Inclusions from Gardiner and Kovdor Ultramafic Alkaline Complexes: Implications for Carbonatite Genesis. J Petrology 39, 2015–2031.

Vervoort, J., 2015. Lu-Hf Dating: The Lu-Hf Isotope System. Encyclopedia of Scientific Dating Methods. Encyclopedia of Scientific Dating Methods, 1-20.

Vervoort, J.D., Patchett, P.J., Blichert-Toft, J., Albarède, F., 1999. Relationships between Lu–Hf and Sm–Nd isotopic systems in the global sedimentary system. Earth and Planetary Science Letters 168, 79–99.

Verwoerd, W.J., 1986. Mineral deposits associated with carbonatites and alkaline rocks, in: Anhaeusser, C.R., Maske, S. (Eds.), Mineral Deposits of Southern Africa 2. The Geological Society of South Africa, Johannesburg, 2173–2191.

Walker, R.J., Shirey, S.B., Hanson, G.N., Rajamani, V., Horan, M.F., 1989. Re-Os, Rb-Sr, and O isotopic systematics of the Archean Kolar schist belt, Karnataka, India. Geochimica et Cosmochimica Acta 53, 3005–3013.

Wallace, M.E., Green, D.H., 1988. An experimental determination of primary carbonatite magma composition. Nature 335, 343–346.

Walter, M.J., Bulanova, G.P., Armstrong, L.S., Keshav, S., Blundy, J.D., Gudfinnsson, G., Lord, O.T., Lennie, A.R., Clark, S.M., Smith, C.B., Gobbo, L., 2008. Primary carbonatite melt from deeply subducted oceanic crust. Nature 454, 622–625.

Wang, C.Y., Campbell, I.H., Allen, C.M., Williams, I.S., Eggins, S.M., 2009. Rate of growth of the preserved North American continental crust: Evidence from Hf and O isotopes in Mississippi detrital zircons. Geochimica et Cosmochimica Acta 73, 712–728.

Wang, C.Y., Campbell, I.H., Stepanov, A.S., Allen, C.M., Burtsev, I.N., 2011. Growth rate of the preserved continental crust: II. Constraints from Hf and O isotopes in detrital zircons from Greater Russian Rivers. Geochimica et Cosmochimica Acta 75, 1308–1345.

Watkinson, D.H., Wyllie, P.J., 1971. Experimental Study of the Composition Join NaAlSiO4-CaCO3-H2O and the Genesis of Alkalic Rock—Carbonatite Complexes. J. Petrology 12, 357–378.

Wedepohl, H.K., 1995. The composition of the continental crust. Geochimica et Cosmochimica Acta 59, 1217–1232.

Weidendorfer, D., Schmidt, M.W., Mattsson, H.B., 2016. Fractional crystallization of Si-undersaturated alkaline magmas leading to unmixing of carbonatites on Brava Island (Cape Verde) and a general model of carbonatite genesis in alkaline magma suites. Contrib Mineral Petrol 171, 43.

Weyer, S., Ionov, D.A., 2007. Partial melting and melt percolation in the mantle: The message from Fe isotopes. Earth and Planetary Science Letters 259, 119–133.

White, R.S., 1989. Asthenospheric control on magmatism in the ocean basins. Geological Society, London, Special Publications 42, 17–27.

White, W.M., 2013. Geochemistry, 1st ed. Wiley-Blackwell, Hoboken, NJ.

Widom, E., Hoernle, K.A., Shirey, S.B., Schmincke, H.-U., 1999. Os Isotope Systematics in the Canary Islands and Madeira: Lithospheric Contamination and Mantle Plume Signatures. Journal of Petrology 40, 279–296.

Wiedenmann, D., Zaitsev, A.N., Britvin, S.N., Krivovichev, S.V., Keller, J., 2009. Alumoåkermanite, (Ca,Na)2(Al,Mg,Fe2+)(Si2O7), a new mineral from the active carbonatite-nephelinite-phonolite volcano Oldoinyo Lengai, northern Tanzania. Mineralogical Magazine 73, 373–384.

Williams, H.M., Peslier, A.H., McCammon, C., Halliday, A.N., Levasseur, S., Teutsch, N., Burg, J.-P., 2005. Systematic iron isotope variations in mantle rocks and minerals: The effects of partial melting and oxygen fugacity. Earth and Planetary Science Letters 235, 435–452.

Williams, H.M., Prytulak, J., Woodhead, J.D., Kelley, K.A., Brounce, M., Plank, T., 2018. Interplay of crystal fractionation, sulfide saturation and oxygen fugacity on the iron isotope composition of arc lavas: An example from the Marianas. Geochimica et Cosmochimica Acta 226, 224–243.

Wohlgemuth-Ueberwasser, C.C., Viljoen, F., Petersen, S., Vorster, C., 2015. Distribution and solubility limits of trace elements in hydrothermal black smoker sulfides: An in-situ LA-ICP-MS study. Geochimica et Cosmochimica Acta 159, 16–41.

Wolff, J.A., 1994. Physical properties of carbonatite magmas inferred from molten salt data, and application to extraction patterns from carbonatite–silicate magma chambers. Geological Magazine 131, 145–153.

Woolley, A.R., 1987. Alkaline rocks and carbonatites of the world: Part 1: North and South America. British Museum Natural History, London.

Woolley, A.R., 1969. Some aspects of fenitization with particular reference to Chilwa Island and Kangankunde, Malawi. Bulletin of the British Museum (Natural History), Mineralogy 2, 189–219.

Woolley, A.R., Church, A.A., 2005. Extrusive carbonatites: A brief review. Lithos 85, 1–14.

Woolley, A.R., Kempe, D.R.C., 1989. Carbonatites: nomenclature, average chemical compositions and element distribution, in: Bell, K. (Ed.), Carbonatite Genesis and Evolution. Unwin Hyman Ltd., London, 1–14.

Woolley, A.R., Kjarsgaard, B.A., 2008. Carbonatite occurrences of the world: map and database (No. 5796).

Workman, R.K., Hart, S.R., 2005. Major and trace element composition of the depleted MORB mantle (DMM). Earth and Planetary Science Letters 231, 53–72.

Wyllie, P.J., 1965. Melting relationships in the system CaO-MgO-CO2-H2O, with petrological applications. Journal of Petrology 6, 101–123.

Xiong, Y., Wood, S.A., 1999. Experimental determination of the solubility of ReO2 and the dominant oxidation state of rhenium in hydrothermal solutions. Chemical Geology 158, 245–256.

Yang, J., Gao, S., Chen, C., Tang, Y., Yuan, H., Gong, H., Xie, S., Wang, J., 2009. Episodic crustal growth of North China as revealed by U–Pb age and Hf isotopes of detrital zircons from modern rivers. Geochimica et Cosmochimica Acta 73, 2660–2673.

Yang, Y.-H., Wu, F.-Y., Wilde, S.A., Xie, L.-W., 2011. A straightforward protocol for Hf purification by single step anion-exchange chromatography and isotopic analysis by MC-ICP-MS applied to geological reference materials and zircon standards. International Journal of Mass Spectrometry 299, 47–52.

Yaxley, G.M., Crawford, A.J., Green, D.H., 1991. Evidence for carbonatite metasomatism in spinel peridotite xenoliths from western Victoria, Australia. Earth and Planetary Science Letters 107, 305–317.

Yaxley, G.M., Green, D.H., Kamenetsky, V., 1998. Carbonatite Metasomatism in the Southeastern Australian Lithosphere. J Petrology 39, 1917–1930.

Young, B.N., Parsons, I., Threadgould, R., 1994. Carbonatite near the Loch Borralan intrusion, Assynt. Journal of the Geological Society 151, 945–954.

Young, E.D., Manning, C.E., Schauble, E.A., Shahar, A., Macris, C.A., Lazar, C., Jordan, M., 2015. High-temperature equilibrium isotope fractionation of non-traditional stable isotopes: Experiments, theory, and applications. Chemical Geology 395, 176–195.

Zaitsev, A.N., Keller, J., 2006. Mineralogical and chemical transformation of Oldoinyo Lengai natrocarbonatites, Tanzania. Lithos 91, 191–207.

Zhang, J.Y., Yin, A., Liu, W.C., Wu, F.Y., Lin, D., Grove, M., 2012. Coupled U-Pb dating and Hf isotopic analysis of detrital zircon of modern river sand from the Yalu River (Yarlung Tsangpo) drainage system in southern Tibet: Constraints on the transport processes and evolution of Himalayan rivers. Geological Society of America Bulletin 124, 1449–1473.

Zhao, X., Zhang, H., Zhu, X., Tang, S., Tang, Y., 2010. Iron isotope variations in spinel peridotite xenoliths from North China Craton: implications for mantle metasomatism. Contrib Mineral Petrol 160, 1–14.

Zhu, M., Zhang, L., Dai, Y., Wang, C., Peng, Z., 2017. Hydrothermal modification of zircon geochemistry and Lu–Hf isotopes from the Hongtoushan Cu–Zn deposit, China. Ore Geology Reviews 86, 707–718.

Zindler, A., Hart, S., 1986. Chemical Geodynamics. Annual Review of Earth and Planetary Sciences 14, 493–571.

Chapter 10 : Appendix

10.1. Introduction

Table 10.1 List of minerals and their mineral formulas occurring in carbonatites and mentioned in the thesis, sorted alphabetically.

Aegirine	$NaFeSi_2O_6$
Aegirine-augite	$(Ca,Na)(Mg,Fe_2)[Si_2O_6]$
Ankerite	$Ca(Fe,Mg,Mn)(CO_3)_2$
Apatite	$Ca_5[(F,Cl,OH)\|(PO_4)_3]$
Arfvedsonite	$Na_3Fe_5(Si_8O_{22})(OH)_2$
Baddeleyite	ZrO_2
Barite	$BaSO_4$
Base metal sulphides (BMS)	*i.e.* FeS_2, $CuFeS_2$, Cu_5FeS_4, ZnS, $Fe_{1-x}S$, $(Fe,Ni)_9S_8$
Bastnäsite	$(Ce,La)CO_3(F,OH)$
Calcite	$CaCO_3$
Calzirtite	$CaZr_3TiO_9$
Dolomite	$CaMg(CO_3)_2$
Fluorite	CaF_2
Gregoryite	$(Na_2,K_2,Ca)CO_3$
Ilmenite	$FeTiO_3$
Isoferroplatinum	$(Pt,Pd)_3(Fe,Cu)$
Magnetite	Fe_3O_4
Mertieite	$Pd_{11}(Sb,As)_4$, $Pd_8(Sb,As)_3$
Monazite	$(Ce,La,Nd,Th)PO_4$
Nyerereite	$Na_2Ca(CO_3)_2$
Olivine	$(Mg,Fe)_2SiO_4$
Orthoclase	$KAlSi_3O_8$
Parisite	$Ca(Ce,La)_2(CO_3)_3F_2$
Perovskite	$CaTiO_3$
Phlogopite	$KMg_3AlSi_3O_{10}F(OH)$
Pyrochlore	$(Na,Ca)_2Nb_2O_6(OH,F)$
Siderite	$FeCO_3$
Strontianite	$SrCO_3$
Thorite	$ThSiO_4$
Uraninite	UO_2
Vermiculite	$(Mg,Fe,Al)_3(Al,Si)_4O_{10}(OH)_2 \times 4(H_2O)$
Xenotime	$(Y,Yb)PO_4$
Zircon	ZrSiO4
Zirconolite	$CaZrTi_2O_7$

Mineral formulas from https://www.webmineral.com

10.2. Methods

10.2.1. Diagrams and tables for the HSE procedure

Table 10.2 **Composition of the mixed highly siderophile element spike for basalt samples used in the Arthur Holmes Laboratories, Durham University.**

	Os [mol/g]	Ir [mol/g]	Ru [mol/g]	Pt [mol/g]	Pd [mol/g]	Re [mol/g]
Basalt spike	7.30^{-13}	3.62^{-12}	5.56^{-12}	9.15^{-11}	2.42^{-10}	1.86^{-10}

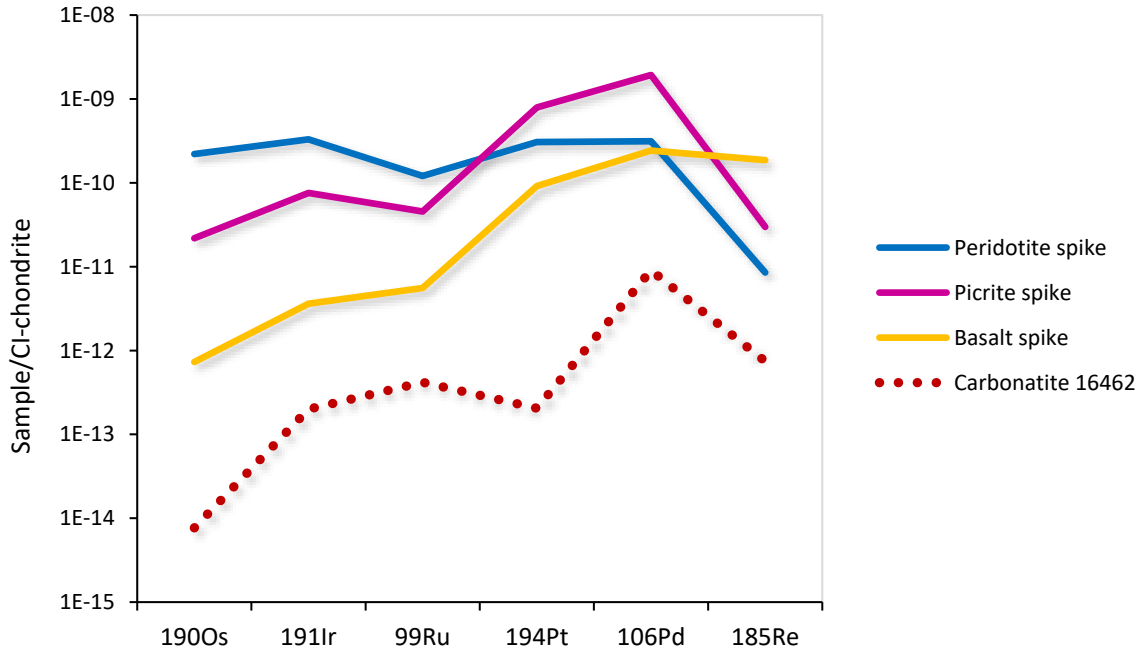

Figure 10.1 **CI-chondrite normalised HSE patterns for peridotite spike (blue), picrite spike (pink), basalt spike (yellow) and a carbonatite sample (red dashed line).**

Table 10.3 Comparison of Carius tube and HP Asher results for 10 samples from different localities and of different compositions. All samples are blank and spike corrected, but the detection limit was not taken into account for better comparison.

Sample No	OL-1		4808		16462	
Sample Type	Natrocarbonatite		Carbonatite		Carbonatite	
Method	Carius tube	HP Asher	Carius tube	HP Asher	Carius tube	HP Asher
Re [ppt]	7751.1	7881.6	1789.9	1824.4	137.1	140.7
Ir [ppt]	10.6	1.1	0.03	<0	21.49	104.9
Ru [ppt]	55.4	<0	39.7	<0	41.3	10.4
Pt [ppt]	8890.1	8706.6	27.2	18.4	42.8	27.6
Pd [ppt]	4927.7	2666.9	15.8	<0	957.8	205.7
Os [ppt]	0.5	1.6*	12.6	14.9*	1.4	1.6
$^{187}Os/^{188}Os_m$	0.1636	0.1115	48.6605	18.2743	5.5287	5.7579

Sample No	COQ-1			91/60 - C5		
Sample Type	Carbonatite std			Magnesiocarbonatite		
Method	Carius tube		HP Asher**	Carius tube		HP Asher
Re [ppt]	1211.9	1003.6	1428.8	29.1	36.8	41.1
Ir [ppt]	8.2	3.2	13.9	1.4	1.7	1.3
Ru [ppt]	73.1	21.4	<0	8.9	7.6	6.8
Pt [ppt]	49.7	20.9	13.8	20.9	23.8	33.8
Pd [ppt]	286.0	237.2	4586.9	166.8	107.0	75.7
Os [ppt]	3.8	2.9	3.3	4.8	5.0	5.1
$^{187}Os/^{188}Os_m$	4.6124	5.5063	6.6711	0.3705	0.3621	0.3577

Sample No	J1-C1		91/66 - C2		91/62 - C4	
Sample Type	Calciocarbonatite		Magnesiocarbonatite		Ferrocarbonatite	
Method	Carius tube	HP Asher	Carius tube	HP Asher	Carius tube	HP Asher
Re [ppt]	205.8	208.9	45.5	40.4	48.3	51.5
Ir [ppt]	0.18	0.0	1.15	1.4	0.22	<0
Ru [ppt]	27.3	6.5	6.7	9.8	1.9	3.6
Pt [ppt]	47.7	31.3	47.1	54.8	125.4	35.7
Pd [ppt]	188.3	516.9	<0	77.3	<0	<0
Os [ppt]	0.5	0.5	0.5	0.3	0.3	0.4
$^{187}Os/^{188}Os_m$	9.6890	12.0131	0.8569	1.8764	1.5398	1.2021

*low signal intensities

**Re, Ir, Ru, Pt & Pd likely cross-contaminated due to spattering sample

Continuation of Table 10.3

Sample No	19780		19781	
Sample Type	Carbonatite		Ferrocarbonatite	
Method	Carius tube	HP Asher**	Carius tube	HP Asher**
Re [ppt]	14.9	204.8	6.5	185.1
Ir [ppt]	10.64	0.2	<0	<0
Ru [ppt]	19.1	<0	20.4	<0
Pt [ppt]	41.6	10.4	4.2	4.6
Pd [ppt]	171.4	10.0	311.2	3317.8
Os [ppt]	1.3	1.2	0.4	0.6
$^{187}Os/^{188}Os_m$	6.7043	7.5614	1.0247	0.6872

*low signal intensities

**Re, Ir, Ru, Pt & Pd likely cross-contaminated due to spattering sample

Table 10.4 Spike corrected highly siderophile element and $^{187}Os/^{188}Os$ blanks for Carius tube digestions including average and detection limit. The detection limit was calculated as 3 × the standard deviation of "realistic blank" analyses (*c.f.* Chapter 3.7.8).

Re [ppt]	Ir [ppt]	Ru [ppt]	Pt [ppt]	Pd [ppt]	Os [ppt]	$^{187}Os/^{188}Os_m$
1.1	46.0	32.2	6.2	66.1	0.38	0.1632
1.1	0.9	13.7	2.9	47.7	0.27	0.1774
1.5	0.2	29.3	4.5	113.1	0.96	0.2150
0.6	121.1	58.2	30.2	87.1	0.72	0.2202
1.9	<0	23.2	2.8	112.4	DNR	DNR
0.7	16.6	19.5	5.8	66.3	0.19	0.2020
<0	0.8	16.2	6.3	10.3	0.30	0.1696
<0	1.0	14.5	4.9	9.9	0.09	0.2109
1.9	0.6	23.9	2.2	577.4	2.19	<0
1.9	48.4	34.7	16.3	1293.8	0.77	0.2248
Average						
1.3	26.2	26.5	8.2	238.40	0.65	0.1979
Detection limit						
2.3	1.0	23.2	12.7	120.9	0.9	2.3

Table 10.5 **Spike corrected highly siderophile element and $^{187}Os/^{188}Os$ blanks for high pressure Asher digestions including average and detection limit. The detection limit was calculated as 3 x the standard deviation of all analyses.**

Re [ppt]	Ir [ppt]	Ru [ppt]	Pt [ppt]	Pd [ppt]	Os [ppt]	$^{187}Os/^{188}Os_m$
48.8	26.8	39.4	113.3	59.23	0.43	0.1509
3176.6	2.1	42.4	8.3	62.2	0.34	0.1840
294.5	4.4	47.4	9.9	199.0	0.31	0.1574
1.5	4.6	71.4	10.2	72.46	0.23	0.1566
2.2	1.5	52.5	1.4	10.38	0.24	0.2927
Average						
704.7	7.9	50.6	28.6	80.66	0.31	0.1883
Detection limit						
4161.5	31.9	38.0	142.4	211.1	0.24	0.1793

10.2.2. Final column chemistry recipes HSE procedure

Table 10.6 Final recipe for anion column chemistry.

Anion column chemistry		
Column setup		
Step	**Reagent**	**Volume**
Resin cleaning	*MQ*	*10 ml*
	6M HNO_3	*10 ml*
	conc. HNO_3	*10 ml*
	MQ	*2 ml*
	conc. HCl	*10 ml*
	MQ	*2 ml*
Preconditioning	*1M HCl*	*2 ml*
	0.5 M HCl	*2 ml*
Elution procedure		
Step	**Reagent**	**Volume**
Sample loading	**0.5 M HCl incl. sample**	10 ml
Wash-In	*1M HCl*	*10 ml*
	0.8M HNO_3	*4 ml*
Collect Re-Ir-Pt-Ru	**conc. HNO_3**	10 ml
	conc. HNO_3	10 ml
Wash	*MQ*	*2 ml*
Collect Pd	**conc. HCl**	10 ml
	conc. HCl	10 ml
	conc. HCl	10 ml
	conc. HCl	10 ml

Table 10.7 Final recipe for LN-spec column chemistry.

LN-spec column chemistry		
Column setup		
Step	**Reagent**	**Volume**
Resin cleaning	*MQ*	*4 ml*
	6M HCl	*4 ml*
	6M HCl	*4 ml*
	2M HF	*4 ml*
	6M HCl	*4 ml*
	2M HF	*4 ml*
	MQ	*4 ml*
Preconditioning	*1M HCl*	*4 ml*
Elution procedure		
Step	**Reagent**	**Volume**
Load AND collect Pd	**1M HCl**	1 ml
Collect Pd	**1M HCl**	4 ml
Load AND collect Ir-Pt-Re-Ru	**1M HCl**	1 ml
Collect Ir-Pt-Re-Ru	**1M HCl**	5 ml
	1M HCl	2 ml
Wash	*2M HF*	*4 ml*
Cleaning	*2M HF*	*4 ml*
	6M HCl	*4 ml*
	2M HF	*4 ml*
	6M HCl	*4 ml*
	2M HF	*4 ml*
	6M HCl	*4 ml*

10.2.3. Final column chemistry recipes Hf-Nd-Sr chemistry

Table 10.8 **Column chemistry recipe for Sr-spec resin as performed in the Arthur Holmes Laboratories, Durham University.**

Sr-spec column chemistry		
Column setup		
Step	**Reagent**	**Volume**
Cleaning	*MQ*	*1 CV*
	TD 6M HCl	*1 CV*
	MQ	*1 CV*
Resin loading	**Sr-spec resin**	**80 µl**
Resin cleaning	*TD 6M HCl*	*1 CV*
	MQ	*2 CV*
Preconditioning	*3M HNO_3*	*200 µl*
Elution procedure		
Step	**Reagent**	**Volume**
Load AND collect Hf-Nd	**TD 3M HNO_3**	**800-1000 µl**
Collect Hf-Nd	**3M HNO_3**	**200 µl**
	3M HNO_3	**200 µl**
	3M HNO_3	**200 µl**
Collect Sr	**MQ**	**200 µl**
	MQ	**200 µl**
Waste	*2.5M HCl*	*200 µl*
	2.5M HCl	*200 µl*
Collect Pb	**8M HCl**	**200 µl**
	8M HCl	**200 µl**

Table 10.9 **Column chemistry recipe for cation resin as performed in the Arthur Holmes Laboratories, Durham University.**

Cation column chemistry		
Pre-procedure cleaning		
Step	**Reagent**	**Volume**
Cleaning	*TD 29 M HF*	*5 ml*
	MQ	*10 ml*
Preconditioning	*TD 1M HF-1M HCl*	*10 ml*
Elution procedure		
Step	**Reagent**	**Volume**
Load Nd-Hf fraction AND collect Hf	**1M HCl**	**1 ml**
Collect Hf	**1M HF-1M HCl**	**3 ml**
Waste	*TD 2.5M HCl*	*14 ml*
Ba elution	*TD 2M HNO_3*	*10 ml*
Collect Nd	**TD 6M HCl**	**12 ml**
Post-procedure cleaning		
Step	**Reagent**	**Volume**
Cleaning	*TD 29M HF*	*5 ml*
	MQ	*10 ml*
	TD 6M HCl	*10 ml*

Table 10.10 **Column chemistry recipe for anion resin as performed in the Arthur Holmes Laboratories, Durham University.**

Anion column chemistry		
Elution procedure		
Step	**Reagent**	**Volume**
Load Hf sample	**0.52M H_2SO_4-5% H_2O_2**	**1 ml**
Ti elution	*0.52M H_2SO_4-5% H_2O_2*	*5 ml*
	0.52M H_2SO_4-5% H_2O_2	*5 ml*
Collect Hf	**TD 1M HF-2M HCl**	**4 ml**
Post-procedure cleaning		
Step	**Reagent**	**Volume**
Cleaning	*TD 29M HF*	*5 ml*
	MQ	*5 ml*
	12M H_2SO_4	*4 ml*
	MQ	*5 ml*
Preconditioning	*0.52M H_2SO_4-5% H_2O_2*	*5 ml*

10.3. Data

10.3.1. Microprobe data

Table 10.11 Microprobe data and composition of base metal sulphides of five samples from Fen, Norway (TS 531 W, CQW-1, 16462) and Grønnedal-Ika, Greenland (19780, 19781).

Sample name	S (wt%)	Zn (wt%)	Fe (wt%)	Ni (wt%)	Co (wt%)	Cu (wt%)	Total (wt%)	Formula
TS 531 W - 1	54.18	0.00	45.22	0.02	0.12	0.00	99.5	FeS_2
TS 531 W - 2	54.30	0.18	44.64	0.00	0.09	0.02	99.2	FeS_2
TS 531 W - 3	53.74	0.00	44.50	0.05	0.08	0.00	98.4	FeS_2
TS 531 W - 4	53.88	0.00	44.68	0.00	0.07	0.02	98.7	FeS_2
TS 531 W - 5	54.13	0.00	44.64	0.00	0.09	0.05	98.9	FeS_2
TS 531 W - 6	54.02	0.08	44.75	0.00	0.07	0.06	99.0	FeS_2
TS 531 W - 7	53.62	0.04	44.59	0.01	0.07	0.11	98.4	FeS_2
TS 531 W - 8	53.72	0.00	44.53	0.04	0.06	0.00	98.4	FeS_2
TS 531 W - 8	53.38	0.00	44.84	0.03	0.06	0.00	98.3	FeS_2
TS 531 W - 9	52.99	0.13	44.03	0.00	0.08	0.00	97.2	FeS_2
TS 531 W - 9	53.38	0.02	44.48	0.04	0.07	0.00	98.0	FeS_2
TS 531 W - 10	53.44	0.00	44.43	0.02	0.09	0.06	98.0	FeS_2
TS 531 W - 11	53.08	0.01	44.64	0.00	0.09	0.00	97.8	FeS_2
TS 531 W - 12	53.22	0.00	44.35	0.00	0.06	0.00	97.6	FeS_2
TS 531 W - 13	52.96	0.00	44.06	0.00	0.08	0.00	97.1	FeS_2
TS 531 W - 14	53.41	0.02	44.63	0.07	0.06	0.00	98.2	FeS_2
TS 531 W - 15	53.20	0.04	44.31	0.05	0.07	0.10	97.8	FeS_2
TS 531 W - 16	53.47	0.07	44.52	0.08	0.06	0.00	98.2	FeS_2
TS 531 W - 17	53.46	0.00	44.44	0.03	0.06	0.06	98.0	FeS_2
TS 531 W - 18	54.03	0.00	44.72	0.00	0.09	0.00	98.8	FeS_2
TS 531 W - 19	54.01	0.02	44.79	0.08	0.07	0.00	99.0	FeS_2
TS 531 W - 20	54.36	0.00	44.38	0.00	0.07	0.02	98.8	FeS_2
TS 531 W - 21	53.75	0.15	45.06	0.07	0.06	0.02	99.1	FeS_2
TS 531 W - 22	53.19	0.00	44.55	0.00	0.08	0.02	97.8	FeS_2
TS 531 W - 23	53.94	0.00	44.86	0.00	0.09	0.00	98.9	FeS_2
TS 531 W - 24	53.16	0.00	44.76	0.02	0.08	0.00	98.0	FeS_2
TS 531 W - 25	53.32	0.00	44.48	0.00	0.07	0.00	97.9	FeS_2
CQW-1C - 1	54.41	0.02	44.06	0.00	0.17	0.00	98.7	FeS_2
CQW-1C - 2	53.11	0.00	44.06	0.00	0.11	0.00	97.3	FeS_2
CQW-1C - 3	53.77	0.00	44.15	0.02	0.08	0.00	98.0	FeS_2
CQW-1C - 4	53.52	0.07	43.63	0.06	0.08	0.02	97.4	FeS_2
CQW-1C - 5	53.38	0.02	43.93	0.00	0.08	0.00	97.4	FeS_2
CQW-1C - 6	53.42	0.00	44.23	0.00	0.11	0.00	97.8	FeS_2
CQW-1C - 7	53.35	0.01	44.16	0.02	0.07	0.06	97.7	FeS_2
CQW-1C - 8	53.75	0.03	44.14	0.00	0.06	0.00	98.0	FeS_2
CQW-1C - 9	53.10	0.00	43.70	0.00	0.13	0.00	96.9	FeS_2
CQW-1C - 10	53.53	0.04	44.11	0.02	0.09	0.07	97.9	FeS_2
CQW-1C - 11	52.86	0.00	43.94	0.00	0.08	0.00	96.9	FeS_2
CQW-1C - 12	53.83	0.02	43.78	0.00	0.08	0.02	97.7	FeS_2

Table 10.11 (continued)

Sample name	S (wt%)	Zn (wt%)	Fe (wt%)	Ni (wt%)	Co (wt%)	Cu (wt%)	Total (wt%)	Formula
CQW-1C - 13	53.41	0.00	43.69	0.00	0.13	0.03	97.3	FeS_2
CQW-1C - 14	54.28	0.00	44.24	0.00	0.10	0.05	98.7	FeS_2
CQW-1C - 15	52.70	0.06	43.80	0.00	0.11	0.00	96.7	FeS_2
CQW-1C - 16	53.56	0.00	43.70	0.03	0.09	0.00	97.4	FeS_2
CQW-1C - 17	53.58	0.08	44.10	0.02	0.09	0.04	97.9	FeS_2
CQW-1C - 18	52.73	0.04	44.04	0.00	0.06	0.00	96.9	FeS_2
CQW-1C - 19	53.11	0.11	43.89	0.00	0.08	0.00	97.2	FeS_2
CQW-1C - 20	53.93	0.09	43.85	0.00	0.07	0.00	97.9	FeS_2
CQW-1C - 21	53.48	0.00	43.98	0.00	0.06	0.00	97.5	FeS_2
CQW-1C - 22	53.24	0.00	44.13	0.00	0.08	0.00	97.5	FeS_2
CQW-1C - 23	53.88	0.00	44.13	0.01	0.08	0.00	98.1	FeS_2
CQW-1C - 24	53.69	0.00	43.86	0.00	0.08	0.00	97.6	FeS_2
CQW-1C - 25	53.13	0.07	44.11	0.00	0.06	0.03	97.4	FeS_2
CQW-1C - 26	54.00	0.00	44.12	0.00	0.10	0.00	98.2	FeS_2
CQW-1C - 27	53.45	0.00	43.95	0.01	0.10	0.00	97.5	FeS_2
CQW-1A - 1	53.62	0.00	44.45	0.00	0.06	0.05	98.2	FeS_2
CQW-1A - 2	54.12	0.00	43.99	0.00	0.07	0.09	98.3	FeS_2
CQW-1A - 3	54.12	0.00	44.77	0.02	0.09	0.00	99.0	FeS_2
CQW-1A - 4	53.68	0.00	44.46	0.03	0.08	0.06	98.3	FeS_2
CQW-1A - 5	52.81	0.00	44.19	0.05	0.10	0.00	97.2	FeS_2
CQW-1A - 6	54.36	0.00	44.39	0.00	0.09	0.07	98.9	FeS_2
CQW-1A - 7	53.15	0.05	44.05	0.03	0.07	0.00	97.3	FeS_2
CQW-1A - 8	53.26	0.01	44.42	0.01	0.08	0.00	97.8	FeS_2
CQW-1A - 9	53.29	0.00	44.54	0.04	0.10	0.00	98.0	FeS_2
CQW-1A - 10	53.38	0.05	44.10	0.00	0.08	0.00	97.6	FeS_2
CQW-1A - 11	54.55	0.12	44.18	0.02	0.07	0.00	98.9	FeS_2
CQW-1A - 12	53.80	0.05	43.73	0.00	0.18	0.00	97.8	FeS_2
CQW-1A - 13	54.34	0.06	43.76	0.00	0.09	0.08	98.3	FeS_2
CQW-1A - 14	53.91	0.02	44.23	0.01	0.07	0.10	98.3	FeS_2
CQW-1A - 15	52.90	0.00	44.51	0.00	0.09	0.05	97.6	FeS_2
CQW-1A - 16	53.44	0.05	44.40	0.00	0.05	0.03	98.0	FeS_2
CQW-1A - 17	54.08	0.00	44.53	0.03	0.07	0.06	98.8	FeS_2
CQW-1A - 18	53.77	0.03	44.29	0.00	0.14	0.00	98.2	FeS_2
CQW-1A - 19	53.69	0.00	44.55	0.00	0.07	0.00	98.3	FeS_2
CQW-1A - 20	54.23	0.07	44.20	0.02	0.10	0.00	98.6	FeS_2
CQW-1A - 21	54.09	0.13	44.46	0.00	0.05	0.01	98.7	FeS_2
CQW-1A - 22	53.49	0.04	44.35	0.00	0.08	0.10	98.0	FeS_2
CQW-1A - 25	54.05	0.00	44.48	0.03	0.05	0.05	98.7	FeS_2
CQW-1A - 26	53.23	0.01	43.87	0.04	0.10	0.00	97.2	FeS_2
CQW-1A - 27	53.27	0.01	44.14	0.02	0.06	0.00	97.5	FeS_2
CQW-1A - 28	53.36	0.11	43.65	0.05	0.10	0.04	97.3	FeS_2
CQW-1A - 29	53.24	0.02	44.27	0.00	0.08	0.00	97.6	FeS_2
CQW-1A - 30	53.50	0.00	44.47	0.00	0.10	0.06	98.1	FeS_2
CQW-1A - 31	52.64	0.04	44.25	0.07	0.06	0.04	97.1	FeS_2

Table 10.11 (continued)

Sample name	S (wt%)	Zn (wt%)	Fe (wt%)	Ni (wt%)	Co (wt%)	Cu (wt%)	Total (wt%)	Formula
CQW-1A - 32	53.35	0.00	44.32	0.05	0.08	0.04	97.8	FeS_2
CQW-1A - 33	53.37	0.06	44.14	0.04	0.09	0.00	97.7	FeS_2
16462 - 1	40.23	0.00	62.38	0.00	0.07	0.02	102.7	FeS
16462 - 2	39.76	0.00	62.25	0.02	0.07	0.00	102.1	FeS
16462 - 3	39.58	0.01	62.06	0.01	0.00	0.07	101.7	FeS
16462 - 4	55.42	0.00	48.10	0.00	0.56	0.02	104.1	FeS_2
16462 - 5	39.89	0.00	62.45	0.07	0.03	0.00	102.4	FeS
16462 - 6	53.23	0.00	44.90	0.00	2.52	0.05	100.7	FeS_2
16462 - 7	39.89	0.00	62.12	0.00	0.06	0.00	102.1	FeS
16462 - 8	53.06	0.00	46.07	0.03	2.55	0.00	101.7	FeS_2
16462 - 9_incl	38.60	0.00	62.03	0.01	0.17	0.00	100.8	FeS
16462 - 10	39.04	0.00	61.96	0.00	0.05	0.03	101.1	FeS
16462 - 11	39.96	0.00	62.57	0.00	0.06	0.05	102.6	FeS
16462 - 12	39.85	0.07	62.55	0.03	0.03	0.03	102.6	FeS
16462 - 13	39.76	0.00	62.69	0.02	0.04	0.01	102.5	FeS
16462 - 14	40.03	0.00	62.18	0.02	0.05	0.00	102.3	FeS
16462 - 15	39.88	0.00	62.13	0.03	0.02	0.04	102.1	FeS
16462 - 16	39.88	0.05	61.98	0.00	0.08	0.09	102.1	FeS
16462 - 17	54.72	0.05	47.22	0.00	0.76	0.03	102.8	FeS_2
16462 - 18	39.56	0.01	62.89	0.02	0.00	0.00	102.5	FeS
16462 - 19	53.39	0.00	47.57	0.00	0.80	0.00	101.8	FeS_2
16462 - 20	52.89	0.00	47.82	0.00	0.13	0.04	100.9	FeS_2
16462 - 21_incl	39.64	0.08	62.31	0.00	0.06	0.03	102.1	FeS
16462 - 22_incl-1	39.66	0.00	62.92	0.00	0.06	0.01	102.7	FeS
16462 - 22_incl-2	39.95	0.15	62.96	0.00	0.04	0.03	103.1	FeS
16462 - 22_incl-3	40.08	0.00	62.32	0.00	0.06	0.00	102.5	FeS
16462 - 23	39.52	0.04	62.36	0.00	0.00	0.05	102.0	FeS
16462 - 24	39.45	0.00	62.32	0.03	0.01	0.03	101.8	FeS
16462 - 25_incl	40.52	0.00	62.66	0.00	0.00	0.04	103.2	FeS
16462 - 26	54.11	0.00	47.72	0.00	0.03	0.00	101.9	FeS_2
16462 - 27_incl-1	33.36	53.84	11.32	0.06	0.07	0.00	98.7	(Zn,Fe)S
16462 - 27_incl-2	28.92	52.78	12.73	0.00	0.15	0.03	94.6	(Zn,Fe)S
16462 - 28	53.88	0.00	48.98	0.00	0.01	0.01	102.9	FeS_2
16462 - 29	39.46	0.00	62.59	0.01	0.04	0.00	102.1	FeS
16462 - 30	54.43	0.05	48.11	0.00	0.16	0.01	102.8	FeS_2
16462 - 31	39.78	0.11	62.27	0.00	0.01	0.00	102.2	FeS
16462 - 32	40.11	0.00	62.51	0.00	0.00	0.02	102.6	FeS
16462 - 33	54.21	0.00	48.13	0.01	0.13	0.04	102.5	FeS_2
16462 - 34	39.64	0.00	61.72	0.04	0.00	0.00	101.4	FeS
16462 - 35	53.64	0.02	47.84	0.03	0.06	0.00	101.6	FeS_2
16462 - 36	39.98	0.08	62.44	0.00	0.01	0.00	102.5	FeS
16462 - 37	40.24	0.00	63.15	0.02	0.01	0.03	103.4	FeS
16462 - 38	40.00	0.00	62.20	0.00	0.03	0.00	102.2	FeS

Table 10.11 (continued)

Sample name	S (wt%)	Zn (wt%)	Fe (wt%)	Ni (wt%)	Co (wt%)	Cu (wt%)	Total (wt%)	Formula
16462 - 39	40.01	0.08	62.53	0.03	0.01	0.03	102.7	FeS
16462 - 40	51.84	0.02	46.48	0.00	0.73	0.02	99.1	FeS_2
16462 - 41	54.63	0.04	47.76	0.00	1.01	0.03	103.5	FeS_2
16462 - 42	53.83	0.00	47.27	0.00	0.97	0.00	102.1	FeS_2
16462 - 43	51.40	0.00	47.26	0.01	0.58	0.00	99.2	FeS_2
19780 - 1	53.70	0.12	48.44	0.00	0.06	0.03	102.4	FeS_2
19780 - 2	53.58	0.02	48.77	0.01	0.01	0.00	102.4	FeS_2
19780 - 3	52.99	0.09	48.59	0.00	0.00	0.00	101.7	FeS_2
19780 - 4	52.26	0.00	47.09	0.00	0.00	0.00	99.3	FeS_2
19780 - 5	53.02	0.00	48.38	0.00	0.03	0.00	101.4	FeS_2
19780 - 6	53.15	0.00	48.62	0.00	0.00	0.06	101.8	FeS_2
19780 - 7	53.97	0.00	49.18	0.04	0.03	0.00	103.2	FeS_2
19780 - 8	54.30	0.07	48.79	0.04	0.02	0.03	103.3	FeS_2
19780 - 9	55.02	0.00	48.91	0.02	0.08	0.00	104.0	FeS_2
19780 - 10	52.96	0.00	48.58	0.00	0.01	0.00	101.5	FeS_2
19780 - 11	54.67	0.00	48.39	0.01	0.08	0.00	103.1	FeS_2
19780 - 12	53.67	0.03	48.14	0.08	0.02	0.03	101.9	FeS_2
19780 - 13	54.38	0.07	48.85	0.00	0.02	0.00	103.3	FeS_2
19780 - 14	54.06	0.02	48.55	0.00	0.05	0.02	102.7	FeS_2
19780 - 15_incl	50.61	0.00	45.03	0.00	0.00	0.02	95.7	FeS_2
19780 - 16	53.69	0.01	48.50	0.01	0.00	0.00	102.2	FeS_2
19781 - 1	38.06	0.01	55.59	0.00	0.04	0.00	93.7	FeS
19781 - 2	38.49	0.01	62.31	0.00	0.03	0.00	100.8	FeS
19781 - 3	53.88	0.04	48.00	0.01	0.04	0.00	102.0	FeS_2
19781 - 4	54.15	0.00	48.06	0.02	0.09	0.01	102.3	FeS_2
19781 - 5	53.12	0.14	48.60	0.00	0.05	0.01	101.9	FeS_2
19781 - 6	39.56	0.00	61.22	0.00	0.00	0.00	100.8	FeS

Table 10.12 Microprobe data and composition of carbonates of three samples from Fen, Norway (16462) and Grønnedal-Ika, Greenland (19780, 19781). Totals are below 100% because CO_2 was not measured.

Sample name	SiO_2 (wt%)	TiO_2 (wt%)	Al_2O_3 (wt%)	FeO (wt%)	MnO (wt%)	MgO (wt%)	CaO (wt%)	Na_2O (wt%)	K_2O (wt%)	NiO (wt%)	P_2O_5 (wt%)	Total (wt%)	Mineral
19780-1	0	0	0.02	0.51	0.51	0.03	54.0	0.002	0	0	0.041	55.1	calcite
19780-2	0	0	0.003	0.79	0.76	0.10	52.5	0	0	0	0	54.2	calcite
19780-3	0	0	0.002	0.52	0.51	0.04	54.7	0	0	0	0.03	55.8	calcite
19780-4	0	0.009	0.037	1.06	0.65	0.09	53.3	0.001	0.004	0	0.026	55.1	calcite
19780-5	0	0.003	0	0.93	0.62	0.09	53.3	0	0	0	0.025	55.0	calcite
19780-6	0	0	0.005	0.07	0.63	0.02	54.7	0.068	0	0	0.052	55.5	calcite
19780-7	0	0	0.015	0.22	0.52	0.05	53.8	0.018	0.001	0	0	54.7	calcite
19780-8	0	0.029	0.006	0.19	0.45	0.02	55.8	0	0.001	0	0.016	56.5	calcite
19780-9	0	0.079	0.012	0.20	0.37	0.03	55.6	0	0	0	0.031	56.3	calcite
19780-10	0	0	0.002	0.74	0.53	0.09	55.8	0.009	0	0	0	57.1	calcite
19781-1	0	0	0.009	0.41	0.42	0.55	51.4	0.116	0	0	0.003	52.9	calcite
19781-2	0	0.051	0.009	0.37	0.37	0.51	52.2	0.111	0	0	0.024	53.6	calcite
19781-3	0	0	0.014	0.40	0.38	0.44	52.6	0.162	0.021	0	0.045	54.1	calcite
19781-4	0	0	0	0.38	0.37	0.49	50.2	0.1	0	0	0.044	51.6	calcite
19781-5	0	0.003	0.004	0.34	0.32	0.38	51.8	0.105	0.001	0	0.017	52.9	calcite
19781-6	0	0	0	0.46	0.31	0.45	51.0	0.092	0	0	0.018	52.4	calcite
19781-7	0	0	0.002	0.44	0.34	0.52	50.6	0.124	0	0	0.015	52.0	calcite
19781-8	0	0.042	0	0.35	0.36	0.47	51.2	0.05	0	0	0.062	52.5	calcite
19781-9	0	0	0.012	0.37	0.07	0.30	50.1	0.161	0.043	0	0	51.1	calcite
19781-10	0	0.026	0	0.42	0.38	0.49	50.8	0.066	0.005	0	0.017	52.2	calcite
19781-11	0	0	0.005	0.37	0.36	0.51	50.4	0.138	0.002	0	0.03	51.8	calcite
19781-12	0	0.033	0.014	0.42	0.37	0.48	53.1	0.116	0	0	0.01	54.5	calcite
19781-13	0	0.008	0	0.40	0.31	0.36	52.9	0.203	0	0	0.043	54.3	calcite

Table 10.12 (continued)

Sample name	SiO_2 (wt%)	TiO_2 (wt%)	Al_2O_3 (wt%)	FeO (wt%)	MnO (wt%)	MgO (wt%)	CaO (wt%)	Na_2O (wt%)	K_2O (wt%)	NiO (wt%)	P_2O_5 (wt%)	Total (wt%)	Mineral
19781-14	0	0	0	0.32	0.46	0.42	49.2	0.152	0	0	0.044	50.6	calcite
19781-15	0	0.003	0	0.41	0.43	0.38	52.1	0.2	0.009	0	0.064	53.6	calcite
16462-1	0	0.006	0.009	0.34	0.11	0.82	52.9	0.028	0	0	0.018	54.3	calcite
16462-2	0	0.027	0.042	0.49	0.04	0.74	54.2	0	0	0	0.018	55.5	calcite
16462-3	0	0.066	0	0.33	0.09	0.69	54.5	0.044	0.007	0	0.023	55.7	calcite
16462-4	0	0	0.012	0.30	0.11	0.86	54.5	0.049	0	0	0.027	55.9	calcite
16462-5	0	0.03	0.019	0.36	0.14	0.78	52.5	0.035	0	0	0.021	53.9	calcite
16462-6	0	0	0.009	0.39	0.05	0.85	53.6	0.014	0.001	0	0.004	55.0	calcite
16462-7	0	0	0.014	0.32	0.10	0.59	54.0	0.047	0	0	0.037	55.1	calcite
16462-8	0	0	0.001	0.27	0.05	0.87	54.2	0.005	0	0	0.021	55.4	calcite
16462-9	0	0	0	0.30	0.06	0.64	55.5	0.003	0	0	0.017	56.5	calcite
16462-10	0	0.014	0.004	0.33	0.15	0.76	56.4	0	0.009	0	0.034	57.7	calcite
16462-11	0	0.035	0	1.97	0.07	19.0	29.0	0	0.005	0	0.02	50.1	dolomite
16462-12	0	0.019	0.025	2.40	0.13	18.9	28.6	0.022	0.011	0	0.033	50.1	dolomite
16462-13	0	0	0	2.09	0.16	19.0	28.9	0	0.012	0	0.002	50.2	dolomite
16462-14	0	0	0	2.39	0.15	18.6	28.8	0	0.008	0	0.037	49.9	dolomite
16462-15	0	0	0.042	1.93	0.10	18.9	28.8	0	0	0	0	49.8	dolomite
16462-16	0	0.01	0	2.15	0.13	18.7	28.7	0.013	0	0	0.024	49.6	dolomite
16462-17	0	0.003	0	2.24	0.12	18.9	28.8	0	0.008	0	0.022	50.1	dolomite
16462-18	0	0	0.019	2.13	0.12	18.4	28.1	0.007	0	0	0.034	48.8	dolomite
16462-19	0	0.014	0.013	2.41	0.08	19.0	28.5	0.006	0	0	0.033	50.0	dolomite
16462-20	0	0	0.008	1.85	0.09	18.7	28.7	0.039	0	0	0.004	49.3	dolomite

Table 10.13 Microprobe data and composition of apatite of three samples from Fen (16462) and Grønnedal-Ika (19780, 19781).

Sample name	SiO_2 (wt%)	TiO_2 (wt%)	Al_2O_3 (wt%)	FeO (wt%)	MnO (wt%)	MgO (wt%)	CaO (wt%)	Na_2O (wt%)	K_2O (wt%)	P_2O_5 (wt%)	Total (wt%)
19780-1	0	0	0	0.05	0	0	54.3	0.14	0	42.6	97.0
19780-2	0	0	0.013	0.31	0	0	51.0	0.62	0	40.1	92.0
19780-3	0	0	0.009	0	0.01	0.01	53.8	0.04	0.01	43.5	97.3
19780-4	0	0	0.009	0.09	0.00	0.00	49.7	0.94	0.01	39.9	90.6
19780-5	0	0.011	0.005	0	0	0.00	53.7	0.10	0.01	43.4	97.2
19780-6	0	0	0.049	0.08	0	0	47.3	1.51	0.01	37.7	86.6
19780-7	0	0.04	0	0.11	0.06	0	49.3	1.02	0	39.7	90.2
19780-8	0	0	0.027	0.05	0.08	0.01	54.2	0.17	0	41.9	96.4
19780-9	0	0	0	0.05	0.01	0.00	51.0	0.76	0.01	40.0	91.8
19780-10	0	0	0	0.18	0	0	50.5	0.87	0.01	40.9	92.4
19780-11	0	0.03	0.013	0.07	0	0.01	53.7	0.11	0	42.8	96.7
19781-1	0.38	0.01	0	0.04	0.08	0.02	51.6	0.26	0.02	40.1	92.5
19781-2	0	0.07	0	0.05	0.03	0	53.3	0.09	0	43.1	96.6
19781-3	0.87	0	0.02	0.04	0.10	0.03	49.8	0.19	0.01	38.8	89.9
19781-4	0.22	0	0	0.11	0.13	0.09	51.0	0.18	0	31.0	82.7
19781-5	0.81	0	0.011	0.06	0.09	0.05	49.3	0.27	0	37.2	87.7
19781-6	0	0	0	0.05	0.07	0.03	53.2	0.17	0	42.8	96.2
19781-7	1.51	0.01	0.017	0.21	0.07	0.03	47.9	0.28	0.01	37.1	87.1
19781-8	0	0	0	0.19	0.07	0	51.6	0.30	0.01	41.4	93.6
19781-9	0	0	0	0	0.02	0.01	52.2	0.23	0.02	41.6	94.2
19781-10	0	0	0.009	0.02	0.08	0	53.6	0.20	0.00	43.3	97.2
19781-11	0.43	0	0	0.03	0.07	0.02	51.5	0.25	0	40.0	92.3

Table 10.13 (continued)

Sample name	SiO_2 (wt%)	TiO_2 (wt%)	Al_2O_3 (wt%)	FeO (wt%)	MnO (wt%)	MgO (wt%)	CaO (wt%)	Na_2O (wt%)	K_2O (wt%)	P_2O_5 (wt%)	Total (wt%)
19781-12	0.14	0	0.002	0.06	0.10	0.04	51.8	0.28	0.00	40.1	92.5
19781-13	0.88	0.03	0.001	0.12	0.07	0.01	50.7	0.22	0.01	39.0	91.1
19781-14	1.04	0	0.006	0.08	0.13	0.03	50.6	0.24	0.02	39.1	91.3
19781-15	0	0	0.005	0.11	0.08	0.01	52.7	0.34	0	43.2	96.5
19781-16	0.73	0.03	0	0.06	0.08	0	50.1	0.31	0	38.8	90.2
19781-17	0.89	0	0.02	0.14	0.18	0	50.7	0.30	0.01	39.5	91.7
19781-18	0	0	0.011	0.02	0.07	0.01	53.1	0.23	0.01	42.7	96.2
19781-19	0	0	0	0.06	0.03	0.01	52.6	0.27	0	42.9	95.9
19781-20	0	0.02	0.002	0.08	0.01	0.02	52.5	0.25	0	42.3	95.2
19781-21	0	0	0	0.13	0.07	0.01	52.5	0.26	0	42.4	95.4
19781-22	1.3	0	0.01	0.07	0.07	0.02	49.4	0.25	0.00	37.8	88.9
16462-1	0	0	0.013	0.01	0	0.09	53.5	0.22	0	43.0	96.9
16462-2	0	0	0.001	0.04	0.03	0.09	53.2	0.17	0	42.8	96.4
16462-3	0	0	0	0.05	0.02	0.05	53.7	0.14	0.00	42.9	96.9
16462-4	0	0	0	0.01	0.01	0.09	53.1	0.27	0	43.1	96.5
16462-5	0	0	0.007	0.03	0.06	0.09	53.2	0.22	0.01	43.2	96.8
16462-6	0	0.01	0	0.00	0	0.09	53.6	0.22	0	43.5	97.4
16462-7	0	0.04	0.004	0.04	0.03	0.08	53.7	0.16	0.02	43.3	97.3
16462-8	0	0	0.02	0.03	0.04	0.09	53.4	0.27	0	42.7	96.5
16462-9	0	0.08	0	0.03	0.08	0.16	43.0	0.28	0.07	43.6	87.3
16462-10	0	0	0.005	0.05	0.02	0.11	53.1	0.14	0	42.8	96.2
16462-11	0	0.00	0	0.01	0.02	0	53.6	0.21	0	43.1	96.9
16462-12	0	0.05	0.005	0	0.00	0.06	53.8	0.17	0	43.2	97.2
16462-13	0	0	0	0.03	0	0.00	52.6	0.26	0	43.1	96.0

Table 10.14 Microprobe data and composition of silicates of two samples from Fen, Norway (16462) and Grønnedal-Ika, Greenland (19780).

Sample name	SiO_2 (wt%)	TiO_2 (wt%)	Al_2O_3 (wt%)	FeO (wt%)	MnO (wt%)	MgO (wt%)	CaO (wt%)	Na_2O (wt%)	K_2O (wt%)	NiO (wt%)	P_2O_5 (wt%)	Total (wt%)	Mineral
19780-1	53.1	0.30	0.89	27.7	0.012	1.272	0.713	13.3	0.014	0	0.041	97.4	arfvedsonite
19780-2	52.9	1.06	1.26	28.5	0.009	0.411	0.15	14.2	0.014	0	0	98.5	arfvedsonite
19780-3	53.3	0.48	0.84	28.2	0.028	1.229	0.496	13.3	0.036	0	0.039	98.0	arfvedsonite
19780-4	53.1	0.02	0.73	29.8	0.018	0.005	0.126	13.7	0	0	0	97.5	arfvedsonite
19780-5	52.8	0.23	0.49	29.3	0.028	0.552	0.735	13.8	0	0	0.078	98.0	arfvedsonite
19780-6	53.4	0.10	1.03	28.7	0.015	0.986	0.455	13.3	0.02	0	0.027	98.0	arfvedsonite
19780-7	53.4	0	0.82	30.1	0	0.019	0.081	13.6	0.005	0	0.005	98.1	arfvedsonite
19780-8	52.1	0.19	0.86	27.6	0.027	1.052	1.591	13.2	0.007	0	0.014	96.6	arfvedsonite
19780-9	53.7	0.03	1.40	29.6	0.006	0.008	0.067	13.9	0.001	0	0	98.7	arfvedsonite
19780-10	52.9	0.16	0.82	28.8	0	1.054	0.369	13.3	0.045	0	0.009	97.4	arfvedsonite
16462-1	41.5	0.049	12.1	3.4	0.029	26.4	0	0.50	10.5	0	0	94.5	biotite/phlogopite
16462-2	41.7	0.021	12.3	3.4	0.023	26.7	0.008	0.47	10.6	0	0.01	95.3	biotite/phlogopite
16462-3	41.1	0.195	12.5	7.7	0	23.0	0.357	0.06	10.8	0	0.017	95.7	biotite/phlogopite
16462-4	41.1	0.088	13.4	3.6	0.009	26.1	0.021	0.47	10.4	0	0.021	95.2	biotite/phlogopite
16462-5	42.0	0.044	12.6	3.4	0.014	26.1	0.043	0.51	10.6	0	0.006	95.3	biotite/phlogopite
16462-6	41.3	0.039	13.2	3.2	0.026	25.9	0.005	0.57	10.5	0	0.023	94.8	biotite/phlogopite
16462-7	41.7	0.108	12.3	3.3	0.011	26.9	0	0.56	10.7	0	0.017	95.6	biotite/phlogopite
16462-8	41.5	0.087	11.9	3.6	0.003	26.3	0	0.49	10.6	0	0.01	94.5	biotite/phlogopite
16462-9	40.9	0.051	12.5	3.3	0	26.3	0.008	0.51	10.6	0	0	94.1	biotite/phlogopite
16462-10	41.1	0.061	12.5	3.5	0.006	25.9	0.004	0.52	10.5	0	0.033	94.1	biotite/phlogopite

Table 10.15 **Microprobe data and composition of "exotic phases" of three samples from Fen, Norway (16462) and Grønnedal-Ika, Greenland (19780, 19781). The mineral phases are unidentified, and calibration was not carried out for enough potential elements, thus totals are <100%.**

Sample name	Ca (wt%)	P (wt%)	La (wt%)	Ce (wt%)	U (wt%)	Th (wt%)	Cu (wt%)	Zn (wt%)	Co (wt%)	Total (wt%)
16462-1	0.15	4.65	16.1	17.0	0.59	0.10	0.129	0	0.007	**38.7**
16462-2	0.88	0	13.7	13.2	0	0.001	0	0.03	0	**27.8**
16462-3	1.16	0.009	12.1	12.5	0	0	0	0	0	**25.8**
16462-4	1.28	7.20	14.0	15.0	0	0.10	0	0.08	0	**37.7**
16462-5	0.32	8.51	18.2	16.1	1.83	0.29	0	0.02	0.009	**45.3**
16462-6	0.49	9.22	17.7	17.1	0	0.09	0	0	0	**44.6**
16462-7	9.63	0.008	13.9	13.3	0	0	0.05	0	0.012	**37.0**
16462-8	15.9	0.004	15.8	11.6	2.21	0.05	0	0.06	0	**45.6**
16462-9	9.25	0.03	0	0.40	12.3	0.005	0.072	0.03	0.05	**22.2**
16462-10	7.47	0.019	0	0.18	8.05	0	0.003	0.003	0.01	**15.7**
16462-11	0.25	0	0	2.45	0	0.003	0.043	0.07	0	**2.8**
16462-12	0.70	0.006	0	2.56	0	0	0	0.006	0.05	**3.3**
19781-1	24.5	0.01	3.17	3.54	1.84	0	0	0	0.003	**33.1**
19781-2	1.12	8.72	9.95	14.7	0	0.04	0.056	0.05	0	**34.6**
19781-3	41.5	0.02	0.39	0.72	2.59	0.001	0.016	0.02	0	**45.2**
19781-4	10.6	0.24	0.32	1.06	2.90	0.06	0	0.09	0.04	**15.4**
19780-1	0.04	0	0	1.83	0	0	0.055	0	0	**1.9**
19780-2	0.07	0.002	0	2.33	0.83	0.003	0.012	0	0	**3.2**
19780-3	10.3	0	0	0.12	4.52	0	0	0	0.004	**14.9**

Table 10.16 Microprobe data and composition of Fe-oxides (likely magnetite) from Grønnedal-Ika, Greenland (19781).

Sample name	SiO_2 (wt%)	TiO_2 (wt%)	Al_2O_3 (wt%)	FeO (wt%)	MnO (wt%)	MgO (wt%)	CaO (wt%)	Na_2O (wt%)	K_2O (wt%)	NiO (wt%)	P_2O_5 (wt%)	Total (wt%)	Mineral
19781-1	0.11	0.05	0.91	91.0	0.64	0.23	0.16	0	0.004	0	0.02	93.1	Fe-oxide
19781-2	0.11	0.04	0.16	89.7	0.73	0.31	0.07	0	0.02	0	0.0	91.2	Fe-oxide
19781-3	0.05	0.59	2.36	88.5	0.76	0.36	0.27	0.04	0	0	0.0	92.9	Fe-oxide
19781-4	0.02	0.17	0.02	91.7	0.56	0.04	0.17	0	0	0	0.02	92.7	Fe-oxide
19781-5	0.10	0.07	0.15	93.0	0.58	0.17	0.33	0.03	0	0	0.03	94.4	Fe-oxide

10.3.2. Major and trace element data – global study

Table 10.17 Major element data for carbonatite samples from different localities (bdl = below detection limit).

Sample name	SiO_2 [wt.%]	TiO_2 [wt.%]	Al_2O_3 [wt.%]	Fe_2O_3 [wt.%]	MnO [wt.%]	MgO [wt.%]	CaO [wt.%]	Na_2O [wt.%]	K_2O [wt.%]	P_2O_5 [wt.%]	SO_3 [wt.%]	S [wt.%]	BaO [wt.%]	SrO [wt.%]	LOI [wt.%]
BM.2004,P12(132)	1.79	0.06	0.494	1.05	0.26	0.21	13.84	31.32	6.14	1		1.07	0.857	0.978	36.23
4808	0.37	0.02	0.21	3.50	0.38	3.67	47.13	0.0	0.02	0.93	1.69				40.11
16462	1.25	0.03	0.45	1.85	0.25	3.01	48.19	0.01	0.33	4.23	0.35				37.18
19780	1.41	0.02	0.48	1.45	0.28	3.34	47.82	0.0	0.38	3.83	0.08				28.30
19781-1	1.06	0.02	0.41	12.52	1.69	0.81	41.92	0.11	0.02	1.78	0.06				34.40
19781-2	1.04	bdl	0.28	10.51	1.84	0.84	46.1	0.17	bdl	1.44		0.03	0.147	2.70	34.43
AVE 19781	1.05	0.02	0.345	11.52	1.76	0.83	44.01	0.14	0.02	1.61	0.06	0.03	0.147	2.70	34.42
J1-C1	0.13	bdl	bdl	1.80	0.09	1.51	55.05	bdl	0.02	1.9		0.45	0.1	0.68	38.22
91/66 - C2	0.31	0.03	bdl	1.84	0.19	17.16	35.82	bdl	0.07	5.57		0.19	bdl	0.47	38.33
91/62 - C4	1.87	0.07	0.733	28.74	0.26	6.09	33.31	0.14	0.06	19.35		0.12	bdl	0.26	8.90
ASS-1	bdl	bdl	bdl	0.16	0.08	0.78	53.82	bdl	bdl	bdl		0.07	bdl	1.45	43.62
BM.1998,P18(44)	0.73	bdl	0.15	0.60	0.14	1.30	54.28	bdl	0.14	2.2		0.07	bdl	0.57	39.80
BM.1998,P18(229)	0.87	0.05	bdl	4.35	0.36	6.15	48.38	bdl	0.20	3.07		0.51	bdl	0.74	35.12
BM.2000,P11(22)	0.72	0.05	bdl	1.39	0.08	1.75	55.59	bdl	0.08	3.58		0.03	bdl	0.47	36.24
BM.2000,P14(24)	0.88	bdl	bdl	1.58	0.16	2.34	52.34	bdl	0.22	0.05		0.17	bdl	0.63	41.61
BM.2000,P14(25)	0.65	0.05	bdl	3.15	0.17	4.13	49.65	bdl	0.15	1.73		0.05	bdl	0.72	39.54
GGU 252833*	3.05	0.24	0.18	1.95	0.12	5.80	45.89	0.05	0.05	0.02					39.29
GGU 252874*	7.66	0.34	1.42	2.45	0.11	14.06	36.3	0.05	0.15	0.014					34.01
GGU 253528**	2.88	0.37	0.41	2.59	0.11	8.77	41.95	0.05	0.00	0.01					38.84

*(Larsen and Rex, 1992)

**unpublished data from Lotte M. Larsen

Table 10.18 **Raw trace element data used for spider diagrams (Figure 4.3). Values given in ppm. Data was analysed using the general procedure (Chapter 3.5.1; Ottley et al., 2003).**

Sample name	Rb	Ba	Th	U	Nb	Ta	La	Ce	Pb	Pr	Sr	Nd	Zr	Hf	Sm	Eu	Dy	Y	Yb	Lu
GGU 252833	4.50	159.0			3.50		274.0	564.0	22.00		3969	302.0	99.00					38.00	0.00	0.00
GGU 252874	11.00	169.0	3.00		2.80		105.0	210.0	4.00		2288	121.0	79.00					15.00	0.00	0.00
GGU 253528	1.80	89.0			3.10		112.0	249.0	11.00		2578	150.0	66.00		26.29			21.00	0.00	0.00
OL-1.1	132.8	7006	9.02	10.05	92.83	0.27	467.8	553.1	73.33	48.47	10620	125.2	29.69	1.3	9.87	2.19	1.75	12.42	0.43	0.06
OL-1.2	131.2	6070	9.55	10.69	90.03	0.38	395.3	470.2	79.52	50.26	10830	130.7	30.65	1.4	10.39	2.46	1.92	12.34	0.47	0.07
BM.2004,P12 (132)	141.3	7075	11.68	10.89	98.03	0.54	367.1	432.7	89.82	47.27	10730	123.0	54.69	2.7	10.70	2.72	2.61	16.89	0.73	0.11
4808	0.67	1046	20.98	187.3	379.5	145.9	235.6	439.2	96.83	55.11	4909	194.2	21.45	0.9	28.70	7.95	11.99	57.85	3.60	0.56
10160	12.20	891.9	33.69	81.25	477.5	90.67	283.2	578.4	15.43	76.48	5832	278.6	15.59	0.9	42.67	11.79	17.20	84.17	5.38	0.86
16462	11.63	881.4	205.6	240.9	1764.3	332.1	229.7	487.8	28.02	73.91	5949	273.1	114.9	5.5	41.61	11.53	16.55	76.38	4.96	0.77
19777	6.46	155.5	23.89	0.43	69.83	0.40	2015	4815	37.61	685.3	27090	2837.0	23.34	1.7	442.1	111.8	72.66	196.6	9.38	1.42
19780	1.29	766.0	13.88	5.49	454.0	15.32	619.6	1411.0	10.57	191.6	6804	746.6	134.4	5.9	103.2	24.72	37.38	186.6	12.94	1.81
19781	0.94	1258	15.54	15.37	284.6	10.83	743.5	1805	25.00	269.7	22040	1181.0	3.42	0.4	217.0	67.43	77.61	285.0	12.59	1.69
25810	0.85	1427.0	5.24	0.13	14.04	0.06	216.0	558.5	11.21	93.41	10040	455.6	1.75	0.1	119.9	41.36	64.31	200.6	5.39	0.74
J1-C1	0.71	934.5	0.93	0.06	2.25	2.41	148.3	219.0	5.38	36.04	5246	153.1	0.29	0.0	23.38	6.58	9.40	36.65	1.71	0.24
91/66 C2	1.88	308.4	33.41	77.76	235.4	67.82	86.2	183.6	4.63	28.62	3482	133.4	65.52	3.2	21.87	5.55	6.80	21.42	0.83	0.12
91/62 C4	0.72	360.3	2.00	0.24	66.56	55.81	73.6	173.7	9.46	24.52	2208	103.1	554.8	36.3	20.49	6.13	10.48	39.58	1.90	0.27
91/60 C5	0.49	143.8	1.15	0.30	17.80	2.21	48.8	114.9	5.49	15.95	3289	66.9	0.89	0.1	12.79	3.81	6.07	22.40	1.04	0.15
ASS-1	0.06	98.6	0.02	0.01	0.28	0.41	198.8	192.9	16.98	20.41	12060	54.8	0.09	0.008	5.51	1.31	1.78	9.20	0.63	0.11
BM.1998,P18(44)	4.05	362.6	4.50	0.95	4.42	1.66	189.5	388.8	2.25	62.83	4571	233.4	24.63	1.8	35.38	9.56	14.46	59.41	3.16	0.46

Table 10.18 (continued)

Sample name	Rb	Ba	Th	U	Nb	Ta	La	Ce	Pb	Pr	Sr	Nd	Zr	Hf	Sm	Eu	Dy	Y	Yb	Lu
BM.1998,P18 (119)	0.45	1489	7.92	8.01	95.40	8.62	324.4	559.3	7.50	79.56	5775	259.5	111.6	9.4	34.32	9.07	13.7	58.6	3.60	0.53
BM.1998,P18 (183)	0.12	771.7	2.90	0.03	44.06	0.37	180.5	343.5	4.15	52.16	5647	184.0	0.76	0.1	27.00	7.47	11.8	48.9	3.03	0.45
BM.1998,P18 (229)	6.35	583.9	62.72	69.17	750.0	58.42	178.8	376.2	7.50	62.31	5634	228.6	287.5	26.2	34.26	9.15	11.6	41.9	2.07	0.30
BM.2000,P11(14)	0.76	285.5	5.99	0.28	29.26	6.94	188.2	317.5	0.99	49.99	4147	180.7	128.7	11.2	24.81	6.35	7.70	28.0	1.27	0.18
BM.2000,P11(16)	0.08	321.7	0.79	0.04	1.58	0.73	166.2	231.9	1.14	33.88	5024	116.4	13.83	1.1	15.35	4.13	5.41	22.2	1.14	0.17
BM.2000,P11(22)	4.98	467.5	4.22	0.24	6.53	1.97	203.0	295.6	2.17	45.33	4781	160.9	401.5	23.6	21.86	5.74	7.60	29.5	1.56	0.24
BM.2000,P11(23)	4.83	276.9	0.63	0.15	5.69	5.03	70.4	141.9	2.11	17.19	4314	62.8	58.25	3.7	9.73	2.74	4.76	21.7	1.56	0.24
BM.2000,P11(29)	0.17	99.3	6.62	2.99	16.17	2.18	55.7	92.4	2.57	9.43	4118	28.8	25.67	2.0	2.92	0.70	0.81	3.25	0.24	0.04
BM.2000,P11(42)	0.67	144.7	2.26	0.47	5.53	0.55	23.4	42.7	1.14	4.61	4065	14.8	21.65	0.9	1.91	0.51	0.61	2.42	0.21	0.04
BM.2000,P14(24)	9.86	554.3	0.08	6.90	10.18	1.47	79.6	138.7	4.22	15.33	5264	51.1	0.37	0.0	7.56	2.15	4.57	24.0	2.16	0.36
BM.2000,P14(25)	4.26	454.8	0.84	67.15	100.2	12.00	108.0	201.6	6.94	22.95	5856	78.9	1.51	0.1	11.57	3.18	5.42	25.4	1.81	0.28
LI 23/02/08	28.37	632.4	13.18	1.14	59.42	1.72	245.3	455.3	4.29	56.63	8422	219.1	101.2	3.7	34.11	9.69	18.07	93.0	5.86	0.92
BM.2004.P9(9)	240.6	2178	3.32	5.14	37.94	0.39	22.0	35.0	2.98	4.15	2292	14.6	63.93	4.7	2.39	0.79	1.80	12.5	1.11	0.19

Table 10.19 **Raw whole-rock trace element data used for REE plots (Figure 4.4). All values are given in ppm and data was analysed using the general procedure (Chapter 3.5.1, Ottley et al., 2003).**

Sample name	La	Ce	Pr	Nd	Sm	Eu	Gd	Tb	Dy	Ho	Er	Tm	Yb	Lu
OL1-1	475.5	561.7	48.62	125.5	9.94	2.19	5.41	0.50	1.75	0.27	0.61	0.08	0.42	0.06
OL1-2	460.1	544.5	48.31	124.9	9.81	2.19	5.17	0.48	1.75	0.27	0.61	0.08	0.43	0.06
4808	235.6	439.2	55.11	194.2	28.70	7.95	20.77	2.59	11.99	2.01	4.56	0.62	3.60	0.56
10160-1	278.2	569.0	75.75	275.8	42.45	11.74	30.95	3.74	17.15	2.91	6.65	0.91	5.37	0.86
10160-2	288.1	587.7	77.21	281.4	42.89	11.84	31.46	3.77	17.25	2.91	6.70	0.91	5.39	0.86
16462	268.3	565.3	73.40	268.3	40.70	11.29	29.86	3.61	16.39	2.75	6.22	0.84	4.91	0.78
19777	2015	4815	685.3	2837	442.1	111.75	244.2	22.06	72.66	9.12	16.33	1.83	9.38	1.42
19780	619.6	1411	191.6	746.6	103.2	24.72	65.18	7.89	37.38	6.65	16.18	2.26	12.94	1.81
19781-1	749.1	1817	272.3	1195	219.2	68.08	155.1	18.06	78.60	11.94	23.49	2.66	12.69	1.71
19781-2	737.8	1793	267.0	1167	214.8	66.79	152.9	17.83	76.63	11.64	22.90	2.61	12.49	1.68
25810	216.0	558.5	93.4	455.6	119.9	41.36	113.3	14.76	64.31	9.13	15.24	1.37	5.39	0.74
91/62 - C4	73.64	173.7	24.52	103.1	20.49	6.13	17.80	2.26	10.48	1.68	3.41	0.41	1.90	0.27
BM.1998,P18(44)	189.5	388.8	62.83	233.4	35.38	9.56	27.46	3.28	14.46	2.31	4.98	0.62	3.16	0.46
BM.1998,P18(183)	180.5	343.5	52.16	184.0	27.00	7.47	21.35	2.58	11.80	1.94	4.33	0.56	3.03	0.45
BM.2000,P11(14)	188.2	317.5	49.99	180.7	24.81	6.35	17.81	1.89	7.70	1.16	2.27	0.26	1.27	0.18
BM.2000,P11(16)	166.2	231.9	33.88	116.4	15.35	4.13	11.27	1.26	5.41	0.85	1.80	0.22	1.14	0.17
BM.2000,P11(23)	70.35	141.9	17.19	62.76	9.73	2.74	7.72	0.98	4.76	0.82	1.96	0.27	1.56	0.24
BM.2000,P11(29)	55.68	92.40	9.43	28.78	2.92	0.70	1.73	0.19	0.81	0.13	0.29	0.04	0.24	0.04
BM.2000,P11(42)	23.36	42.66	4.61	14.83	1.91	0.51	1.30	0.15	0.61	0.09	0.22	0.03	0.21	0.04

Table 10.20 **Raw whole-rock trace element data used for REE plots (Figure 4.4). All values are given in ppm and data was analysed using a *CETAC Aridus™* following the final procedure described in Chapters 3.5.2 and 3.6.8.**

Sample name	La	Ce	Pr	Nd	Sm	Eu	Gd	Tb	Dy	Ho	Er	Tm	Yb	Lu
LI 23/02/08-1	105.7	221.6	24.6	223.5	33.1	10.0	27.6	3.5	17.3	3.2	7.4	1.1	5.5	0.9
LI 23/02/08-2	94.7	200.5	21.9	201.5	29.9	9.1	24.7	3.1	15.4	2.9	6.6	0.9	4.9	0.8
BM.2004.P9(9)-1	21.1	16.5	4.1	13.9	2.1	0.6	1.7	0.2	1.4	0.3	0.8	0.1	0.9	0.1
BM.2004.P9(9)-2	21.1	41.4	4.2	14.1	2.2	0.7	1.8	0.3	1.5	0.3	0.8	0.1	1.0	0.1
COQ-1	538.7	1006.8	87.5	707.2	78.5	19.8	50.4	5.7	27.6	4.9	11.5	1.7	8.7	1.4
COQ-1	893.4	2013.5	139.4	497.1	56.8	14.7	34.6	4.0	16.5	3.4	7.8	1.2	6.3	1.0
GGU 252833	149.7	316.5	40.9	431.7	66.6	14.4	46.6	4.2	15.9	2.2	4.1	0.5	2.2	0.4
GGU 252874	51.0	107.8	36.0	152.6	24.2	5.4	16.1	1.5	5.5	0.8	1.4	0.2	0.8	0.1
J1-C1	152.8	311.8	31.2	153.1	23.4	6.6	18.2	2.1	8.1	1.5	2.9	0.4	1.6	0.2
91/66 - C2	92.2	229.6	25.5	133.4	21.9	5.8	17.0	1.8	6.5	1.1	2.0	0.2	0.9	0.1
91/60 - C5	48.7	122.5	13.4	70.1	12.8	3.7	11.4	1.4	5.4	1.0	1.9	0.2	1.0	0.1
4808	223.7	475.5	43.1	175.8	26.4	7.4	19.6	2.3	9.8	1.9	4.3	0.6	3.3	0.6
10160	283.5	641.3	62.9	282.9	44.7	11.3	34.0	3.9	16.1	3.2	7.1	1.0	5.5	0.9
16462-1	262.9	624.4	60.6	266.0	40.6	11.3	31.3	3.6	14.7	2.9	6.4	0.9	4.8	0.8
16462-2	246.5	612.1	58.1	250.5	37.4	11.0	28.8	3.3	13.7	2.7	5.9	0.9	4.5	0.8
19780-1	537.5	1433.5	144.3	637.6	90.2	22.8	59.1	6.9	29.6	6.2	14.6	2.2	11.2	1.7
19780-2	486.9	1333.0	133.0	586.5	82.3	20.9	53.7	6.2	27.1	5.7	13.5	2.0	10.4	1.6
19781	531.1	1660.2	177.7	871.0	159.5	50.9	118.2	13.4	53.5	9.4	17.9	2.2	9.4	1.3
BM.1998,P18(119)	399.7	705.7	61.8	243.4	32.1	9.0	22.6	2.7	11.4	2.2	4.7	0.7	3.2	0.5
BM.1998,P18(229)	220.2	503.1	50.2	222.1	35.0	9.3	25.8	2.8	10.8	1.9	3.7	0.5	2.1	0.3
BM.2000,P11(22)-1	129.9	301.1	26.6	114.0	14.8	4.0	10.8	1.2	4.6	0.9	1.7	0.2	1.1	0.2
BM.2000,P11(22)-2	140.9	314.3	27.9	121.2	15.8	4.2	11.6	1.2	4.8	0.9	1.8	0.2	1.1	0.2
BM.2000,P11(22)-3	129.8	298.4	26.4	114.1	14.8	4.0	10.8	1.2	4.6	0.9	1.7	0.2	1.1	0.2

Table 10.20 (continued)

Sample name	La	Ce	Pr	Nd	Sm	Eu	Gd	Tb	Dy	Ho	Er	Tm	Yb	Lu
BM.2000,P14(24)	82.5	141.4	12.7	53.9	7.6	2.1	6.0	0.8	3.6	0.8	2.1	0.3	1.9	0.4
BM.2000,P14(25)	114.0	211.5	19.8	88.3	12.6	3.3	10.3	1.3	5.4	1.1	2.5	0.4	1.9	0.3

Table 10.21 **Raw carbonate fraction trace element data used for REE plots (Figure 4.4). All values are given in ppm and data was analysed using a *CETAC Aridus™* following the final procedure described in Chapters 3.5.2 and 3.6.8.**

Sample name	La	Ce	Pr	Nd	Sm	Eu	Gd	Tb	Dy	Ho	Er	Tm	Yb	Lu
COQ-1	808.6	1303	113.7	413.7	45.9	12.4	30.4	3.5	14.8	3.1	7.3	1.1	5.8	1.0
J1-C1	141.9	282.5	28.8	142.3	22.3	6.3	17.8	2.0	7.9	1.4	2.8	0.4	1.6	0.2
91/66 - C2	74.4	200.3	21.9	110.4	18.3	5.4	14.6	1.6	5.9	1.0	1.8	0.2	0.8	0.1
91/60 - C5	49.1	119.5	14.7	70.6	13.2	3.9	12.1	1.4	5.7	1.1	2.1	0.2	1.1	0.2
4808	188.4	395.7	36.9	168.0	25.5	7.3	20.3	2.5	10.4	2.1	4.7	0.7	3.5	0.6
10160	249.8	574.0	57.5	281.4	43.1	12.0	34.0	4.0	16.7	3.3	7.4	1.1	5.7	1.0
16462-1	251.8	570.3	57.4	284.4	43.4	11.8	34.1	3.9	16.1	3.2	7.1	1.0	5.3	0.9
16462-2	248.4	562.5	56.7	279.8	43.0	11.7	33.8	3.9	16.1	3.2	7.1	1.0	5.3	0.9
19780-1	895.7	2055	224.9	1043	148.5	36.5	94.6	11.1	48.6	10.1	24.1	3.6	17.7	2.6
19780-2	1028	2271	248.0	1182	172.4	39.4	112.4	13.2	56.4	11.9	28.3	4.2	20.4	3.0
19781	940.2	2428	281.2	1489	290.0	88.5	215.4	24.2	93.5	16.8	32.3	3.9	16.6	2.3
BM.1998,P18(119)	495.0	825.0	73.0	318.4	39.5	10.4	28.4	3.4	13.9	2.7	5.8	0.8	3.9	0.6
BM.1998,P18(229)	226.5	514.3	49.7	228.6	33.7	8.5	25.2	2.7	10.2	1.8	3.5	0.4	2.0	0.3
BM.2000,P11(22)-1	167.5	368.7	32.5	141.5	18.1	4.6	13.1	1.4	5.3	1.0	2.0	0.3	1.2	0.2
BM.2000,P11(22)-2	159.0	341.5	30.6	134.7	17.3	4.3	12.6	1.3	5.1	1.0	1.9	0.2	1.2	0.2
BM.2000,P11(22)-3	182.2	398.9	35.8	155.9	20.1	5.1	14.6	1.6	5.9	1.1	2.3	0.3	1.3	0.2
BM.2000,P14(24)	94.1	160.7	14.2	60.0	8.5	2.3	6.7	0.9	4.0	0.9	2.3	0.4	2.1	0.4

Table 10.21 (continued)

Sample name	La	Ce	Pr	Nd	Sm	Eu	Gd	Tb	Dy	Ho	Er	Tm	Yb	Lu
BM.2000,P14(25)	122.3	230.2	21.1	93.0	13.1	3.4	10.3	1.3	5.3	1.1	2.5	0.4	1.9	0.3
BM.2004.P9(9)-1	68.2	119.6	13.1	44.7	7.2	2.3	6.1	0.9	5.1	1.1	2.8	0.5	2.7	0.4
BM.2004.P9(9)-2	71.1	84.9	13.3	46.5	7.4	2.3	6.4	0.9	5.4	1.1	3.0	0.5	2.9	0.4
LI 23/02/08-1	96.6	208.7	22.7	83.6	30.6	9.2	26.5	3.3	16.8	3.1	7.3	1.0	5.3	0.8
LI 23/02/08-2	98.2	210.6	22.8	205.4	30.8	9.3	26.3	3.3	16.7	3.1	7.3	1.0	5.2	0.8
GGU 252833	59.8	159.8	23.9	267.2	45.4	11.0	32.4	3.1	12.0	1.7	3.2	0.4	1.8	0.3
GGU 252874	74.2	73.7	27.7	120.9	20.7	5.0	14.6	1.4	5.3	0.8	1.4	0.2	0.8	0.1

Table 10.22 **Raw non-carbonate fraction trace element data used for REE plots (Figure 4.4). All values are given in ppm and data was analysed using a *CETAC Aridus*^{TM} following the final procedure described in Chapters 3.5.2 and 3.6.8. bdl = below detection limit.**

Sample name	La	Ce	Pr	Nd	Sm	Eu	Gd	Tb	Dy	Ho	Er	Tm	Yb	Lu
COQ-1	919.7	6228	324.4	1039	118.1	32.1	55.9	7.2	31.3	5.2	11.5	1.8	9.7	1.4
J1-C1	47.2	82.0	12.4	44.6	8.7	2.2	6.7	0.7	3.1	0.5	1.2	0.0	0.6	bdl
91/66 - C2-1	25.0	114.8	13.0	47.8	8.6	2.3	5.1	0.7	3.2	0.5	0.9	0.1	0.6	0.1
91/66 - C2-2	23.6	88.7	11.3	42.5	7.9	1.9	5.0	0.6	2.5	0.4	0.7	0.1	0.5	0.07
91/60 - C5	26.5	51.0	8.2	30.6	6.7	1.7	5.8	0.6	2.9	0.5	1.1	0.1	0.6	bdl
4808	1885	3201	378.0	1295	127.7	22.4	55.8	3.6	9.2	1.2	2.1	0.2	1.1	0.09
10160	1278	2224	261.2	883.3	85.1	16.7	38.4	2.7	8.0	1.2	2.2	0.3	1.5	0.18
16462-1	1653	2831	258.1	973.2	91.4	16.2	39.0	3.3	10.6	1.8	3.4	0.4	2.2	0.32
16462-2	1691	2882	264.7	1012	96.4	17.1	41.7	3.5	11.4	1.9	3.7	0.5	2.4	0.33
19780-1	16.9	40.9	4.6	21.5	3.2	0.7	2.0	0.2	1.0	0.2	0.7	0.2	2.2	0.64
19780-2	19.5	48.0	5.3	25.0	3.7	0.9	2.3	0.3	1.2	0.2	0.8	0.2	2.2	0.63
19781	79.6	186.2	23.6	123.5	20.4	5.3	12.6	1.2	4.1	0.6	1.1	0.1	0.6	0.09

Table 10.22 (continued)

Sample name	La	Ce	Pr	Nd	Sm	Eu	Gd	Tb	Dy	Ho	Er	Tm	Yb	Lu
BM.1998,P18(119)	74.0	122.4	11.7	48.2	6.9	1.6	5.5	0.7	3.0	0.6	1.3	0.2	1.0	0.15
BM.1998,P18(229)	80.4	237.1	23.3	102.6	15.4	3.6	9.0	1.0	3.4	0.5	1.0	0.1	0.8	0.07
BM.2000,P11(22)-1	16.1	30.7	3.6	16.9	2.5	0.6	1.8	0.2	0.8	0.1	0.3	0.0	0.4	0.03
BM.2000,P11(22)-2	14.3	28.2	3.4	16.9	2.6	0.6	1.8	0.2	0.8	0.1	0.3	0.0	0.4	0.04
BM.2000,P11(22)-3	4.6	9.3	1.1	5.5	0.8	0.2	0.6	0.1	0.3	0.0	0.1	0.0	0.2	0.01
BM.2000,P14(24)	9.8	15.0	1.5	6.8	1.0	0.2	0.8	0.1	0.5	0.1	0.3	0.0	0.3	0.05
BM.2000,P14(25)	13.5	21.2	2.2	9.1	1.4	0.3	1.1	0.1	0.6	0.1	0.3	0.0	0.2	0.04
LI 23/02/08	57.2	122.0	17.3	70.4	12.7	3.5	10.0	1.3	6.3	1.0	2.2	0.3	2.0	0.44
LI 23/02/08	67.3	139.1	19.5	80.0	14.2	3.9	11.3	1.4	6.9	1.2	2.5	0.4	2.2	0.48
BM.2004.P9(9)	3.8	8.2	0.8	2.5	0.4	0.1	0.3	0.0	0.2	0.1	0.2	0.0	0.3	0.06
BM.2004.P9(9)	4.8	9.8	1.0	3.1	0.5	0.1	0.4	0.1	0.3	0.1	0.2	0.1	0.4	0.08
GGU 252833	387.2	725.1	220.1	787.2	96.5	17.8	49.7	4.5	16.0	2.1	3.5	0.4	1.8	0.27
GGU 252874	150.8	125.5	35.3	121.5	15.1	2.9	7.6	0.7	2.5	0.3	0.6	0.1	0.3	0.05

Table 10.23 Measured and dilution corrected whole-rock concentrations of Lu, Hf, Sm, Nd, Rb and Sr for carbonatite samples from the global study. Data determined by Q-ICP-MS in combination with a desolvator using the final method for Hf chemistry (Chapter 3.6.8.).

Sample name	Lu (ppm)	Hf (ppm)	Sm (ppm)	Nd (ppm)	Rb (ppm)	Sr (ppm)
COQ-1	0.99	0.29	56.82	497.1	14.65	13,147
COQ-1_repl	0.99	0.32	57.47	531.8	18.39	15,671
J1-C1	0.24	0.01	23.38	153.1	0.67	5,894
91/66 - C2	0.12	0.98	21.87	133.4	2.08	4,152
91/60 - C5	0.15	0.02	12.85	70.14	0.55	3,787
4808	0.56	0.14	26.40	175.8	0.64	5,446
10160	0.93	0.27	44.68	282.9	13.95	6,603
16462	0.81	1.66	40.61	266.0	13.58	7,035
16462_repl	0.76	1.46	37.42	250.5	14.46	7,146
19780	1.68	1.74	90.15	637.6	1.29	7,016
19780_repl	1.58	1.71	82.27	586.5	1.29	7,096
19781	1.29	0.10	159.5	871.0	0.95	17,085
BM.1998,P18(119)	0.51	1.95	32.06	243.4	0.48	6,411
BM.1998,P18(229)	2.10	6.53	34.95	222.1	7.64	6,549
BM.2000,P11(22)	0.17	3.11	14.80	114.0	4.44	4,162
BM.2000,P11(22)_repl	0.18	2.64	15.80	121.2	5.26	4,215
BM.2000,P11(22)_repl	0.17	2.63	14.83	114.1	4.44	4,139
BM.2000,P14(24)	0.36	0.01	7.59	53.92	10.89	5,644
BM.2000,P14(25)	0.34	0.04	12.64	88.28	4.65	6,108
LI 23/02/08	0.86	1.04	33.31	223.5	34.07	9,423
LI 23/02/08	0.75	0.91	30.06	201.5	31.85	8,856
BM.2004.P9(9)	0.14	1.28	2.14	13.86	282.2	2,403
BM.2004.P9(9)	0.15	1.31	2.21	14.06	288.0	2,438
GGU 252833	0.36	2.10	66.33	431.7	3.46	4,734
GGU 252874	0.14	1.11	24.26	152.6	8.85	933.8

Table 10.24 Measured and dilution corrected concentrations of Lu, Hf, Sm, Nd, Rb and Sr for carbonate fractions of carbonatite samples from the global study. Data determined by Q-ICP-MS in combination with a desolvator using the final method for Hf chemistry (Chapter 3.6.8.).

Sample name	Lu (ppm)	Hf (ppm)	Sm (ppm)	Nd (ppm)	Rb (ppm)	Sr (ppm)
COQ-1	0.95	0.01	45.88	413.7	14.44	13,501
J1-C1	0.24	0.003	22.26	142.3	0.52	6,143
91/66 - C2	0.11	0.03	18.30	110.4	0.59	4,307
91/60 - C5	0.16	0.01	13.17	70.6	0.31	3,761
4808	0.61	0.01	25.49	168.0	0.51	5,845
10160	1.01	0.02	43.12	281.4	8.42	7,310
16462	0.92	0.04	43.44	284.4	7.34	7,420
16462_repl	0.92	0.04	42.99	279.8	7.48	7,316
19780	2.63	0.05	148.5	1043	0.60	11,790
19780_repl	3.02	0.06	172.4	1182	0.57	11,716
19781	2.26	0.02	290.0	1489	0.94	20,722
BM.1998,P18(119)	0.63	0.05	39.50	318.4	0.46	7,512
BM.1998,P18(229)	0.30	0.36	33.72	228.6	4.52	6,571
BM.2000,P11(22)	0.19	0.01	18.13	141.5	2.40	4,700
BM.2000,P11(22)_repl	0.18	0.01	17.30	134.7	2.13	4,328

Table 10.24 (continued)

Sample name	Lu (ppm)	Hf (ppm)	Sm (ppm)	Nd (ppm)	Rb (ppm)	Sr (ppm)
BM.2000,P11(22)_repl	0.21	0.01	20.12	155.9	2.53	5,100
BM.2000,P14(24)	0.39	0.002	8.47	59.98	11.30	6,256
BM.2000,P14(25)	0.33	0.01	13.06	93.04	5.30	7,370
LI 23/02/08	0.84	0.04	30.98	205.4	9.18	9,382
LI 23/02/08	0.84	0.05	30.72	83.60	8.57	3,835
BM.2004.P9(9)	0.42	0.19	7.21	44.67	47.81	2,916
BM.2004.P9(9)	0.44	0.21	7.46	46.47	44.59	2,933
GGU 252833	0.30	0.002	45.64	267.2	0.39	2,242
GGU 252874	0.15	0.003	20.79	120.9	0.82	1,372

Table 10.25 Measured and dilution corrected concentrations of Lu, Hf, Sm, Nd, Rb and Sr for non-carbonate fractions of carbonatite samples from the global study (bdl = below detection limit). Data determined by Q-ICP-MS in combination with a desolvator using the final method for Hf chemistry (Chapter 3.6.8.).

Sample name	Lu (ppm)	Hf (ppm)	Sm (ppm)	Nd (ppm)	Rb (ppm)	Sr (ppm)
COQ-1	1.37	2.69	118.09	1,039	26.98	665.6
J1-C1	bdl	bdl	8.72	44.62	14.33	1512
91/66 - C2	0.07	40.89	7.91	42.47	24.56	442.0
91/60 - C5	bdl	bdl	6.72	30.62	8.89	1401
4808	0.09	3.83	127.7	1,295	4.94	743.7
10160	0.18	7.85	85.06	883.3	169.2	631.2
16462	0.32	45.58	91.38	973.2	145.8	1851
16462_repl	0.33	51.47	96.39	1012	147.6	1961
19780	0.64	6.31	3.20	21.55	2.70	49.17
19780_repl	0.63	6.22	3.69	25.04	2.62	85.02
19781	0.09	0.61	20.44	123.5	1.04	305.8
BM.1998,P18(119)	0.15	20.47	6.90	48.17	0.67	832.1
BM.1998,P18(229)	0.07	109.23	15.37	102.6	30.45	896.4
BM.2000,P11(22)	0.03	75.06	2.52	16.94	33.43	273.3
BM.2000,P11(22)_repl	0.04	101.4	2.59	16.87	36.80	159.3
BM.2000,P11(22)_repl	0.01	32.39	0.84	5.45	29.86	54.98
BM.2000,P14(24)	0.05	0.12	1.02	6.79	3.22	451.7
BM.2000,P14(25)	0.04	0.57	1.37	9.11	1.04	558.3
LI 23/02/08	0.44	15.45	12.80	70.37	268.6	261.1
LI 23/02/08	0.48	15.62	14.18	80.00	267.5	429.5
BM.2004.P9(9)	0.06	1.61	0.37	2.50	359.0	450.3
BM.2004.P9(9)	0.08	1.80	0.46	3.11	358.9	538.0
GGU 252833	0.27	21.27	96.95	787.2	16.12	361.3
GGU 252874	0.05	2.54	15.17	121.5	29.89	161.0

Table 10.26 **Measured and dilution corrected whole-rock concentrations of Lu, Hf, Sm, Nd, Rb and Sr of carbonatite samples from the global study. Data determined by Q-ICP-MS in solution mode.**

Sample name	Lu (ppm)	Hf (ppm)	Sm (ppm)	Nd (ppm)	Rb (ppm)	Sr (ppm)
OL-1	0.06	0.42	9.87	125.2	132.8	10,620
OL-1_repl	0.07	0.46	10.39	130.7	131.2	10,830
BM.2004,P12(132)	0.11	0.84	10.70	123.0	141.3	10,730
BM.2004,P12(132)_repl	0.10	0.72	9.00	108.81	112.67	8,884
19777	1.42	0.54	442.05	2837.00	6.46	27,090
19780	1.81	1.83	103.20	746.60	1.29	6,804
19780_repl	1.96	1.79	100.74	756.92	1.14	6,471
19781	1.69	0.13	216.95	1181.00	0.94	22,040
25810	0.74	0.03	119.90	455.60	0.85	10,040
4808	0.56	0.28	28.70	194.20	0.67	4,909
10160	0.86	0.28	42.67	278.60	12.20	5,832
16462	0.77	1.69	41.61	273.13	11.63	5,949
16462_repl	0.75	1.46	36.28	263.48	9.28	5,290
16462_repl	0.70	1.37	33.32	244.54	8.69	5,191
ASS-1	0.11	0.003	5.51	54.81	0.06	12,060
91/66 - C2	0.12	1.01	17.64	115.98	1.62	3,312
91/62 - C4	0.24	8.05	16.80	90.92	0.61	1,940
BM.1998,P18(119)	0.44	1.44	25.19	213.61	0.34	4,744
BM.1998,P18(229)	0.27	6.00	26.82	201.83	5.03	4,732
BM.2000,P11(14)	0.18	3.12	21.01	164.46	0.65	3,837
BM.2000,P11(22)	0.17	3.68	13.69	117.56	3.54	3,168
COQ-1	0.98	0.25	48.49	485.5	10.05	10,201

Table 10.27 **Measured and dilution corrected concentrations of Lu, Hf, Sm, Nd, Rb and Sr for carbonate fractions of carbonatite samples from the global study. Data determined by Q-ICP-MS in solution mode. Data is given in ng, because the sample weight of the carbonate fraction was not weighed prior to chemical treatment.**

Sample name	Lu (ng)	Hf (ng)	Sm (ng)	Nd (ng)	Rb (ng)	Sr (ng)
BM.2004,P12(132)	25.98	157.53	2,553	30,396	31098	2,037,800
16462	156.2	3.26	7,255	49,020	1045	1,133,740
19780	468.5	10.12	28,776	196,832	151.2	1,715,700
91/66 - C2	26.78	2.9	4,092	26,156	125.3	761,080
91/62 - C4	49.68	50.76	3,463	19,450	79.7	401,480
BM.1998,P18(119)	94.32	11.06	5,521	46,212	51.32	1,042,440
BM.1998,P18(229)	56.82	15.2	5,690	41,094	522.5	983,680
BM.2000,P11(14)	35.62	27.77	4,221	34,050	31.72	753,580
BM.2000,P11(22)	33.34	1.37	2,710	22,520	218.2	614,800
COQ-1	147.4	1.5	6,991	69,858	1388	1,964,500

Table 10.28 **Measured and dilution corrected concentrations of Lu, Hf, Sm, Nd, Rb and Sr for non-carbonate fractions of carbonatite samples from the global study. Data determined by Q-ICP-MS in solution mode. Data is given in ng, because the sample weight of the carbonate fraction was not weighed prior to chemical treatment.**

Sample name	Lu (ng)	Hf (ng)	Sm (ng)	Nd (ng)	Rb (ng)	Sr (ng)
BM.2004,P12(132)	3.73	49.44	145.9	1646	768.5	593,520
16462	2.92	318.8	663.7	6869	1,334	23,520
19780	41.43	402.8	233.0	1,521	135.9	7,953
91/66 - C2	2.06	112.3	309.8	1,794	276.7	45,588
91/62 - C4	2.10	1,706	92.725	463.3	49.47	10,118
BM.1998,P18(119)	1.49	322.6	64.78	456.3	30.18	7,695
BM.1998,P18(229)	1.78	501.1	276.1	1,872	729.1	29,011
BM.2000,P11(14)	1.10	124.6	125.4	888.2	110.4	21,852
BM.2000,P11(22)	0.44	270.3	41.39	280.5	537.1	6,958
COQ-1	26.08	46.68	2,295	21,506	921.2	59,676

10.3.3. Trace element data – Fen case study

Table 10.29 **Raw REE trace element data in ppm for whole-rock, carbonate, non-carbonate fractions and mineral separates of carbonatite samples from Fen, Norway. REE data was used for Figure 7.14 and Figure 7.15.**

Sample name	La	Ce	Pr	Nd	Sm	Eu	Gd	Tb	Dy	Ho	Er	Tm	Yb	Lu
Whole-rock														
TS 498 E	95.1	188.2	17.3	137.8	10.8	2.0	4.1	0.3	1.2	0.2	0.4	0.1	0.4	0.1
TS 498 E_repl	97.5	190.1	17.4	140.7	10.9	2.0	4.0	0.3	1.2	0.2	0.4	0.1	0.4	0.1
TS 51.5 E	59.8	141.9	17.6	172.5	24.1	6.4	17.5	1.9	8.1	1.3	2.6	0.3	1.6	0.3
TS 51.5 E_repl	60.8	145.2	17.9	178.7	25.0	6.6	18.1	2.0	8.3	1.3	2.7	0.4	1.6	0.3
MTGS	101.1	257.5	28.5	258.4	33.0	9.0	19.8	2.2	9.9	1.6	3.3	0.4	2.3	0.3
MTGS_repl	101.2	258.9	28.7	255.6	34.2	9.5	21.0	2.3	10.2	1.6	3.3	0.4	2.3	0.3
THY	89.6	243.9	25.5	216.0	30.4	9.4	21.8	2.6	12.1	2.1	4.8	0.7	3.9	0.7
THY_repl	78.3	229.6	24.1	207.6	28.8	8.8	21.5	2.6	11.9	2.1	4.6	0.7	3.6	0.6
CQW-1	93.2	208.1	58.7	221.1	34.1	9.0	27.1	3.1	14.7	2.5	5.4	0.8	3.7	0.6
CQW-1_repl	96.6	215.2	24.4	233.1	36.4	9.5	28.3	3.3	15.1	2.5	5.5	0.8	3.8	0.6
CQW-2	96.6	198.5	23.5	221.8	34.8	9.2	28.1	3.3	15.1	2.6	5.6	0.8	3.9	0.6
CQW-2_repl	105.7	232.0	64.0	242.6	37.4	9.7	29.8	3.5	16.7	2.9	6.4	0.9	4.7	0.8
COQ-1	538.7	1006.8	87.5	707.2	78.5	19.8	50.4	5.7	27.6	4.9	11.5	1.7	8.7	1.4
Carbonate fraction														
TS 498 E	81.7	152.3	37.9	112.5	9.4	1.7	3.8	0.3	1.1	0.2	0.4	0.1	0.3	0.1
TS 498 E_repl	78.4	146.8	36.1	107.8	9.1	1.7	3.6	0.3	1.1	0.2	0.4	0.1	0.3	0.1
TS 51.5 E	49.7	124.4	40.5	149.0	22.2	5.8	16.7	1.8	7.8	1.2	2.5	0.3	1.5	0.2
TS 51.5 E_repl	49.5	124.8	40.5	149.7	22.3	5.9	16.7	1.8	7.7	1.2	2.5	0.3	1.5	0.2
MTGS	123.7	244.0	67.8	224.7	29.1	7.8	18.9	2.0	9.1	1.5	3.0	0.4	2.0	0.3
MTGS_repl	123.0	244.4	68.1	224.5	29.4	7.9	18.6	2.0	9.0	1.5	3.0	0.4	2.0	0.3

Table 10.29 (continued)

Sample name	La	Ce	Pr	Nd	Sm	Eu	Gd	Tb	Dy	Ho	Er	Tm	Yb	Lu
THY	98.3	237.3	26.7	248.0	36.4	10.4	28.5	3.3	16.2	2.8	6.4	0.9	4.8	0.8
THY_repl	95.4	228.2	25.9	241.3	35.7	10.1	27.9	3.3	15.8	2.8	6.2	0.9	4.7	0.8
CQW-1	69.4	173.2	50.8	177.4	27.3	7.8	21.3	2.6	12.0	2.1	4.5	0.6	3.3	0.6
CQW-1_repl	68.6	171.3	50.0	177.0	27.1	7.8	21.2	2.5	11.9	2.0	4.5	0.6	3.2	0.5
CQW-2	73.8	186.7	38.2	196.0	30.3	8.8	24.2	3.0	14.1	2.4	5.3	0.8	3.8	0.7
CQW-2_repl	60.3	153.7	45.2	159.2	24.8	7.3	19.6	2.4	11.5	2.0	4.4	0.6	3.2	0.5
Non-carbonate fraction														
TS 498 E	1735	2644	669.7	2134	159.7	22.5	51.9	3.4	13.3	2.1	4.9	0.9	5.9	1.24
TS 498 E_repl	1986	3036	777.8	2482	185.7	26.2	59.4	3.8	14.3	2.2	5.1	0.9	6.2	1.25
TS 51.5 E	1003	1658	180.7	581.1	51.0	9.8	24.5	1.7	5.3	0.7	1.2	0.1	0.7	0.11
TS 51.5 E_repl	1201	2016	216.5	696.4	59.4	11.1	27.3	1.9	5.3	0.6	1.0	0.1	0.6	0.09
MTGS	100.8	286.3	37.0	359.4	50.7	12.6	32.0	3.6	16.1	2.5	5.1	0.7	3.7	0.63
MTGS_repl	99.7	279.4	36.5	350.6	49.7	12.3	31.2	3.6	15.7	2.4	5.0	0.7	3.5	0.61
THY	1490	962.3	249.5	829.8	82.3	15.3	38.3	2.9	10.0	1.4	2.7	0.4	1.6	0.27
THY_repl	830.9	540.4	139.9	478.4	51.2	10.3	27.9	2.5	10.2	1.6	3.4	0.5	2.4	0.42
CQW-1	289.3	396.4	82.8	286.9	37.7	8.7	19.2	2.0	8.2	1.1	2.0	0.2	1.1	0.14
CQW-1_repl	239.7	325.1	68.6	236.9	31.3	7.3	16.2	1.7	7.0	0.9	1.8	0.2	1.0	0.13
CQW-2	127.1	279.5	68.7	230.5	25.4	5.2	12.4	1.1	4.4	0.6	1.2	0.2	0.8	0.11
CQW-2_repl	139.2	296.6	73.7	248.9	27.1	5.5	13.3	1.2	4.6	0.7	1.3	0.2	0.8	0.13

Table 10.29 (continued)

Sample name	La	Ce	Pr	Nd	Sm	Eu	Gd	Tb	Dy	Ho	Er	Tm	Yb	Lu
Mineral separates														
CQW-1 calcite	156.4	301.9	36.84	139.65	22.86	6.61	17.89	2.24	11.05	1.95	4.52	0.67	3.52	0.61
CQW-1 calcite	151.6	290.7	35.32	134.34	22.08	6.41	17.63	2.20	10.95	1.94	4.50	0.67	3.54	0.62
CQW-1 phlogopite	18.44	42.55	4.84	16.46	1.98	0.32	1.13	0.11	0.48	0.08	0.16	0.02	0.11	0.02
CQW-1 phlogopite	15.26	40.44	4.00	13.65	1.81	0.37	1.14	0.12	0.53	0.08	0.18	0.02	0.12	0.02
CQW-1 phlogopite	13.65	35.36	3.81	12.84	1.70	0.37	1.08	0.12	0.52	0.08	0.17	0.02	0.12	0.02
CQW-1 magnetite	4.99	12.38	1.20	4.27	0.55	0.13	0.37	0.04	0.16	0.03	0.05	0.01	0.03	0.004
CQW-1 magnetite	6.16	13.67	1.37	4.86	0.61	0.13	0.40	0.04	0.17	0.03	0.05	0.01	0.03	0.004
CQW-1 magnetite	7.43	17.08	1.62	5.64	0.67	0.15	0.43	0.04	0.18	0.03	0.06	0.01	0.03	0.005
CQW-1 apatite	107.1	204.3	26.76	97.35	12.50	2.79	8.44	0.85	3.51	0.53	1.05	0.13	0.28	0.08
CQW-1 chlorite	14.04	31.14	3.24	11.11	1.21	0.00	0.67	0.06	0.27	0.04	0.09	0.01	0.07	0.01

Table 10.30 **Measured and dilution corrected concentrations of Lu, Hf, Sm, Nd, Rb and Sr for whole-rock, carbonate and non-carbonate fractions of carbonatite samples from Fen, Norway. Data determined by Q-ICP-MS in combination with a desolvator using the final method for Hf chemistry (Chapter 3.6.8.).**

Sample name	Lu (ppm)	Hf (ppm)	Sm (ppm)	Nd (ppm)	Rb (ppm)	Sr (ppm)
Whole-rock						
TS 51.5 E	0.26	0.04	24.08	172.5	0.01	4,753
TS 51.5 E_repl	0.26	0.04	24.93	178.7	0.01	4,775
TS 498 E	0.07	0.15	10.84	137.8	2.69	4,260
TS 498 E_repl	0.07	0.15	10.81	140.7	2.65	4,186
MTGS	0.33	3.56	33.36	258.4	102.3	1,508
MTGS_repl	0.34	3.72	34.55	255.6	92.88	1,417
THY	0.65	0.18	30.53	216.0	3.84	7,319
THY_repl	0.61	0.18	29.09	207.6	3.76	6,961
CQW-1	0.62	1.79	34.32	221.1	13.12	2,366
CQW-1_repl	0.62	1.86	36.76	233.1	13.71	2,487
CQW-2	0.64	1.31	34.75	221.8	1.13	2,362
CQW-2_repl	0.64	1.31	37.72	242.6	1.18	2,415
Carbonate						
TS 51.5 E	0.25	0.01	22.35	149.0	0.01	1,786
TS 51.5 E_repl	0.25	0.01	22.37	149.7	0.01	1,797
TS 498 E	0.06	0.04	9.47	112.5	0.36	1,723
TS 498 E_repl	0.06	0.04	9.10	107.8	0.34	1,697
MTGS	0.26	0.05	29.09	224.7	104.6	845
MTGS_repl	0.26	0.05	29.50	224.5	106.8	890
THY	0.84	0.01	36.44	248.0	1.09	7,813
THY_repl	0.82	0.01	35.61	241.3	0.97	7,428
CQW-1	0.55	0.02	27.43	177.4	8.51	2,997
CQW-1_repl	0.54	0.02	27.17	177.0	8.18	3,002
CQW-2	0.66	0.03	30.17	196.0	1.29	3,395
CQW-2_repl	0.55	0.02	25.06	159.2	1.10	2,888
Non-carbonate						
TS 51.5 E	0.11	2.62	51.53	581.1	0.71	978.4
TS 51.5 E_repl	0.09	3.20	59.44	696.4	0.10	628.2
TS 498 E	1.24	8.74	159.3	2,134	250.6	469.6
TS 498 E_repl	1.25	8.77	185.4	2,482	105.8	706.0
MTGS	0.63	11.80	50.78	359.4	73.24	362.4
MTGS_repl	0.61	11.55	50.08	350.6	76.48	362.6
THY	0.27	16.46	82.36	829.8	147.8	1052
THY_repl	0.42	7.63	51.72	478.4	71.45	2040
CQW-1	0.14	19.50	37.79	286.9	69.31	304.7
CQW-1_repl	0.13	15.31	31.37	236.9	61.89	448.8
CQW-2	0.11	10.61	25.54	230.5	2.15	172.7
CQW-2_repl	0.13	10.96	27.19	248.9	1.71	128.1

Table 10.31 **Measured and dilution corrected concentrations of Lu, Hf, Sm, Nd, Rb and Sr in mineral separates of carbonatite samples from Fen, Norway. Data determined by Q-ICP-MS in combination with a desolvator using the final method for Hf chemistry (Chapter 3.6.8.).**

Sample name	Fraction	Lu (ppm)	Hf (ppm)	Sm (ppm)	Nd (ppm)	Rb (ppm)	Sr (ppm)
Mineral separates							
CQW-1	Calcite	0.61	0.01	22.9	144.5	0.07	8136.2
CQW-1	Calcite	0.62	0.01	22.1	148.4	0.07	7892.8
CQW-1	Phlogopite	0.02	0.08	1.98	16.5	357.1	221.9
CQW-1	Phlogopite	0.02	0.10	1.81	13.6	360.0	216.1
CQW-1	Phlogopite	0.02	0.15	1.70	12.8	369.98	219.9
CQW-1	Magnetite	0.004	0.23	0.55	4.27	0.66	29.8
CQW-1	Magnetite	0.004	0.25	0.61	4.86	0.66	28.6
CQW-1	Magnetite	0.005	0.18	0.67	5.64	0.43	29.6
CQW-1	Apatite	0.08	1.64	12.5	97.4	2.09	399.1
CQW-1	Chlorite	0.01	0.15	1.21	11.1	357.79	111

10.3.4. Isotope data – lithophile elements

Table 10.32 **Measured and age corrected Hf isotopic composition in whole-rock (WR), carbonate (C) and non-carbonate (NC) fractions of carbonatites using different chemical procedures. Samples are sorted by age and USGS reference material COQ-1 is given at the end of each batch. Data was normalised to 0.282785 (Bouvier et al., 2008) and ε-values and corresponding errors were calculated using the spreadsheet from Ickert (2013). Reproducibility given by external standard JMC475 is highlighted by superscripts next to $^{176}Hf/^{177}Hf_m$ values and given as footnotes below the table. DNR = sample did not run.**

Sample name	Fraction	Beam size ^{179}Hf (V)	$^{176}Hf/^{177}Hf_m$	2SE	$^{176}Lu/^{177}Hf$	2SE	$^{176}Hf/^{177}Hf_t$	εHf_t	2SE
Standard procedure (Chapter 3.6.1), parent isotope ratio with Q-ICP-MS in solution mode									
OL-1	WR	0.35	0.282601[a]	0.000020	0.022581	0.001129	0.282601	-6.5	0.8
4808	WR	0.01	0.283923[a]	0.000698	0.277999	0.013900	0.281111	-51.3	25.3
10160	WR	0.01	0.281327[a]	0.000363	0.422680	0.021134	0.277052	-197.5	15.2
19777	WR	2.19	0.291736[a]	0.000006	0.368290	0.018414	0.282695	26.1	16.4
19780	WR	9.05	0.285038[a]	0.000003	0.137388	0.006869	0.281666	-10.4	6.1
19871	WR	0.02	0.323911[a]	0.000202	1.870519	0.093526	0.277992	-140.7	83.6
25810	WR	0.02	0.379868[a]	0.000194	3.558009	0.177900	0.292523	374.6	158.7
Standard procedure and addition of Al-solution (Chapter 3.6.3 a), parent isotope ratio with Q-ICP-MS in solution mode									
OL-1	WR	0.57	0.282300[b]	0.000016	0.022581	0.001129	0.282300	-17.2	0.7
BM.2004,P12(132)	WR	2.16	0.282471[b]	0.000006	0.017437	0.000872	0.282471	-11.1	0.5
ASS-1	WR	0.02	0.288843[b]	0.000253	6.126882	0.306344	0.243608	-1377.8	82.4
4808	WR	0.25	0.284867[b]	0.000026	0.277999	0.013900	0.282055	-13.8	5.2
16462	WR	1.14	0.282325[b]	0.000013	0.060539	0.003027	0.281713	-25.9	1.2
19780	WR	7.05	0.284938[b]	0.000009	0.137388	0.006869	0.281565	-14.0	6.1
19781	WR	0.05	0.326682[b]	0.000137	1.870519	0.093526	0.280763	-42.5	83.5
COQ-1	WR	0.33	0.282187[b]	0.000025	0.484011	0.024201	0.281128	-56.0	2.1

Table 10.32 (continued)

Sample name	Fraction	Beam size ^{179}Hf (V)	$^{176}Hf/^{177}Hf_m$	2SE	$^{176}Lu/^{177}Hf$	2SE	$^{176}Hf/^{177}Hf_t$	εHf_t	2SE
Final procedure (Chapter 3.6.8), parent isotope ratio with Q-ICP-MS in solution mode									
BM.2004,P12(132)	WR	0.97	0.282641[d]	0.000010	0.019802	0.002427	0.282641	-5.1	0.5
	C	0.05	0.283062[c]	0.000620	0.022960	0.001846	0.283062	9.8	21.9
	NC	0.13	0.282646[c]	0.000049	0.010506	0.002810	0.282646	-4.9	1.8
91/66 - C2	WR	1.83	0.282881[d]	0.000008	0.016363	0.000409	0.282841	4.9	0.5
	C	0.11	0.283489[c]	0.000052	1.285877	0.386166	0.280340	-83.6	33.5
	NC	0.02	0.283688[c]	0.000250	0.002554	0.000055	0.283682	34.6	8.9
91/62 - C4	WR	17.47	0.282822[d]	0.000003	0.004232	0.000076	0.282811	3.8	0.4
	C	0.53	0.283084[c]	0.000014	0.136285	0.003087	0.282750	1.7	0.7
	NC	0.25	0.282824[c]	0.000026	0.000171	0.000003	0.282823	4.3	1.0
BM.1998,P18(119)	WR	8.80	0.283038[d]	0.000004	0.042717	0.002407	0.282750	6.8	0.7
	C	-	DNR	-	1.187505	0.063328	-	-	-
	NC	10.21	0.282804[c]	0.000002	0.000643	0.000032	0.282800	8.5	0.4
BM.1998,P18(229)	WR	4.67	0.282831[d]	0.000006	0.006191	0.000087	0.282789	8.2	0.4
	C	0.02	0.283635[c]	0.000302	0.520528	0.074646	0.280125	-86.1	20.8
	NC	0.13	0.282929[c]	0.000040	0.000495	0.000052	0.282926	13.0	1.5
BM.2000,P11(14)	WR	7.49	0.282803[d]	0.000003	0.007942	0.000059	0.282747	7.1	0.4
	C	0.06	0.2838120[c]	0.000076	0.178610	0.006314	0.282548	0.1	3.2
	NC	0.56	0.282801[c]	0.000015	0.001229	0.000048	0.282792	8.7	0.6
BM.2000,P11(22)	WR	-	DNR	-	0.006339	0.000077	-		
	C	0.05	0.290589[c]	0.000060	3.388690	0.572126	0.266463	-569.2	144.5
	NC	0.27	0.282748[c]	0.000028	0.000227	0.000004	0.282747	7.1	1.1

Table 10.32 (continued)

Sample name	Fraction	Beam size ^{179}Hf (V)	$^{176}Hf/^{177}Hf_m$	2SE	$^{176}Lu/^{177}Hf$	2SE	$^{176}Hf/^{177}Hf_t$	εHf_t	2SE
16462	WR	0.05	0.282723[d]	0.000114	0.070547	0.000882	0.282009	-16.0	4.1
	C	0.01	0.297685[c]	0.000458	6.671057	0.384914	0.230214	-1849.2	141.2
	NC	4.02	0.282015[c]	0.000048	0.001276	0.000048	0.282002	-15.7	1.7
19780	WR	7.39	0.285038[d]	0.000003	0.152811	0.003622	0.281287	-23.9	3.4
	C	0.00	0.320080[c]	0.001454	7.240487	1.445046	0.142334	-4952.0	1261.1
	NC	12.55	0.282348[c]	0.000002	0.014322	0.001194	0.281996	1.3	1.1
COQ-1	WR	0.24	0.283777[d]	0.000026	0.556422	0.014535	0.282560	-5.4	1.6
	C	-	DNR	-	13.685226	19.186419	-	-	-
	NC	0.29	0.283057[c]	0.000022	0.077797	0.001998	0.282887	6.2	0.9
Final procedure (Chapter 3.6.8), parent isotope ratio with Q-ICP-MS and *CETAC Aridus™*									
LI 23/02/08	WR	12.2	0.283055[h]	0.000008	0.115544	0.000128	0.283046	9.3	0.5
	C	0.0099	0.282635[i]	0.000360	2.810786	0.176917	0.282415	-13.0	12.7
	NC	13.7	0.283046[h]	0.000002	0.003947	0.000102	0.283046	9.3	0.4
LI 23/02/08	WR	10.9	0.283051[h]	0.000002	0.115394	0.003000	0.283042	9.2	0.4
	C	0.013	0.282748[i]	0.000328	2.590410	0.029717	0.282545	-8.4	11.6
	NC	13.89	0.283038[h]	0.000002	0.004235	0.000141	0.283038	9.0	0.4
BM.2004.P9(9)	WR	11.1	0.283045[h]	0.000002	0.015418	0.002197	0.283044	9.2	0.4
	C	0.82	0.283054[i]	0.000012	0.305081	0.021988	0.283030	8.8	0.6
	NC	6.4	0.283041[h]	0.000004	0.005575	0.000335	0.283041	9.1	0.4
BM.2004.P9(9)	WR	15.8	0.283042[h]	0.000002	0.015844	0.002170	0.283041	9.1	0.4
	C	0.73	0.283035[i]	0.000012	0.288800	0.005836	0.283012	8.1	0.6
	NC	1.84	0.283041[h]	0.000008	0.005874	0.000558	0.283041	9.1	0.5

Table 10.32 (continued)

Sample name	Fraction	Beam size ^{179}Hf (V)	$^{176}Hf/^{177}Hf_m$	2SE	$^{176}Lu/^{177}Hf$	2SE	$^{176}Hf/^{177}Hf_t$	εHf_t	2SE
J1-C1	WR	0.23	0.287567[e]	0.000026	3.989559	0.521224	0.277798	-173.5	45.3
	C	0.06	0.299161[f]	0.000180	12.462634	1.871505	0.268643	-497.3	162.7
	NC	0.03	0.283280[g]	0.000234	0.059254	0.014694	0.283135	15.3	8.4
91/66 - C2	WR	7.94	0.282852[e]	0.000004	0.016810	0.000885	0.282811	3.8	0.4
	C	0.29	0.283638[f]	0.000029	0.516048	0.044040	0.282374	-11.6	4.0
	NC	6.9	0.282816[h]	0.000004	0.000230	0.000032	0.282815	4.0	0.4
91/60 - C5	WR	0.399	0.284500[e]	0.000018	1.292754	0.178762	0.281334	-48.4	15.5
	C	0.06	0.285925[f]	0.000164	3.049107	0.986688	0.278458	-150.1	85.7
	NC	0.029	0.283315[g]	0.000264	0.075678	0.015741	0.283129	18.7	9.3
BM.1998,P18(119)	WR	8.27	0.283060[e]	0.000004	0.036529	0.003105	0.282814	9.0	0.8
	C	0.24	0.293164[f]	0.000022	1.740273	0.111494	0.281428	-40.0	27.0
	NC	10.7	0.282807[g]	0.000002	0.001029	0.000059	0.282800	8.6	0.4
BM.1998,P18(229)	WR	15.3	0.282844[e]	0.000002	0.006698	0.000351	0.282799	8.5	0.4
	C	0.34	0.283188[f]	0.000024	0.114233	0.003345	0.282418	-5.0	1.2
	NC	11.06	0.282805[g]	0.000004	0.000108	0.000005	0.282804	8.7	0.4
BM.2000,P11(22)	WR	14.55	0.282785[e]	0.000002	0.007513	0.000268	0.282732	6.6	0.4
	C	0.03	0.294723[f]	0.000114	2.729877	0.678876	0.275287	-256.9	171.3
	NC	3.73	0.282740[g]	0.000006	0.000075	0.000016	0.282739	6.8	0.4
BM.2000,P11(22)_repl	WR	4.93	0.282801[e]	0.000004	0.009257	0.000320	0.282735	6.7	0.4
	C	0.015	0.294784[f]	0.000293	2.671660	0.369419	0.275762	-240.1	93.9
	NC	16.5	0.282737[g]	0.000002	0.000055	0.000012	0.282737	6.8	0.4
BM.2000,P11(22)_repl	WR	15.27	0.282792[e]	0.000006	0.008853	0.000281	0.282729	6.5	0.4
	C	0.021	0.296202[f]	0.000225	3.445154	0.560748	0.271673	-384.8	141.8
	NC	12.095	0.282740[g]	0.000002	0.000065	0.000019	0.282740	6.9	0.4

Table 10.32 (continued)

Sample name	Fraction	Beam size ^{179}Hf (V)	$^{176}Hf/^{177}Hf_m$	2SE	$^{176}Lu/^{177}Hf$	2SE	$^{176}Hf/^{177}Hf_t$	εHf_t	2SE
BM.2000,P14(24)	WR	0.14	0.300607[e]	0.000050	8.058082	1.325164	0.243235	-1391.3	334.7
	C	0.05	-	-	-	-	-	-	-
	NC	0.0446	0.284436[g]	0.000116	0.043685	0.008225	0.284125	51.4	4.4
BM.2000,P14(25)	WR	0.19	0.288184[e]	0.000032	1.143744	0.048823	0.280041	-88.7	12.7
	C	0.07	0.300730[f]	0.000084	4.223609	0.329748	0.270659	-420.7	83.9
	NC	0.31	0.283070[g]	0.000022	0.010029	0.000505	0.282999	16.1	0.9
4808	WR	0.81	0.288188[e]	0.000014	0.562800	0.037282	0.282496	1.8	13.5
	C	0.02	0.343655[f]	0.000194	8.865412	1.016654	0.253991	-1007.4	365.8
	NC	0.21	0.283314[g]	0.000030	0.002997	0.001360	0.283284	29.7	1.2
10160	WR	2.94	0.286711[e]	0.000006	0.478731	0.012665	0.281869	-20.4	4.9
	C	0.06	0.339658[f]	0.000114	8.071371	0.780058	0.258025	-864.6	281.1
	NC	0.58	0.282942[g]	0.000014	0.003930	0.000069	0.282902	16.2	0.6
16462	WR	5.81	0.282447[e]	0.000032	0.068153	0.003638	0.281758	-24.3	1.8
	C	0.008	0.305906[f]	0.000582	2.892233	0.146731	0.276654	-205.0	57.5
	NC	4.66	0.282584[g]	0.000004	0.000960	0.000215	0.282574	4.6	0.4
16462_repl	WR	5.84	0.282233[e]	0.000012	0.072228	0.008544	0.281502	-33.4	3.1
	C	0.016	0.305750[f]	0.000264	3.347381	0.171230	0.271895	-373.5	63.4
	NC	4.33	0.282569[g]	0.000004	0.000938	0.000053	0.282560	4.0	0.4
19780	WR	14.3	0.284996[e]	0.000002	0.134179	0.005559	0.281702	-9.2	4.9
	C	0.027	0.395603[f]	0.000199	7.470670	0.381627	0.212207	-2473.9	339.9
	NC	8.89	0.282345[g]	0.000004	0.014402	0.000899	0.281991	1.4	0.4
19780_repl	WR	14.88	0.284887[e]	0.000002	0.128668	0.004746	0.281728	-8.2	4.2
	C	0.04	0.388258[f]	0.000112	7.086217	0.254909	0.214300	-2399.6	232.1
	NC	11.15	0.282349[g]	0.000006	0.014735	0.000751	0.281987	1.4	1.5

Table 10.32 (continued)

Sample name	Fraction	Beam size ^{179}Hf (V)	$^{176}Hf/^{177}Hf_m$	2SE	$^{176}Lu/^{177}Hf$	2SE	$^{176}Hf/^{177}Hf_t$	εHf_t	2SE
19781	WR	0.15	0.324579[e]	0.000038	1.866070	0.065817	0.278769	-113.2	60.0
	C	0.13	0.830822[f]	0.000099	20.647462	1.763571	0.323951	1489.3	1548.1
	NC	1.74	0.284027[g]	0.000008	0.019634	0.000379	0.283545	55.5	1.0
GGU 252833	WR	13.87	0.281890[i]	0.000002	0.023656	0.001886	0.280524	-11.4	3.9
	C	0.025	0.755442[i]	0.000310	18.450269	4.572056	-0.309996	-21038.0	9410.6
	NC	14.31	0.281112[h]	0.000002	0.001791	0.000039	0.281009	5.8	0.8
GGU 252874	WR	7.23	0.281601[i]	0.000004	0.017450	0.000931	0.280593	-9.0	2.0
	C	0.036	0.468840[i]	0.000186	6.753495	2.059897	0.078849	-7192.4	4238.3
	NC	8.95	0.281289[h]	0.000004	0.002483	0.000079	0.281146	10.7	0.8
COQ-1	WR	2.81	0.283695[e]	0.000006	0.484011	0.024956	0.282637	-2.7	2.0
	C	0.004	0.292841[f]	0.001510	11.591184	2.857419	0.267494	-538.3	227.6
	NC	3.05	0.282915[g]	0.000016	0.058336	0.004169	0.282788	1.7	0.7

[a] JMC475 $^{176}Hf/^{177}Hf$ 0.282136 ±0.000004 2SD (n=9)
[b] JMC475 $^{176}Hf/^{177}Hf$ 0.282154 ±0.000013 2SD (n=6)
[c] JMC475 $^{176}Hf/^{177}Hf$ 0.282161 ±0.000012 2SD (n=12)
[d] JMC475 $^{176}Hf/^{177}Hf$ 0.282142 ±0.000012 2SD (n=8)
[e] JMC475 $^{176}Hf/^{177}Hf$ 0.282153 ±0.000014 2SD (n=18)
[f] JMC475 $^{176}Hf/^{177}Hf$ 0.282146 ±0.000019 2SD (n=16)
[g] JMC475 $^{176}Hf/^{177}Hf$ 0.282161 ±0.000021 2SD (n=15)
[h] JMC475 $^{176}Hf/^{177}Hf$ 0.282150 ±0.000008 2SD (n=17)
[i] JMC475 $^{176}Hf/^{177}Hf$ 0.282149 ±0.000009 2SD (n=18)

Table 10.33 **Measured and age corrected Nd isotopic composition in whole-rock (WR), carbonate (C) and non-carbonate (NC) fractions of carbonatites from different localities using different chemical procedures. Samples are sorted by age and USGS reference material COQ-1 is given at the end of each batch. Data was normalised to 0.51263 (Bouvier et al., 2008) and ε-values and corresponding errors were calculated using the spreadsheet from Ickert (2013). Reproducibility given by external standard *JNd$_i$* is highlighted by superscripts next to $^{143}Nd/^{144}Nd_m$ values and given as footnotes below the table. JNd$_i$ was measured pure and doped with Sm (Sm/Nd=0.2), the values given represent the averages of both standards.**

Sample name	Fraction	$^{143}Nd/^{144}Nd_m$	2SE	$^{147}Sm/^{144}Nd$	2SE	$^{143}Nd/^{144}Nd_t$	εNd_t	2SE
Standard procedure (Chapter 3.6.1), parent isotope ratio with Q-ICP-MS in solution mode								
OL-1	WR	0.512665[a]	0.000004	0.049885	0.006751	0.512665	0.7	0.2
4808	WR	0.512447[a]	0.000004	0.093064	0.013010	0.512118	3.9	1.0
10160	WR	0.512449[a]	0.000004	0.096930	0.005309	0.512107	3.6	0.5
19777	WR	0.511940[a]	0.000005	0.098138	0.022341	0.511103	2.8	3.7
19780	WR	0.511843[a]	0.000004	0.087060	0.008745	0.511100	2.8	1.5
19871	WR	0.512104[a]	0.000004	0.115504	0.007732	0.511119	3.1	1.3
25810	WR	0.512531[a]	0.000004	0.165753	0.008826	0.511117	3.1	1.5
Standard procedure and addition of Al-solution (Chapter 3.6.3 a), parent isotope ratio with Q-ICP-MS in solution mode								
OL-1	WR	0.512650[b]	0.000008	0.049885	0.002494	0.512650	0.4	0.3
OL-2	WR	0.512648[b]	0.000011	0.054790	0.002740	0.512648	0.4	0.3
ASS-1	WR	0.512216[b]	0.000010	0.063299	0.003165	0.512053	-1.4	0.3
4808	WR	0.512463[b]	0.000008	0.093064	0.004653	0.512135	3.8	0.4
16462	WR	0.512449[b]	0.000012	0.095543	0.004777	0.512112	3.4	0.5
19780	WR	0.511845[b]	0.000008	0.087060	0.004353	0.511102	2.8	0.8
19781	WR	0.512106[b]	0.000006	0.115504	0.005775	0.511121	3.2	1.0

Table 10.33 (continued)

Sample name	Fraction	$^{143}Nd/^{144}Nd_m$	2SE	$^{147}Sm/^{144}Nd$	2SE	$^{143}Nd/^{144}Nd_t$	εNd_t	2SE
COQ-1	WR	0.512849[b]	0.000010	0.071983	0.003599	0.512794	6.1	0.3
Final procedure (Chapter 3.6.8), parent isotope ratio with Q-ICP-MS in solution mode								
OL-2	WR	0.512658[c]	0.000010	0.052112	0.005669	0.512658	0.6	0.3
	C	0.512676[c]	0.000007	0.053941	0.003817	0.512676	0.9	0.3
	NC	0.512702[c]	0.000009	0.055826	0.013559	0.512702	1.4	0.3
91/66 - C2	WR	0.512654[c]	0.000014	0.095819	0.000448	0.512572	2.1	0.3
	C	0.512646[c]	0.000005	0.098532	0.009958	0.512562	1.9	0.3
	NC	0.512673[c]	0.000008	0.108807	0.001428	0.512580	2.3	0.3
91/62 - C4	WR	0.512656[c]	0.000006	0.116361	0.020547	0.512556	1.8	0.4
	C	0.512566[c]	0.000006	0.112148	0.002880	0.512470	0.2	0.2
	NC	0.512645[c]	0.000007	0.126052	0.002964	0.512537	1.5	0.3
BM.1998,P18(119)	WR	0.512686[c]	0.000007	0.074267	0.002764	0.512511	6.7	0.3
	C	0.512686[c]	0.000006	0.075243	0.002375	0.512509	6.7	0.3
	NC	0.512692[c]	0.000013	0.089416	0.003013	0.512481	6.1	0.4
BM.1998,P18(229)	WR	0.512718[c]	0.000007	0.083687	0.001136	0.512521	6.9	0.3
	C	0.512717[c]	0.000007	0.087204	0.002603	0.512511	6.7	0.3
	NC	0.512697[c]	0.000007	0.092893	0.003918	0.512478	6.1	0.3
BM.2000,P11(14)	WR	0.512661[c]	0.000007	0.080473	0.012058	0.512461	6.2	0.6
	C	0.512650[c]	0.000005	0.078083	0.000920	0.512456	6.1	0.3
	NC	0.512662[c]	0.000008	0.088896	0.002101	0.512441	5.8	0.3

Table 10.33 (continued)

Sample name	Fraction	$^{143}Nd/^{144}Nd_m$	2SE	$^{147}Sm/^{144}Nd$	2SE	$^{143}Nd/^{144}Nd_t$	εNd_t	2SE
BM.2000,P11(22)	WR	0.512680[c]	0.000015	0.073353	0.000981	0.512498	6.9	0.4
	C	0.512636[c]	0.000007	0.075787	0.001219	0.512448	6.0	0.3
	NC	0.512660[c]	0.000010	0.092942	0.004185	0.512429	5.6	0.4
16462	WR	0.512463[c]	0.000006	0.085829	0.001892	0.512160	4.7	0.3
	C	0.512470[c]	0.000007	0.093221	0.005755	0.512141	4.0	0.5
	NC	0.512343[c]	0.000006	0.060856	0.000967	0.512128	3.7	0.3
19780	WR	0.511847[c]	0.000008	0.083826	0.001128	0.511132	3.4	0.4
	C	0.511850[c]	0.000007	0.086310	0.011484	0.511114	3.0	2.0
	NC	0.512123[c]	0.000006	0.096456	0.005097	0.511300	6.7	0.9
COQ-1	WR	0.512865[c]	0.000009	0.062901	0.001219	0.512816	6.6	0.3
	C	0.512857[c]	0.000006	0.063026	0.002038	0.512809	6.4	0.2
	NC	0.512869[c]	0.000011	0.067215	0.000996	0.512818	6.6	0.3
Final procedure (Chapter 3.6.8), parent isotope ratio with Q-ICP-MS and *CETAC Aridus™*								
LI 23/02/08	WR	0.512970[e]	0.000004	0.103147	0.001552	0.512967	6.7	0.2
	C	0.512984[f]	0.000006	0.101741	0.002785	0.512981	7.0	0.2
	NC	0.512988[f]	0.000006	0.114548	0.005297	0.512985	7.0	0.2
LI 23/02/08	WR	0.512981[e]	0.000004	0.102880	0.007319	0.512978	6.9	0.2
	C	0.512982[f]	0.000006	0.231458	0.005240	0.512976	6.8	0.2
	NC	0.512999[f]	0.000006	0.111655	0.003701	0.512996	7.2	0.2

Table 10.33 (continued)

Sample name	Fraction	$^{143}Nd/^{144}Nd_m$	2SE	$^{147}Sm/^{144}Nd$	2SE	$^{143}Nd/^{144}Nd_t$	εNd_t	2SE
BM.2004.P9(9)	WR	0.513037[e]	0.000006	0.136745	0.110627	0.513033	8.0	0.2
	C	0.512991[f]	0.000004	0.101640	0.005741	0.512988	7.1	0.2
	NC	-	0.000014	0.092290	0.002229	-0.000003		0.3
BM.2004.P9(9)	WR	0.513019[e]	0.000006	0.103719	0.002476	0.513016	7.6	0.2
	C	0.512999[f]	0.000006	0.101131	0.002844	0.512996	7.2	0.2
	NC	-	0.000012	0.093752	0.005967	-0.000003		0.3
J1-C1	WR	0.512637[b]	0.000006	0.096217	0.001525	0.512555	1.8	0.2
	C	0.512639[d]	0.000006	0.098526	0.003091	0.512555	1.8	0.2
	NC	0.512655[d]	0.000016	0.102916	0.002581	0.512567	2.0	0.4
91/66 - C2	WR	0.512653[b]	0.000006	0.103235	0.001966	0.512565	2.0	0.2
	C	0.512643[d]	0.000008	0.104457	0.003623	0.512553	1.8	0.3
	NC	0.512649[d]	0.000006	0.112873	0.006214	0.512552	1.8	0.3
91/60 - C5	WR	0.512582[b]	0.000006	0.115353	0.009569	0.512483	0.4	0.3
	C	0.512585[d]	0.000006	0.117560	0.001774	0.512484	0.4	0.2
	NC	0.512643[d]	0.000014	0.116315	0.002695	0.512543	1.6	0.3
BM.1998,P18(119)	WR	0.512680[b]	0.000006	0.082944	0.003013	0.512485	6.2	0.3
	C	0.512679[d]	0.000006	0.078136	0.000895	0.512495	6.4	0.3
	NC	0.512681[d]	0.000012	0.089343	0.004812	0.512470	5.9	0.4
BM.1998,P18(229)	WR	0.512716[b]	0.000006	0.099114	0.003512	0.512482	6.1	0.3
	C	0.512708[d]	0.000006	0.092905	0.011151	0.512489	6.3	0.6
	NC	0.512699[d]	0.000004	0.093437	0.006170	0.512479	6.1	0.4

Table 10.33 (continued)

Sample name	Fraction	$^{143}Nd/^{144}Nd_m$	2SE	$^{147}Sm/^{144}Nd$	2SE	$^{143}Nd/^{144}Nd_t$	εNd_t	2SE
BM.2000,P11(22)	WR	0.512620[b]	0.000004	0.081752	0.002253	0.512416	5.3	0.3
	C	0.512628[d]	0.000006	0.080652	0.000950	0.512427	5.6	0.3
	NC	0.512726[d]	0.000012	0.089842	0.009723	0.512502	7.0	0.6
BM.2000,P11(22)_repl	WR	0.512632[b]	0.000006	0.082063	0.001413	0.512428	5.6	0.3
	C	0.512634[d]	0.000006	0.080911	0.002487	0.512433	5.7	0.3
	NC	0.512748[d]	0.000012	0.094380	0.003090	0.512513	7.2	0.4
BM.2000,P11(22)_repl	WR	0.512622[b]	0.000006	0.081878	0.000416	0.512418	5.4	0.3
	C	0.512621[d]	0.000006	0.081294	0.003422	0.512419	5.4	0.3
	NC	0.512945[d]	0.000018	0.094098	0.007904	0.512711	11.1	0.6
BM.2000,P14(24)	WR	0.512459[b]	0.000008	0.088598	0.000259	0.512239	1.9	0.3
	C	0.512468[d]	0.000008	0.088897	0.002067	0.512247	2.0	0.3
	NC	0.512534[d]	0.000050	0.097311	0.024916	0.512292	2.9	1.6
BM.2000,P14(25)	WR	0.512507[b]	0.000008	0.090210	0.001157	0.512283	2.7	0.3
	C	0.512514[d]	0.000008	0.088415	0.000707	0.512294	3.0	0.3
	NC	0.512556[d]	0.000020	0.092026	0.005042	0.512327	3.6	0.5
4808	WR	0.512469[b]	0.000008	0.094578	0.001502	0.512135	3.8	0.3
	C	0.512487[d]	0.000006	0.095562	0.002364	0.512150	4.1	0.3
	NC	0.512348[d]	0.000006	0.062305	0.003487	0.512128	3.7	0.4
10160	WR	0.512466[b]	0.000006	0.099457	0.002174	0.512115	3.5	0.3
	C	0.512473[d]	0.000008	0.096500	0.000622	0.512132	3.8	0.3
	NC	0.512325[d]	0.000006	0.060316	0.000868	0.512112	3.4	0.3

Table 10.33 (continued)

Sample name	Fraction	$^{143}Nd/^{144}Nd_m$	2SE	$^{147}Sm/^{144}Nd$	2SE	$^{143}Nd/^{144}Nd_t$	εNd_t	2SE
16462	WR	0.512455[b]	0.000008	0.096166	0.002231	0.512115	3.5	0.3
	C	0.512464[d]	0.000006	0.096186	0.001324	0.512124	3.6	0.3
	NC	0.512489[d]	0.000066	0.058909	0.000950	0.512281	6.7	1.3
16462_repl	WR	0.512456[b]	0.000008	0.094077	0.004251	0.512124	3.6	0.4
	C	0.512459[d]	0.000006	0.096759	0.002461	0.512117	3.5	0.3
	NC	0.512343[d]	0.000006	0.059862	0.006505	0.512132	3.8	0.5
19780	WR	0.511850[b]	0.000006	0.089057	0.004409	0.511090	2.6	0.8
	C	0.511836[d]	0.000006	0.089690	0.000631	0.511071	2.2	0.4
	NC	0.512082[d]	0.000014	0.089188	0.002572	0.511321	7.1	0.6
19780_repl	WR	0.511846[b]	0.000004	0.088347	0.001455	0.511092	2.6	0.4
	C	0.511839[d]	0.000006	0.091877	0.001731	0.511055	1.9	0.5
	NC	0.512040[d]	0.000004	0.091227	0.009615	0.511262	5.9	1.6
19781	WR	-	-	0.115362	0.002890	-	-	-
	C	0.512113[d]	0.000006	0.122693	0.003315	0.511066	2.1	0.6
	NC	0.511982[d]	0.000006	0.103517	0.001651	0.511099	2.8	0.4
GGU 252833	WR	0.510690[e]	0.000006	0.098036	0.001988	0.508743	0.6	2.0
	C	0.510855[e]	0.000004	0.107585	0.006413	0.508221	-0.4	2.6
	NC	0.510357[f]	0.000006	0.077570	0.000544	0.509189	1.5	0.9
GGU 252874	WR	0.510729[e]	0.000008	0.100152	0.006200	0.508740	0.0	2.5
	C	0.510857[e]	0.000006	0.108252	0.002549	0.508707	-0.6	1.2
	NC	0.510415[f]	0.000006	0.078662	0.004961	0.508853	2.3	2.1

Table 10.33 (continued)

Sample name	Fraction	$^{143}Nd/^{144}Nd_m$	2SE	$^{147}Sm/^{144}Nd$	2SE	$^{143}Nd/^{144}Nd_t$	εNd_t	2SE
COQ-1	WR	0.512843[b]	0.000006	0.071983	0.001637	0.512788	6.0	0.2
	C	0.512850[d]	0.000008	0.069841	0.001077	0.512796	6.2	0.3
	NC	0.512849[d]	0.000010	0.074327	0.006033	0.512792	6.1	0.3

[a] JNd_i $^{143}Nd/^{144}Nd$ 0.512106 ±0.000017 2SD (n=15)
[b] JNd_i $^{143}Nd/^{144}Nd$ 0.512116 ±0.000011 2SD (n=17)
[c] JNd_i $^{143}Nd/^{144}Nd$ 0.512118 ±0.000005 2SD (n=17)
[d] JNd_i $^{143}Nd/^{144}Nd$ 0.512117 ±0.000011 2SD (n=21)
[e] JNd_i $^{143}Nd/^{144}Nd$ 0.512111 ±0.000008 2SD (n=17)
[f] JNd_i $^{143}Nd/^{144}Nd$ 0.512126 ±0.000011 2SD (n=19)

Table 10.34 **Measured and age corrected Sr isotopic composition in whole-rock (WR), carbonate (C) and non-carbonate (NC) fractions of carbonatites from different localities using different chemical procedures. Samples are sorted by age and USGS reference material COQ-1 is given at the end of each batch. Data was normalised to 0.7045 (DePaolo and Wasserburg, 1976b). Reproducibility given by external standard NBS987 is highlighted by superscripts next to $^{87}Sr/^{86}Sr_m$ values and given as footnotes below the table.**

Sample name	Fraction	$^{87}Sr/^{86}Sr_m$	2SE	$^{87}Rb/^{86}Sr$	2SE	$^{87}Sr/^{86}Sr_t$
Standard procedure (Chapter 3.6.1), parent isotope ratio with Q-ICP-MS in solution mode						
OL-1	WR	0.704382[a]	0.000011	0.035285	0.000874	0.704383
4808	WR	0.703005[a]	0.000012	0.000388	0.000024	0.703002
10160	WR	0.703063[a]	0.000009	0.005904	0.000144	0.703018
19777	WR	0.702976[a]	0.000009	0.000673	0.000005	0.702964
19780	WR	0.703496[a]	0.000011	0.000534	0.000007	0.703487
19871	WR	0.702803[a]	0.000010	0.000120	0.000004	0.702801
25810	WR	0.702870[a]	0.000010	0.000238	0.000003	0.702866
Standard procedure and addition of Al-solution (Chapter 3.6.3 a), parent isotope ratio with Q-ICP-MS in solution mode						
OL-1	WR	0.704406[b]	0.000006	0.034193	0.001908	0.704406
OL-2	WR	0.704398[b]	0.000006	0.037169	0.001616	0.704398
ASS-1	WR	0.704857[b]	0.000006	0.000014	0.000003	0.704857
4808	WR	0.703040[b]	0.000005	0.000388	0.000024	0.703037
16462	WR	0.703128[b]	0.000006	0.005506	0.000215	0.703086
19780	WR	0.703520[b]	0.000005	0.000534	0.000003	0.703510
19781	WR	0.702827[b]	0.000007	0.000119	0.000004	0.702866

Table 10.34 (continued)

Sample name	Fraction	$^{87}Sr/^{86}Sr_m$	2SE	$^{87}Rb/^{86}Sr$	2SE	$^{87}Sr/^{86}Sr_t$
COQ-1	WR	0.703310[b]	0.000006	-	-	-
Final procedure (Chapter 3.6.8), parent isotope ratio with Q-ICP-MS in solution mode						
OL-2	WR	0.704414[c]	0.000007	0.035798	0.048247	0.704414
	C	0.704437[c]	0.000008	0.044567	0.053924	0.704437
	NC	0.704397[b]	0.000008	0.003655	0.056762	0.704397
91/66 - C2	WR	0.705069[c]	0.000007	0.001380	0.048247	0.705066
	C	0.705083[c]	0.000008	0.000465	0.055201	0.705082
	NC	0.705086[b]	0.000012	0.017129	0.085143	0.705055
91/62 - C4	WR	0.705746[c]	0.000005	0.000884	0.038314	0.705744
	C	0.705753[c]	0.000010	0.000560	0.069249	0.705751
	NC	0.705754[b]	0.000010	0.013800	0.070952	0.705729
BM.1998,P18(119)	WR	0.703214[c]	0.000008	0.000200	0.053924	0.703213
	C	0.703212[c]	0.000008	0.000139	0.053924	0.703212
	NC	0.703236[b]	0.000008	0.011069	0.056762	0.703180
BM.1998,P18(229)	WR	0.703293[c]	0.000006	0.002998	0.043990	0.703278
	C	0.703292[c]	0.000008	0.001499	0.059600	0.703285
	NC	0.703677[b]	0.000012	0.070933	0.085143	0.703319
BM.2000,P11(14)	WR	0.703589[c]	0.000007	0.000476	0.049667	0.703587
	C	0.703597[c]	0.000078	0.000119	0.553427	0.703596
	NC	0.703663[b]	0.000008	0.014262	0.056762	0.703587

Table 10.34 (continued)

Sample name	Fraction	$^{87}Sr/^{86}Sr_m$	2SE	$^{87}Rb/^{86}Sr$	2SE	$^{87}Sr/^{86}Sr_t$
BM.2000,P11(22)	WR	0.703431[c]	0.000008	0.003153	0.058181	0.703414
	C	0.703427[c]	0.000009	0.001002	0.062438	0.703421
	NC	0.704693[b]	0.000010	0.217874	0.070952	0.703533
16462	WR	0.703154[c]	0.000007	0.004725	0.052505	0.703118
	C	0.703606[c]	0.000003	0.002602	0.019867	0.703586
	NC	0.707929[b]	0.000008	0.160095	0.056762	0.706719
19780	WR	0.703537[c]	0.000008	0.000498	0.056762	0.703528
	C	0.703558[c]	0.000009	0.000249	0.062438	0.703554
	NC	0.704134[b]	0.000010	0.048230	0.070952	0.703251
COQ-1	WR	0.703329[c]	0.000008	0.002781	0.053924	0.703325
	C	0.703333[c]	0.000007	0.001994	0.049667	0.703330
	NC	0.703376[b]	0.000010	0.043572	0.070952	0.703305
Final procedure (Chapter 3.6.8), parent isotope ratio with Q-ICP-MS and *CETAC Aridus™*						
LI 23/02/08	WR	0.703121[f]	0.000010	0.010204	0.000061	0.703120
	C	0.703123[g]	0.000010	0.002761	0.000093	0.703123
	NC	0.703306[g]	0.000008	2.956818	0.047295	0.703133
LI 23/02/08	WR	0.703126[f]	0.000010	0.010152	0.000425	0.703125
	C	0.703119[g]	0.000008	0.002548	0.000004	0.703119
	NC	0.703246[g]	0.000010	1.763014	0.039708	0.703143

Table 10.34 (continued)

Sample name	Fraction	$^{87}Sr/^{86}Sr_m$	2SE	$^{87}Rb/^{86}Sr$	2SE	$^{87}Sr/^{86}Sr_t$
BM.2004.P9(9)	WR	0.703294[f]	0.000012	0.331465	0.013349	0.703275
	C	0.703182[g]	0.000010	0.018686	0.000438	0.703181
	NC	0.703318[g]	0.000008	2.250467	0.022776	0.703186
BM.2004.P9(9)	WR	0.703173[f]	0.000010	0.333485	0.004253	0.703153
	C	0.703172[g]	0.000008	0.017507	0.000095	0.703171
	NC	0.703273[g]	0.000012	1.882939	0.055334	0.703163
J1-C1	WR	0.705162[d]	0.000008	0.000319	0.000008	0.705161
	C	0.705165[e]	0.000008	0.000238	0.000001	0.705165
	NC	0.705209[e]	0.000008	0.123111	0.002954	0.704984
91/66 - C2	WR	0.705054[d]	0.000008	0.001411	0.000051	0.705051
	C	0.705047[e]	0.000010	0.000385	0.000177	0.705047
	NC	0.705950[e]	0.000012	0.482892	0.002792	0.705066
91/60 - C5	WR	0.705595[d]	0.000008	0.000407	0.000003	0.705594
	C	0.705593[e]	0.000010	0.000230	0.000015	0.705593
	NC	0.705612[e]	0.000008	0.014031	0.001145	0.705586
BM.1998,P18(119)	WR	0.703196[d]	0.000010	0.000213	0.000006	0.703195
	C	0.703186[e]	0.000010	0.000174	0.000003	0.703185
	NC	0.703191[e]	0.000008	0.055013	0.003424	0.702914
BM.1998,P18(229)	WR	0.703129[d]	0.000008	0.003291	0.000147	0.703112
	C	0.703274[e]	0.000080	0.001940	0.000032	0.703264
	NC	0.703780[e]	0.000006	0.124270	0.003168	0.703153

Table 10.34 (continued)

Sample name	Fraction	$^{87}Sr/^{86}Sr_m$	2SE	$^{87}Rb/^{86}Sr$	2SE	$^{87}Sr/^{86}Sr_t$
BM.2000,P11(22)	WR	0.703247[d]	0.000008	0.003009	0.000035	0.703231
	C	0.703400[e]	0.000008	0.001444	0.000025	0.703392
	NC	0.705279[e]	0.000010	0.298496	0.011698	0.703690
BM.2000,P11(22)_repl	WR	0.703252[d]	0.000010	0.003522	0.000054	0.703234
	C	0.703403[e]	0.000008	0.001388	0.000071	0.703396
	NC	0.706938[e]	0.000012	1.297122	0.078619	0.700034
BM.2000,P11(22)_repl	WR	0.703237[d]	0.000008	0.003030	0.000040	0.703221
	C	0.703404[e]	0.000008	0.001399	0.000009	0.703397
	NC	0.711632[e]	0.000012	0.035607	0.001521	0.711443
BM.2000,P14(24)	WR	0.703917[d]	0.000010	0.005448	0.000153	0.703888
	C	0.704045[e]	0.000008	0.005098	0.000203	0.704018
	NC	0.704088[e]	0.000009	0.013092	0.000817	0.704018
BM.2000,P14(25)	WR	0.703673[d]	0.000010	0.002151	0.000067	0.703661
	C	0.703842[e]	0.000008	0.002031	0.000045	0.703831
	NC	0.703856[e]	0.000008	0.005266	0.000000	0.703828
4808	WR	0.703044[d]	0.000008	0.000334	0.000007	0.703041
	C	0.703045[e]	0.000008	0.000246	0.000005	0.703043
	NC	0.705275[e]	0.000007	0.676490	0.018079	0.700162
10160	WR	0.703095[d]	0.000010	0.005962	0.000202	0.703050
	C	0.703062[e]	0.000008	0.003251	0.000541	0.703037
	NC	0.712126[e]	0.000014	0.935681	0.049471	0.705055

Table 10.34 (continued)

Sample name	Fraction	$^{87}Sr/^{86}Sr_m$	2SE	$^{87}Rb/^{86}Sr$	2SE	$^{87}Sr/^{86}Sr_t$
16462	WR	0.703148[d]	0.000008	0.005447	0.000112	0.703107
	C	0.703047[e]	0.000010	0.002794	0.000061	0.703026
	NC	0.709101[e]	0.000010	0.166822	0.004764	0.707840
16462_repl	WR	0.703142[d]	0.000008	0.005712	0.000215	0.703099
	C	0.703058[e]	0.000008	0.002885	0.000090	0.703036
	NC	0.709212[e]	0.000008	0.035422	0.001212	0.708945
19780	WR	0.703532[d]	0.000008	0.000521	0.000005	0.703522
	C	0.703531[e]	0.000010	0.000144	0.000007	0.703529
	NC	0.705245[e]	0.000008	0.151087	0.008247	0.702479
19780_repl	WR	0.703533[d]	0.000008	0.000512	0.000011	0.703524
	C	0.703535[e]	0.000008	0.000138	0.000005	0.703532
	NC	0.704495[e]	0.000006	0.019655	0.001121	0.704135
19781	WR	0.702853[d]	0.000008	0.000157	0.000008	0.702850
	C	0.702853[e]	0.000008	0.000128	0.000038	0.702851
	NC	0.702993[e]	0.000008	0.003772	0.000178	0.702924
GGU 252833	WR	0.701637[f]	0.000010	0.002063	0.000050	0.701548
	C	0.701543[f]	0.000014	0.000197	0.000006	0.701535
	NC	0.705966[g]	0.000010	0.125337	0.003974	0.700590
GGU 252874	WR	0.701899[f]	0.000012	0.010854	0.000322	0.701433
	C	0.701529[f]	0.000010	0.000682	0.000012	0.701500
	NC	0.719748[g]	0.000010	0.529436	0.009157	0.697037

Table 10.34 (continued)

Sample name	Fraction	$^{87}Sr/^{86}Sr_m$	2SE	$^{87}Rb/^{86}Sr$	2SE	$^{87}Sr/^{86}Sr_t$
COQ-1	WR	0.703310[d]	0.000008	0.003146	0.000039	0.703305
	C	0.703304[e]	0.000010	0.003018	0.000105	0.703299
	NC	0.703500[e]	0.000007	0.010898	0.000623	0.703482

[a] NBS987 $^{87}Sr/^{86}Sr$ 0.710240 ±0.000011 2SD (n=9)

[b] NBS987 $^{87}Sr/^{86}Sr$ 0.710263 ±0.000010 2SD (n=10)

[c] NBS987 $^{87}Sr/^{86}Sr$ 0.710278 ±0.000016 2SD (n=9)

[d] NBS987 $^{87}Sr/^{86}Sr$ 0.710270 ±0.000008 2SD (n=12)

[e] NBS987 $^{87}Sr/^{86}Sr$ 0.710263 ±0.000007 2SD (n=13)

[f] NBS987 $^{87}Sr/^{86}Sr$ 0.710259 ±0.000010 2SD (n=10)

10.3.5. Isotope data – highly siderophile elements

Table 10.35 **Highly siderophile element data for carbonatites from different localities (*c.f.* Table 1.2). Values indicated by '<' are defined by the detection limit. T_{MA} model age and age corrected $^{187}Os/^{188}Os_t$ calculated using a decay constant of 1.66×10^{11} (Smoliar et al., 1996) and $^{187}Os/^{188}Os$ and $^{187}Re/^{188}Os$ of primitive upper mantle (Becker et al., 2006).**

Sample name	$^{187}Os/^{188}Os_m$	2SE	Os [ppt]	Ir [ppt]	Ru [ppt]	Pt [ppt]	Pd [ppt]	Re [ppt]	$^{187}Re/^{188}Os$	$^{187}Os/^{188}Os_t$	T_{MA} (Ma)
OL-1	0.1636*	0.0007	<0.9	10.6	55.38	8890	4928	7751	-	-	-
BM.2004,P12(132)	0.2623	0.0167	1.15	1.76	<23.2	82.37	<120.9	10181	41777	0.2623	0.19
LI 23/02/08	0.3367	0.0007	2.47	<1	<23.2	78.57	287.2	9.28	17.8	0.3355	716
BM.2004.P9(9)	0.1477	0.0005	2.30	<1	84.81	46.36	258.2	17.8	36.6	0.1452	30
J1-C1	9.689*	0.0081	<0.9	<1	27.34	47.68	188.3	206	-	-	-
91/66 - C2	0.8569*	0.0027	<0.9	1.15	<23.2	47.1	<120.9	45.5	-	-	-
91/62 - C4	1.540*	0.0027	<0.9	<1	<23.2	125.41	<120.9	48.3	-	-	-
91/60 - C5	0.3705	0.0003	4.84	1.69	<23.2	23.80	166.8	36.8	36.0	0.2921	407
ASS-1	55.61	0.1024	1.15	3.28	<23.2	<12.7	233.3	206	848.9	50.04	3816
BM.1998,P18(44)	1.097*	0.0118	<0.9	<1	<23.2	<12.7	<120.9	12.3	-	-	-
BM.1998,P18(183)	0.2867	0.0028	3.50	<1	<23.2	40.67	<120.9	159	214.6	<0	44
BM.1998,P18(229)	-	-	-	6.37	<23.2	159.5	664.7	136	-	-	-
BM.2000,P11(22)	0.5383*	0.0017	<0.9	<1	30.45	75.86	582.7	11.7	-	-	-
BM.2000,P14(24)	2.119*	0.0045	<0.9	<1	<23.2	<12.7	<120.9	24.1	-	-	-
4808	48.66	0.0434	12.62	<1	39.75	27.20	<120.9	1790	670.8	42.63	4210
16462	5.773	0.0106	1.46	38.2	41.35	39.78	957.8	138	446.6	1.759	757
19780	6.704	0.0702	1.19	10.6	<23.2	41.58	171.4	14.9	59.0	5.417	>Earth
19781	1.025*	0.0066	<0.9	<1	<23.2	<12.7	311.2	6.46	-	-	-
GGU 252833	0.6551	0.0111	3.91	<1	<23.2	<12.7	<120.9	3.21	3.88	0.4568	>Earth
GGU 252874	47.64	0.0461	1.63	<1	<23.2	<12.7	<120.9	19.6	56.9	44.72	>Earth

*Os concentrations below detection limit

Table 10.36 **HSE data for USGS reference material BHVO-2 and COQ-1 as given in the literature (top) and determined in this study (bottom). HPA-S: High pressure Asher digestion; CT = Carius tube digestion. Values indicated by '<' are defined by the detection limit. Errors on averages given as 2SD.**

Sample	Method	$^{187}Os/^{188}Os_m$	Os [ppt]	Ir [ppt]	Ru [ppt]	Pt [ppt]	Pd [ppt]	Re [ppt]	Reference
					Literature data				
BHVO-2	CT	0.1463	118	76	132	12000	2580	511	Chu et al. (2015)
BHVO-2	CT	0.1461	122	81	138	8470	2670	544	Chu et al. (2015)
BHVO-2	CT	0.1462	124	86	142	5700	2750	521	Chu et al. (2015)
BHVO-2	CT	0.1496	110	76	138	8420	2680	529	Chu et al. (2015)
BHVO-2	HPA-S	0.1461	101	58	129	1010	2940	543	Meisel and Moser (2004b)
					This study				
BHVO-2	HPA-S	0.1447	92	56	235	8558	2993	551	
BHVO-2	HPA-S	0.1615	58	62	294	6043	2670	549	
BHVO-2	CT	0.1540	95	80	204	17300	2960	568	
BHVO-2	CT	0.1449	131	90	289	6702	2639	560	
BHVO-2	CT	0.1323	548	113	348	12767	4084	586	
Average		**0.1475** *±0.02*	**185** *±409*	**80** *±11*	**274** *±73*	**10274** *±9444*	**3069** *±1180*	**563** *±30*	
COQ-1	HPA-S	6.7	3.3	14	<23.2	14	4587	1429	
COQ-1	CT	4.6	3.8	8.2	73	50	286	1212	
COQ-1	CT	5.5	2.9	3.2	<23.2	21	237	1004	
Average		**5.6** *±2.06*	**3.3** *±1*	**8.4** *±11*	**31** *±61*	**28** *±38*	**1703** *±4995*	**1215** *±425*	

Table 10.37 **Modal abundance and compositions of BMS of two samples from Grønnedal-Ika (19781 and 19780) and one sample from Fen (16462). Highly siderophile element concentrations were calculated based on whole-rock concentrations and modal abundances of BMS. Samples 19780 and 19781 have HSE concentrations below detection limit (*c.f.* Table 10.35). To calculate estimated concentrations in BMS, the measured values (not recorded in Table 10.35 and <bdl) were used, except for Ir in 19781, which was negative. The type of BMS for Kovdor come from Rudashevsky et al., (2004).**

Sample name	Modal abundance	Type of BMS	Os (ppm)	Ir (ppm)	Ru (ppm)	Pt (ppm)	Pd (ppm)	Re (ppm)
16462	1.70%	po; py; sph (63%/32%/4%)	0.0001	0.0022	0.0024	0.0023	0.0563	0.0081
19780	0.19%	py	0.0006	0.0056	0.0100	0.0219	0.0902	0.0078
19871	0.02%	po; py (50%/50%)	0.0019	<0.005	0.1022	0.0208	1.5559	0.0323
BM.2000, P11(22)	0.02%	po; py; cp; pn	0.0006	<0.00005	0.0015	0.0038	0.0291	<0.00045

10.3.6. Isotope data – Fen case study

Table 10.38 **Measured and age corrected Hf isotopic composition in whole-rock (WR), carbonate (C), non-carbonate (NC) fractions and mineral separates of carbonatites from Fen, Norway and USGS reference material COQ-1. Data was normalised to 0.282785 (Bouvier et al., 2008) and ε-values and corresponding errors were calculated using the spreadsheet from Ickert (2013). Reproducibility given by external standard JMC475 is highlighted by superscripts next to $^{176}Hf/^{177}Hf_m$ values and given as footnotes below the table. DNR = sample did not run.**

Sample name	Fraction	Beam size ^{179}Hf (V)	$^{176}Hf/^{177}Hf_m$	2SE	$^{176}Lu/^{177}Hf$	2SE	$^{176}Hf/^{177}Hf_t$	εHf_t	2SE
Sample preparation described in Chapter 3.6.8, mother isotope ratio determined with Q-ICP-MS using a *CETAC Aridus™*									
TS 498 E	WR	2.21	0.283056[a]	0.000006	0.067192	0.004171	0.282376	-2.4	1.6
	C	0.16	0.284317[b]	0.000034	0.208368	0.021829	0.282210	-8.3	7.9
	NC	3.01	0.282631[a]	0.000006	0.019680	0.000688	0.282432	-0.5	0.5
TS 498 E_repl	WR	2.15	0.283055[a]	0.000006	0.067336	0.005797	0.282374	-2.5	2.1
	C	0.59	0.284370[b]	0.000014	0.223628	0.026013	0.282108	-11.9	9.4
	NC	0.82	0.282638[a]	0.000012	0.019892	0.001394	0.282437	-0.3	0.7
TS 51.5 E	WR	0.43	0.290546[a]	0.000018	0.893909	0.039923	0.281505	-33.3	14.7
	C	-	-	-	-	-	-	-	-
	NC	0.3	0.282699[a]	0.000024	0.005859	0.001012	0.282640	6.9	1.0
TS 51.5 E_repl	WR	0.6	0.290471[a]	0.000018	0.866711	0.051710	0.281705	-26.2	18.8
	C	-	-	-	-	-	-	-	-
	NC	0.33	0.282693[a]	0.000018	0.003989	0.000733	0.282653	7.3	0.8
MTGS	WR	16	0.282592[a]	0.000002	0.012938	0.000199	0.282461	0.6	0.4
	C	0.03	0.287991[b]	0.000166	0.749216	0.037804	0.280413	-71.9	15.0
	NC	14.74	0.282546[a]	0.000002	0.007489	0.000166	0.282470	0.9	0.4

Table 10.38 (continued)

Sample name	Fraction	Beam size ^{179}Hf (V)	$^{176}Hf/^{177}Hf_m$	2SE	$^{176}Lu/^{177}Hf$	2SE	$^{176}Hf/^{177}Hf_t$	εHf_t	2SE
MTGS_repl	WR	16.78	0.282593[a]	0.000002	0.012734	0.000825	0.282464	0.7	0.5
	C	0.06	0.288230[b]	0.000082	0.770968	0.050709	0.280432	-71.3	18.6
	NC	14.88	0.282542[a]	0.000002	0.007357	0.000501	0.282468	0.8	0.4
THY	WR	1.14	0.287189[b]	0.000012	0.510573	0.037993	0.282025	-14.9	13.7
	C	0.022	0.387947[b]	0.000234	13.075166	1.316807	0.255706	-946.7	474.4
	NC	1.23	0.282714[a]	0.000008	0.002280	0.000202	0.282691	8.7	0.5
THY_repl	WR	1.4	0.286744[b]	0.000012	0.474720	0.018193	0.281943	-17.8	6.8
	C	0.01	0.382150[b]	0.000520	12.557013	4.818916	0.255149	-966.4	1726.4
	NC	0.2	0.282819[a]	0.000028	0.007613	0.000587	0.282742	10.5	1.1
CQW-1	WR	4.97	0.282970[b]	0.000006	0.048463	0.002311	0.282480	1.2	0.9
	C	0.051	0.315187[b]	0.000074	3.784788	0.216691	0.276908	-196.0	79.0
	NC	12.66	0.282538[a]	0.000006	0.000973	0.000049	0.282528	2.9	0.4
CQW-1_repl	WR	2.89	0.282963[b]	0.000006	0.046679	0.000882	0.282491	1.6	0.5
	C	0.03	0.315211[b]	0.000200	3.617514	0.504241	0.278624	-135.3	181.2
	NC	12.42	0.282538[a]	0.000002	0.001182	0.000034	0.282526	2.9	0.4
CQW-2	WR	4.76	0.283146[b]	0.000004	0.067959	0.003293	0.282459	0.5	1.2
	C	0.02	0.311842[b]	0.000196	3.301082	0.711201	0.278455	-141.3	255.1
	NC	8.28	0.282524[a]	0.000004	0.001406	0.000123	0.282510	2.3	0.4
CQW-2_repl	WR	4.9	0.283137[b]	0.000004	0.068772	0.000793	0.282441	-0.1	0.5
	C	0.09	0.314218[b]	0.000102	3.373743	1.120525	0.280096	-83.2	401.5
	NC	6.96	0.282527[a]	0.000004	0.001594	0.000099	0.282511	2.3	0.4

Table 10.38 (continued)

Sample name	Fraction	Beam size ^{179}Hf (V)	$^{176}Hf/^{177}Hf_m$	2SE	$^{176}Lu/^{177}Hf$	2SE	$^{176}Hf/^{177}Hf_t$	εHf_t	2SE
COQ-1	WR	0.69	0.283813[b]	0.000012	0.433539	0.011617	0.282865	5.4	1.1
Mineral separates prepared as described in Chapter 3.6.9, mother isotope ratios determined by Q-ICP-MS using a *CETAC Aridus™*									
CQW-1	Calcite	-	DNR	-	16.512229	1.306862	-	-	-
CQW-1	Calcite	-	DNR	-	16.657261	1.647242	-	-	-
CQW-1	Phlogopite	0.65	0.282961[c]	0.000014	0.031882	0.010352	0.282639	6.8	3.8
CQW-1	Phlogopite	0.49	0.282865[c]	0.000016	0.025995	0.003017	0.282602	5.6	1.3
CQW-1	Phlogopite	1.38	0.282724[c]	0.000008	0.017548	0.000361	0.282547	3.6	0.5
CQW-1	Magnetite	-	DNR		0.002417	0.000773	DNR	-	-
CQW-1	Magnetite	0.015	0.282719[c]	0.000284	0.002335	0.001757	0.282695	8.9	10.1
CQW-1	Magnetite	0.011	0.282589[c]	0.000424	0.003509	0.001498	0.282554	3.8	15.0
CQW-1	Apatite	0.01	0.282282[c]	0.000390	0.006975	0.000589	0.282211	-8.3	13.8
CQW-1	Chlorite	0.44	0.282708[c]	0.000014	0.011159	0.001912	0.282595	5.3	0.9

[a] JMC475 $^{176}Hf/^{177}Hf$ 0.282150 ±0.000008 2SD (n=17)

[b] JMC475 $^{176}Hf/^{177}Hf$ 0.282149 ±0.000009 2SD (n=18)

[c] JMC475 $^{176}Hf/^{177}Hf$ 0.282149 ±0.000012 2SD (n=10)

Table 10.39 **Measured and age corrected Nd isotopic composition in whole-rock (WR), carbonate (C), non-carbonate (NC) fractions and mineral separates of carbonatites from Fen, Norway and USGS reference material COQ-1. Data was normalised to 0.51263 (Bouvier et al., 2008) and ε-values and corresponding errors were calculated using the spreadsheet from Ickert (2013). Reproducibility given by external standard JNd_i is highlighted by superscripts next to $^{143}Nd/^{144}Nd_m$ values and given as footnotes below the table. JNd_i was measured pure and doped with Sm (Sm/Nd=0.2), the values given represent the averages of both standards.**

Sample name	Fraction	$^{143}Nd/^{144}Nd_m$	2SE	$^{147}Sm/^{144}Nd$	2SE	$^{143}Nd/^{144}Nd_t$	εNd_t	2SE
Sample preparation described in Chapter 3.6.8, mother isotope ratio determined with Q-ICP-MS using a *CETAC Aridus™*								
TS 498 E	WR	0.512317[a]	0.000006	0.053890	0.001502	0.512127	4.0	0.4
	C	0.512333[b]	0.000006	0.052991	0.000516	0.512146	4.1	0.3
	NC	0.512302[b]	0.000006	0.046996	0.003339	0.512136	3.9	0.4
TS 498 E_repl	WR	0.512327[a]	0.000006	0.053863	0.001075	0.512137	4.3	0.4
	C	0.512338[b]	0.000006	0.053174	0.005586	0.512150	4.1	0.5
	NC	0.512300[b]	0.000008	0.047042	0.001531	0.512134	3.8	0.3
TS 51.5 E	WR	0.512420[a]	0.000004	0.095125	0.000941	0.512084	3.3	0.3
	C	0.512451[b]	0.000006	0.094486	0.000050	0.512117	3.5	0.3
	NC	0.512314[b]	0.000008	0.055852	0.004200	0.512117	3.5	0.4
TS 51.5 E_repl	WR	0.512421[a]	0.000004	0.095205	0.003935	0.512085	3.4	0.6
	C	0.512452[b]	0.000006	0.094131	0.001887	0.512120	3.5	0.3
	NC	0.512299[b]	0.000006	0.053758	0.000671	0.512109	3.3	0.3
MTGS	WR	0.512413[a]	0.000006	0.089486	0.005798	0.512097	3.7	0.3
	C	0.512407[b]	0.000006	0.081538	0.001915	0.512119	3.5	0.3
	NC	0.512434[b]	0.000006	0.094220	0.004863	0.512101	3.6	0.4

Table 10.39 (continued)

Sample name	Fraction	$^{143}Nd/^{144}Nd_m$	2SE	$^{147}Sm/^{144}Nd$	2SE	$^{143}Nd/^{144}Nd_t$	εNd_t	2SE
MTGS_repl	WR	0.512404[a]	0.000006	0.089698	0.004308	0.512087	3.2	0.3
	C	0.512403[b]	0.000006	0.082742	0.006463	0.512111	3.4	0.5
	NC	0.512438[b]	0.000006	0.094458	0.002295	0.512104	3.6	0.4
THY	WR	0.512441[a]	0.000006	0.097755	0.005320	0.512096	3.7	0.4
	C	0.512446[a]	0.000006	0.099562	0.002967	0.512094	3.5	0.5
	NC	0.512356[b]	0.000006	0.062513	0.003693	0.512135	3.9	0.4
THY_repl	WR	0.512447[a]	0.000004	0.097231	0.005203	0.512104	3.9	0.5
	C	0.512448[a]	0.000006	0.099400	0.009780	0.512097	3.6	0.6
	NC	0.512365[b]	0.000006	0.068085	0.000800	0.512125	3.6	0.3
CQW-1	WR	0.512468[a]	0.000004	0.097786	0.004446	0.512123	3.6	0.4
	C	0.512475[a]	0.000004	0.097393	0.003473	0.512131	3.8	0.3
	NC	0.512432[b]	0.000006	0.082965	0.004812	0.512139	3.9	0.4
CQW-1_repl	WR	0.512465[a]	0.000006	0.099308	0.000999	0.512114	3.4	0.3
	C	0.512477[a]	0.000006	0.096667	0.002836	0.512136	3.9	0.3
	NC	0.512433[b]	0.000008	0.083421	0.002938	0.512138	3.9	0.4
CQW-2	WR	0.512466[a]	0.000006	0.098660	0.004184	0.512118	3.5	0.4
	C	0.512473[a]	0.000004	0.096953	0.002485	0.512131	3.8	0.3
	NC	0.512371[b]	0.000006	0.069810	0.003217	0.512125	3.6	0.4
CQW-2_repl	WR	0.512467[a]	0.000006	0.097929	0.005490	0.512121	3.6	0.5
	C	0.512479[a]	0.000004	0.099163	0.004356	0.512129	3.7	0.4
	NC	0.512373[b]	0.000008	0.068827	0.002468	0.512130	3.8	0.3

Table 10.39 (continued)

Sample name	Fraction	$^{143}Nd/^{144}Nd_m$	2SE	$^{147}Sm/^{144}Nd$	2SE	$^{143}Nd/^{144}Nd_t$	εNd_t	2SE
COQ-1	WR	0.512847[a]	0.000006	0.070535	0.001894	0.512793	6.1	0.2
Mineral separates prepared as described in Chapter 3.6.9, mother isotope ratios determined by Q-ICP-MS using a *CETAC Aridus™*								
CQW-1	Calcite	0.512513[c]	0.000010	0.095806	0.005102	0.512175	4.6	0.5
CQW-1	Calcite	0.512493[c]	0.000006	0.097791	0.003160	0.512148	4.1	0.3
CQW-1	Phlogopite	0.512433[c]	0.000006	0.075655	0.009670	0.512166	4.5	0.7
CQW-1	Phlogopite	0.512462[c]	0.000006	0.083528	0.000911	0.512167	4.5	0.3
CQW-1	Phlogopite	0.512479[c]	0.000008	0.083592	0.003646	0.512184	4.8	0.4
CQW-1	Magnetite	0.512419[c]	0.000008	0.081596	0.004689	0.512131	3.8	0.4
CQW-1	Magnetite	0.512403[c]	0.000006	0.078717	0.000687	0.512125	3.7	0.3
CQW-1	Magnetite	0.512385[c]	0.000008	0.075144	0.001776	0.512120	3.5	0.3
CQW-1	Apatite	0.512403[c]	0.000006	0.080848	0.001650	0.512118	3.5	0.3
CQW-1	Chlorite	0.512927[c]	0.000008	0.068764	0.006635	0.512684	14.6	0.5

[a] JNd_i $^{143}Nd/^{144}Nd$ 0.512111 ±0.000008 2SD (n=17)

[b] JNd_i $^{143}Nd/^{144}Nd$ 0.512126 ±0.000011 2SD (n=19)

[c] JNd_i $^{143}Nd/^{144}Nd$ 0.512116 ±0.000008 2SD (n=9)

Table 10.40 **Measured and age corrected Sr isotopic composition in whole-rock (WR), carbonate (C), non-carbonate (NC) fractions and mineral separates of carbonatites from Fen, Norway and USGS reference material COQ-1. Data was normalised to 0.7045 (DePaolo and Wasserburg, 1976b). Reproducibility given by external standard NBS987 is highlighted by superscripts next to $^{87}Sr/^{86}Sr_m$ values and given as footnotes below the table.**

Sample name	Fraction	$^{87}Sr/^{86}Sr_m$	2SE	$^{87}Rb/^{86}Sr$	2SE	$^{87}Sr/^{86}Sr_t$
Sample preparation described in Chapter 3.6.8, mother isotope ratio determined with Q-ICP-MS using a *CETAC Aridus™*						
TS 498 E	WR	0.702955[a]	0.000010	0.001784	0.000072	0.702942
	C	0.702956[b]	0.000010	0.000240	0.000003	0.702954
	NC	0.707239[b]	0.000010	1.546044	0.012618	0.695555
TS 498 E_repl	WR	0.702962[a]	0.000012	0.001785	0.000028	0.702949
	C	0.702958[b]	0.000006	0.000230	0.000010	0.702956
	NC	0.705999[b]	0.000010	0.429980	0.005631	0.702750
TS 51.5 E	WR	0.703044[a]	0.000010	0.000007	0.000015	0.703044
	C	0.703037[b]	0.000010	0.000007	0.000000	0.703037
	NC	0.703170[b]	0.000010	0.002115	0.004375	0.703154
TS 51.5 E_repl	WR	0.703029[a]	0.000012	0.000008	0.000006	0.703029
	C	0.703039[b]	0.000008	0.000007	0.000000	0.703039
	NC	0.703276[b]	0.000010	0.000465	0.000169	0.703272
MTGS	WR	0.704677[a]	0.000010	0.191460	0.015985	0.703230
	C	0.704216[b]	0.000008	0.141587	0.000660	0.703146
	NC	0.708032[b]	0.000008	0.570411	0.041369	0.703721

Table 10.40 (continued)

Sample name	Fraction	$^{87}Sr/^{86}Sr_m$	2SE	$^{87}Rb/^{86}Sr$	2SE	$^{87}Sr/^{86}Sr_t$
MTGS_repl	WR	0.704651[a]	0.000012	0.184982	0.004060	0.703253
	C	0.704126[b]	0.000012	0.137102	0.000618	0.703090
	NC	0.708222[b]	0.000010	0.595217	0.004866	0.703724
THY	WR	0.703045[a]	0.000012	0.001482	0.000048	0.703034
	C	0.703031[b]	0.000008	0.000393	0.000011	0.703028
	NC	0.709807[b]	0.000008	0.098850	0.001182	0.709060
THY_repl	WR	0.703031[a]	0.000010	0.001523	0.000018	0.703019
	C	0.703023[b]	0.000008	0.000368	0.000020	0.703020
	NC	0.704824[b]	0.000008	0.105639	0.004512	0.704026
CQW-1	WR	0.703003[a]	0.000012	0.006349	0.000091	0.702955
	C	0.702984[b]	0.000010	0.003231	0.000208	0.702960
	NC	0.708188[b]	0.000010	0.645086	0.026003	0.703313
CQW-1_repl	WR	0.703003[a]	0.000008	0.006314	0.000337	0.702955
	C	0.702978[b]	0.000008	0.003094	0.000049	0.702955
	NC	0.706115[b]	0.000008	0.387930	0.014328	0.703183
CQW-2	WR	0.702972[a]	0.000010	0.000549	0.000015	0.702968
	C	0.702972[b]	0.000008	0.000434	0.000026	0.702969
	NC	0.703538[b]	0.000006	0.035729	0.001592	0.703268
CQW-2_repl	WR	0.702979[a]	0.000010	0.000563	0.000009	0.702975
	C	0.702974[a]	0.000010	0.000430	0.000011	0.702971
	NC	0.703700[b]	0.000010	0.038574	0.000749	0.703408

Table 10.40 (continued)

Sample name	Fraction	$^{87}Sr/^{86}Sr_m$	2SE	$^{87}Rb/^{86}Sr$	2SE	$^{87}Sr/^{86}Sr_t$
COQ-1	WR	0.703296[a]	0.000012	0.003312	0.000044	0.703291
Mineral separates prepared as described in Chapter 3.6.9, mother isotope ratios determined by Q-ICP-MS using a *CETAC Aridus™*						
CQW-1	Calcite	0.702950[c]	0.000006	0.000027	0.000001	0.702950
CQW-1	Calcite	0.702940[c]	0.000010	0.000027	0.000003	0.702940
CQW-1	Phlogopite	0.736743[c]	0.000010	4.541449	0.148404	0.702423
CQW-1	Phlogopite	0.738196[c]	0.000012	4.701406	0.071348	0.702667
CQW-1	Phlogopite	0.737881[c]	0.000012	4.749753	0.058689	0.701986
CQW-1	Magnetite	0.703494[c]	0.000010	0.062745	0.001629	0.703020
CQW-1	Magnetite	0.703532[c]	0.000008	0.065449	0.002855	0.703037
CQW-1	Magnetite	0.703331[c]	0.000010	0.040634	0.000885	0.703024
CQW-1	Apatite	0.703126[c]	0.000010	0.014793	0.000782	0.703014
CQW-1	Chlorite	0.778888[c]	0.000012	9.089951	0.084447	0.710194

[a] NBS987 $^{87}Sr/^{86}Sr$ 0.710259 ±0.000010 2SD (n=10)

[b] NBS987 $^{87}Sr/^{86}Sr$ 0.710240 ±0.000015 2SD (n=14)

[c] NBS987 $^{87}Sr/^{86}Sr$ 0.710270 ±0.000019 2SD (n=8)

Table 10.41 **Highly siderophile element data for carbonatites from the Fen case study. Values indicated by '<' are defined by the detection limit. T_{MA} model age and age corrected $^{187}Os/^{188}Os_t$ calculated using a decay constant of 1.66×10^{11} (Smoliar et al., 1996) and $^{187}Os/^{188}Os$ and $^{187}Re/^{188}Os$ of primitive upper mantle (Becker et al., 2006).**

Sample name	$^{187}Os/^{188}Os_m$	2SE	Os [ppt]	Ir [ppt]	Ru [ppt]	Pt [ppt]	Pd [ppt]	Re [ppt]	$^{187}Re/^{188}Os$	$^{187}Os/^{188}Os_t$	T_{MA} (Ma)
CQW-1	202.72	0.0497	4.4	<1	46.80	<12.7	<120.9	626	671.2	196.7	>Earth
CQW-1	246.66	0.0421	4.3	<1	45.01	<12.7	<120.9	620	678.9	240.6	>Earth
CQW-1	222.34	0.0608	4.4	<1	37.55	<12.7	<120.9	612	652.3	216.5	>Earth
CQW-2	265.66	0.1220	3.6	<1	43.53	<12.7	670.1	558	723.8	259.1	>Earth
TS 498 E	238.85	0.0603	3.3	<1	40.44	<12.7	246.5	495	710.2	232.5	>Earth
TS 51.5 E	22.68*	0.0096	<0.9	5.47	46.66	<12.7	<120.9	58.4	-	-	-
MTGS	16.38*	0.0490	<0.9	<1	<23.2	43.12	<120.9	86.1	-	-	-

*Os concentration below detection limit

10.4. Stable Fe isotope study

The stable Fe isotope study was carried out as a short study in addition to the Lu-Hf and Re-Os isotope study when the latter was not yielding usable results (April 2017). However, due to later success and large datasets for the radiogenic isotope studies, the focus was emphasized on Lu-Hf and Re-Os systems and thus the stable Fe isotope work is only briefly presented here in the appendix. In collaboration with Dr. Edward Inglis (former Durham University) this data will likely be used for an independent stable Fe-Zn isotope study of global carbonatites.

10.4.1. Methods

Roughly 20 mg of sample powder was dissolved by the addition of 0.5 ml 3 M HNO_3 and 2 ml 29 M HF in a Savillex PTFE Teflon® screwtop beaker, capped and left on a hotplate set at 100 C overnight. The sample was then evaporated to dryness, taken up in 2 ml 10.3M HCl and dried down at 100°C immediately to break down any remaining fluorite phases. To ensure that ΣFe fully oxidised to Fe^{3+}, the sample residue was taken up in 0.5 ml 30% H_2O_2 and evaporated to dryness. The residue was then taken up in 1 ml 6 M HCl ready for column chemistry. Iron is separated using *Bio-Rad AG1 X8* Anion resin, with the matrix being eluted in 6M HCl and the Fe fraction being collected in 9 ml 0.4 M HCl. This ion exchange chemistry is based on the protocol of Dauphas et al. (2004). The Fe fraction was dried down at 80°C and then re-dissolved in 5 ml 0.5 M HNO_3. Because the solubility of Fe in HNO_3 is poor, the appropriate amount of 16M HNO_3 was added to the sample first to aid re-dissolution before being diluted down with MQ to form a 0.5 M HNO_3 solution. If the samples did not dissolve during the first attempt, the beaker was heated to 150 C and once it was hot, 16M HNO_3 was added and the sample was further treated in an ultrasonic bath to ensure all Fe was fully in solution.

Samples were analysed on a *Thermo Scientific® NeptunePlus* MC-ICP-MS, which was run in solution mode. Samples were introduced to the instrument using a quartz cyclonic spray chamber in combination with a PFA 50 µl/min nebuliser. To correct for or monitor isobaric interferences on ^{54}Fe and ^{58}Fe, ^{53}Cr and ^{60}Ni were collected alongside all Fe masses. Mass bias corrections were carried out by using sample-standard-bracketing, with IRMM-014 as bracketing standard. To assess precision and accuracy, the secondary in-house reference solution (Durham FeWire) and external USGS reference material BIR-1 were analysed. BIR-1 was analysed four times and yielded an average $\delta^{56}/^{54}Fe_{IRMM14}$ of 0.067 ±0.03 (2SD) and $\delta^{57}/^{54}Fe_{IRMM14}$ of 0.11 ±0.03 (2SD). This compares well with previously published values for

this reference material (Millet et al., 2012). Repeat analyses of Durham FeWire (n=24) yielded $\delta^{56}/^{54}Fe_{IRMM14}$ of 0.23 ±0.04 (2SD) and $\delta^{57}/^{54}Fe_{IRMM14}$ of 0.35 ±0.06 (2SD), which further shows reproducibility of the measurements.

10.4.2. Results

All data is presented in standard delta (δ) notation ($\delta^{56}Fe = ((^{X}Fe/^{54}Fe_{sample}/^{X}Fe/^{54}Fe_{standard}) -1) \times 1000$) and is normalised to external standard IRMM-014, where X is equal to 56 or 57. All of the data for the samples analysed as part of this study are presented in Table 10.42, with both $\delta^{56}Fe$ and $\delta^{57}Fe$ given to demonstrate the mass dependency of the data (Figure 10.3).

Table 10.42 **$\delta^{56}Fe$ and $\delta^{57}Fe$ normalised to IRMM-014 in ‰ for carbonatite samples from different localities. Errors are given as 2SD defined by four repeat analyses of the same sample aliquot.**

Sample name	$\delta^{56/54}Fe_{IRMM-014}$	$\delta^{57/54}Fe_{IRMM-014}$
J1-C1	-0.28 ±0.02	-0.40 ±0.07
91/66 - C2	-0.17 ±0.02	-0.24 ±0.02
91/62 - C4	0.08 ±0.03	0.13 ±0.06
BM.1998,P18(44)	-0.24 ±0.02	-0.34 ±0.03
BM.1998,P18(229)	-0.13 ±0.04	-0.18 ±0.04
BM.2000,P11(22)	0.10 ±0.04	0.17 ±0.07
BM.2000,P14(24)	-0.03 ±0.04	-0.03 ±0.06
BM.2000,P14(25)	0.15 ±0.04	0.25 ±0.06
4808	-0.36 ±0.04	-0.50 ±0.05
16462	-0.09 ±0.02	-0.11 ±0.07
19780	0.05 ±0.05	0.09 ±0.08
19781	-0.07 ±0.04	-0.09 ±0.07

The carbonatites from this study show a large spread of $\delta^{56}Fe$ that ranges from -0.36 ±0.04 to +0.1 ±0.04‰ (Table 10.42, Figure 10.2 and Figure 10.3), which is within the range observed for other carbonatites and their mineral separates (*c.f.* Figure 10.2; Johnson et al., 2010). However, the mean $\delta^{56}Fe$ of carbonatites from this study (-0.08 ±0.32‰) is heavier than that of whole-rock carbonatites from Johnson et al. (2010) (-0.25 ±0.35‰) and in fact more similar to the mean of mica in carbonatites (-0.05 ±0.37‰, Johnson et al., 2010). In general, samples show strong variation between each locality (*e.g.* $\delta^{56}Fe$ Jacupiranga: 0.08 to -0.28‰) with no locality yielding the same $\delta^{56}Fe$ value.

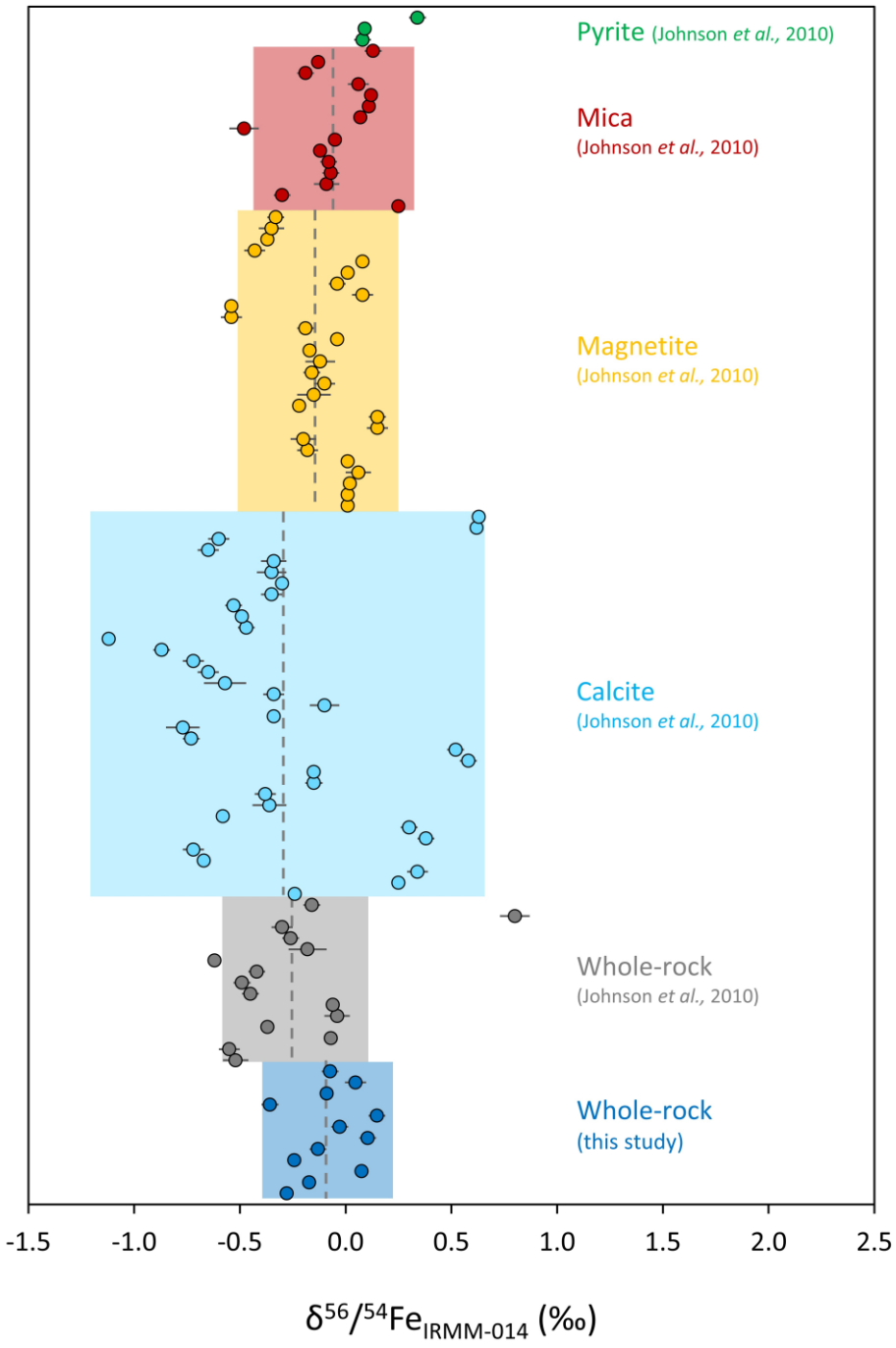

Figure 10.2 **Variation in $\delta^{56}Fe$ in carbonatites from this study as well as whole-rock and mineral separate results from global carbonatites from Johnson et al. (2010). Grey dashed line represents the mean and shaded areas ±2SD from the mean of each set of data.**

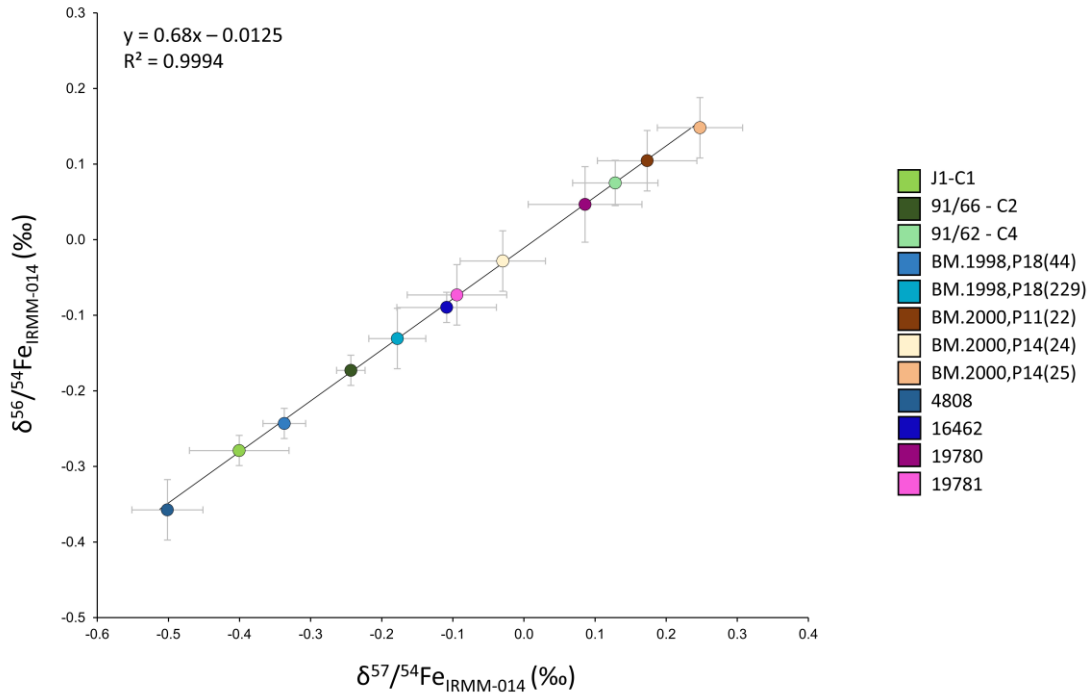

Figure 10.3 A plot showing $\delta^{56}Fe$ vs. $\delta^{57}Fe$ for carbonatite samples measured as part of this study.

10.4.3. Discussion

For samples from Jacupiranga, the $\delta^{56}Fe$ trend towards heavier values with temporal emplacement (from sequence C1 to C4, *c.f.* Figure 10.4). Thus, Fe-isotopes might be affected by the processes producing the different carbonatite sequences as described in chapter 1.1. This was also observed for $\delta^{18}O$ values in African carbonatites, where $\delta^{18}O$ values are higher in the later sequences (Suwa et al., 1975).

When comparing the whole-rock data from this study to the mineral fraction data from Johnson et al. (2010), micas have similarly high $\delta^{56}Fe$ values as sample 91/62 – C4. However, in sample 91/62 – C4 the dominant minor mineral phase is magnetite and not mica (*c.f.* Chapter). In contrast, sample J1-C1 contains no magnetite but minor amounts of mica and sample 91/66 – C2 contains both, magnetite and mica but in lower abundances than 91/62 – C4 (*c.f.* Table 2.1). Thus, the presence of those mineral phases can be responsible for the observed signatures even though the modal abundances do not perfectly match the observed signatures for whole-rock samples in comparison to mineral separates. However, minerals analysed by Johnson et al. (2010) might be derived from a different sequence of carbonatite emplacement and could thus not be representative of samples from our study. Additionally, petrography descriptions (*c.f.* Chapter 2 and Table 2.1) are only based on small fractions of the sample and could also bear uncertainties in the modal abundance of mineral phases.

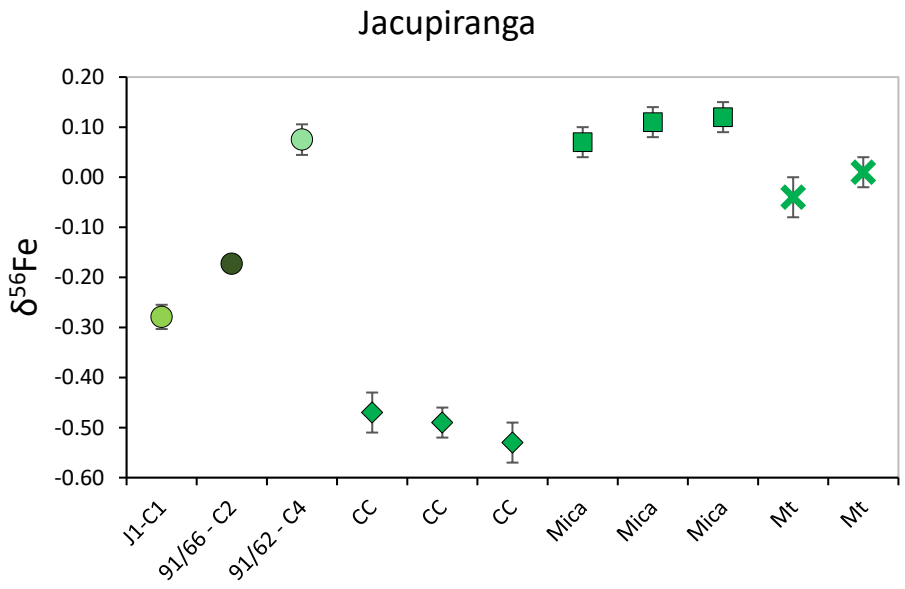

Figure 10.4 **Comparison of δ^{56}Fe for whole-rock samples from Jacupiranga from this study (circles) to mineral fractions (diamonds, squares and Xs) from Johnson et al. (2010). CC = calcite, Mt = magnetite.**

For Kovdor samples, there is no clear differentiation sequence as observed for Jacupiranga. Whole-rock δ^{56}Fe values from this study (Figure 10.5) are variable and are similar to δ^{56}Fe values observed for magnetite and mica from Johnson et al. (2010). The sample with the highest abundance in carbonate and lowest abundance in mica and magnetite also has the lowest δ^{56}Fe value (BM.2000,P14(24)), while the sample with the largest abundance in magnetite (BM.2000,P14(25), *c.f.* Table 2.1) shows the highest δ^{56}Fe value. This would suggest that sample/phase heterogeneity dominantly controls the whole-rock δ^{56}Fe signatures within these samples. However, the whole-rock values for BM.2000,P11(22) and BM.2000,P14(25) are higher than observed in the mineral fractions (Johnson et al., 2010). Thus, mica and magnetite alone are not responsible for the observed higher δ^{56}Fe unless values for mineral fractions from Johnson et al. (2010) are not representative of samples from this study. They could not be representative due to, for example, different source compositions of the mineral phases or different processes affecting Fe-isotope systematics (*e.g.* redox condition or coordination, e.g. Dauphas et al., 2017, 2009 and references therein).

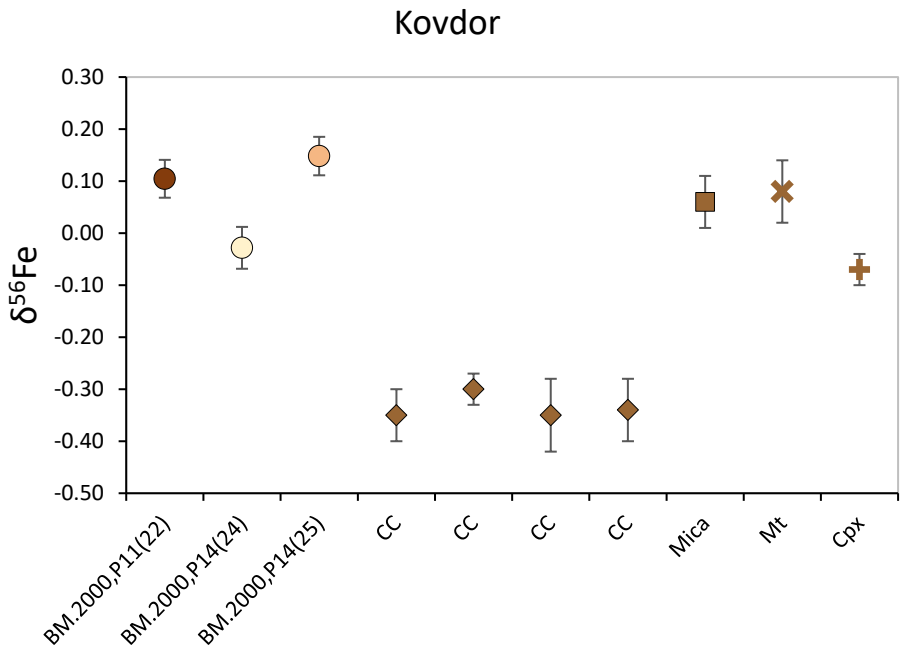

Figure 10.5 **Comparison of δ^{56}Fe for whole-rock samples from Kovdor from this study (circles) to mineral fractions (diamonds, square, X and cross) from Johnson et al. (2010). CC = calcite, Mt = magnetite, Cpx = clinopyroxene.**

Although carbonatites are dominated by carbonate phases, the carbonates do not host much Fe (Johnson et al., 2010). Consequently, small abundances of Fe-rich phases will affect the whole-rock signature (*c.f.* Figure 10.4 and Figure 10.5). Partial melting can enrich heavier Fe isotopes in the melt (Weyer and Ionov, 2007; Williams et al., 2005) and fractionation of heavy Fe isotopes into Fe^{3+}-bearing sites as are present in *i.e.* magnetite (*e.g.* Schuessler et al., 2007; Shahar et al., 2008; Williams et al., 2018; Young et al., 2015) could also be responsible for heavy Fe isotope signatures observed in carbonatites. However, fractionation during partial melting has only been investigated for silicate melts and it is unknown whether the same applies to carbonatite melts, whose genesis is poorly understood (*c.f.* Chapter 1.2). In contrast, Schuessler et al. (2007) determined that pyrrhotite, which is a common sulphide found in carbonatites, prefers to incorporate light over heavy Fe isotopes, which could be responsible for lighter δ^{56}Fe values observed in whole-rock samples. However, in the study by Johnson et al. (2010), pyrites found in carbonatites have relatively heavy δ^{56}Fe values (0.08 to 0.34‰, *c.f.* Figure 10.2).

Johnson et al. (2010) proposed that δ^{56}Fe values in carbonatites shift to ≤-0.3‰ due to crystal fractionation or liquid immiscibility processes from silicate melts. The stronger the fractionation from the silicate melt, the more negative δ^{56}Fe values become. However, a lot of carbonatites show δ^{56}Fe values clearly higher than -0.3‰ (*c.f.* Table 10.42 and Johnson et

al., 2010). During emplacement and cooling, carbonatites experience a loss of fluids and volatiles resulting in fenitisation reactions with the country rock and chemical modification of the outer part of the carbonatite body. Johnson et al. (2010) suggest that in context with this fenitisation, Fe^{3+}-rich fluids are released, which in return overprint the outer area of the carbonatite body, altering it to more positive $\delta^{56}Fe$ values. Thus, in this scenario it would be expected that carbonatite bodies show zoning from light $\delta^{56}Fe$ values in the core to heavy $\delta^{56}Fe$ values at the rim of the body.

While Johnson et al. (2010) suggest a combination of crystal fractionation and overprinting by a Fe^{3+}-rich fluid as cause of observed isotopic variation, it could also be a consequence of strong disequilibrium in combination with modal abundances and distribution of mineral phases. Disequilibrium between mineral phases can be caused by *e.g.* metasomatism (Beard and Johnson, 2004; Dauphas et al., 2017; Roskosz et al., 2015; Weyer and Ionov, 2007; Zhao et al., 2010) which can lead to light shifts in association to kinetic fractionation during diffusion of Fe (*e.g.* Richter et al., 2009), and to a heavy shift due to partial melting events or melt-solid interaction (Weyer and Ionov, 2007).

10.4.4. Genesis model

Figure 10.6 shows two simplified potential paths of carbonatite genesis and corresponding changes in $\delta^{56}Fe$ values. The left path shows direct partial melting of mantle material (1), which results in fractionation of Fe that enriches the heavier Fe isotopes in the melt. This is followed by ascent through mantle and crust, during which the carbonatitic melt could interact with adjacent mantle and crust (3). If base metal sulphides (BMS) with light Fe isotopic signatures (Bilenker et al., 2018; Schuessler et al., 2007) were assimilated, this could result in a decrease of $\delta^{56}Fe$, while assimilation of Fe^{3+}-site bearing minerals like magnetite could result in further increase. During cooling of the carbonatite melt in the shallow crust (4), volatiles and fluids can be lost due to fenitisation of the adjacent rocks. If in this case an Fe^{3+}-rich fluid is lost, which would result in a decrease of $\delta^{56}Fe$. However, if fluid was released by alkaline silicate melt that has separated from the carbonatite melt in the mantle (2), it could overprint the carbonatite and thus increase $\delta^{56}Fe$ values (4). At the surface, carbonatites can be affected by post-magmatic alteration and weathering processes, which could either increase or decrease $\delta^{56}Fe$ values depending on the process of alteration or the degree of weathering. The effects on $\delta^{56}Fe$ values caused by volatile or fluid loss, post-magmatic alteration or weathering of carbonatites is currently unknown and demands

further investigations. Thus, in Figure 10.6 changes in $\delta^{56}Fe$ values are marked with a question mark.

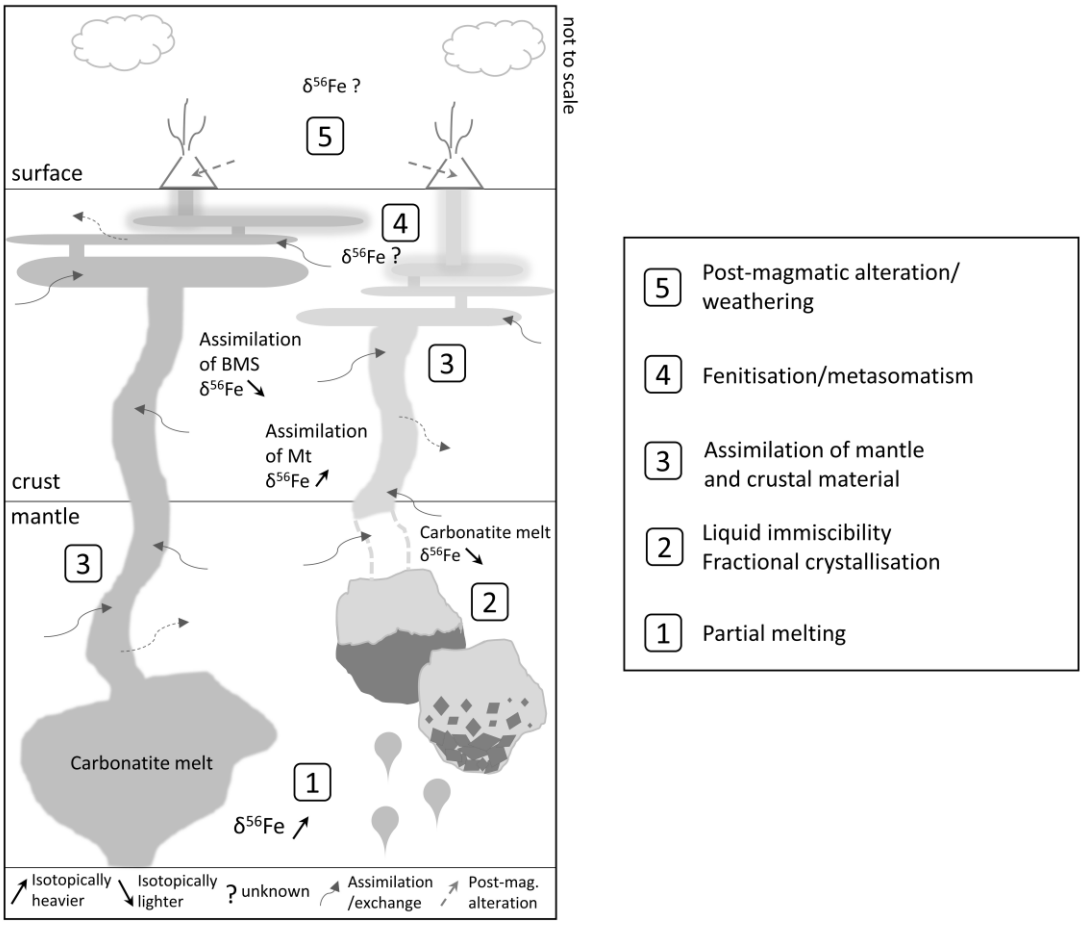

Figure 10.6 Schematic cartoon showing the possible changes in $\delta^{56}Fe$ values during two types of carbonatite genesis. Left: direct partial melting producing a carbonatite melt, right: partial melting followed by crystal fractionation/liquid immiscibility to produce a carbonatite melt; immiscibility and fractionation processes could also occur in the crust. Idea and elements from this figure were taken from Bilenker et al. (2018) and references therein (Mercier-Langevin et al., 2012; Naldrett, 1997). BMS = base metal sulphides, Mt = magnetite.

10.4.5. Conclusion

In this study we present high precision Fe stable isotope data for a suite of 12 carbonatite samples from five different localities ranging in age from 131 to 1299 Ma. Our data differs clearly from the value of Earth's mantle ($\delta^{56}Fe$ = +0.025±0.025‰, Craddock et al., 2013), being on average lighter ($\delta^{56}Fe$ = -0.08 ±0.32‰) but similar to global carbonatites presented in Johnson et al. (2010). Our data shows variations within each outcrop, which is thought to be caused by either modal abundance and distribution of isotopically light or heavy mineral phases or related to processes responsible for emplacement sequences as are observed in carbonatites from Jacupiranga, Brazil. As was already shown in the main chapters of this thesis (*c.f.* chapters Chapter 5, Chapter 6 and Chapter 7), carbonatites have experienced a complex petrological history and extensive post-magmatic alteration. Thus, in addition to the control by modal abundances of isotopically light/heavy minerals phases, Fe isotopes in whole-rock carbonatites are likely fractionated due to processes such as 1) partial melting, 2) crystal fractionation and/or immiscibility processes, 3) assimilation of mantle or crustal components during ascent, 4) metasomatism and/or 5) post-magmatic alteration, weathering or fenitisation processes.